Interfacial dynamics driven by Marangoni stresses on a slowly moving liquid film

A thesis submitted to the University of Sheffield for the degree of
Doctor of Philosophy

Buddhika Naleen Hewakandamby

Department of Chemical and Process Engineering

2002 September

Supervised by: W.B.J. Zimmerman

To my parents

Acknowledgements

There are many people I would like to thank for their involvement in this project. Without the help and guidance of my supervisor, Will Zimmerman, this work would have been impossible. He has been an endless pool of resources, knowledge and help to which I am in debt most.

I would like to express my gratitude to Dr. Andrew Yeckel for many interesting discussions on FEM code and related matters. My thanks also extend to Dr. Ralph Goodwin III who kindly gave us permission to use the FEM code.

A big thanks to all group members and friends, specially Laurent for endless encouragements and support through out last three years.

Finally, I would like to thank my parents, my wife Nilmini and my brother Mahesh for unconditional love and morale support at difficult times.

Abstract

Differential surface tension is a common phenomenon in many chemical and biomedical processes. Localised surface tension gradients due to differential surface loading in thin films give rise to a moving shock front in the direction of higher surface tension. Existence of a background flow enhances the shock wave giving rise to wave breaking and wave separation mechanisms. The effect of a background flow field on Marangoni stress induced shock fronts were investigated in this thesis. Furthermore, a numerical procedure to find approximate solutions to the fully nonlinear flow problem that arises due to Marangoni spreading is proposed.

A set of surface evolution equations that incorporates the effects of the background flow field is studied in two major respects: (i) breaking the horizontal symmetry and (ii) nonlinear accretion leading to shock front breaking or separation. The evolution of the surface is evaluated by numerical simulations for a wide range of parameter values. The investigation showed that there are two breaking mechanisms switched by the value of Péclet number. Furthermore it showed that the life time of the shock front is determined by the volumetric flow rate of the film. It is shown here that a weak Marangoni force generates a pure capillary gravity wave that propagates faster than the surfactant front.

It is customary to use the lubrication approximations to simplify thin film problems. As a result, the inertial terms in flow equations and nonlinear terms in surface stress balances become excluded. To analyse the fully nonlinear flow, a finite element (FEM) analysis is proposed. The simulations shows that the lubrication theory holds globally in predicting the spreading rates but fails to do so locally until a quasi-steady state is reached. The FEM model shows the formation of two counter-rotating vortices at the beginning which diminish as time evolves. The FEM results are compared with the lubrication theory simulations. FEM model shows rapid film thinning forming extremely thin films within a short period of time. Though detailed transport mechanisms differ, both methods are in close agreement in predicting the spreading rates.

Contents

Bibliography

List of Figures

List of Tables

Chapter 1

Introduction

1.1 Film flows and surface tension

Spreading of surfactant on a liquid substrate has been the centre of a stream of investigation for years. Simply, the spreading alone has posed an interesting problem due to the surface physics involved. The related fingering instability leading to film rupture and formation of a dry spot due to excessive thinning of the film under the influence of a surfactant still poses a challenge that has to be resolved. The physical system is modelled using heavy simplification, namely lubrication theory, where one assumes that the inertial terms compared to viscous terms in flow equations are negligible. It is customary to use lubrication theory approximations to simplify the modelling of thin films. Through these assumption, two coupled evolution equations have been derived by Gaver and Grotberg [33] and studied by many others, focusing on similarity solutions [54, 55, 52, 99]. A detailed discussion of these developments will be presented in chapter 2.

When a surfactant drop is placed on a quiescent substrate, the resulting force imbalance induces a shear stress differential causing fluid flow locally, giving rise to a shock wave. In the case of a drop, this wave forms a ring that moves radially outward with decaying wave height given that the surfactant mass remains constant. In the case of a planar front it is a ridge extended along the span-wise direction. In either case, a depression behind the shock front can be observed. The sole mechanism of flow induction is the capillary traction caused by the differential surface tension across a relatively small distance.

For a fixed concentration profile with a localised sharp gradient imposed on a *flowing* liquid film, Zimmerman [119] showed the possibility of the existence of a hydraulic fall or jump depending on the ratio of surface tensions upstream and downstream at inviscid limit. In a later study Hewakandamby and Zimmerman showed that the flow always becomes unstable if sharp surface tension gradients exist along the flow direction on a thin film [44, 43], even for small Reynolds numbers. Considering a step change in surface tension, Zimmerman deduced an evolution equation for a surface as

$$\eta_t + (1 + \sqrt{Fr_i})\eta_x + \frac{5}{2}\varepsilon\eta\eta_x + \beta_i\delta^2\eta_{xxx} = 0$$

in the inviscid limit [119]. η is the deviation of the surface from its undisturbed position. Fr_i and β_i assume different values across the surface tension jump. This produces a hydraulic bore like structure on the surface. However, this does not describe either the evolution of the flow field within the bulk or the spreading of the surfactant fully.

Film flow on an inclined plane was studied by Yih [115] and then developed by many others in many aspects. The stability of the free surface film flow is studied in detail by many among which the work of Yih [115], Benjamin [7] and Smith [98] explain the stability in great detail. The propagation of waves on the free surface of such flows were analysed in great detail by a numerous number of researchers. The work of Nakaya [77], Tilley *et al.* [102] and Ramaswamy *et al.* [85] among others describe the wave evolution for both incline and vertical film flows with finite but constant surface tension. For a comprehensive summary the reader is referred to [13] and references therein. We use the lubrication theory approximation (only up to $\mathcal{O}(1)$ terms) to combine the Marangoni effects and capillary wave driven by pressure gradient or body forces.

The spreading and propagation of the resulting shock front under the influence of bulk flow is important in many areas especially medical science and newly emerging microfluidics technology. In next section we discuss some of the engineering applications where the spreading influenced by the bulk flow is important.

1.2 Applications of surface tension gradients

Flow induction due to surface tension gradients occurs in many applications. Delivery of medicine in the form of inhaler mist to treat pulmonary diseases including Surfactant Replacement Therapy (SRT) is one of the major applications. Occurrence of flow anomalies that retard the performance of pack-bed distillation towers are attributed to surface tension gradients. We first describe the Marangoni effect on distillation columns as a motivation for this study.

Low throughput packed bed distillation columns

Marangoni effects in distillation columns are known to influence the efficiency of the column [84]. In distillation, a reflux with increasing surface tension is referred to as a positive system, whereas decreasing surface tension is called a negative system. The surface tension variation of the reflux is attributed to the concentration distribution rather than the temperature gradient along the column. It is now a well established fact that the sign of the surface tension gradient affects the tray behaviour, especially for small columns [84]. A positive system creates a stable film on the packing surface. Film breakup, dry spots, rivulet flows and capillary waves were reported in negative systems [106]. Figure 1.1 shows these two flow patterns with respect to flow over a saddle packing schematically (according to the description given in [106]). These

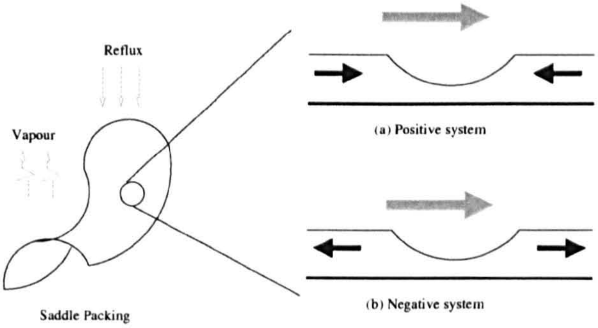

Figure 1.1: Schematic representation of possible flow anomalies on a saddle packing. Positive systems stabilise the film due to Marangoni induced flow while negative systems destabilise it by forming dry spots, giving rise to rivulets. The blue colour arrow marks the overall flow direction and the dark arrows indicate the local flow directions.

flow anomalies on packing surfaces hinder the separation process and thus lower the column efficiency. Figure 1.2 from Proctor [84] shows the plots of height of overall gas–phase transfer unit (H_{og}) against the liquid rate per unit packing area. The difference in performance is clearly visible for positive and negative systems. In positive systems the film uniformity is enhanced by liquid flow towards the thinned areas which have relatively high surface tension. This flow enriches the depleted area, enhancing the performance. In negative systems the thinned areas have relatively low surface tension which destabilise the film on the packing surface. To mitigate this problem, a thorough understanding of hydraulic behaviour enforced by the surface tension gradients is necessary. Furthermore, the effects of surface tension gradients on mass transfer are considered to be important [106]. Local flow cells formed by surface tension gradients alter mass transfer rates. An introductory description of the observations on these effects can be found in [120]. It is reported that these effects vanishes with high liquid flow rates (high reflux rates).

Pulmonary lubrication by surfactant replacement therapy

Though a background flow is not directly involved, the Marangoni induced flow within the pulmonary capillaries due to aerosol droplets is an important process

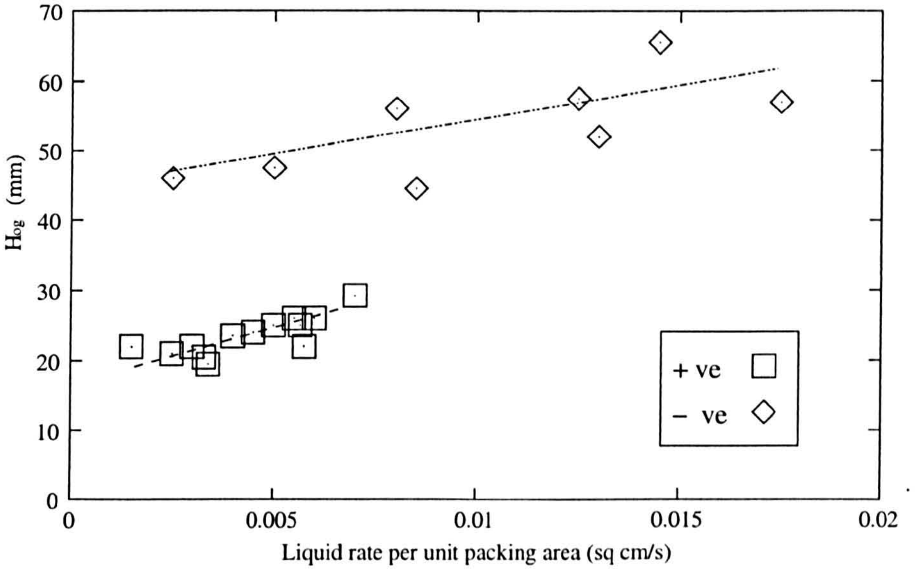

Figure 1.2: HTU values for Sulzer "DX" structured gauze packing. After Proctor *et al.* [84]

to consider. Alveoli, airways and trachea collectively have a surface area of about 100m^2 in a lung of an adult [36]. The inner wall of the pulmonary system is covered by a thin liquid lining enriched with naturally occurring surfactant. The surfactant reduces the surface tension of the lining, reducing the work done by an individual during the respiration cycle. Under the influence of the surfactants, the liquid lining flows against gravity to keep the all surfaces wet and functional. The medical condition that arises from insufficient surfactant concentration in the pulmonary fluids is the cause for respiratory distress syndrome (RDS); a common ailment that pre–mature babies suffer due to glandular malfunctions. As a medication, surfactants are introduced externally in the form of a mist. This is generally called surfactant replacement therapy (SRT). When aerosol droplets are deposited on the inner lining, the resulting surface tension gradient spreads the surfactant and medicine. Spreading within the lung is due to Marangoni advection as well as diffusion. However the concentrations of the cocktail of medication and surfactant in aerosol mist have to be carefully determined to prevent the formation of dry spots which may be harmful to alveoli walls. The spreading actually occurs on a thin film subjected to cyclic motion (in phase with the respiratory cycle). The spreading of surfactant drops on a lung lining, both passive and soluble, were studied by Grotberg and Jensen [37], Grotberg, Jensen and Halpern [38] and more recently by Craster and Matar [17] considering the bilayer configuration with non–Newtonian characteristics of the mucus.

Microfluidics

Understanding of surface tension variations and interactions with bulk flows of small magnitudes are demanded in the newly emerging class of technology called *microfluidics*. Microfluidics, still in the research and development stage, is a hybrid of the disciplines of biology, chemistry and engineering where the possibility of fabricating miniaturised process equipment for unit operations is investigated. It also researches the ability to integrate and automate such equipment. Microfluidics is a combination of three branches of research: 1. development of new methods to fabricate fluidic systems, 2. invention of components from which to assemble functionally complex fluidic devices and 3. examination of fundamental behaviour of fluids in micro-channels [112].

Micro–channels are generally fabricated by using photolithographic methods using silicon or glass substrates by rapid prototyping of polyelastomers or by precision machining [73]. In contrast to the conventional, etched micro–channels, a new type which uses surface tension properties to confine the liquid was tested recently [62]. A thin liquid layer held between two parallel surfaces form two menisci due to capillarity, holding the liquid between them(see Figure 1.3). A hydrophilic pattern is generated on a hydrophobic substrate. Two surfaces, with mirror image patterns placed one on the top of the other, spaced using a spacer (60–100μm), forms the basic device (see Figure 1.3). The liquid stream supplied to the device by means of capillary flow or a fluidic pump, only wets the channels guided with the hydrophilic patterns. The two surfaces provides the top and bottom guides. Surface tension

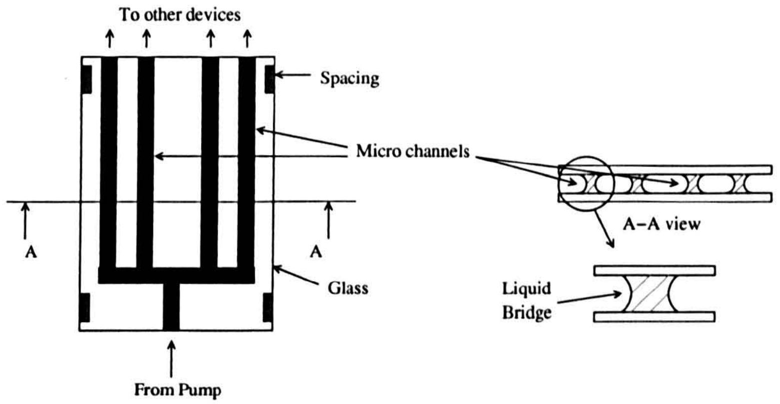

Figure 1.3: The surface tension confined microfluidic device (STCM). Nanofilms of selective hydrophilic chemical were deposited to form patterns on a glass substrate. Two plates with mirror images of a pattern are put together to form the channel guide. Surface tension forms a liquid bridge completing the confinement of the bulk. Micro-channels of $200 - 1800\mu m$ in width and $100\mu m$ in depth can be easily produced. After Lam *et al.* [62].

effects form the side walls (capillary forces). The liquid flow occurs within the two surfaces, and the menisci has less flow resistance than conventional channels. The method is called Surface Tension Confined Microfluidics (STCM) and provides a cheaper method of fabricating micro-channels. The patterns are simply printed on to substrate by altered plotting devices. The depth of the channel is decided by the thickness of the spacer used. Channel widths that can vary from $200 - 1800\mu m$ were reported [62]. Figure 1.3 shows a STCM unit in detail.

The liquid streams were mixed or made to react within STCM units. When new materials form within the liquid bridge, there is a possibility of variations in surface tension making the confined walls unstable or there may be waves propagating along the channel in the form of shock fronts. The flow in STCM is a subject of on going research [62].

The existence of a background flow in the above cases relates them directly to the scope of this thesis. There are many other applications of surfactants and surface tension effects such as anti-icing coatings, de-wetting micro chips etc. which we do not consider here. In the next section we define the scope of this thesis.

1.3 Scope of this thesis

As mentioned above, the spreading of surfactant drops, strips and fronts on stationary substrates were well studied over the passing decade but very little or no attention has been focused on the study of the influence of a background flow on spreading as well as on the evolution of the resulting capillary wave. Existence of an induced pressure gradient or the body force component due to inclination would effect the wave propagation and spreading rates. Furthermore the simplifications made in lubrication theory approximations to eliminate the strong nonlinear effects of the bulk phase [33, 52, 54, 56, 99] were taken for granted. The initial effect of large surfactant gradients almost violates the very basic assumptions of the lubrication theory. Nevertheless, the predictions made using this simplified theory hold closely with the limited experimental data available.

Within the framework of this thesis we investigate

- the onset and propagation of surface disturbances under surface tension gradients on flowing films
- the appropriateness of lubrication theory for modelling free surface flows

To analyse the problem, we developed a numerical simulation engine using the method of lines. Coupled sets of evolution equations were derived using lubrication theory approximations incorporating a background flow field and spatio–temporal evolution of surface loading and the resulting capillary wave was examined for a wide range of parameter space. We formulate a Marangoni number that measures the sensitivity of the substrate surface tension to concentration differences.

The importance of the nonlinear inertial terms in the flow equations that are dropped in almost all previous work were examined qualitatively and quantitatively. A finite element code was adopted and modified to simulate the fully nonlinear system of equations. The two methods, namely lubrication theory evolution equations and the fully nonlinear flow system, were compared to estimate the strengths and weaknesses of either system in predicting the evolution of the dynamical system in space and time.

1.4 Overview of the thesis

In chapter 2, we discuss fundamental ideas related to surface physics and then summarise briefly the work of many others with emphasis on the simplifications. We introduce the phenomenon of surface tension and discuss the effects of surfactants on liquid interfaces. The literature survey is divided into three main parts for mathematical modelling of insoluble and soluble surfactants and for experimental investigations.

In chapter 3, we discuss the mathematical model and numerical solution schemes. We derive evolution equations for film height and surface loading using lubrication theory approximations. The inclusion of a background flow results in an equation with combined components for capillary wave and Marangoni excitation of the surface evolution. In the second part of the chapter, we present the development of solution schemes for the problem. The coupled surface evolution equations were solved using method of lines (MOL). A detailed description of the implementation of MOL is given. The finite element method using the weak (Galerkin's method) formulation is discussed briefly. The use of elliptic mesh generation coupled with diffusion type equations to enable mesh movements to capture the free surface dynamics are described in this chapter.

Results from lubrication theory evolution equations using MOL are presented in chapter 4. Two configurations of surfactant gradients are examined. The influence of parameters such as Marangoni number, Péclet number etc. are investigated. We use stream functions to illustrate changes to the bulk flow. The Marangoni number and Péclet numbers initiate different dynamics under the influence of bulk flow.

Unlike for the stationary substrate where the capillary ridge exists for a long time, the wave breaks within a short, finite period.

The FEM analysis is carried out in chapter 5. The simulation results were discussed, putting emphasis on the differences and similarities with the LT model. We extract a ratio of length scales using the nonlinear model. The flow within the liquid substrate is discussed in this chapter.

Chapter 6 we investigate the effects of nonlinearity for a wide range of parameter values. Finally, the conclusions are made in chapter 7.

Chapter 2

Surface tension, surfactants and Marangoni effect

2.1 Introduction

Though small compared to many force fields, surface tension gives rise to many important phenomena that has fascinated many scientists. It gives rise to many commonplace phenomena in every day life as well. Formation of soap bubbles, though mundane, vividly illustrates several surface tension effects. The effects of surface and interfacial tension have been used in many industrial applications too. Langmuir-Blogget film coating and slide coating (a precision coating process) are two of many applications with direct surface tension effects. Foams, colloids, cosmetics and pharmaceuticals provide a rich array of processes where variation in surface tension occurs over short lengths, motivating the setting for this thesis.

Variation of air–liquid surface tension gives rise to interesting transport phenomena. Although the Rayleigh-Bénard instability is attributable to buoyancy effects, the original experiments actually demonstrate surface tension variation induced pattern formation [23] . However, the differential cooling/heating or uneven spreading of surface contaminants can cause surface tension to vary along a liquid film surface, causing instabilities to form and propagate. We refer readers to [118] for a full review of the surface waves induced on a film at rest due to transverse temperature gradients. This may affect product quality in the case of film coating processes. In this thesis we examine the nonlinear wave dynamics of the thin films under such surface tension gradients with particular concern for cases where the film is in motion.

In §2.2 we briefly discuss the surface physics of liquid films. Here we introduce the terms and physics that we use in later chapters. The behaviour of surface tension in the presence of surfactants is described in §2.3. Additionally, we examine the nature of surfactants. Section 2.4 summarises the theoretical and experimental research on the effects of surface tension variations in thin films to date. A brief description of a few industrial applications of surface tension is given in chapter 1, §1.2.

2.2 Physics of surface tension

In the case of systems experiencing capillary forces, i.e. where a surface separates two or more bulk phases, the mechanical equilibrium is not only decided by factors such as hydrostatic pressure and gravitational pull, but also by the forces associated with surface tension, taking in to account its physicochemical nature. Whenever two immiscible fluids are in contact with one another they are separated by a molecularly thin layer called an interface whose properties are different from the two bulk phases. Throughout this work, the interface between liquid/gas system in referred to as a *surface* .

A fluid interface is not truly a two-dimensional material entity though frequently referred to as a one. It consists of molecular layers in equilibrium. But with respect to macroscales treated in this thesis, an interface is considered as a two-dimensional, singular surface. This generalisation comes from the assumption that the fluids can be described by a continuum approximation such that it is possible to define an element of liquid that is small compared to active length scale of intermolecular forces but large enough to contain sufficient number of molecules. For a complete discussion on this the reader is referred to Israelivich [49].

2.2.1 Surface tension

Surface or interfacial tension (represented by σ) is described as the force tangential to the liquid surface, acting normal to a line of unit length hypothetically drawn on the surface. It has the dimensions of force per unit length and is usually expressed in dyne cm^{-1}.

The origins of surface tension can be explained more rigorously using the mean field approximation in the context of a gas/liquid interface. Liquid molecules in the bulk are attracted to each other by intermolecular forces. These intermolecular forces induce molecules to move randomly but averaged over time have no net effect. Conversely, there is an imbalance of forces on a molecule at the gas/liquid interface due to the fact that it is partially surrounded by molecules of the liquid bulk. Consequently, the molecules at the surface are pulled into the bulk of the liquid which tends to shrink the surface. Therefore the surface of the liquid behaves as if it were under tension as a stretched membrane. This phenomenon is called the surface tension. Many hydrostatic situations can be simply analysed by the variational principle of minimum surface area due to this feature.

An alternative description based on free energy can be given as follows. As described in above paragraph, attractive energy per molecule at the surface must be a fraction of one in the bulk. Therefore the energy of a surface molecule should be higher than that of an interior one. To minimise the energy at the surface, the interface tends to contract, giving rise to membrane-like behaviour. Therefore surface tension can be redefined as the surface free energy per unit area at constant temperature. At constant temperature and surface concentration, this explanation results in a thermodynamic equation for surface tension $\sigma = \frac{\partial F}{\partial A}$ with Helmholtz free energy $F = U - TS$ and with surface area A. We use this equation to examine the factors that affect the surface tension in next section.

2.2.2 Factors that affects surface tension

The two dimensional approach to the interface enables us to treat it as a thermodynamic entity with its own internal energy U^s and entropy S^s (the superscript s denotes the quantities that are defined for an interface). Let the number of molecules of various species be ${n_j}^s$. The first law of thermodynamics for the interface can be written as [20, 63]:

$$dU^s = TdS^s + \sum_j \mu_j dn_j^s + \sigma dA \tag{2.1}$$

where T is the temperature and μ_j are interfacial chemical potential.

Using the $F = U - TS$ together with (2.1) and assuming n_j^s to be a constant (surface loading does not change), one can write

$$d(Af - A\sigma) = -S^s dT - Ad\sigma \tag{2.2}$$

where f is the specific Helmholtz free energy. Hence $f = \sigma$. Therefore the Equation 2.2 reduces to

$$\left(\frac{\partial \sigma}{\partial T}\right)_{n_j} = -\frac{S^s}{A} < 0 \tag{2.3}$$

therefore

$$\left(\frac{\partial \sigma}{\partial T}\right)_{n_j} < 0 \tag{2.4}$$

This shows that at constant surface concentration, surface tension decreases with an increase in temperature. This phenomenon is called normal thermocapillarity.

In practise, the surface tension decreases approximately linearly with increasing temperature. A typical value for liquid air interface is about $\frac{\partial \sigma}{\partial T} = -0.1\,\mathrm{mN\,m^{-1}\,K^{-1}}$ [83].

The extensive form of (2.1) can be written as

$$U^s = TS^s + \sum_j \mu_j n_j^s + \sigma A \tag{2.5}$$

when the intensive variables T and σ are assumed constants. The variational form of (2.5) can be combined with (2.1) to obtain

$$-S^s dT + \sum_j n_j^s d\mu_j + A d\sigma = 0. \tag{2.6}$$

which is generally known as the Gibbs adsorption equation. Assuming that there is only one species present at the interface to simplify the equation, when temperature is constant, one can find

$$n^s = -A \left(\frac{\partial \sigma}{\partial \mu}\right)_T . \tag{2.7}$$

By definition the surface loading $\Gamma = \frac{n^s}{A}$. Therefore the surface loading can be rewritten as

$$\Gamma = -\left(\frac{\partial \sigma}{\partial \mu}\right)_T , \tag{2.8}$$

immediately followed by the chain rule expansion

$$\Gamma = -\left(\frac{\partial \sigma}{\partial \Gamma}\right)_T \left(\frac{\partial \Gamma}{\partial \mu}\right)_T . \tag{2.9}$$

Since the surface loading $\Gamma > 0$, the thermodynamic inequality $\left(\frac{\partial \Gamma}{\partial \mu}\right)_T > 0$ forces the sensitivity of interfacial tension with respect to surface loading to be

$$\left(\frac{\partial \sigma}{\partial \Gamma}\right)_T < 0. \tag{2.10}$$

Therefore the interfacial tension decreases as the surface concentration increases. This phenomenon is sometimes referred to as solutocapillarity [78]. Unlike for the case of temperature, the change of surface tension with increase of surface concentration is complex. There are many equations of state relating surface tension and concentration [31, 27] which we discuss in detail in §2.3. An oscillatory instability of surface tension with increasing surface loading was recorded by Kovalchuk *et al.* [60, 59]. Instead of decreasing smoothly, the surface tension tends to oscillate within a narrow band while keeping an overall tendency of a negative gradient. We neglect this behaviour as the time averaged surface tension falls on a smooth line.

The dependency of surface tension on surface concentration and temperature give rise to an imbalance in surface stresses requiring the underlying fluid to move. We discuss this in detail in next section.

2.2.3 Marangoni Stresses and induced flow

Surface tension of a pure liquid at constant temperature is a constant and is a thermodynamic property of the liquid (e.g. water at 20°C has a surface tension of 74 dyne cm^{-1}). As shown above the surface tension is affected by the temperature and/or surface concentration of a dissolved substance. A non-uniform temperature or concentration distribution along the surface results in variation in surface tension. The surface tension at a hot or high surface loading point is reduced relative to its neighbourhood. This causes an imbalance in surface forces drawing the liquid surface to move toward the higher surface tension. This motion set up by a surface tension gradient is called the Marangoni effect (Fig.2.1). The surface forces arising from differential surface tension are called Marangoni stresses [96]. Figure 2.1 is a schematic representation of the situation. The dark circles shows hydrophilic heads attracted to the liquid phase and the density of circles is representative of the surfactant concentration. Shear flow establishes in the opposite direction of the concentration gradient.

Figure 2.2 shows the Marangoni induced flow in a deep liquid. The velocity field

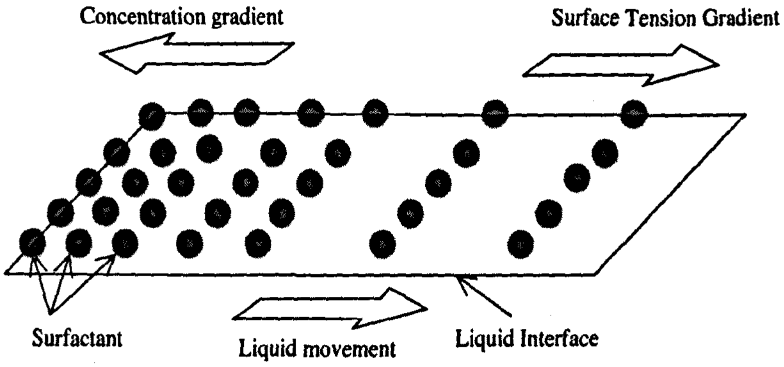

Figure 2.1: Marangoni effect due to a concentration gradient. The surface concentration lowers the surface tension giving rise to a gradient in the direction of decreasing concentration. Resulting surface stress cause the fluid to move in the direction of higher surface tension.

penetrates into the bulk due to viscous diffusion. The localised flow regime migrating into a quiescent fluid adjusts the pressure field in the case of a deep layer so that the surface is forced to corrugate at the leading edge of the spreading layer. In thin layers, viscous diffusion quickly sets a boundary layer flow in motion, compelling liquid mass in the direction of the surface tension gradient. Conservation laws demand a change in liquid height; thus forms the well known advancing capillary ridge.

Marangoni effects due to temperature variations have been well studied [16]. The Bénard–Marangoni instability with free surface is accredited to buoyancy as well as to the Marangoni effect. A dimensionless number called the Marangoni number is defined based on temperature sensitivity of surface tension as

$$Ma = \frac{(-\partial\sigma/\partial T)\Delta T d}{\mu\kappa} \tag{2.11}$$

where κ is the thermal conductivity of the liquid. The wave instability of a surface heated from above (density gradient is stable) is directly controlled by the Marangoni effects (see [32] and references therein). Note that there are different sign conventions for heating from below [23] and above [32]. Takashima *et al.* has shown that there is a critical (minimum) Marangoni Number, $Ma = 10^4 - 10^5$, above which the

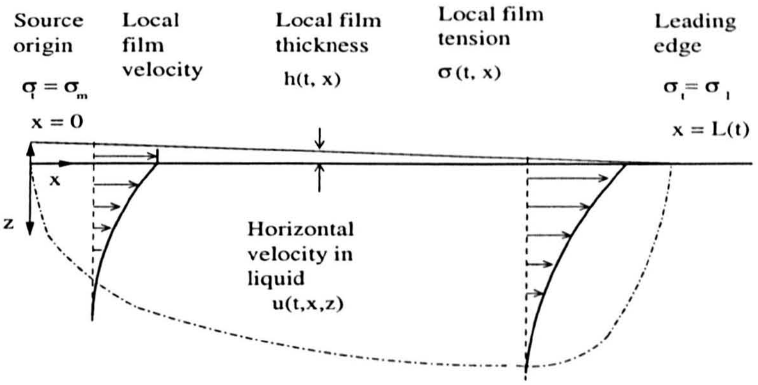

Figure 2.2: Spreading of an oil film on water due to surface tension. The z scale has been expanded to show detail in the water phase. The surface stress force the movement of water just below the surface forming a boundary layer. A higher surface velocity can be seen at the oil/water boundary where the surface tension gradient (i.e. concentration gradient) is maximum. The viscous forces transfer the momentum in to the bulk with time in the case of a deep liquid layer. (After Camp and Berg [11]).

liquid layer is unstable for heating from above [100].

2.2.4 Spreading coefficient

When a liquid drop is placed on a liquid or solid surface, it spreads according to

$$S = \sigma_l - \sigma_d - \sigma_{l,d} \tag{2.12}$$

where σ_l and σ_d are the surface tension of liquid substrate and the drop respectively, while $\sigma_{l,d}$ is the surface tension of the interface between bulk liquid and the drop. Therefore if $S > 0$ for a solution drop, then it spreads spontaneously (i.e. decreasing free energy) on the substrate until it covers the surface completely, forming a monomolecular layer (e.g. an oil drop on water). On the other hand, if $S < 0$, the drop may initially spread but retract forming a stable lens (e.g. benzene on water). For a spreading surfactant monolayer one can define a spreading coefficient $S = \sigma_0 - \sigma_m$ where σ_0 and σ_m are the surface tension of pure liquid and surfactant saturated liquid respectively.

Since we have discussed the physical phenomenon of surface tension we now look toward the effects of surface active material on a liquid film.

2.3 Surface tension and Surfactants

2.3.1 Behaviour of surfactants

From (2.10) one can deduce that $\left(\frac{\partial\sigma}{\partial n}\right)_T < 0$. Then the effect of molecules of a secondary substance present at the interface becomes clear. There is a specific class of chemicals that is active at interfaces between solid/liquid, liquid/liquid, or liquid/gas pairs of phases. They are known as surfactants or SURface ACTive AgeNTs. These chemicals not only accumulate at interfaces, but drastically change the properties of those interfaces. Soap is a common example.

The above described characteristic feature of surfactants occurs due to the amphiphilic molecular structure. In the context of an aqueous/gas interface, surfactant molecules have a hydrophilic "head" that has an affinity for the liquid and a hydrophobic "tail" that is expelled from the liquid phase. The hydrophilic group of the surfactant is either polar or charged. In most common surfactants, either an cationic or anionic charge composes the hydrophilic head. The hydrophobic tail most commonly is a simple hydrocarbon group [15]. The ionic head is attracted to the aqueous phase due to the bipolar nature of the bulk fluid while it repels the hydrocarbon group, making the substance active at the interface only. The amphiphilic structure enables surfactants to have different forms at the interface. If sufficiently soluble, at low concentration it forms a monolayer at the interface. At high concentrations, surfactant molecules aggregate to form micelles. Micelles are the collection of molecules with their hydrophobic tails inward and hydrophilic heads outward (minimising surface energy of the micelles). They can be spherical, disks or cylindrical in geometry. The minimum concentration at which micelle formation

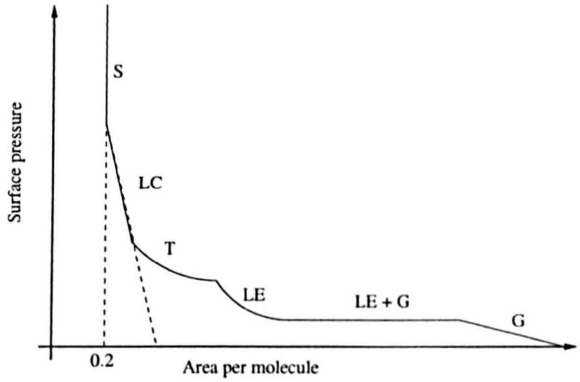

Figure 2.3: Generalised $\pi - A$ isotherm for insoluble monolayers at the air/warter interface showing the relationship of the various phases. G = gaseous; LE = Liquid–expanded; T = transition; LC = Liquid–Condensed; S = solid. In G surface pressure roughly inversely proportional to area per molecule. LE +G is a mixed phase region. In this coexistence region surface pressure is constant at very low values. i.e. very low interactions between adjacent molecules. In liquid–expanded (LE) region molecules are not closely packed. Greater degree of lateral molecular interactions occur in region T. Surfactants undergo a first order transition from LE to LC. Further compression leads to a solid phase S, through condensing process at LC. Further compression leads to a total collapse of monolayer (After Clint [15]).

occur is called critical micelle concentration (CMC). Since the surfactant molecules can exist as monomers, there may be a dynamic equilibrium, molecules leaving and joining the aggregate at a timescale that can be as fast as microseconds [15]. The lower the CMC, the more active the surfactant is. Therefore strong surfactants form a monomolecular layer at the interface with very small diffusion into the bulk. These kinds of surfactants can be categorised as insoluble since the bulk concentration is negligible. When the surfactant is insoluble, upon the compression of the surfactant monomolecular layer, several stages of phase changes occur due to the intermolecular interactions. Adamson [1] and later, Clint [15], discussed these changes in detail with respect to a surfactant monolayer at a liquid/gas interface. For the completion of this discussion we reproduce the surface pressure–area ($\pi - A$) diagram. (The surface pressure π is the difference between the surface tension of pure liquid and the surface tension of the solution). Figure 2.3 shows the distinct phases that exist when compression takes place.

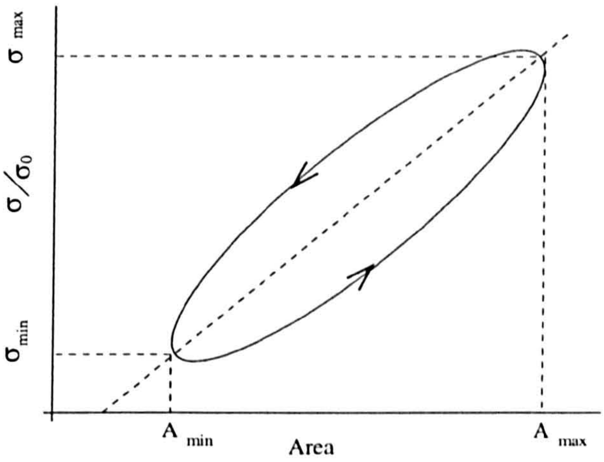

Figure 2.4: A diffusion model $\sigma - A$ hysteresis loop derived from Horn and Davis[46]. Surface area A is subjected to cyclic oscillation and the corresponding traverse on curve is counterclockwise.

Another important feature is the apparent surface tension hysteresis when the interface (with a surfactant) is subjected to a cyclic oscillation of surface area [46]. Under these circumstances, the σ–A plot is not a single valued function but is a loop as shown in Figure 2.4 since the surface tension has two values depending on its processing history. Horn and Davis [46] studied the apparent surface tension hysteresis analytically on an oscillating liquid sphere and concluded that the effect can be produced by at least four independent mechanisms: (i) the bulk liquid contains a soluble surfactant and sorption is diffusion limited; (ii) sorption kinetics at the interface determine the exchange rates of the soluble surfactant between the surface and the bulk liquid; (iii) the surface layer is insoluble but exhibits viscoelastic properties; and (iv) the bulk liquid, independent of the interface, exhibits viscoelastic properties. The Lucassen type waves [65, 118] that appear at surfaces due to imposed conditions (mechanical force or surface tension variation), would oscillate the surface longitudinally forcing surface area to oscillate incorporating the conditions (iii) and (iv) above. However, this effect is not examined within the scope of this thesis.

2.3.2 Equations of State

The behaviour of surfactants on a substrate can be described to a certain degree of accuracy using thermodynamic rules (e.g. Henry's law). Since no material is absolutely insoluble, the adsorption/desorption isotherms are applicable to almost all surfactants. For dilute surfactant concentrations intermolecular interactions are unimportant and therefore the variation of surface tension with concentration can be considered as linear [1]. We seek the simplest relationship

$$\sigma^*(\Gamma) = \sigma_0 - \frac{(\sigma_0 - \sigma_m)}{(\Gamma_m - \Gamma_\infty)}\Gamma^* \tag{2.13}$$

where

$$\sigma_m \leq \sigma^*(\Gamma) \leq \sigma_0 \qquad \text{when} \qquad \Gamma_m \geq \Gamma^* \geq \Gamma_\infty$$

where σ_0 and σ_m are the maximum and minimum surface tensions respectively. The maximum σ_0 is the surface tension of uncontaminated surface and the minimum surface tension σ_m occurs at micelle concentration or the maximum concentration Γ_m. Γ_∞ is the concentration at a far away point from Γ_m and usually assumed as zero. Apart from this linear assumption there are many nonlinear equations of state in use. For instance, Borgas and Grotberg [10] demonstrated an equation of state

$$\sigma^*(\Gamma) = (\beta + 1)(1 + \Theta(\beta)\Gamma^*)^{-3} - \beta$$

where

$$\Theta(\beta) = \left(\frac{\beta+1}{\beta}\right)^{\frac{1}{3}} - 1 \qquad \text{and} \qquad \beta = \frac{\sigma_m}{S}$$

for monolayers. But assuming the CMC to be very small, many have used the linear equation of state (2.13) [99, 50, 2]. This assumption of low surface concentration leads to a secondary assumption that the interactions of adsorbed molecules are negligible. This correspond to the $LE + G$ and G regions in Figure 2.3. Considering the analogous behaviour of an ideal gas, one can write the total kinetic energy of a two–dimensional surface as $(\sigma_0 - \sigma^*)A = \mathrm{k}T$ where A is the surface area, k is the Boltzmann constant and T is the temperature in Kelvin. With the analogy between the mechanisms, the linear approximation of $\sigma - \Gamma$ relationship can be justified. For a detailed discussion on this point reader is referred to [31].

2.4 Previous studies on Marangoni induced flow

Instabilities that arise due to surface tension gradients (as a result of uneven distribution of a surface active chemical or temperature) have posed an interesting engineering and scientific problem. Many have investigated the phenomenon in the last two decades with an emphasis on spreading of a surface active material on a substrate. The main lines of investigations on surface tension induced flow are: (i) thermocapillary flows; (ii) spreading of a liquid on a solid and (iii) spreading of a surfactant drop on another liquid. Thermocapillary flows were studied in great detail with regard to the Bénard–Marangoni instability [16]. Transient thermocapillary convection flows have been studied as well [81, 45, 110]. For a detailed review of theory see Davis [19], and for a concise survey of recent experiments reader is referred to Schatz and Neitzel [92]. Spreading of a thin liquid film on a plate driven by a thermal gradient counteracting gravity was first examined by Ludviksson and Lightfoot [66]. They investigated the rise of liquid film beyond the equilibrium menisci experimentally as well as theoretically. Later on, Bertozzi *et al.* [76, 9, 8] formed a more rigorous theoretical analysis which predict the spreading more accurately. They included the curvature effects in their theory which Ludviksson and Lightfoot excluded in their study. The fingering instability that occurs at the advancing contact line, attributed to the precursor film thickness has been studied in detail by Bertozzi [8] and later on by Parrot [80]. The effect of surface active material spreading on a liquid substrate has been well investigated. We examine the results of those studies in detail in section §2.4.1 and §2.4.2. For a concise review of thin film dynamics including thermocapillary and solutocapillary flows see Oron *et al.* [79].

2.4.1 Theoretical analysis for solutocapillary flow

The theoretical treatment of surfactants spreading on liquid fall into two categories depending on the value of the ratio $\epsilon = h/L$ where h is the liquid depth and L is the longitudinal length. Where the aspect ratio $\epsilon \ll 1$, the film is considered to be thin while $\epsilon \gg 1$ is treated as a deep fluid. These two cases are treated differently. When the liquid layer is thin, a long wave approximation is used in which ϵ is treated as a small parameter to simplify the flow equations, otherwise known as lubrication theory. This leads to two mutually coupled evolution equations for liquid layer height (h) and surface loading(Γ). On the other hand for deep liquid layer theories, more complex in nature, the surfactant transport is coupled to an unsteady viscous boundary layer flow [51].

The induced flow due to a surface tension gradient was first treated by Levich [64] assuming the surface tension varies linearly along the flow. The shortcomings of Levich's theory were pointed out and corrected by Yih [116]. He employs simplified flow equations based on longwave approximations. In his model, flow in a long channel between two reservoirs in which liquid levels and contaminant concentration is maintained is examined. At steady state, he assumes the flow is essentially unidirectional. He expands this analysis to investigate the occurrence of boundary layers at vertical walls placed in a flow regime induced by surface tension gradient [117]. Though an advection-diffusion equation (considering the steady state) for surface is introduced, the surface loading is detached from surface dynamics in the analysis. Adler and Sowerby [2] expanded Yih's work by developing a three-dimensional model. All three theories assume surface tension as a function of spatial co-ordinates of which the profile is known *a priori*. No efforts were made to examine the changes that occur in surface tension due to coupling of solutal transport and motion since the existence of steady flow under the imposed surface tension is assumed.

Insoluble surfactants

The surface tension gradients attributed to differential surface loading need to be modelled using local variations. Borgas and Grotberg [10] considered the above fact and deduced linked equations for spatio-temporal evolution of surface position and surface loading in a moving frame of reference. They applied lubrication theory to the flow equations and the conservation equation for surface loading to arrive at

$$H_t + \left(H^2\Gamma_x\right)_x = 0, \qquad \Gamma_t + \left(\Gamma\Gamma_x H\right)_x = 0 \tag{2.14}$$

which set the precedent for modelling evolution of surface active materials on thin layers of liquid substrate. In (2.14a,b), $\Gamma(x,t)$ and $H(x,t)$ represents the local values of surface loading and film height respectively. The subscripts denote the derivatives with respect to independent variables time t and spatial co-ordinate x. They considered a situation where the surfactant is deterred from flowing downstream by placing a partial barrier blocking only the surface. They predicted a shock front twice the height of the undisturbed flow. The formation of a definitive coherent structure when a surfactant drop is placed on a static liquid substrate relative to parameters such as surface Péclet number, gravity, surface concentration, etc. was examined by Gaver and Grotberg [33]. They showed that the moving capillary ridge that forms beyond the moving surfactant front is enhanced by low surface diffusivity. Using characteristics of nonlinear kinematic shock waves, they deduce that the ridge is approximately twice the height of the undisturbed substrate when $1/Pe \rightarrow 0$. Gravity, coupled to capillary forces, gives a surface flattening effect. Their axisymmetric one-dimensional numerical study on the equivalent of (2.14) shows that the sudden Marangoni pull at the leading edge of the drop drags liquid beneath it, forming the capillary ridge which moves radially outward (see Figure 2.5). The induced velocity field enhances the transport of the chemicals. Spreading, initially diffusive, becomes fast once augmented by advection and enhances the transportation of chemicals at the surface. Viscous diffusion of momentum eventually retards the flow, slowing down the spreading.

The unsteady Marangoni induced flow is asymptotically self-similar at large times. Jensen and Grotberg [52] used a constraint on the mass of surfactant such that

$$M = \int_{-\infty}^{+\infty} \Gamma dx = Qt^{\alpha} \tag{2.15}$$

where Q is a constant. The parameter α provides a handle to set the mass for different scenarios of interest ($\alpha = 0$ for constant mass and for a source $\alpha > 0$). This kind of analysis is generally called the "similarity solutions of the first kind". They incorporated van der Waals forces into evolution equations which enhances the film thinning, though film rupture was not completely arrested by inclusion of van der Waals forces. However, they have showed that a dilute surfactant monolayer strip, containing a fixed mass, spreads like $t^{1/3}$ and an axisymmetric monolayer drop, also of fixed mass, spreads like $t^{1/4}$. Furthermore they deduced that a monolayer spreading from a line or point source of constant surfactant concentration spreads like $t^{1/2}$. If the initial concentration of the monolayer is above the CMC (while holding $\alpha = 0$ in (2.15)), the spreading has two distinct stages [99]. Faster spreading rates can be observed during the first stage where the concentration at the centre remains above the CMC. Within this region, the front spreads like $t^{1/2}$. The second stage comes when the concentration at the centre falls below the CMC giving a slower moving front proportional to $t^{1/4}$. Starov [99] also showed that the thickness at the centre diminishes as $t \to \infty$, forming a dry spot. In a different approach to similarity analysis, Jensen [50] introduced the use of a phase plane to describe the dominant physics of the spreading system. In the phase–plane method, as an advantage over similarity solutions of first kind, he showed that it can identify similarity solutions for the systems that fail to satisfy global constraints (i.e. systems that cannot be solved by considering differential or local physical balances alone, e.g. closing of an axisymmetric hole in a monolayer).

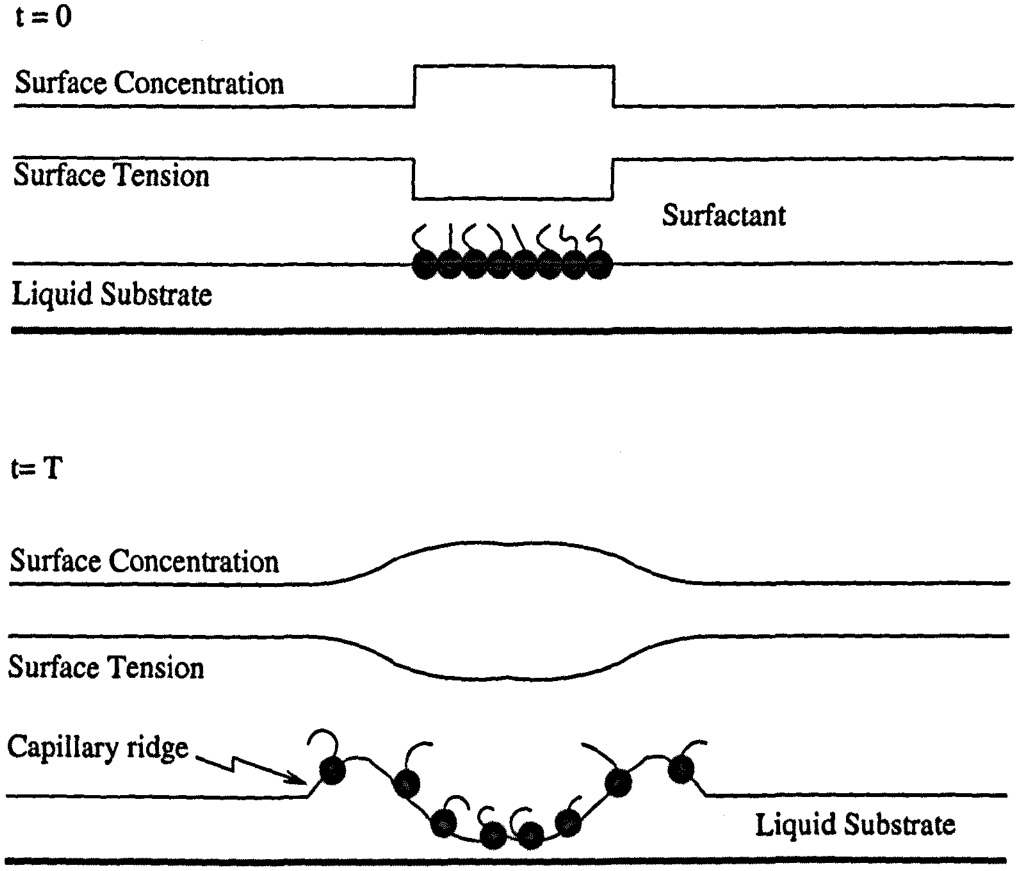

Figure 2.5: Surfactant drop spreading on a liquid substrate. The sharp fall of surface tension at initial time t=0 suggests the existence of large surface stress. The resulting flow field drag the liquid mass outward. The mass balance suggests that the surface deformation is imminent. The Marangoni pull is maximum at t=0 and as the diffusion occur the sharpness of the capillary ridge decreases. t=T shows the surface profile of the substrate after a finite time interval.

The leading edge of the insoluble monolayer that spreads under the action of Marangoni stress behaves as a flat rigid plate. The resulting integrable stress singularity at the advancing front is not captured by the lubrication approximation. This discrepancy is studied by Jensen and Halpern for a thin film [54, 55] assuming that the surface is flat under the influence of capillarity or gravity. They analysed the viscous and inertial effects of weak contaminant surfactant on thin films using boundary element methods together with Hopf and matched eigenfunction methods. They showed that in the strong gravity limit, spreading is unaffected by surface deformations. Thus a single nonlinear governing equation $\Gamma_t = \mathcal{A}(\Gamma\Gamma_x)_x$ predicts the surfactant distribution. Furthermore they treat the integrable singularity (which we make use of in our finite element analysis). The spreading of surfactants on non–Newtonian fluids differ greatly from what we have discussed so far [17]. In non-Newtonian fluids the yield stress is strong enough to overcome Marangoni stresses, limiting the spreading process to surface diffusion.

In the case of Newtonian fluids, the coherent structure that forms under the influence of Marangoni stresses decays slowly. One can observe a fingering instability starting at the centre of the surfactant drop, forming a dry surface, that moves radially outward following the moving front [104]. The linear stability analysis of (2.14), apparently fails to predicts the physically observed instability. Normal mode analysis at quasi–steady state showed that the flow is stable for disturbances of all wavenumbers [68]. The linear operators that govern the disturbance flow are highly non-normal (i.e. the operator is not self–adjoint). Hence the quasi-steady analysis provides reasonable results only as $t \to \infty$. Transient growth analysis shows that the algebraic amplification of pseudo–modes of the non–normal operator are large enough to cause the fingering instability [69]. Matar and Troian, in their 2–dimensional numerical studies on a surfactant strip, showed that a transverse disturbance placed ahead of the monolayer would fall behind the advancing front decaying with time [71, 70]. The failure to capture an existing instability might be a result of the simplification of the flow equations used in deriving the evolution equations (2.14a,b).

Soluble surfactants

The effects of soluble surfactants on aqueous films has drawn little attention compared to insoluble surfactant spreading. The mathematical models used in most cases are similar to the insoluble surfactant models but with a modified evolution equation accounting for surface concentration to including bulk/interface mass transfer. Furthermore an additional transport equation for concentration has to be solved in the bulk phase.

Halpern and Grotberg [39] analysed the dynamics of a soluble surfactant on a viscous liquid substrate resting on a perfect absorber wall (i.e. concentration at wall is always zero) for the weak solubility limit. They assumed that the bulk Péclet number is small compared to the surface Péclet number which decouples the otherwise coupled surface and bulk concentration transport equations. With gravity neglected, the surfactant concentration develops a local maximum behind the advancing front after a long gestation period. This dip forces a back flow trailing the front. This effect enhances with large Péclet numbers [39]. Small but finite gravity effects act as a restoring force by creating a bi-directional flow, and therefore diminish the vertical flux of surfactant across the air–liquid interface.

If the wall beneath the aqueous substrate is impermeable, utilising linearised sorption kinetics to combine surface and bulk concentrations, Jensen and Grotberg [53] showed the occurrence of a sharp pulse in the film height just upstream of the leading edge of the surfactant distribution. The evolution depends on the sorption kinetics. At an early transient stage, the sorptive fluxes between surface and bulk is rather high whereas at longer times, when the active species is considerably diffused into the bulk, the two distributions are in local instantaneous equilibrium. Jensen and Grotberg treated the two situations using two sets of evolution equations with cross sectionally averaged concentration fluctuations in the bulk. In the case of fast kinetics, for constant surfactant mass, the shock front initially grows but rapidly decays, smoothing outwardly (as a result of concentration diffusion killing the large gradients) at large times. The advection of dissolved surfactant appears to cause fluid to be driven into this pulse from its upstream end, enhancing the film elevations. The steepness of the pulse depends on the solubility of the species in the bulk [53]. The surface active substance placed at the interface diffuses into the bulk increasing the bulk concentration (bulk diffusion is fast as the Péclet number is small). With time, the two concentrations attain an equilibrium transforming the shock front to a pulse. The numerical results of Jensen and Grotberg [53] show that once the equilibrium stage is reached, the film height increases above $2H$ where H is the initial film height, in contrast to the insoluble surfactant spreading where the maximum height increase can be at most $2H$. Both systems (i.e. soluble and insoluble) are asymptotically stable as the initial shock front decays after a certain threshold time.

Marangoni induced flow in deep fluids

The first investigations of surfactant affected flow in deep liquid layers considered the steady advance of a localised, insoluble monolayer against a uniform stream. In those cases the monolayer was treated as a rigid plate along its length creating a Blasius boundary layer beneath it [21]. Di Pietro *et al.* argued that when a large volume of oil spreads on the interface, a band of oil (surface active material) of sub-micron thickness (i.e. a monolayer) would form ahead of the bulk of the oil due to Marangoni spreading. They assumed that the bulk of the oil is restrained by a barrier placed at the surface so that a steady state can be achieved. The spreading is then against the flow and the shear at the surface due to the advancing oil slick creates the Blasius boundary layer. In a similarity solution analysis, Foda and Cox [28] showed that the leading edge of the surfactant on a unidirectional flow spreads as $t^{3/4}$. Further, they showed that the surfactant distribution has a Blasius boundary layer locally, but they had to compute the boundary layer flow numerically over the remainder of the monolayer, patching this to a further inner region near the stationary source of surfactant. Camp and Berg [11] ran creeping flow ($Re = 0$) experiments to study the unidirectional spreading of oil slicks on deep layers and the data they found were consistent with numerical similarity solution of Foda and Cox. Harper [40] re-examined the flow configuration of DiPietro *et al.* in the zero Reynolds number limit to conclude that the monolayer acts as a rigid plate only at its leading edge. The existence of a ridge (Reynolds ridge) at the leading edge of the monolayer has been experimentally verified by Scott [94]. This phenomenon was modelled by Harper and Dixon [41]. The advancing monolayer, acting like a rigid plate, forces a downward displacement of oncoming fluid. The free surface adjusts to balance the non–uniform pressure distribution (by means of gravity and surface tension) caused by the flow anomaly at the leading edge. Unsteady spreading of an insoluble monolayer containing fixed mass of surface active material over an initially horizontal free surface was examined by Jensen [51]. Distinctive phases of flow dynamics were identified by a time $T = H^2/\nu$ where H is the fluid depth and ν is the kinematic viscosity. For times $t \ll T$, a Blasius sublayer was generated. Once $t = \mathcal{O}(T)$, vorticity created at the free surface diffuses down to the lower boundary changing the flow characteristics. Jensen showed that a surfactant drop of fixed mass would spread like a $t^{3/8}$ and a strip spreads like $t^{1/2}$ for $t < T$.

2.4.2 Experimental analysis on solutocapillary flow

Experiments on thin films are hampered by the inherent disturbances that occur in depositing the surfactant causing film rupture (dry spot). In almost all experiments on spreading of a surfactant on thin films, it has been observed that the fingering instability starts at the inner region and spreads outward radially [34]. Ahmed and Hansen [3] studied the spreading of Oleic acid($\sigma = 32.5$ dyne cm^{-1}) on a thin film of glycerol ($\sigma = 63.40$ dyne cm^{-1}). They observed the moving front and the depression of the substrate layer in the neighbourhood of the deposited surfactant. The experimental results showed that the monolayer spreads like $t^{1/2}$, a result in agreement with similarity solutions [52] for a constant supply rate of surfactant. Hussain *et al.* [48] examined the rate of spreading on a thin layer of substrate(water) formed on an inclined glass surface. These experiments commence with large volumes of surfactants and do not provide much detailed information about the surface activity of the droplet or convection field within the liquid substrate. Gaver and Grotberg [34] ran the oleic/glycerol experiment on planar axisymmetric geometry paying a higher attention to the flow within the substrate as well as surface kinetics. They found that the droplet leading edge and the convection front are distinctively different. They conclude that this difference is caused by the gravity induced bi-directional flow. They also observed the film rupture. Starov *et al.* [99] studied the spreading of sodium dodecyl sulfate(SDS) solutions above CMC. The spreading front clearly showed the two distinctive rates: initially, a fast rate as $t^{1/2}$ and later once the concentration of the drop fall bellow CMC, a rate of approximately $t^{1/4}$. They observed that the surfactant occupies more area than the depressed zone but were not informative about how far it extends. A different kind of test was done by Santiago–Rosanne *at al.* [91] under tightly controlled conditions. They placed a small nitroethane ($\sigma = 39$ dyne cm^{-1}) droplet on a thick (13 mm) water layer. Spreading and dissolution of weakly miscible nitroethane give rise to a variety of wave trains. They observed that the solvent drop spread as a central cap surrounded by a primary film. An instance after the deposition, patterns like daisy flower petals appear in water film and then disappear in a short period of time followed by a drastically disturbed free surface with erratic motions. They capture the waves using a Schlieren device sensitive to density gradients and surface deformations. They suggested that the initial "daisy petal" patterns were caused by interacting surface waves initiated by the imbalanced Marangoni stresses.

Fingering instability in a spreading surfactant drop was first observed by Marmur and Lelah [67]. They observed dendritic spreading of a surfactant drop when deposited on a solid substrate. Later Troian *et al.* [104] showed that the presence of a thin liquid layer(film height $> 1\mu\ m$) with different surface tension is essential for the fingering instability to occur. Troian *et al.* have demonstrated that the fingering process is highly dependent on the ambient film thickness. An increase of film thickness by an order of magnitude led to an approximate rescaling of the finger width. Furthermore they found that the growth rate of the fingers obeys a power law t^{β}, where $\beta = 0.7$ and 0.66 for thick and thin films respectively. The same kind of fingering instability was observed by Frank and Garoff [30] and He and Ketterson [42] for many combinations of surfactants and substrates and geometries, leading to the conclusion that the instability is driven by the Marangoni forces. Troian *et al.* [103] developed a mathematical model for the fingering instability of the spreading surfactant drop. The computational solutions showed that under the dominant effects of Marangoni stresses the immediate neighbourhood of the deposited drop is suppressed to a very thin layer, becoming an analogue to the Saffman-Taylor instability in Hele-Shaw flow. Though the theory does not capture the fingering instability, it gives strong insight into the physical processes that occur.

Experiments by Vanhook *et al.* [109] on surface tension driven Bénard-Marangoni convection of thin silicone oil films shows that long-wave instabilities evolve in to either 'dry spots' (localised depressions) as in solutocapillary flows explained above or to 'high spots' (localised elevations) depending on the physical properties of the oil. Furthermore the air gap above the oil also influences the dynamics of the system. They developed a two layer model which describe the system to a greater accuracy. For details of the experiments and theoretical development see Vanhook [109] and the references therein.

2.5 Summary

The concepts related to surface tension were discussed briefly. The Marangoni stresses arise at liquid/gas interfaces due to surface tension gradients inducing local flow regimes. Such gradients in surface tension can arise due to differential heating or spreading of surfactants. Then we detailed the theories and literature available. The investigations into Marangoni induced flow can be categorised into two major sections; (i)Thermocapillary flows; (ii)Solutocapillary flows. We are concerned about the second group. The solutocapillary flows fall in to three subcategories; (a) effects of insoluble surfactants; (b) spreading of soluble surfactants and (c) fingering instability. The amount of experiments carried out is few in number and most of them were qualitative in nature. The fingering instability though observed in nature has not been analysed successfully thus far.

In this work, as we discussed in chapter 1, we add to the above accumulated knowledge, a study of spreading of a surfactant front on a flowing film enhancing the surface disturbances. Then we carry out, for the first time, fully nonlinear simulations on the spreading problem, comparing the results with the lubrication theory model. We discuss the degree of accuracy in using lubrication theory on free surface flows. To analyse the surface waves induced by surfactant gradients on a flowing film, we begin by developing a mathematical model. In next chapter, we presents a detailed description of two numerical methods used: 1. method of lines to solve the evolution equations and 2. finite element method that is used to simulate the fully nonlinear equations. We begin by deriving two evolution equations for the surface height and surface loading.

Chapter 3

A free surface flow model and numerical solution methods

3.1 Introduction

In this chapter we discuss two flow models for propagation of waves and surface active material on a flowing thin films with a deformable free surface and the methods of solutions to those models. The first model consists of the fully nonlinear flow equations (i.e. Navier–Stokes) with free surface boundary conditions which we intend to solve using a finite element method. The second model is derived by simplifying the full nonlinear system using a longwave approximation. The result is a coupled set of evolution equations for the free surface height and the surface loading of a pressure driven liquid film with localised Marangoni stresses. The evolution equations were solved approximately by using specialised numerical methods.

The model considers an insoluble, non-volatile (passive) surface active material spreading on a slowly flowing liquid film. The surface tension gradient in the neighbourhood of the contact line between the liquid and the surface active substance causes shear stresses at the surface [29, 25], initiating surface wavefronts. These wavefronts may either grow or decay with time depending on the flow characteristics of the bulk. For spreading of a surfactant drop on a stationary liquid layer the wave front develops quickly in amplitude and then decays slowly, reaching a quasi-steady state that evolves on a slow time scale.

In most studies, lubrication approximations were used to simplify the flow equations and to derive a coupled evolution equation for the deformable free surface [33, 52]. In many cases, the height averaged velocity field was used, eliminating the internal dynamics of the liquid layer[1]. There are exceptions in some cases. Roberts [88] used a centre manifold theory approach to simplify film flows using slaved velocity modes. We intend to solve the fully nonlinear flow equations (using FEM) to compare the two models so that the effects of the physics neglected by simplification can be discussed.

3.2 The Governing Equations

A semi-infinite incompressible liquid layer flowing over an horizontal plane is considered. The liquid layer is bounded by the horizontal plane at the bottom and a deformable free surface at the top (see Figure 3.1). The average thickness of the liquid layer is d. The liquid density ρ and dynamic viscosity μ remain constant. The surfactant that spreads along the interface is insoluble and non-volatile. Thickness of the surface active layer is negligible since it is considered as a monomolecular layer. The flow is induced by an imposed pressure drop of $\mathcal{O}(1)$ in x direction. The air phase above the liquid is assumed to be passive. Therefore no shear stress appears at the interface due to air friction.

The spatial co-ordinates are x,y and z with x axis along the horizontal plane towards the flow direction, y in the transverse direction and z axis is in the direction normal to x − y plane. The velocities involved are $u(x, y, z, t)$, $v(x, y, z, t)$ and $w(x, y, z, t)$ along x, y and z axis respectively. The pressure field is denoted by $p(x, y, z)$. The

---

[1] Almost all the previous work on surfactant spreading is based of height averaged velocity field.

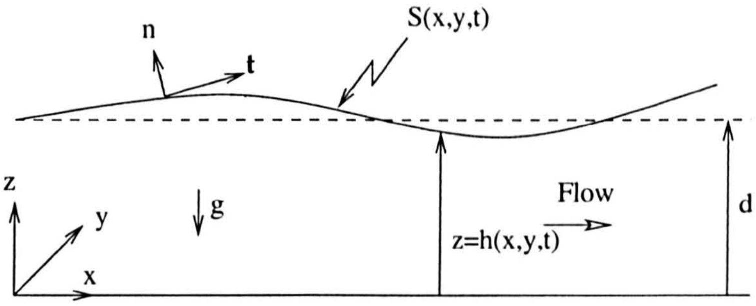

Figure 3.1: Liquid film flow over an horizontal plane. The deviation of deformable free surface S from average height d is given by $z - h(x, y, t) = 0$.

surface tension $\sigma(\Gamma)$ is taken to be a function of position in $x - y$ plane and time t since surface concentration (or *surface loading*) $\Gamma(x, y, t)$ is a function of those co-ordinates only.

3.2.1 Flow equations

The flow in the bulk is described by Navier-Stokes (N-S) equations and the equation for mass balance (Continuity equation) [61, 5, 6]:

$$\frac{\partial v_i}{\partial t} + v_j v_{i,j} = \frac{1}{\rho}\sigma_{ij,j} + g_{3,j} \tag{3.1}$$

$$v_{i,j} = 0 \tag{3.2}$$

where the stress tensor is given by

$$\sigma_{ij} = -p\delta_{ij} + 2\mu\epsilon_{ij} \qquad \epsilon_{ij} = \frac{1}{2}(v_{i,j} + v_{j,i}). \tag{3.3}$$

The comma-subscript represents the index convention for partial differentiation with respect to x_i. δ_{ij} is the Kronecker delta and the summation convention is assumed. ϵ_{ij} is the deformation tensor. The $g_{3,j}$ is the gravity, active only in z direction.

The boundary condition at the lower planar surface, $z = 0$ is no-slip:

$$v_i = 0 \tag{3.4}$$

The boundary conditions at the upper free surface is complicated and derived using normal and tangential stress balances. To obtain the required boundary conditions, a function that characterises the free surface is needed. We assume that the position of free surface in space and time is given by $S(x,y,t) = z - h(x,y,t) = 0$. Therefore the motion of the deformable free surface is given by $\frac{DS(x,y,t)}{Dt} = 0$ which expands to give the kinematic boundary condition:

$$h_t + uh_x + vh_y - w = 0 \tag{3.5}$$

where the subscripts denotes the differentiation with respect to variables represented by the corresponding letters. Since the function $h(x,y,t)$ that maps the elevation of the material surface is known, the normal and tangential unit vectors can be written immediately as:

$$\begin{aligned} \mathbf{n} &= \frac{(-h_x, -h_y, 1)}{N} \\ \mathbf{t} &= \frac{(1, 0, h_x)}{N} \quad \text{or} \quad \frac{(0, 1, h_y)}{N} \\ N &= (1 + {h_x}^2 + {h_y}^2)^{1/2} \end{aligned} \tag{3.6}$$

The conservation of linear momentum on the free surface gives rise to stress conditions imposed upon the bulk-flow stress fields. A fuller description on derivation of stress conditions for a Newtonian interface was given in Scriven [95] and more recently in Edwards *et al.* [25]. The surface stress is given by $\sigma_{ij} \cdot \mathbf{n}$. Resolving the surface stress into tangential and normal components respectively yields the tangential and normal stress boundary conditions.

The tangential stress due to visco-inertial forces should be balanced by the surface tension gradients.

$$\mathbf{t} \cdot \sigma_{ij} \cdot \mathbf{n} = (\mathbf{t} \cdot \nabla)\sigma$$

where $\nabla = (\frac{\partial}{\partial x}, \frac{\partial}{\partial y}, \frac{\partial}{\partial z})$. Expansion of above equation results in two boundary conditions: x component:

$$\mu[2(w_z - u_x)h_x - (u_y + v_x)h_y - (w_y + v_z)h_xh_y + (1 + {h_x}^2)(u_z + w_x)] = N\sigma_x \tag{3.7}$$

y component:

$$\mu[2(w_z - v_y)h_y - (v_x + u_y)h_x - (w_y + v_z)h_x h_y + (1 + {h_y}^2)(v_z + w_y)] = N\sigma_y \quad (3.8)$$

The normal stresses should be balanced by the excess pressure jump caused by the combination of curvature $\mathcal{K}(h)$ and the surface tension.

$$\mathbf{n} \cdot \sigma_{ij} \cdot \mathbf{n} = \sigma\mathcal{K}$$
$$\mathcal{K}(h) = \frac{h_{xx} + h_{yy}}{N^3}$$

Therefore the normal stress balance becomes:

$$-p + \frac{2\mu}{N^2}[u_x({h_x}^2 - 1) + v_y({h_y}^2 - 1) + (u_y + v_x)h_x h_y - (u_z + w_x)h_x - (w_y + v_z)h_y] = \sigma\mathcal{K}(h) \quad (3.9)$$

The equations (3.7)–(3.9) are free of the terms that arise from surface dilational and kinematic viscosities of the surfactant as we assume these quantities are relatively small in all circumstances that are to be considered here. In reality, most surfactant –adsorbed fluid interfaces exhibit shear thinning behaviour. However we adhere to the Newtonian fluid assumption. This is a common assumption in the literature [25]. However, these terms have to be included in the model if the substrate is a non-Newtonian fluid.

3.2.2 Transport of surfactants

Surface tension depends on the concentration of the surfactant. To describe the surface dynamics due to the compositionally-induced Marangoni effects, simultaneous evolution of the associated species conservation equation has to be observed [105, 74]. The latter is coupled to the equation of motion through the dependence of the surface tension upon surface loading of the surfactant (RHS of (3.7) and (3.8)). The conservation of the secondary phase (surfactant) in a two dimensional surface (x–y plane) gives the advection-diffusion type equation for the concentration $\Gamma(x, y, t)$ [74, 25]:

$$\Gamma_t + \nabla_s(u_s\Gamma) - \mathcal{D}_s\nabla_s^2\,\Gamma = \mathcal{F} \tag{3.10}$$

(3.10) is restricted to the surface and has to be evaluated at $z = h(x, y, t)$. The surface Laplacian operator ∇_s in above equation is defined as,

$$\nabla_s = (\mathbf{I} - \mathbf{nn}) \cdot \nabla,$$

where $\mathbf{I}$ is the spatial idemfactor and $\mathbf{nn}$ is a dyadic tensor. $\mathcal{D}_s$ is the surface diffusivity of the surfactant and is held constant. $\mathcal{F}$ is the normal diffusive flux of the surfactant from the bulk phase if the surfactant is soluble. In this study the surfactant is assumed to be insoluble (i.e. it has a very large bulk Péclet number). Therefore $\mathcal{F} = 0$.

(3.10) illustrates the mechanisms of spreading. To see this clearly, $\nabla_s(u_s\Gamma)$ can be re-written using the components of surface velocity u_s along the surface, and normal to the surface [54]:

$$\nabla_s(u_s\Gamma) = u_s\nabla_s\Gamma + \Gamma(\nabla_s \cdot \mathbf{n})u \cdot \mathbf{n} \tag{3.11}$$

The first term on the r.h.s of (3.11) is the spreading of the surfactant by advection and the second part gives the spreading due to expansion/contraction of the free surface by change of area($\nabla_s \cdot \mathbf{n}$ is the curvature $\mathcal{K}(h)$). The other mechanism is the surface diffusion of surfactants characterised by diffusion coefficient $\mathcal{D}_s$.

Finally we consider the relationship that links the surface loading and the surface tension. As discussed in chapter 2 §§2.3.2, we assume a linear equation of state for surface tension $\sigma(x, y, t)$ as a function of surface loading Γ.

$$\sigma(\Gamma) = \sigma_0 - \left(\frac{\partial\sigma}{\partial\Gamma}\right)\Gamma \tag{3.12}$$

Above equations describe the flow with localised Marangoni stresses fully. In the absence of the surfactant there exists a family of steady state solutions for velocity vector $\mathbf{v}$ and the pressure p which are commonly termed 'half Poiseuille flow'. In full nonlinear simulations, this steady state is taken as the base solution and the evolution of the disturbance caused by the introduction of surfactant is examined.

3.3 Base state flow

When there is no surface loading, (3.1) and (3.2) have a set of steady, hydrostatic and undeformed solutions. These solutions are independent of x and y co-ordinates and only depend on z. The liquid film height $h(x, y, t) = d$. Flow is unidirectional since $\frac{\partial p}{\partial y} = 0$. Then the steady state equations becomes

$$\begin{aligned}
0 &= -\frac{1}{\rho}\frac{\partial p}{\partial x} + \nu\frac{\partial^2 u}{\partial z^2} && && (3.13)\\
0 &= \frac{\partial^2 v}{\partial z^2} && && (3.14)\\
0 &= -\frac{1}{\rho}\frac{\partial p}{\partial z} - g && && (3.15)\\
u &= v = 0 && \text{at} \quad z = 0 && (3.16)\\
\frac{\partial u}{\partial z} &= \frac{\partial v}{\partial z} = 0 && \text{at} \quad z = d && (3.17)\\
p &= 0 && \text{at} \quad z = d && (3.18)
\end{aligned}$$

where ν is the kinematic viscosity. The solutions to above system are:

$$\begin{aligned}
U(z) &= \frac{1}{2\mu}P_x(2dz - z^2) && (3.19)\\
V &= W = 0 && (3.20)\\
p &= \rho g(d - z) && (3.21)
\end{aligned}$$

U, V and W are the velocities in x, y and z directions at steady state. The pressure p above gives only the hydrostatic head. $P_x = \frac{\partial p}{\partial x}$ that appears in (3.19) is the imposed uniform pressure gradient. P_x can be related to volumetric flow rate Q, defined as

$$Q = \int_0^d U(z)dz \tag{3.22}$$

The velocity $U(z)$ at d is the maximum velocity of the flow field at steady state. The first derivative of $U(z)$ with respect to z vanishes at $z = d$ since there are no surface stresses in x direction. The velocity profile is half the profile of the plane Poiseuille flow bounded by two rigid plates.

3.4 Derivation of coupled evolution equations for the free surface

In §3.2 we discussed the fully nonlinear flow equations for a liquid film. In this section a simplification method is used to reduce the governing equations and associated boundary conditions so that the full nonlinear system reduces to a simpler system to deal with. Before going any further we generalise the flow equations by nondimensionalising the variables. Then we scale the variables and order the terms so that dominant physics is retained.

3.4.1 Scaling and Nondimensionalization

The surface waves that arise due to Marangoni stresses in length and span-wise directions may be of larger scale than the liquid layer height d (long wave assumption). Therefore to derive an evolution equation for the free surface we introduce a length scale $\mathcal{L} \gg d$. We assume that $\varepsilon = \frac{d}{\mathcal{L}} \ll 1$. $\mathcal{L}$ is the length scale associated with flow direction. Considering the fact that the u velocity should be an order higher than vertical velocity, we use εU_s to scale w. Since we investigate an evolution of a dynamical system under pressure induced flow, the flow field dominates in the physical mechanisms of instabilities. Therefore we employ inertial scales:

$$t^* = \frac{U_s t}{\mathcal{L}} \qquad \mathbf{x}^* = \frac{\mathbf{x}}{\mathcal{L}} \qquad u^*, v^* = \frac{u, v}{U_s} \qquad w^* = \frac{w}{\epsilon U_s} \quad p^* = \frac{p}{{U_s}^2 \rho} \qquad \Gamma^* = \frac{\Gamma}{\Gamma_{max} - \Gamma_\infty}$$

where U_s is a reference velocity. We assume U_s to be the maximum velocity of the flow field at unperturbed state, i.e. the velocity at the surface. Γ_{max} and Γ_∞ are the micelle forming concentration or the maximum concentration and the concentration of the far field respectively. Γ_∞ can either be zero or have a small value indicating slight contamination of the substrate. The asterisks refer to dimensionless variables. All above equations are transformed in to nondimensional form and asterisks were dropped for clarity. Henceforth all the calculations are given in dimensionless variables.

Dimensional analysis yields the following parametric groups:

1. Reynolds number $Re = \frac{U_s d}{\nu}$
2. Froude number $Fr = \frac{U_s}{\sqrt{gd}}$
3. Marangoni number $\mathcal{M}a = \frac{d(\partial\sigma/\partial\Gamma)\Delta\Gamma}{\mu U_s \mathcal{L}}$
4. Péclet number $\mathcal{P}e_s = \frac{U_s d}{\mathcal{D}_s}$
5. Capillary number $Ca = \frac{\mu U_s}{\sigma_0}$

In Marangoni number, $\Delta\Gamma = (\Gamma_{max} - \Gamma_\infty)$. Re and Fr characterise the flow while $\mathcal{M}a$ represents the ratio of surface tension forces arising from concentration gradients to inertial forces. Surface Péclet number $\mathcal{P}e_s$ is a measure of the relative importance of advection to diffusion along the surface. Capillary number is a relative measure of surface tension forces over inertial forces. Smaller the capillary number the stronger the surface tension forces become.

3.4.2 The evolution equations

By applying the above scaling to (3.1)–(3.9) one can obtain the flow equations as follows. The asterisk has been omitted for clarity.

$$\varepsilon\left[\frac{\partial u}{\partial t} + u\frac{\partial u}{\partial x} + v\frac{\partial u}{\partial y} + w\frac{\partial u}{\partial z}\right] = -\varepsilon\frac{\partial p}{\partial x} + \frac{1}{Re}\left[\varepsilon^2\frac{\partial^2 u}{\partial x^2} + \varepsilon^2\frac{\partial^2 u}{\partial y^2} + \frac{\partial^2 u}{\partial z^2}\right] \tag{3.23}$$

$$\varepsilon\left[\frac{\partial v}{\partial t}+u\frac{\partial v}{\partial x}+v\frac{\partial v}{\partial y}+w\frac{\partial v}{\partial z}\right]=-\varepsilon\frac{\partial p}{\partial y}+\frac{1}{Re}\left[\varepsilon^2\frac{\partial^2 v}{\partial x^2}+\varepsilon^2\frac{\partial^2 v}{\partial y^2}+\frac{\partial^2 v}{\partial z^2}\right] \tag{3.24}$$

$$\varepsilon^2\left[\frac{\partial w}{\partial t}+u\frac{\partial w}{\partial x}+v\frac{\partial w}{\partial y}+w\frac{\partial w}{\partial z}\right]=-\frac{\partial p}{\partial z}+\frac{\varepsilon}{Re}\left[\varepsilon^2\frac{\partial^2 w}{\partial x^2}+\varepsilon^2\frac{\partial^2 w}{\partial y^2}+\frac{\partial^2 w}{\partial z^2}\right]-\frac{1}{Fr^2} \tag{3.25}$$

$$\frac{\partial u}{\partial x}+\frac{\partial v}{\partial y}+\frac{\partial w}{\partial z}=0 \tag{3.26}$$

The nondimensional tangential stress balances in x and y directions at h are

$$2\varepsilon^2(w_z-u_x)h_x-\varepsilon^2(u_y+v_x)h_y-\varepsilon^2(\varepsilon^2w_y+v_z)h_xh_y+(1+\varepsilon^2h_x^2)(u_z+\varepsilon^2w_x)=N\mathcal{M}a\Gamma_x \tag{3.27}$$

$$2\varepsilon^2(w_z-v_y)h_y-\varepsilon^2(u_y+v_x)h_y-\varepsilon^2(\varepsilon^2w_y+v_z)h_xh_y+(1+\varepsilon^2h_y^2)(v_z+\varepsilon^2w_y)=N\mathcal{M}a\Gamma_y \tag{3.28}$$

and the normal stress balance at the free surface become

$$\begin{aligned}-p+\frac{2\varepsilon}{Re}\Big[&u_x(\varepsilon^2h_x^2-1)+v_y(\varepsilon^2h_y^2-1)+\\ &\varepsilon^2(u_y+v_x)h_xh_y+(u_z+\varepsilon^2w_x)h_x+\\ &\qquad(v_z+\varepsilon^2w_y)h_y\Big]\\ &=\frac{\mathcal{K}(h)}{Re}\Big(\frac{\varepsilon^2}{Ca}-\varepsilon\mathcal{M}a\Gamma\Big).\end{aligned} \tag{3.29}$$

Here we have used the equation of state $\sigma=\sigma_0-(\partial\sigma/\partial\Gamma)\Gamma$ where σ_0 is the surface tension of the pure substrate. We assume a regular perturbation expansion in velocity vector $\mathbf{u}$

$$\mathbf{u}=\mathbf{u_0}+\varepsilon\mathbf{u_1}+\varepsilon^2\mathbf{u_2}+\dots \tag{3.30}$$

The pressure gradient that drives the film flow is expected to be of unit order. Therefore

$$p=\varepsilon^{-1}\{\,p_0+\varepsilon p_1+\varepsilon^2p_2\dots\}. \tag{3.31}$$

By substituting (3.30) and (3.31) into the equations (3.23)–(3.26) and also into the transformed boundary conditions, we obtain a sequence of linear problems at each order of ε.

$$\mathcal{O}(\varepsilon^{-1}): \quad \frac{\partial p_0}{\partial z} = 0 \tag{3.32}$$

$$p_0 = 0 \qquad \text{at } z = h(x,y,t) \tag{3.33}$$

$$\mathcal{O}(1): \quad \frac{\partial p_0}{\partial x} = \frac{1}{Re}\frac{\partial^2 u}{\partial y^2} \tag{3.34}$$

$$\frac{\partial p_0}{\partial y} = \frac{1}{Re}\frac{\partial^2 v}{\partial y^2} \tag{3.35}$$

$$\frac{\partial p_1}{\partial y} = \frac{1}{Fr^2} \tag{3.36}$$

$$\frac{\partial u_0}{\partial x} + \frac{\partial v_0}{\partial y} + \frac{\partial w_0}{\partial z} = 0 \tag{3.37}$$

$$u_0 = v_0 = w_0 = 0 \qquad \text{at } z = 0 \tag{3.38}$$

$$p_1 = 0 \qquad \text{at } z = h(x,y,t) \tag{3.39}$$

$$\frac{\partial u_0}{\partial z} = \mathcal{M}a\Gamma_x \qquad \text{at } z = h(x,y,t) \tag{3.40}$$

$$\frac{\partial v_0}{\partial z} = \mathcal{M}a\Gamma_y \qquad \text{at } z = h(x,y,t) \tag{3.41}$$

The $\mathcal{O}(1)$ approximations are the lubrication approximation to the N–S equations in general. The $\mathcal{O}(1)$ kinematic boundary condition is

$$h_t + u_s h_x + v_s h_y - w = 0 \tag{3.42}$$

The solution to $\mathcal{O}(\varepsilon^{-1})$ equation is $p_0 = P(x,y,t)$, i.e. only the z dependence is constrained. The $\mathcal{O}(1)$ equations yield,

$$u_0 = \frac{Re\,P_x}{2}(2hz - z^2) + \mathcal{M}a\Gamma_x z \tag{3.43}$$

$$v_0 = \frac{Re\,P_y}{2}(2hz - z^2) + \mathcal{M}a\Gamma_y z \tag{3.44}$$

The velocities u_0 and v_0 have two contributions: the flow induced by the imposed pressure gradient and the flow induced due to Marangoni stresses. Without loss of generality the initial pressure gradient is taken along x direction and thus $P_y = 0$.

The vertical velocity component w_0 can be evaluated by substituting u_0 and v_0 in (3.37).

$$w_0 = \frac{Re\, P_x}{2} h_x z^2 - \frac{\mathcal{M}a}{2}(\Gamma_{xx} + \Gamma_{yy})z^2 \tag{3.45}$$

Using the above (3.43), (3.44) and (3.45) together with (3.42) we derive an equation for the time–evolution of the surface.

$$h_t + Re\, P_x h^2 h_x - \frac{\mathcal{M}a}{2}(\Gamma_x h^2)_x - \frac{\mathcal{M}a}{2}(\Gamma_y h^2)_y = 0 \tag{3.46}$$

The associated evolution of surface concentration is given by

$$\Gamma_t + \frac{Re\, P_x}{2}(\Gamma h^2)_x - \mathcal{M}a[\Gamma(\Gamma_x h)]_x - \mathcal{M}a[\Gamma(\Gamma_y h)]_y - \frac{1}{\mathcal{P}_s}(\Gamma_{xx} + \Gamma_{yy}) = 0. \tag{3.47}$$

The coupled equations (3.46) and (3.47) are the leading order two dimensional lubrication approximation to surface evolution of a Newtonian liquid with a surfactant monolayer spreading above it. The effects of the vertically downward gravitational field is absent from above equations since the terms are two orders of magnitudes smaller. Matar and Troian [69] have argued that some of $\mathcal{O}(\varepsilon^2)$ terms can become significant and therefore should be included in the equations. However most of the studies on spreading [52, 39, 56] have omitted these terms. The above equations contain the convective terms due to Marangoni effects as well as pressure induced terms. Film flow down an inclined plane can be retrieved by replacing P_x by $Fr^{-1}\ Sin\theta$ where θ is the inclination angle.

3.4.3 The capillary induced flow

The Marangoni number $\mathcal{M}a$ measures the strength of the surface tension gradient over a selected length scale. The Marangoni number and the capillary number are interdependent on each other via the equation of state. Surface tension of the substrate $\sigma > 0$ for all cases. Therefore $\frac{1}{Ca} \geq \varepsilon^{-1}\mathcal{M}a\Gamma$. The magnitude of the induced shear stress is proportional to the Marangoni number. The term $P_x Re h^2 h_x$ appear in (3.46) couples the bulk flow with the surface evolution equation. Similar terms in (3.47) gives the advection due to background flow. By setting $P_x \rightarrow 0$, one can obtain the evolution equations for stationary substrate [33, 52]. The effect of background flow on evolution of surface waves due to Marangoni stresses were studied in detail in chapter 4.

The shear stress is given by $\sigma_x \propto \mathcal{M}a$ assumes large values at the tip of the surfactant monolayer (contact line). The lubrication model we used here fails to capture this integrable discontinuity properly. For instance if we assume a step change in surface loading, the shear stress become exceedingly large. Hence a change over a length Δl has to be considered. However, the surface tension gradient cause the liquid substrate to move in the direction of larger surface tension. The shear force due to surfactant gradient does not have any effect beyond the contact line. Hence a sharp shock wave exists [52]. We introduce a numerical tool that solve fully nonlinear flow equations resolving the aforementioned singularity within the scope of this thesis.

The evolution equations (3.46) and (3.47) forms a stiff PDE system that is difficult to solve even numerically. In next section we discuss the numerical approach to evaluate the spatio–temporal evolution of them. Furthermore we discuss the finite element approach to simulate the fully nonlinear equations.

3.5 Numerical Solutions

The evolution equations (3.46) and (3.47) are only weakly nonlinear since the lubrication approximation limits the range of curvatures acceptable in a non–local elliptic–parabolic system. Nevertheless in general, partial differential equations (PDE) with nonlinear combinations of variables and their derivatives produce a very difficult system to solve even numerically. The difficulty arises from the fact that the Jacobian that results from the discretisation has eigenvalues with negative real parts of very large magnitude making initially small errors grow. The growth of the error effects the numerical stability of the problem eventually breaking it down. In order to attain a numerically stable solution in using standard numerical methods like Adams methods or Euler method, the step size is forced to be extremely small (smaller than it would appear to be necessary based on a consideration of the truncation error). To resolve this difficulty of using extremely small step sizes, one should seek methods that include the entire negative real axis in its stability region. Implicit methods usually fulfil this requirement with the penalty of excessive matrix manipulations (e.g. use of backward difference (BD) formulae). The method of lines (MOL) greatly simplifies the problem by reducing the PDEs to ODEs at each discretisation step. This allows the use of relatively large step sizes with explicit integration methods cutting down the computing time as well as programming difficulties.

On the other hand the flow equations (3.1)–(3.10) represent a fully nonlinear PDE system which needs to be solved over a fixed domain. The stress balance boundary conditions at the free boundary need to be treated with great care to observe the topological changes due to Marangoni stresses. Grid based finite elements method (Galerkin's method) equipped with a special grid diffusion mechanism is utilised to obtain approximate solutions to N-S equations subjected to BCs that describe the free surface. To this purpose we adapt a code developed by Goodwin and Schowalter [35] and also maintained by Andrew Yeckel[114]. An outline of the method is given in §3.5.2.

3.5.1 The Method of Lines

The coupled evolution equations (3.46) and (3.47) were solved numerically using method of lines (MOL). The numerical method of lines is a well established numerical technique for the analysis of wave evolution and other boundary value problems in physics [113]. MOL is regarded as a special finite difference method but more effective with respect to accuracy and computational time than the regular finite difference method. It basically involves discretising a given differential equation in one or two dimensions while using marching algorithms in the remaining direction. MOL has the merits of both the finite difference method and numerical integration method; it does not yield spurious modes nor have the problem of relative convergence [90].

Besides, the method of lines has the following advantages:

1. Computational efficiency: the semi analytical approach of the formulation leads to a simple and compact algorithm,which yields accurate results with less computational effort than other techniques.
2. Numerical stability: by separating discretisation in space and time, it is easy to establish stability and convergence.
3. Reduced programming effort: by making use of state–of–art well documented reliable ODE solvers, the programming time can be substantially reduced.

The method of lines has a wide range of applicability and is used to solve hyperbolic, parabolic, and even elliptic PDEs. The use of explicit integrators is not always possible. If the PDEs are very stiff, the use of implicit methods is inevitable.

Outline of the method

Here we outline the method using a paradigm initial–boundary value problem.

Consider the pde system:

$$\dot{U} = f(U, \nabla, x, t) \qquad 0 < x < 1 \qquad t > 0 \tag{3.48}$$

$$U(0,t) = d_0(t) \qquad U(1,t) = d_1(t) \qquad t \geq 0 \tag{3.49}$$

$$U(x,0) = g(x) \qquad 0 \leq x \leq 1 \tag{3.50}$$

where f is a function of U which may depend on derivatives of U, indicated by ∇ and also depend on spacial co-ordinate x and time t. $\dot{U}$ denotes the time derivative of U. Functions d_0, d_1 and g are assumed given and smooth. Partial differential equation systems like (3.48) are encountered in describing dynamic physical systems.

The essential features of a MOL solution of (3.48)–(3.50) are:

1. The discretisation of the spatial derivatives in (3.48).
2. The integration of the temporal derivative, $\dot{U}$, in (3.48) which requires the integration of a system of ordinary differential equations in t as a result of the spatial discretisation of feature 1.

The essence of the system lies on the semi–discretisation of the PDE mentioned in feature 1. The x domain upon which the function is defined is divided into strips by N straight lines parallel to t axis. The evolution of the numerical solution $U(x,t)$ for 3.48 from $t = 0$ is sought along N lines of constant x as illustrated in Figure 3.2 (hence the name *method of lines*). The solution at a particular value of t is given by the corresponding values of $U(x,t)$ along each of the lines.

We discretise (3.48) by approximating the spatial derivatives using fourth order formulae [93]. This results in algebraic formulae in terms of u_j where $0 \leq j \leq N$. The functions $u_j(t)$ are intended to be approximations of $U(x,t)$. The final form can be written in matrix form:

$$\dot{\mathbf{u}}(t) = \Lambda \mathbf{u}(t) + \mathbf{g}(t) \qquad \mathbf{u}(0) = \mathbf{u}_0 \tag{3.51}$$

Λ is the Jacobian that arises from approximating the partial differentials from difference equations. The order of Λ is $N-1$. The vectors $\mathbf{u}(t)$, $\mathbf{u}_0$ and $\mathbf{g}(t)$ are defined

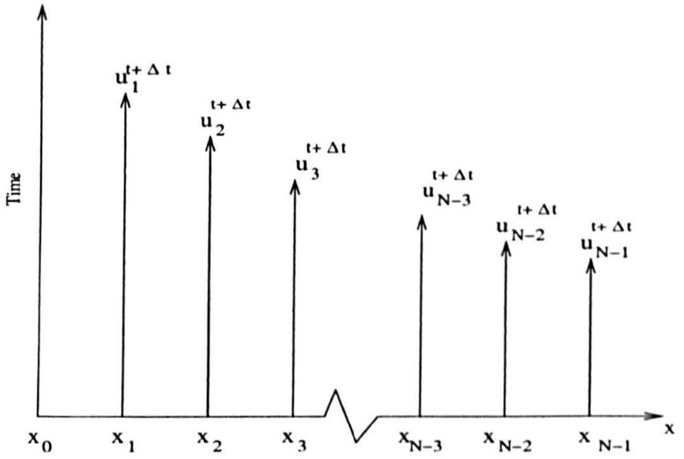

Figure 3.2: Schematic representation of MOL. The spatial domain x discretized in to N lines and $u(x_i, t)$ evaluated along those lines. (After Shiesser [93])

as:

$$\mathbf{u}(t) = [u_1(t), \ldots, u_{N-1}(t)]^T \qquad \mathbf{u}_0 = [f(x_1), \ldots, f(x_{N-1})]^T$$

$$\mathbf{g}(t) = [\frac{1}{\delta^2}d_0(t) + G(x_1, t), G(x_2, t), \ldots, G(x_{N-2}, t), \frac{1}{\delta^2}d_1(t) + G(x_1, t)]^T.$$

$G(x, t)$ is the functional that contains all terms other than spatial derivatives in (3.48). Furthermore the $\delta = \frac{1}{N}$ and $x_j = j\delta$. In definitions of $\mathbf{u}$ and $\mathbf{g}$, the superscript T indicates the matrix transpose, so that $\mathbf{u}$ and $\mathbf{g}$ are column vectors of length $N-1$.

The equation (3.51) is the method of lines approximation to (3.48)–(3.50). The algebraic approximations to spatial derivatives results in N differential equations with respect to t. The temporal integration mentioned in feature 2 should be carry out on (3.51) as for any PDE using one of many methods available(e.g. Euler method, Runge–Kutta).

Spacial discretisation

In most numerical schemes (e.g. [86]) three point discretisation of space co-ordinates are employed. Though it is expensive in computing time, a five point centred finite difference scheme with fourth order accuracy [93] has been used to discretise spatial derivatives. The higher order accuracy is necessary at this stage since the error minimisation in the time integration process does not compensate for discretisation errors. In solving (3.46) and (3.47), the x domain discretized into $(N-1)$ elements which result in N nodes. In the case of two dimensional domain, the $x-y$ plane is divided into $(N-1)\times(M-1)$ elements. The resulting $(N)\times(M)$ nodes are equispaced in x and y directions but not necessarily equal to each other.

The evolution equations (3.46) and (3.47) contain first and second derivatives of h and Γ with respect to x and y. The differentiation matrix that arises from algebraic approximation of derivatives with respect to x are as follows.

$$\frac{d\tilde{h}}{dx}=\frac{1}{4!\Delta x}\begin{bmatrix} -50 & 96 & -72 & 32 & -6 \\ -6 & -20 & 36 & -12 & 2 \\ 2 & -16 & 0 & 16 & -2 \\ -2 & 12 & -36 & 20 & 6 \\ 6 & -32 & 72 & -96 & 50 \end{bmatrix}\tilde{h}+\mathcal{O}(\Delta x^4) \tag{3.52}$$

$$\frac{d^2\tilde{h}}{dx^2}=\frac{1}{4!\Delta x}\begin{bmatrix} \begin{bmatrix} 45 & -154 & 214 & -156 & 61 & -10 \\ 10 & -15 & -4 & 14 & -6 & 1 \end{bmatrix} \\ \begin{matrix} -1 & 16 & -30 & 16 & -1 \end{matrix} \\ \begin{bmatrix} 10 & -15 & -4 & 14 & -6 & 1 \\ 45 & -154 & 214 & 156 & 61 & -10 \end{bmatrix} \end{bmatrix}\tilde{h}+\mathcal{O}(\Delta x^4) \tag{3.53}$$

Similar set of differentiation matrices exists for y derivatives. The corresponding approximation to spatial derivatives results in $(N)\times(M)$ differential algebraic equations. The discretized form of equations (3.46) and (3.47) can be represented as a matrix equation:

$$\frac{\partial \mathbf{q}}{\partial t}=\mathbf{M}\,\mathbf{q} \tag{3.54}$$

where

$$\mathbf{q} = [h_{0,0}, h_{1,0}, \ldots, h_{(N-1),(M)}, h_{N,M}, \Gamma_{0,0}, \Gamma_{1,0}, \ldots, \Gamma_{N-1,M}, \Gamma_{N,M}]^T$$

M is the Jacobian matrix resulting from the discretisation. The temporal integration of **q** along respective lines were carried out using RKF45 scheme developed by Shampine and Watts [97].

Temporal integration

There are many methods available for integration of differential equations of the form (3.54). One can use either implicit or explicit methods depending on the problem definitions. When the Jacobian **M** is stiff (i.e. it has eigenvalues with negative real parts of very large magnitude), implicit methods offer better stability. But the solution methods are complicated and involve matrix manipulations which become expensive in computer time. Considering these facts we used the Runge–Kutta–Fehlberg (RKF45) integrator with adaptive step size. RKF45 is a fifth order explicit method that can handle moderately stiff systems. It uses the fifth order solution to estimate the local error in Runga–Kutta method of order 4. Working with a predetermined global error ($\leq$ local error), the next step size is determined at the end of each integration depending on the current step within the required bounds ($\Delta t_{new} = 0.9[\textit{largest local error/Error tolerance}]^{0.2}\Delta t_{old}$). For a complete description of RKF45 method, reader is referred to Matthews [72]. The algorithm and coefficients of RKF45 are given in appendix A.

Several numerical tests to check the performance of the code were carried out on the time evolution of a one dimensional Korteweg de–Vries (KdV) equation (eqn 3.55) for $\Delta x = 0.5, 0.25$ and 0.1 and also for different tolerance values with fixed spacial step sizes. The well known KdV equation

$$u_t + 6uu_x + u_{xxx} = 0 \tag{3.55}$$

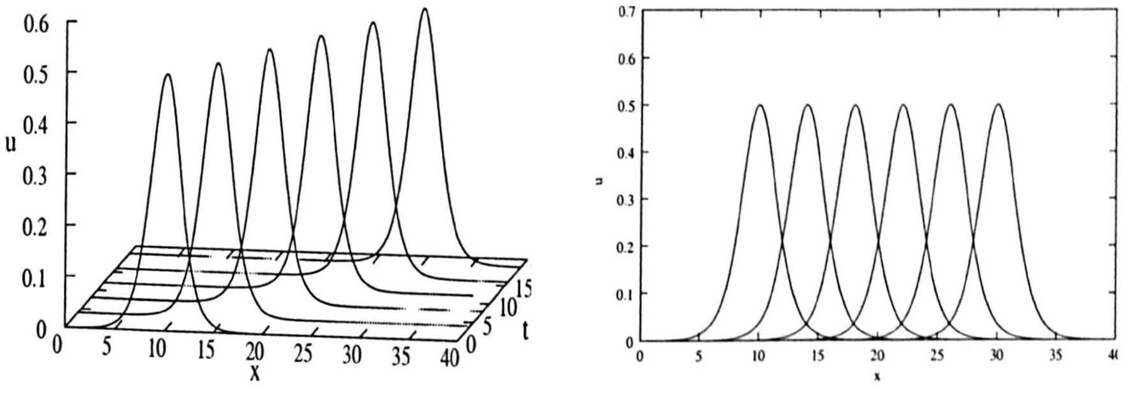

(a) (b)

Figure 3.3: 1–D evolution of KdV equation. Time evolution of KdV equation with $c = 1$ and $\Delta x = 0.2$ at t=0,4,8,12,16 and 20.

has an exact solution[22]

$$u(x,t) = f(x-ct) = \frac{1}{2}c \; sech^2\{\frac{1}{2}\sqrt{c}(x-ct)\} \tag{3.56}$$

where c is the phase velocity of the wave. We considered $u(x,0)$ as the initial condition and required $\frac{\partial u}{\partial x} \to 0$ and $\frac{\partial^3 u}{\partial x^3} \to 0$ as $x \to \pm\infty$. A seven point centred finite difference scheme was adopted to treat the u_{xxx} term in (3.55). Figure 3.3(a) shows the evolution of the wave in time t and space up to t=20. The accuracy of the numerical scheme is tested by evaluating the error $\tilde{\epsilon}$ according to

$$\tilde{\epsilon} = \frac{\sum_i |u_i^{exact} - u_i^{numerical}|}{N}.$$

The exact solution, u_{exact}, was evaluated using (3.56).

The tolerance in RKF45 demands that the error between four step and five step evaluations to be less than a minimum value. Figure 3.4(a) shows the effect of spatial discretisation. The tolerance was kept 1.0×10^{-4} while changing N. The table 3.1(a) shows the Δx and $\tilde{\epsilon}$. It is evident that the finer girds give a higher accuracy. The effect of tolerance was checked against a coarse grid with $\Delta x = 0.66$.

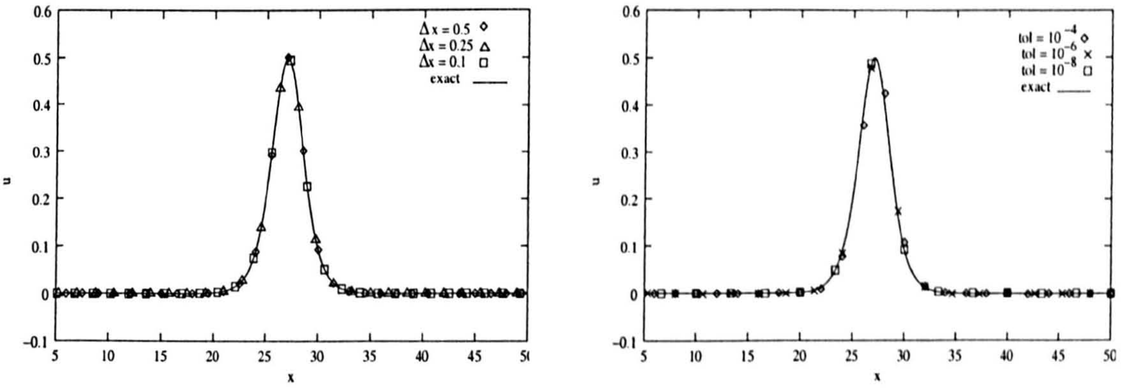

(a) (b)

Figure 3.4: The effects of discretisation and tolerance on numerical scheme. (a) Time evolution of KdV equation with $c = 1$, at $t = 12$ for $\Delta x = 0.5, 0.25$ and 0.1. Tolerance is kept constant for all Δx at 1.0×10^{-4} (see table 3.1(a)). (b) The effect of tolerance on numerical calculation.$\Delta x = 0.66$ and tolerances were 10^{-4}, 10^{-6} and 10^{-8}. (Also see table 3.1(b)).

Figure 3.4(b) shows the results for tolerance values 10^{-4}, 10^{-6} and 10^{-8}. The table 3.1(b) shows that the accuracy increases at a lower rate with tolerance. This comes with a heavy penalty of re-evaluating the time step size, increasing the number of iterations. For example, there is a five fold increase in number of iterations when tolerance is set to 10^{-8} over tolerance 10^{-4}. When it comes to solving a 2D-problem, this becomes very expensive in computer time. Therefore we use a balance of grid sizes with tolerances in the range of $10^{-4} - 10^{-6}$ depending on the performance of the code.

The temporal integration of the 2–D system was tested on the unsteady heat equation

$$\begin{aligned} \frac{\partial \phi}{\partial t} &= \nabla^2 \phi \\ \phi(x, y, 0) &= \cos\frac{\pi x}{4} \cos\frac{\pi y}{2} \\ \phi &= 0 \quad \text{on } \partial\Omega \end{aligned} \tag{3.57}$$

where $\partial\Omega$ denotes the domain boundary explicitly $[-2, 2] \times [-1, 1]$. Figure 3.5 shows

Tolerance $= 1.0 \times 10^{-4}$	
Δx	$\tilde{\epsilon}$
0.5	7.8199×10^{-4}
0.25	3.1831×10^{-5}
0.1	5.8952×10^{-6}

a

$\Delta x = 0.66$	
Tolerance	$\tilde{\epsilon}$
10^{-4}	9.7349×10^{-3}
10^{-6}	5.4608×10^{-3}
10^{-8}	1.2331×10^{-3}

b

Table 3.1: Error variation with discretisation and tolerance. By selecting a finer discretisation approach the accuracy can be largely increased.

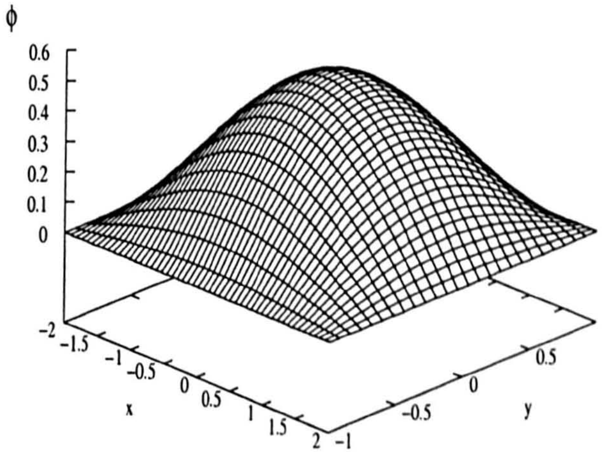

Figure 3.5: Numerical solution for unsteady heat equation at t=0.25.

the numerical solutions at $t = 0.25$. The results were tested against the results generated using implicit time stepping and spectral methods [86] and found they are in very good agreement.

The lubrication theory model equations were to be integrated using the MOL code developed. The code can simulate 3-D evolutions. However, it is used to simulate the concentration distribution and film height using nonlinear evolution equations. Therefore velocity fields are not directly evaluated. The selection of Δx is important in achieving accuracy.

In the next section, a detailed description the finite element approach is given. The fully nonlinear flow equations together with conservation of surfactant at the interface is solved using the weak formulation.

3.5.2 Numerical solutions to full N-S system with free surfaces

The method of lines solves a set of reduced equations that describe the evolution of the surface. The nonlinear terms associated with N-S equations are dropped as a result of the lubrication theory approximations. All the work related to the spreading problem so far is based on this lubrication theory approach and the stability analysis so based fails to unfold the fingering instability. We therefore aimed to solve the full nonlinear problem numerically using the finite element method. In doing so, we try to quantify the accuracy of the lubrication theory predictions of the dynamical system.

There are many commercial packages available for solving the Navier Stokes equations numerically. These codes basically consist of three major elements; namely a grid generation programme, a pde solver and a post processor (plotting programme). The grid generator provides the facility of adopting complex geometries into the computational domain. The purpose is to approximate a large region with discrete small but finite sub regions on which the equations are to be solved approximately. The pde solver transforms the flow equations (differential or integral) into discrete algebraic operations involving the values of unknowns at the mesh points. Finite difference (FD), finite elements (FEM), finite volume (FVM) and boundary elements (BEM) are a few of the methods available to approximate pdes over the meshed region in pde solvers. The major discrepancy of the commercial programs is that they were produced to cater wider commercial needs by generalising the approach. In doing so they leave elements of more scientific nature out of the product. For instance, the free surface flow solving mechanisms were not incorporated in most of those packages until recently. The free surface problem defined in §3.2 needs special treatment to implement deforming boundaries. Goodwin and Schowalter [35] successfully used a set of diffusion equations as an elliptic mesh generation scheme to address such free boundary flow problems. A brief description of the methodology of FEM used is given below with emphasis to implementation of the moving boundary. The results of the problem solved is presented in chapter 5.

Outline of FEM solution method

A finite element method is used to solve conservation of momentum, heat, and species equations in arbitrary two-dimensional geometries, both planar and axisymmetric. As the procedure for generating finite element counterparts of the flow equations (3.1)–(3.10) are well described elsewhere [47], we only outline the mathematical procedure with respect to the momentum conservation equation. Similar methodology applies to mass, heat and species equations too. The weak formulation or the Galerkin formulation involved in multiplying the conservation equations by weight functions Φ and taking the integral over the computational domain Ω yields

$$\int_{\Omega} \Phi \left\{ \frac{\partial \mathbf{v}}{\partial t} + \nabla \mathbf{v}\mathbf{v} + \frac{1}{\rho}\nabla p - \nu \nabla^2 \mathbf{v} - f \right\} dA = 0 \tag{3.58}$$

The vector–valued weight function (also called test functions) Φ can be any continuous function with a piecewise continuous derivative and dA is an element of differential area. f simply denotes the body forces. Integration by parts (i.e. divergence theorem) produces

$$\begin{aligned} \int_{\Omega} \left\{ \Phi \frac{\partial \mathbf{v}}{\partial t} + \Phi \nabla \mathbf{v}\mathbf{v} - \frac{1}{\rho} p \nabla \Phi - \Phi f + \nu [\nabla \mathbf{v} + (\nabla \mathbf{v})^T] \nabla \Phi \right\} dA \\ + \int_{\partial \Omega} \Phi \left\{ p\mathbf{n} - \nu [\nabla \mathbf{v} + (\nabla \mathbf{v})^T] \mathbf{n} \right\} ds = 0. \end{aligned} \tag{3.59}$$

The $\partial\Omega$ denotes the boundary that confines the domain Ω and ds represent an element length along the boundary. Here $\mathbf{n}$ is the unit vector normal to the boundary pointing outward direction. It is important to observe that there are no derivatives of pressure in the above equation. Similarly suppose that the weight function Θ is piecewise continuous. Then the continuity equation provides

$$\int_{\Omega} \Theta \nabla \mathbf{v} \, dA = 0. \tag{3.60}$$

Equations (3.59) and (3.60) are the weak form of a flow problem. Suppose the grid contains E elements and N nodes. The solution vector for each element, $\mathbf{v}$, can be approximated using

$$\mathbf{v} = \sum_{i=1}^{N} \hat{\mathbf{v}}_i \phi_i \qquad p = \sum_{i=1}^{N} \hat{p}_e \theta_i \tag{3.61}$$

where $\hat{\mathbf{v}}_i$ is the value of $\mathbf{v}$ at node n and $\hat{p}_e$ is the value of p at element e. The functions ϕ and θ are called the trial functions or the basis functions which are defined over the finite element. By setting $\Phi = \phi$ and $\Theta = \theta$ one can convert the weak form into Galerkin's method. Goodwin and Schowalter used quadrilateral elements with nine nodes to descretize the physical domain. Figure 3.6 shows the details of the element. The field variables, except pressure, were approximated by using biquadratic trial functions while pressure was approximated by a linear function. This combination of trial functions allows divergence free velocity fields without causing spurious pressure modes associated with other forms of combinations. By substituting (3.61) into the weak form (Galerkin) equations and performing the integrations one would obtain $2N + E$ scalar equations to determine the unknown coefficients $\mathbf{v}_i$ with the incorporation of boundary conditions. The resulting nonlinear algebraic equations forms a residual matrix

$$\mathbf{R}(\mathbf{X}) = 0 \tag{3.62}$$

where $\mathbf{X}$ is the vector of coefficients for the basis functions. Details of the form of the residual equations can be found, for instance in Kistler and Scriven [58].

The implementation of free surface dynamics is built around the core of the FEM making use of the mesh generation equations and the sparse matrix solvers used in the solution procedure. In next section we discuss this issue.

The elliptic mesh generation and implementation of deformable boundary

Grid generation is fundamental to FEM solutions since it allows accurate representation of complex geometries and inclusion of dissimilar materials and also enables an accurate representation of the solutions within each element bringing out local effects. The treatment of large gradients at initial time in the problem at hand is an advantage of this feature of FEM, since the weak form permits discontinuous field variables.

The mesh generation method in the package developed by Goodwin and Yeckel [114] is essentially an elliptic method. The elliptic mesh generation uses two elliptic pdes to map complex physical geometries into a simpler logical space without overlapping of grid lines. This method requires the knowledge of physical co-ordinates of all boundaries. Figure 3.6 shows a schematic representation of the process in general. The transformation of $x - y$ plane into logical co-ordinate system, say $\xi(x, y)$ and $\eta(x, y)$, sets a one-to-one correspondence between physical space and logical space. One of the most general elliptic transformations in use is the Poisson system:

$$\nabla^2 \bar{\xi} = P^i \qquad i = 1, 2 \tag{3.63}$$

where $\bar{\xi} = (\xi, \eta)$. For an in depth description of elliptic and other methods of mesh generation techniques, reader is referred to Thompson *at al.* [101]

The difficulty of solving free boundary problems arises in determining the position of the free boundary. Cristodoulou and Scriven[18] employed a set of pdes to control the orthogonality and smoothness in a FEM approach. Cliffe *at al.* [14] used the Cauchy-Reimann equations for orthogonal grid adaptation. Goodwin and Schowalter uses an efficient method by capitalising on the FEM solution methods together with a modification to Poisson mesh transformation. By assuming P^i in (3.63) to be $-(\nabla D \cdot \nabla \bar{\xi})/D$, where inhomogeneous diffusivity $D(\bar{\xi})$ is a control function, one

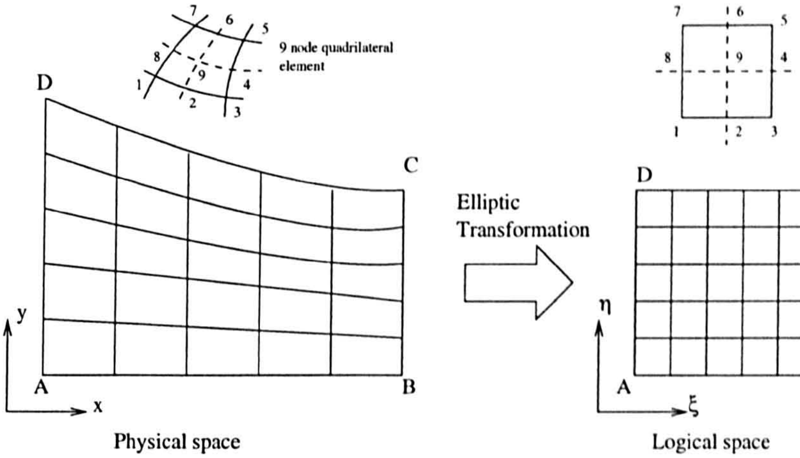

Figure 3.6: Elliptic meshing.Transformation of physical space to logical space. After Anderson [4]

could obtain a set of grid equations

$$
\begin{aligned}
&\nabla \cdot D_\xi(\bar{\xi})\nabla\xi = 0 \\
&\nabla \cdot D_\eta(\bar{\xi})\nabla\eta = 0
\end{aligned}
\qquad (3.64)
$$

that would disperse the grid within the physical space keeping the original orthogonality and smoothness[101]. The Goodwin and Yeckel FEM programme which we adapted makes use of $(3.64)(a, b)$ treating them as two ordinary scalar diffusion equations. The grid diffusivities $D_\xi(\bar{\xi})$ and $D_\eta(\bar{\xi})$ can be anisotropic and heterogeneous. The grid is controlled by specifying grid diffusivities and grid equation BCs. The grid diffusivities are specified locally for each element using the undeformed grid so that it preserves the initial sizing. In the logical coordinate system, the elements are all of the same size, shape and orientation with element boundaries on coordinate lines.

The free surface $S(x, t)$ (as in figure 3.1) is a curve of constant η in logical space. The grid is coupled to the flow using the 2–D form of the kinematic boundary condition (3.5). At any fixed time t_m, the kinematic boundary can be defined as $\mathbf{v}_m \cdot \mathbf{n} = 0$. (This also implies that the velocity is tangential to the surface). Given that the velocity vector $\mathbf{v}_m$ is already evaluated, the kinematic boundary condition serves as a boundary condition for the grid equations, enabling one to evaluate local free surface height. The grid mapping procedure is first to specify the locations of the nodes along the boundaries of the domain and then to use an interpolation scheme to locate the interior nodes. The effect of surface tension enters the surface defining step through the velocity vector. The tangential and normal stress balances are the boundary conditions required in solving the flow field. The surface tension gradients that arise along the surface due to differential spreading of a surfactant is incorporated into the tangential stress boundary condition via a Marangoni number defined as:

$$Ma_n = \frac{h\sigma_\Gamma \Gamma_x}{\mu U_s} \tag{3.65}$$

It is important to mention here that the implementation of surface concentration as a function along the surface (or attributing values at nodes) is not possible since the boundary nodal values in FEM in general are not accessible. Thus we pose the problem differently which we describe in detail in chapter 5.

The grid diffusion equations are also solved using finite element method. $3.64(a, b)$ multiplied by a weight function $\Psi(x, y)$ and integrated over the entire computational domain forms the weak equations. The resulting equations are incorporated into the coefficient matrix equation $\mathbf{R}(\mathbf{X}) = 0$ and solved simultaneously for the grid positions with the physical variables. The inclusion of grid equations does not violate the sparseness of the matrix. This makes the package efficient since no iterative re–griding procedure is necessary as in many other cases (e.g. FIDAP).

Solution procedure

Implementation of the Galerkin method on the conservation equations (flow, heat, species,etc.) together with grid equations forms the nonlinear algebraic residual equations $\mathbf{R}(\mathbf{X}) = 0$ (i.e. (3.62)). Solving (3.62) requires a root finding procedure. The simulation engine uses the Newton's method to solve (3.62) iteratively. Then the next iterate of the approximate solution becomes:

$$\Delta \mathbf{X}^{(k+1)} = -\left[\left(\frac{\partial \mathbf{R}}{\partial \mathbf{X}}\right)^{(k)}\right]^{-1} \mathbf{R}^{(k)} \tag{3.66}$$

The superscript k indicates the iteration number, $\Delta \mathbf{X}$ is the change in solution vector, and $\frac{\partial \mathbf{R}}{\partial \mathbf{X}}$ is the analytically evaluated Jacobian matrix of the sensitivities. Gaussian elimination by the frontal method [24] is used to solve the sparse nonsymmetric matrix problem associated with (3.66). The convergence criteria were that both $||\mathbf{R}||$ and $||\Delta \mathbf{X}||/||\mathbf{X}||$ be less than 10^{-4}, where $||\cdot||$ denotes an L_2 norm.

3.6 Summary

In this chapter, beginning with the Navier–Stokes equations, continuity equation and a species conservation equation, we derived a set of surface evolution equations for the spreading of a surface active secondary phase on a flowing liquid substrate. The inertial forces of the background flow are coupled with the equations by means of the nonlinear term $P_x \, Re \, h^2 h_x$.

We aim to solve the spreading problem using two different techniques. First is to solve the evolution equations derived using lubrication theory approximations. The well established MOL numerical scheme is used together with Runge–Kutta–Fehlberg integration scheme to solve the two equations simultaneously. The code we developed was briefly described. Solutions to well known KdV equation is presented as a measure of accuracy of the code. The 2D simulation engine was tested with a Helmholtz equation.

The second method is to solve the full N–S system by means of a FEM scheme which facilitates free surface problems. The code initially developed by Goodwin and Schowalter [35] was modified to include soluto-capillary flow effects. The main steps of the numerical scheme were described.

The numerically computed solutions to evolution equations are presented in next chapter and the FEM solutions are presented in chapter 5.

Chapter 4

Onset and evolution of surface instabilities under Marangoni stresses on a flowing thin film

4.1 Introduction

The primary objective of this chapter is to investigate the propagation of surface waves initiated by the surface tension gradient on a *flowing* film and the subsequent spreading of the surfactant. The spreading of a surfactant drop on a *stationary* liquid substrate has been the focus of several recent studies. Jensen and Grotberg and many others [52, 99, 54, 56] studied the spreading rates using asymptotic and similarity solutions. Matar and Troian [68, 71, 70] studied the fingering instability of the spreading system. A summary of these findings is presented in chapter 2 §2.4. All these studies were based on lubrication approximations. The driving force for fluid flow in these cases is the surface stress induced by the surfactant concentration gradient, under the influence of which the substrate surface deforms. However, in numerical simulations, the resulting perturbation is found to be long lived and decaying [33] whereas the experiments recorded film rupture and formation of a 'dry spot' [99, 34].

Presence of a background flow introduces an inertial coupling to the evolution equation which changes the dynamics of the system. The dynamical equations were derived in chapter 3 using lubrication theory. The evolution equations for substrate film height and surfactant concentration are:

$$h_t + Re\, P_x h^2 h_x - \frac{\mathcal{M}a}{2}(\Gamma_x h^2)_x - \frac{\mathcal{M}a}{2}(\Gamma_y h^2)_y = 0 \qquad (3.46)$$

$$\Gamma_t + \frac{Re\, P_x}{2}(\Gamma h^2)_x - \mathcal{M}a[\Gamma(\Gamma_x h)]_x - \mathcal{M}a[\Gamma(\Gamma_y h)]_y - \frac{1}{\mathcal{P}e_s}(\Gamma_{xx} + \Gamma_{yy}) = 0. \qquad (3.47)$$

The terms $ReP_x h^2 h_x$ and $\frac{Re P_x}{2}(\Gamma h^2)_x$ in (3.46) and (3.47) respectively incorporate inertial effects from background flow into the surface evolution equations. These contributions are non-trivial modifications to the systems studied in two major respects: (i) breaking the horizontal symmetry; (ii) nonlinear accretion leading to shock front breaking. We investigate the effects of the background flow field on wave fronts generated by Marangoni stresses and on transporting the monolayer material for various values of parameters $ReP_x, \mathcal{M}a$ and $\mathcal{P}e_s$. The evolution equations (3.46) and (3.47) were solved numerically using the method of lines (MOL) described in detail in chapter 3 for initial and boundary conditions that defines the physical setting. All simulations were carried out on two grids; the second grid refined doubly as a check on convergence.

This chapter is organised as follows. In §4.2 we discuss the flow configurations which we will investigate in §4.5 and §4.6. We discuss energy and mass conservation of the system in §4.3 and §4.4 respectively. The energy terms gives the length averaged strength of individual components over the evolution time. The mass conservation provides a measure of accuracy. In §4.5, the case of surfactant gradient in the same direction of flow is analysed in detail. Influence to adverse surfactant gradient is examined in §4.6. To draw more clarity into the evolution patterns we analyse the flow in the bulk by employing stream functions in §4.7. As we mentioned, we begin with defining the flow configuration.

4.2 Flow configuration of the physical problem

There are two distinct cases for spreading and evolution of surface waves that arise from introducing a preferred direction of the bulk flow. First is the surfactant front moving in the same direction as the flow producing a surface tension gradient along the flow direction. Since the induced velocity field has the same orientation as the bulk flow, faster rates of spreading can be expected. The physical setting is schematically presented in figure 4.1(a) where the arrow marks the bulk flow direction. The concentration profile is shown by the line with end values $\Gamma_{-\infty} = 1.0$ and $\Gamma_{+\infty}$ and the concentration change from $\Gamma_{-\infty}$ to $\Gamma_{+\infty}$ is abrupt but continuous. The second case is the surfactant front still moving with the substrate but the gradient is opposite to the flow direction. The Marangoni induced surface stress oppose the flow. The symmetry of the spreading problem is broken by the existence of the preferred direction of the background flow. Figure 4.1(b) shows the general setting.

The effect of the concentration gradient depends on the sensitivity of the surface to surfactants. The Marangoni number $\mathcal{M}a$ defined for the flow system characterises the relative importance of surface tension forces over dissipative forces. The background flow field transports the surfactant layer into the domain and therefore sets the scale for surfactant flux. Marangoni effects can *a priori* modify the transport rate of surfactant *locally.*

In the case of a planar surfactant layer, the concentration changes are only x and t dependent. This allows us to eliminate the y dependency of the equations (3.46) and (3.47), reducing the evolution equations to one dimensional in space. However

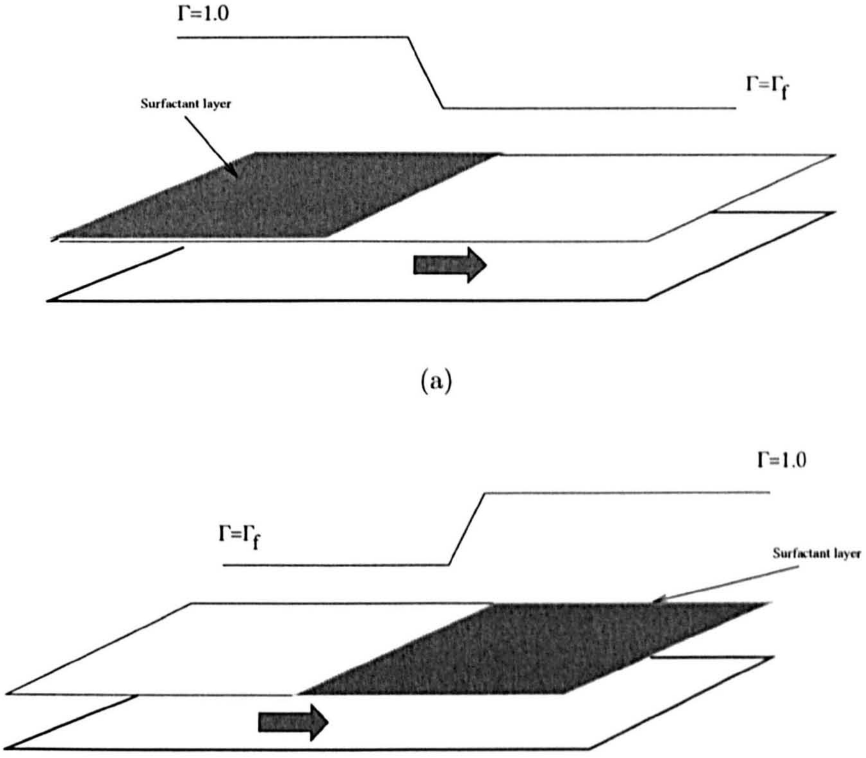

(a)

(b)

Figure 4.1: Schematic representation of the flow configurations investigated. (a) shows the case with concentration gradient along the flow and (b) shows the case of adverse concentration gradient. The arrow marks the direction of flow which is the positive x direction

before moving on to numerical simulation results, we introduce two global measures:

- Length average energy intensity.
- Overall mass balance.

The length averaged energy terms provide a measure of the importance of individual terms over time whereas overall mass balance sets a test to check the accuracy of the transport mechanisms of the evolving system with reference to a physical constraint. The numerical accuracy of the each time step is set by an L_2 norm tolerance which is a simulation parameter independent of the physics involved. However the mass balance sets a test for the overall fidelity of the calculation.

4.3 The length averaged energy of individual components of evolution equations

We trace the behaviour of each term in the two evolution equations to find out the dominant terms in time evolution. Although we calculate them at each grid point as a part of solution methodology, it is more physically revealing to investigate the time evolution of each mechanism separately. Therefore we define the mechanical energy as

$$E = \|u\| = \frac{1}{2}\langle u \cdot u \rangle \tag{4.1}$$

for a vector or scalar quantity u. The $\langle \cdot \rangle$ represents the integration over the computational domain. The two evolution equations contain two physical variables h and Γ. We take $u = (h, \Gamma)$. Using the above definition we formulate the energy of evolution of the surface by taking the inner product of (3.46) and (3.47) with u.

$$\frac{\partial}{\partial t}\langle u^2 \rangle = 2\frac{\partial}{\partial t}E_u = \Big\langle N(u, \mathcal{P}e_s, \mathcal{M}a, P_x, Re) \cdot u \Big\rangle \tag{4.2}$$

ID	Expression	Physical description
I_0	$\int_{-\infty}^{+\infty} \frac{1}{2}h \cdot h\, dx$	Total flow energy
I_1	$Re\, P_x \int_{-\infty}^{+\infty} \frac{1}{2}h \cdot h^2 h_x\, dx$	Stream wise bulk flow inertial coupling
I_2	$\frac{\mathcal{M}}{2} \int_{-\infty}^{+\infty} h \cdot \left(\Gamma_x h^2\right)_x dx$	Stream wise Marangoni flow
I_3	$\int_{-\infty}^{+\infty} \frac{1}{2}\Gamma \cdot \Gamma\, dx$	Total chemical energy
I_4	$\frac{Re\, P_x}{2} \int_{-\infty}^{+\infty} \Gamma \cdot \left(\Gamma h^2\right)_x dx$	advection supported by bulk flow
I_5	$\frac{\mathcal{M}}{2} \int_{-\infty}^{+\infty} \Gamma \cdot \Gamma\left(\Gamma_x h^2\right)_x dx$	Marangoni advection

Table 4.1: Individual energy terms arising from evolution equations.

$N(u, \mathcal{P}e_s, \mathcal{M}a, P_x, Re)$ represents the nonlinear terms of the evolution equation. The resulting E_h is the total energy of the surface height evolution and E_Γ is the total energy of the concentration evolution; the total energy of the system E_T is given by $E_h + E_\Gamma$. Table 4.1 gives the individual components with physical description.

The energy integrals were numerically evaluated using the trapezoidal rule [82], taking advantage of the refined mesh simulations.

4.4 Conservation of surfactant mass

The surfactant layer that sits on the substrate will be carried into the frame of reference by the bulk flow. The mass of surfactant should be conserved globally. To compute the amount of surfactant mass we integrate (4.8) over the interval $-\infty < x < +\infty$.

$$\frac{\partial}{\partial t}\int_{-\infty}^{+\infty}\Gamma(x,t)dx = \frac{Re\,P_x}{2}\int_{-\infty}^{+\infty}(\Gamma h^2)_x dx + \mathcal{M}a\int_{-\infty}^{+\infty}[\Gamma(\Gamma_x h)]_x dx + \frac{1}{\mathcal{P}e_s}\int_{-\infty}^{+\infty}(\Gamma_{xx})dx \quad (4.3)$$

As shown in figure 4.1, the boundary values of concentration, $\Gamma(-\infty,t)$ and $\Gamma(+\infty,t)$, remain constant throughout the period of observation (we discuss boundary conditions in detail in §4.5). Therefore $\Gamma_x = 0$ at the boundaries. Since there is no concentration gradient at the boundary, the film height remains unchanged at unity. Evaluating the integrals and applying these boundary conditions yields:

$$\frac{\partial}{\partial t}\mathcal{G}(t) = \frac{Re\,P_x}{2}\Big[\Gamma(-\infty,t)-\Gamma(+\infty,t)\Big] \quad (4.4)$$

$$\text{where} \qquad \mathcal{G}(t) = \int_{-\infty}^{+\infty}\Gamma(x,t)dx \quad (4.5)$$

Integrating (4.4) once and within the period t_0 to t and considering the fact that $\Gamma(\pm\infty,t)$ remains constant for the period of observation results in

$$\mathcal{G}(t)-\mathcal{G}(t_0) = \frac{Re\,P_x}{2}\Big[\Gamma_{-\infty}-\Gamma_{+\infty}\Big](t-t_0) \quad (4.6)$$

$\mathcal{G}(t)$ is the mass of surfactant in the observation frame at any time t while $\mathcal{G}(t_0)$ is the initial amount of surfactant mass in the system which can be calculated by integrating (4.9) over the domain. Therefore the surfactant mass can be evaluated analytically. In the case of numerical simulations we can calculate the total surfactant mass by integrating the calculated profile $\Gamma(x,t)$ over the domain for any time interval. The numerical accuracy can be assessed by comparison with the analytic values. We observed this rule during all the simulations. Similarly by considering the evolution equation for film height, we can show that the initial mass should be conserved during the period of observation.

4.5 A planar surfactant front with concentration gradient supporting the flow

The substrate flows in the positive x direction under an imposed pressure gradient. A planar surfactant front is introduced at $t = 0$ as the initial condition. The surfactant concentration drops rapidly around a prescribed point marking the contact line (See Fig.4.1(a)). There is a continuous inflow of surfactant with the moving surface for all $t > 0$. There are no distributed sources. Concentrations at $\pm\infty$ stays constant during the period of observation since the mutual alterations to flow and concentration due to Marangoni stresses do not reach either boundary during that time.

The evolution equations are

$$h_t + Re\,P_x h^2 h_x - \frac{\mathcal{M}a}{2}(\Gamma_x h^2)_x = 0 \tag{4.7}$$

$$\Gamma_t + \frac{Re\,P_x}{2}(\Gamma h^2)_x - \mathcal{M}a[\Gamma(\Gamma_x h)]_x - \frac{1}{\mathcal{P}e_s}(\Gamma_{xx}) = 0 \tag{4.8}$$

initial conditions are

$$\Gamma(x,0) = \frac{\Gamma_I}{2}\left(1.0 - Tanh\left[\frac{(x-x_0)}{\Delta l}\right]\right) \tag{4.9}$$

$$h(x,0) = 1.0 \tag{4.10}$$

We select boundary conditions to model the physical situation of the problem.

$$\Gamma = \Gamma_{-\infty} = 1.0 \qquad \text{at} \quad x = -\infty \tag{4.11}$$

$$\Gamma = \Gamma_{+\infty} \qquad \text{at} \quad x = +\infty \tag{4.12}$$

$$h = 1 \qquad \text{at} \quad x = \pm\infty \tag{4.13}$$

In (4.9), $\Gamma_I = \Gamma|_{max}/\Delta\Gamma$ and Δl is the length over which the change takes place. Both are parameters that control the nature of the initial condition. For numerical simulations of a planar front, we chose $\Gamma_I = 1.0$ and $\Delta l = 2.0$. Figure 4.2 clarifies the

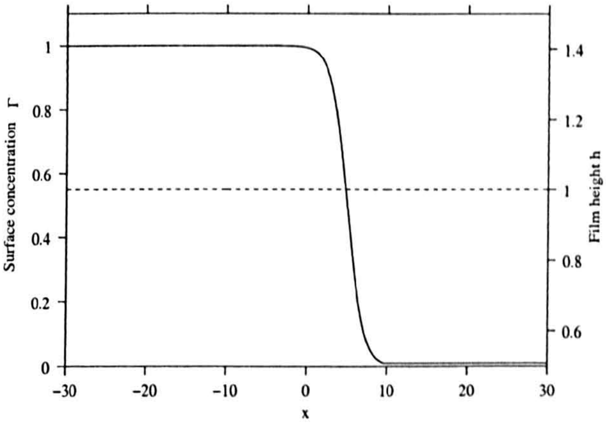

Figure 4.2: Initial conditions (4.9) and (4.10). Left y axis scales the concentration while right y axis scales the initial film profile. Dashed line represents the surface height and the thick line is the surfactant concentration.

initial conditions. The surface concentration changes dramatically around $x_0 = 5.0$. The substrate surface is initially flat (Dashed line in Figure 4.2, to be read with right axis). The semi infinite layer of surfactant moves into the frame of reference at a constant rate set by the bulk flow (i.e. $P_x Re$).

The equations (4.7) and (4.8) were solved numerically using the MOL algorithm described in Chapter 3. The system becomes numerically unstable for pure downstream surfaces due to the sharp change of concentration specially when Marangoni assisted advection is maximum. To tackle this sharp changes the grid has to be very fine. Since the equations are of $\mathcal{O}(1)$, to maintain the validity of equations (4.7) and (4.8) during numerical simulations, we have to use $\Delta x \gg \varepsilon$ [77]. This requirement sets a lower limit on grid refinement. On the other hand by setting $\Gamma_{+\infty} > 0$ but small, the sharp changes in Γ can be smoothed out. By setting non-zero $\Gamma_{+\infty}$, the dynamics of the system would not be affected greatly[52]. Therefore we assume a contaminated surface downstream and set the contamination to 1% of Γ_I. Therefore (4.9) changes from 1.0 to 0.01 and also $\Gamma_{-\infty} = 0.01$. The numerical accuracy was checked by: 1. refining the mesh 2. observing the conservation laws and 3. changing the discretisation methods whenever necessary (e.g. Centred FDs to upwind schemes).

4.5.1 Spatio–temporal evolution of the film surface and surfactant layer

Surface tension varies according to the distribution of surface loading. The functional relationship between surface tension and concentration is given by the equation of state. The Marangoni number that appears in equations (4.7) and (4.8) constitutes a measure for the relative strength of the surface tension gradient. A surface tension gradient induces a surface stress field proportional to $\mathcal{M}a\Gamma_x$ in magnitude in the direction of the gradient (i.e. in this case in the direction flow). Hence the liquid is dragged towards the relatively clean substrate surface giving rise to a surface wave. Figure 4.3 shows the evolution of surface height and surfactant concentration over time for fixed parameter values $\mathcal{P}e_s = 100$, $P_x Re = 0.25$ and $\mathcal{M}a = 1.0$. It is evident from the simulations that the shock grows to its maximum height within a very short time and then decays. The trough deepens with time while the decaying peak moves away from the trough. The predominant mode of surfactant spreading in this case is obviously the advection. The trough is a direct result of the surfactant gradient and moves synchronised with the surfactant front, giving the maximum trough depth at the point where the surface stress is maximum (see Fig.4.4).

The surfactant flows into the system with the bulk flow at a constant rate as described in the previous section §4.4. At large $\mathcal{P}e_s$ the spreading through diffusion is limited. There are two time scales in competition in this problem.

$$\begin{aligned} \text{Inertial timescale} \qquad \tau_I &= \frac{d}{U_s} \\ \text{Diffusion timescale} \qquad \tau_D &= \frac{d^2}{\mathcal{D}_s} = \mathcal{P}e_s\,\tau_I \end{aligned} \tag{4.14}$$

For $\mathcal{P}e_s \gg 1$, diffusion is a slow process compared to advection. At early times,

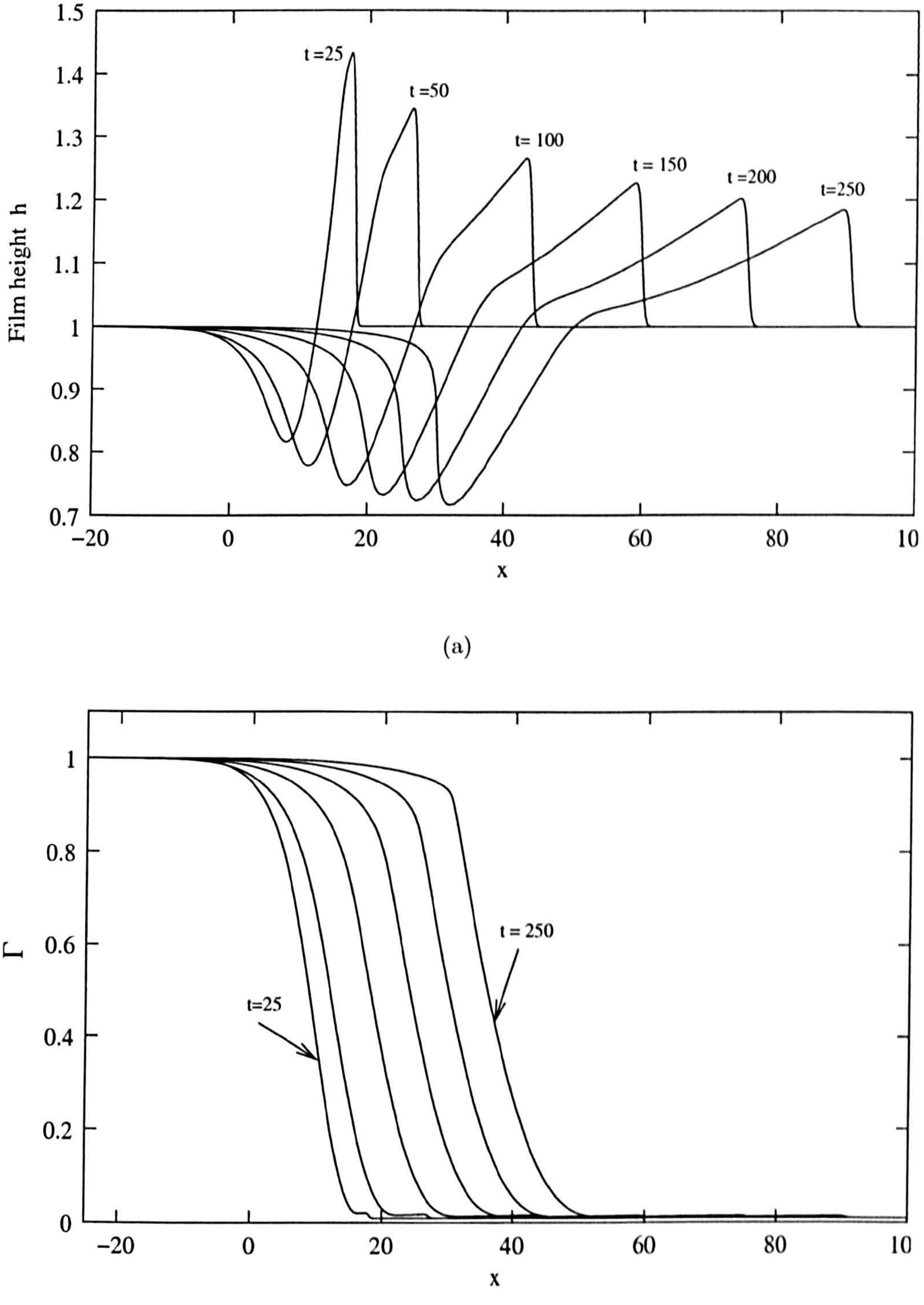

(a)

(b)

Figure 4.3: Spatio–temporal evolution of the film surface and the surfactant layer. (a) the surface evolution in time; (b) the corresponding surfactant concentration at $t = 25, 50, 100, 150, 200$ and 250. $\mathcal{P}e_s = 100$, $\mathcal{M} = 1.0$, $P_xRe = 0.25$ and the contamination downstream $\Gamma_{+\infty} = 0.01$.

the Marangoni induced local velocity field which is super-imposed on the bulk flow, smooths out the initially steep concentration gradient. Therefore the surface stress, σ_x, decreases. During the initial moments the Marangoni induced inertial activity is dominant and the spreading is due to advective movements. For the case of spreading of a monomolecular surfactant drop on a stationary substrate with high Péclet number (=100), as examined by Jensen and Grotberg [53], the concentration plots for early time evolution shows a sharp contact lines indicating $|\Gamma_x| > 0$ at contact line (Figure 1(a) in [53]). The late time evolution plots shows that the contact line becomes hazy as the front become tangential to $\Gamma = 0$ line showing the dominance of diffusion. The transition takes place as shear induced advection decays with decreasing Γ_x due to Marangoni assisted spreading. However in the presence of a background flow and slightly contaminated surface, we can see a formation of a step in concentration profile behind the contact line which persists throughout the evolution (see Figure 4.3). We have tried the planar front simulation in absence of a background flow and found that there is no step formation in concentration around the contact line. We observed that the step is formed as the front of the capillary ridge get steeper. The concentration drops to $\Gamma_{+\infty}$ just in front of the steep edge of the shock. The excessive surfactant mass is transported by the combined effect of Marangoni induced stress and the bulk velocity. As time increases, the capillary ridge stretches thinning the surfactant quantity across the ridge. Hence the thickness of the step drops. However, a sharp drop of concentration marking a clear contact line exists just behind the shock front through out the simulation time. Therefore the shock, though diminishing in height, retains the steep front for all time.

One can expect the shear stress to decay in magnitude throughout if there is no bulk flow (i.e. an stagnant substrate) [52]. Since the advection is a faster process than diffusion in this case, more surfactant is transported into the diffusive regime with bulk flow (Bulk flow is discussed in detail in §4.7). This effectively slows down the

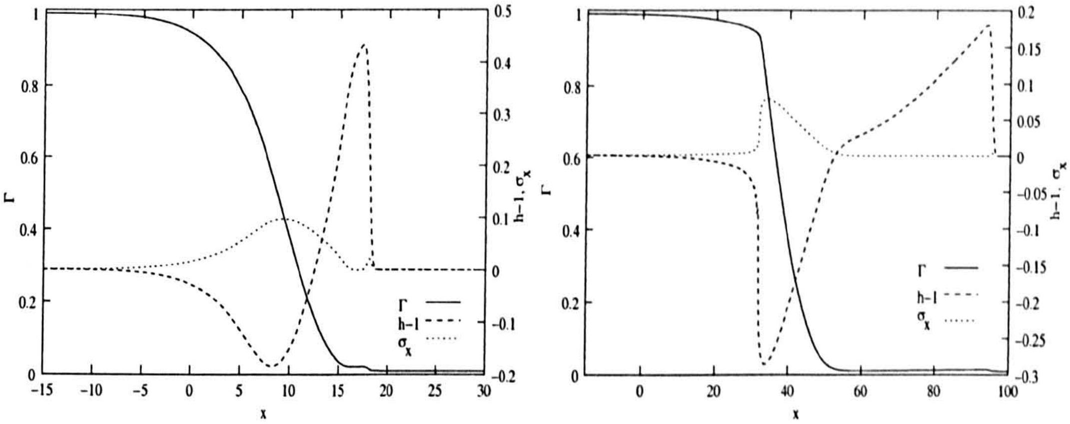

(a)

(b)

Figure 4.4: Wave breaking mechanism. The figures shows the concentration $\Gamma(x)$, surface height $h(x) - 1$ and the surface stress σ_x for parameter values $\mathcal{M} = 1.0$, $P_x Re = 0.25$, $\mathcal{P}e_s = 100$ and the contamination down stream $\Gamma_{+\infty} = 0.01$. Figure (a) and (b) shows Γ, $(h-1)$ and σ_x at an early time $t = 25$ and just before breaking at $t = 265$ respectively. Note the trough coincides with the maximum stress.

decaying rate of σ_x and eventually shows a slight increase behind the moving front. In figure 4.3(b), the concentration curves show that advection is faster than the diffusion, hence the development of the 'cusp' resulting in a large change in gradient as time increases. Since there is a buildup of concentration, the Marangoni stresses again should play a role in the neighbourhood of the buildup. The shear stress σ_x falls initially, showing the rapid spreading due to Marangoni induced flow. Plots of shear stress along the surface in Figure 4.5 shows that the initial drop occurs as envisaged, but then the peak stress remains unchanged for a long time. This effect is enforced by the advection of surfactant towards the moving front. The plot of the magnitude of Marangoni advection energy in Figure 4.6 shows this behaviour clearly. The initially higher value represents the relatively large stress induced by the initial condition. The magnitude decays with the spreading of surfactant since the gradient decays, reaching a minimum around $t = 130$. Then the magnitude of the energy due to Marangoni advection increases at a lower rate according to the

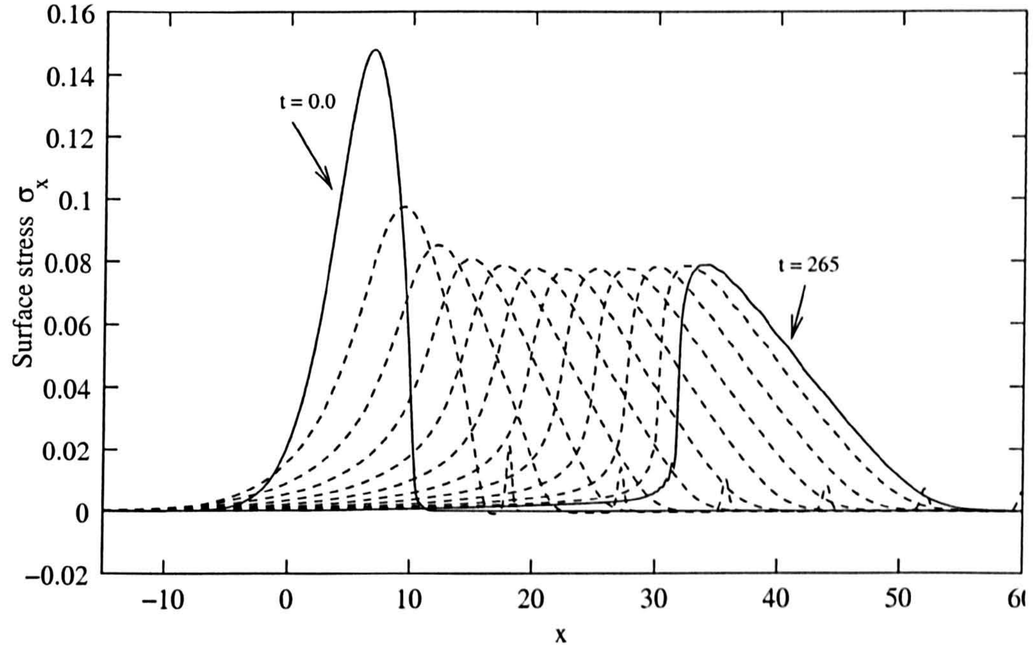

Figure 4.5: Surface stress evolution in time. The parameters are as same as for Fig. 4.3. The two thick profiles shows the initial surface stress distribution at $t = 0$ and just before breaking at $t = 265$. The dashed lines shows the stress distribution in time periods $\Delta t = 25$.

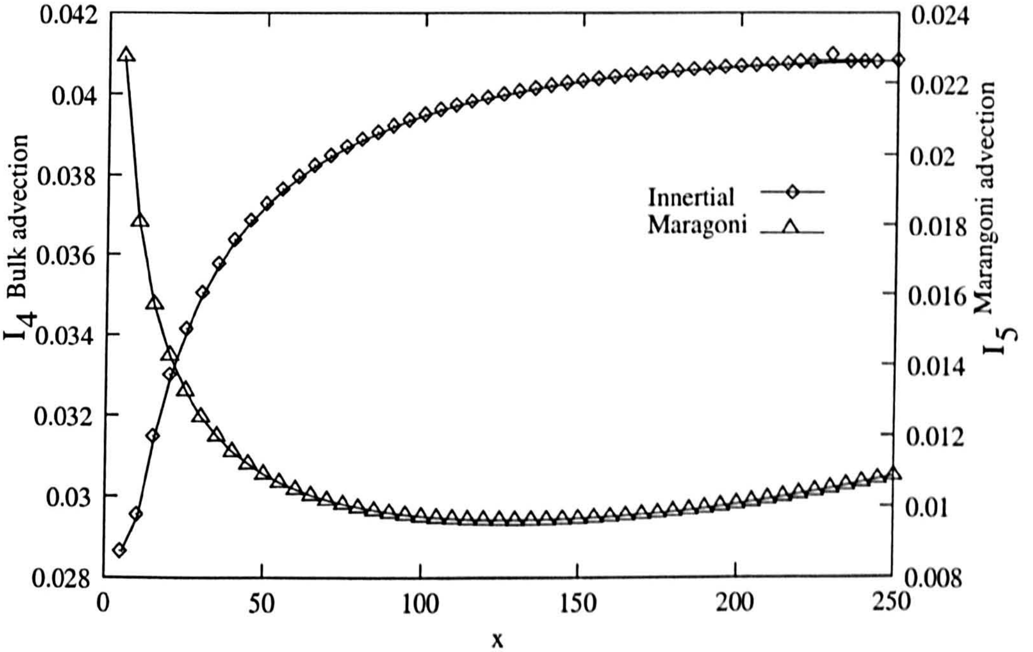

Figure 4.6: The evolution integral components I_4 (bulk advection) and I_5 (Marangoni advection) as defined in table 4.1. Parameters as in 4.3.

concentration buildup at the moving front. Since the surfactant activity beyond the trough is nearly non-existent, this increase in energy can be totally attributed to the effect described above. This secondary effect influences the wave to break just behind the trough. In simulations, this effect causes numerical instability since the code cannot handle the topological changes. To address any suspicions that this is a numerical relic, we have carried out simulations with refined grids and smaller time step changes. Although the time integration uses an adaptive step size, the maximum step size can be controlled. On both occasions the breaking time remains within a 2% margin.

The trough and the peak move with different velocities. These velocities were evaluated by tracking the distance they travelled. Figure 4.7 gives the position of the peak and trough against time. After the effects of the initial condition are smoothed out, the profiles of both curves become linear. The trough velocity $V_t = 0.096$ and the peak velocity $V_p = 0.302$ for the parameters given in Figure 4.3.

4.5.2 Effects of Péclet number

The work of Gaver and Grotberg [33] describes the effect of $\mathcal{P}e_s$ for an axisymmetric spreading of a surfactant drop. They showed that the geometry of the wave as well as the spreading rates are dependent on $\mathcal{P}e_s$ numbers. Large $\mathcal{P}e_s$ numbers result in shock fronts with higher peaks. This is due to the slow spreading which takes a longer time to smooth out the concentration gradients. It is important to point out that in their model the advection is only due to the velocity field induced by the Marangoni stresses.

As we discussed in previous section, when $\mathcal{P}e_s \gg 1$, diffusion is a very slow process. The spreading is a direct result of advection. We can clearly see this fact in Figure 4.8. The Figure 4.8 shows (a) the film heights and (b) the concentration profiles at $t = 10$ with $\mathcal{M}a = 1$ and $P_x Re = 0.25$ for various $\mathcal{P}e_s$ numbers (given in figure

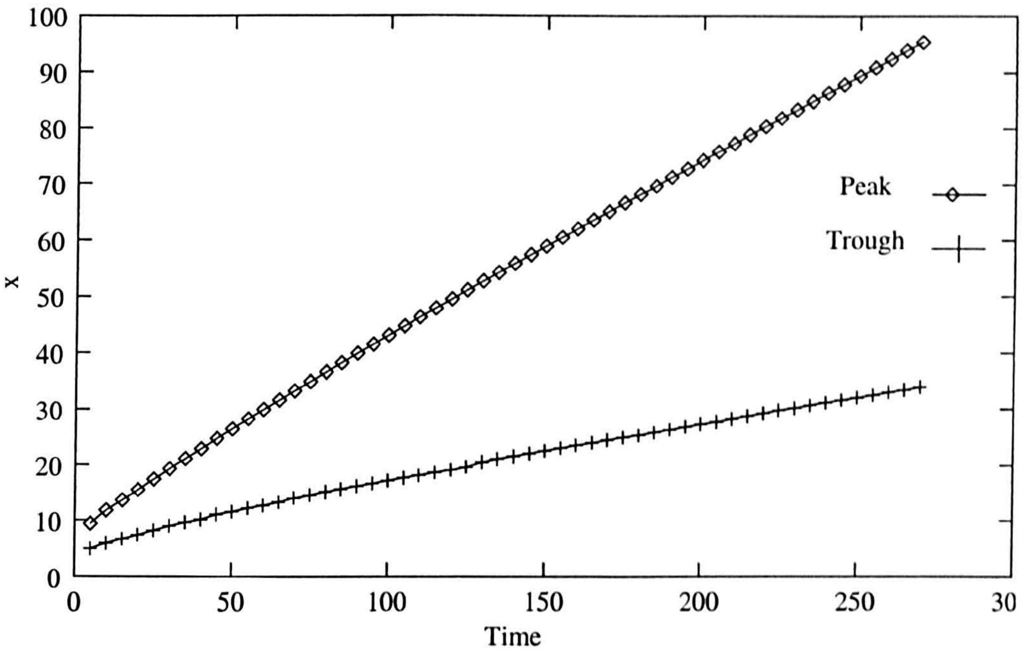

Figure 4.7: The position of peak and trough against time. After the initial accelerated change, both, peak and trough travel with a constant speeds. Peak travels nearly three times faster than the trough. Same parameters as given in Fig. 4.3

caption). The concentration front at higher $\mathcal{P}e_s$ numbers ($\mathcal{P}e_s > 35$) moves with the same speed. Furthermore the resulting capillary waves too have almost the same height and shape. With increasing time, the wave structure for all $\mathcal{P}e_s > 35$ become similar in geometry. The magnitude of $\mathcal{P}e_s$ should have an effect on the amplitude of the shock front, giving a larger ridge and sharper shock at large $\mathcal{P}e_s$, and that is exactly true for spreading on an stationary substrate. The difference is caused by the inertial coupling terms with $P_x Re$ in (4.7) and (4.8). For all $\mathcal{P}e_s > 35$ we observe the strong advection of surfactant at early stages (i.e. the formation of step in concentration plot showing that material is carried along with the shock front) .

The behaviour of the the wave at smaller $\mathcal{P}e_s$ numbers differs from the mechanism described in §4.5.1 due to the faster diffusion rates. Figure 4.9 shows the evolution of the surface and the concentration front for $\mathcal{P}e_s = 1.0$. In Figure 4.9(a) the curve representing $t = 110$ shows the initiation of numerical breakdown due to steep

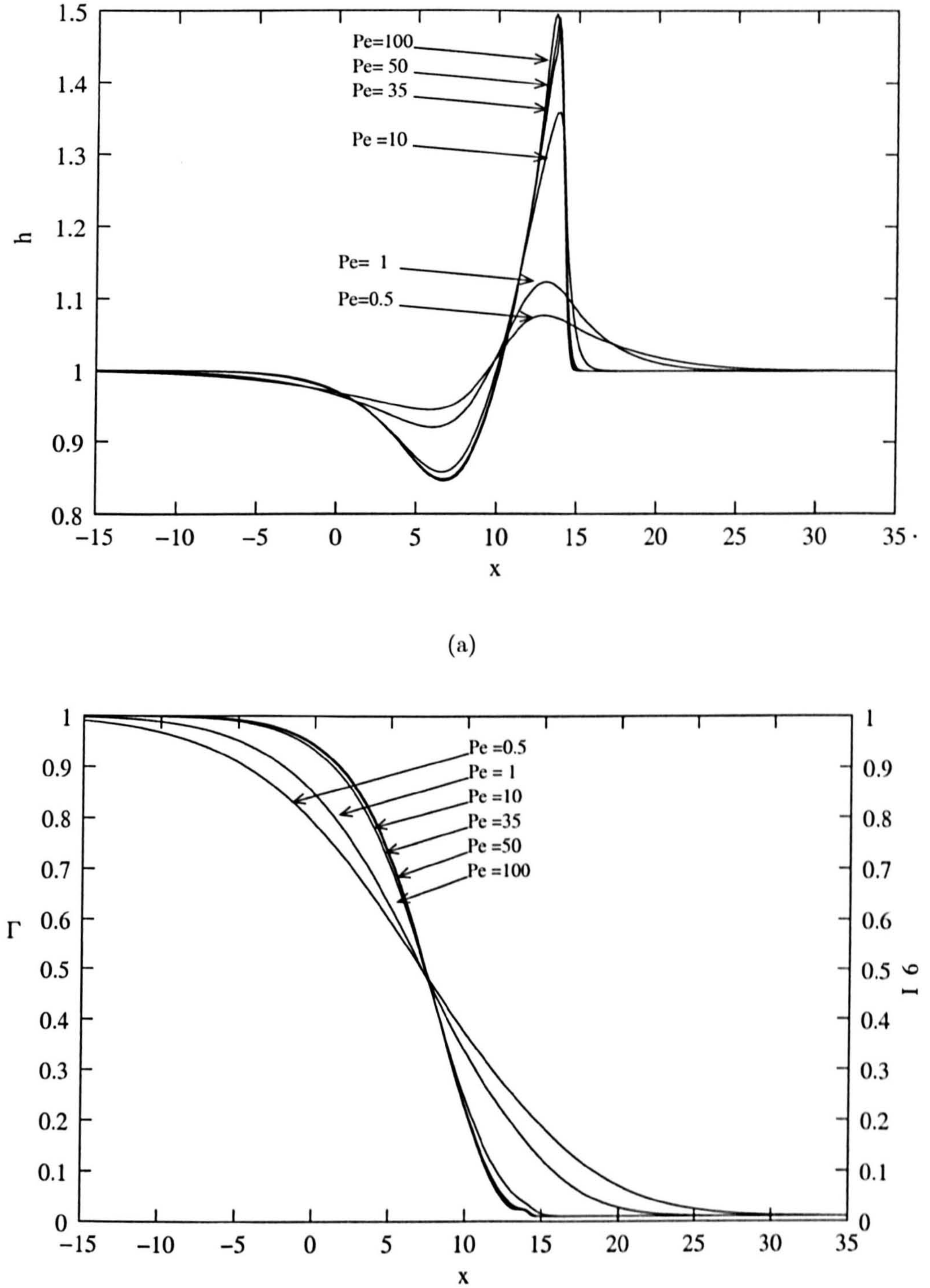

(a)

(b)

Figure 4.8: Influence of $\mathcal{P}e_s$ number on wave propagation. (a) Film height profile for $\mathcal{P}e_s = 0.5, 1, 10, 35, 50$ and 100 at $t = 15$. (b) shows the corresponding concentration curves. $\mathcal{M} = 1.0$, $P_x Re = 0.25$ and the contamination down stream $\Gamma_{+\infty} = 0.01$.

gradient. Unlike for $\mathcal{P}e_s \gg 1$, we can observe faster diffusion processes reducing the induced stresses rapidly. Since the concentration gradient decreases rapidly, the associated stress diminishes at the same rate giving shorter wave heights. The mechanism of advective transport of surfactants towards the diffusion front is active (and has a constant inflow rate) but the high rate of diffusion eliminates any build up behind the contact line, hence no 'cusp' formation. An additional qualitative change occurs when $\mathcal{P}e_s < 30$. Instead of becoming unstable behind the trough, the wave breaks when the peak sharpens to a steep gradient that resembles a folding over. This breaking mechanism is similar to the breaking of a surface wave due to a moving pressure disturbance under forcing [12]. The forcing comes from the bulk flow and also by the weakening Marangoni stresses. Again we used finer grids to verify that the occurrence of the wave breaking is simply not a numerical relic. We used spatial discretisation $0.05 \leq \Delta x \leq 0.2$ and found that the wave breaking occurs independently of the numerical formulation.

The wave breaking time or the life span of the wave since it is excited is measured for various $\mathcal{P}e_s$ numbers in order to explore the transitions between breaking mechanisms. Figure 4.10 shows the nondimensional breaking times against $\mathcal{P}e_s$. We can observe a discontinuity around $\mathcal{P}e_s = 30$. The reason for the discontinuity in T_b is the transition from one breaking mechanism to another. Wave breaking of either type described above is accompanied by the onset of numerical instability, since our simulation methodology requires the interface remain a single topological entity. The pinch-off of a droplet and reattachment are not treatable by this technique. For instance, the low $\mathcal{P}e_s$ peaking instability would break and reconnect, if the simulation permitted, and then later breaking according to the trough instability. However, for $\mathcal{P}e_s > 35$ (with $\mathcal{M}a = 1.0$ and $P_x Re = 0.25$) the wave behaves as described in section 4.5.1. The labels I, II and III in Figure 4.10 marks the regions in$\mathcal{P}e_s$where waves break with different mechanisms. In regime I waves break by the peak becoming unstable; in regime II the advection of surfactant destabilises the

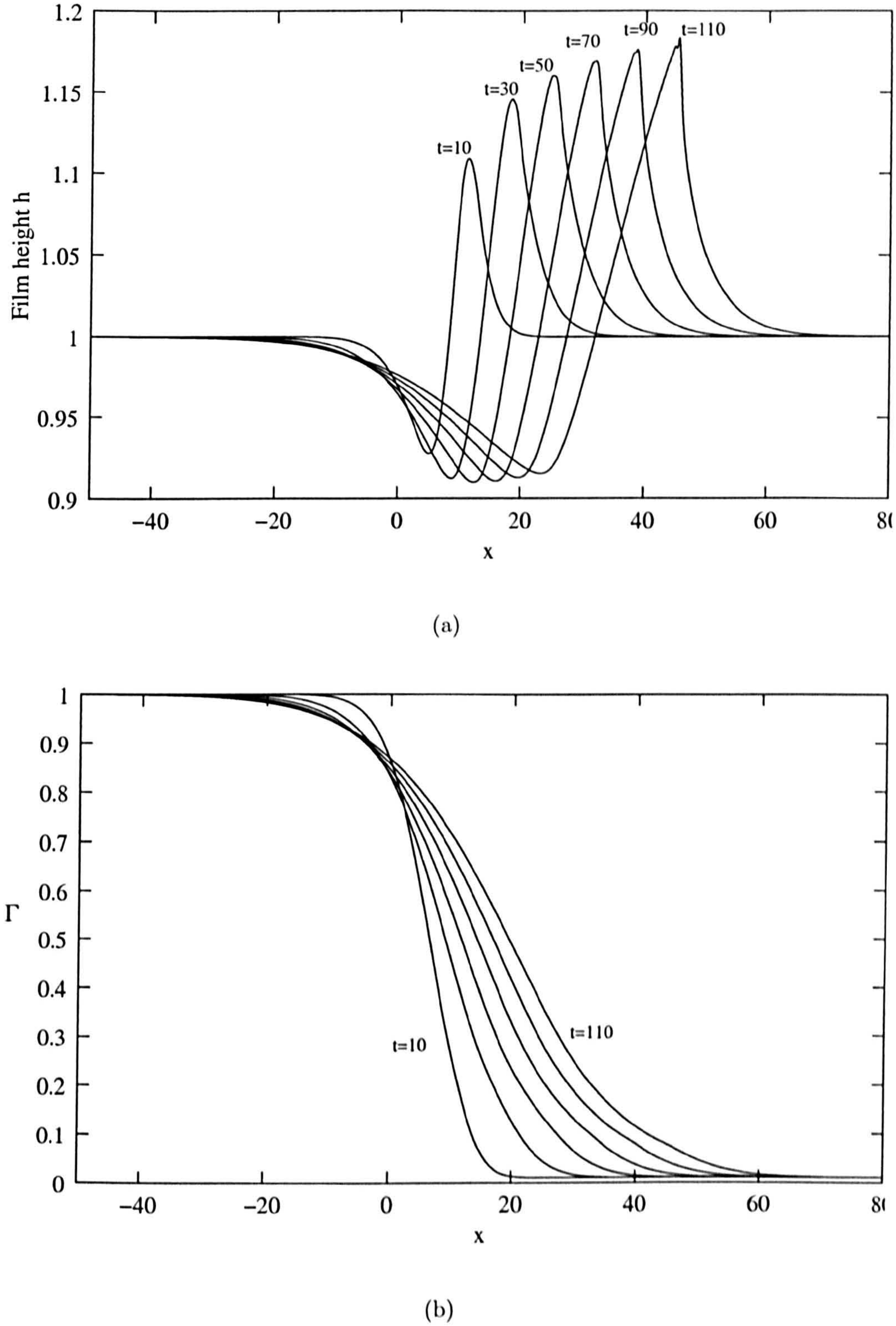

Figure 4.9: Propagation of surface height and concentration for $\mathcal{P}e_s = 1.0$. (a) film height profile for $t = 10$–110 in $\Delta = 20$ steps. (b) shows the corresponding concentration curves.$\mathcal{M} = 1.0$, $P_x Re = 0.25$ and the contamination downstream $\Gamma_{+\infty} = 0.01$. Note the instability setting in at $t = 110$ as the front for the wave become too steep.

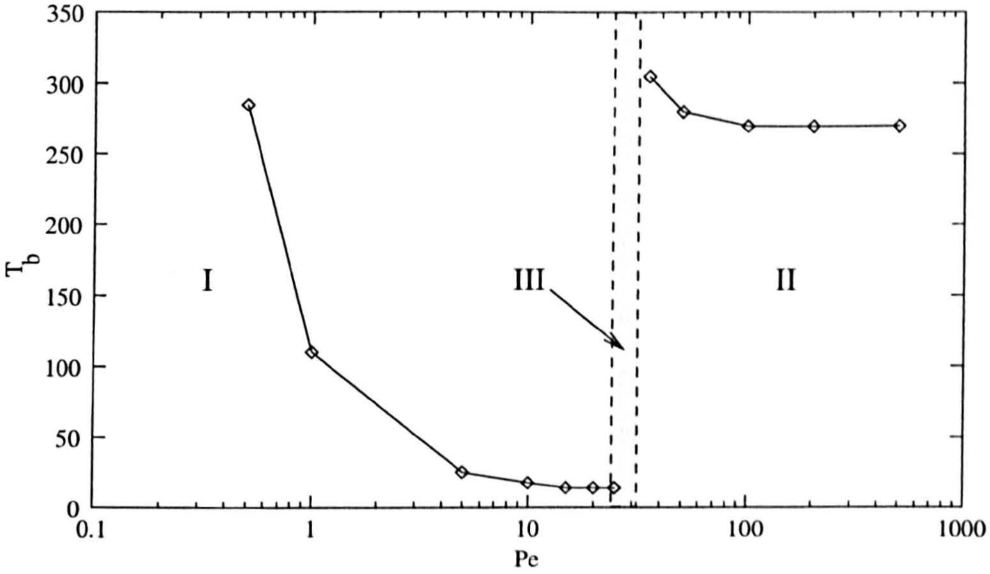

Figure 4.10: The wave breaking times for different $\mathcal{P}e_s$. Breaking time T_b decreases with increase of Péclet number in the range $\mathcal{P}e_s < 30$ (region I) and then attain almost a constant life time span independent of $\mathcal{P}e_s > 35$ (region II). Within a narrow margin $30 < \mathcal{P}e_s < 35$ (region III) an ambiguity exists.

wave behind the trough and in the shaded area III an ambiguity exists.

When the diffusion process is faster than the combined advection processes (film flow + Marangoni advection), i.e. $\mathcal{P}e_s < 30$ in this case, the dominance of Γ_{xx} in equation (4.8) results in rapid reduction of concentration gradient. Hence the relative magnitude of $\mathcal{M}a(\Gamma_x h^2)_x$ in (4.7) decreases in time. Thus the influence of $P_x Re\, h^2\, h_x$ become more dominant. For the sake of the argument, if the Marangoni term is negligible the resulting $h_t + P_x Re\, h^2\, h_x = 0$ represents a free surface wave of a shallow liquid layer up to $\mathcal{O}(1)$ approximation [77]. The strong nonlinearity in $P_x Re\, h^2\, h_x$ results in steepening of the wave which would ultimately result in breaking. The increase in T_b with decreasing $\mathcal{P}e_s$ is a direct effect of the magnitude of the wave amplitude. The smaller the $\mathcal{P}e_s$ becomes, the weaker would be the wave (i.e. smaller amplitudes). The momentum interaction term $P_x Re\, h^2\, h_x$, though, which is the dominant component that controls the evolution, would be small in magnitude. Hence the slow evolution up to the breaking point. However the breaking is caused by the falling over of the peak. For large Péclet numbers ($\mathcal{P}e_s > 35$), the superposed Marangoni advection that carry a small amount of surfactant creates a shock in surfactant concentration right at the peak position, making the wave stable. The existence of a concentration gradient (nearly linear) across the peak is common in the stationary case where the Marangoni stress is the only driving mechanism [52]. The background velocity, however, thins out this linear concentration gradient but keeps a clear jump across the moving contact line. The region $30 < \mathcal{P}e_s < 35$ is where the transition takes place. Hence the ambiguity in minimum T_b that follows (see Figure 4.10).

4.5.3 Effects of $\mathcal{M}a$

In all the above sections we kept $\mathcal{M}a$ constant at 1. The sensitivity of the system for Marangoni number variations is discussed here. $\mathcal{M}a$ describes the relative strength of the surface stresses due to surface tension gradients. Small values of $\mathcal{M}a$ have a weak influence while larger values have a dominant effect on the flow.

When Marangoni number is large, the induced shear stresses that occur due to concentration gradients are large. The surface stress $\sigma_x = \epsilon^{-1}\mathcal{M}a\Gamma_x$. Hence a larger local velocity field occurs that causes displacement of substrate mass locally, making the capillary ridge larger. Figure 4.11(a) shows the surface profiles for different Marangoni numbers at $t = 50$. As the induced velocity is large for large $\mathcal{M}a$, the advective spreading (spreading due to Marangoni induced movement) is large and long lived. Thus the initially sharp concentration gradient smooths out quickly. The concentration plots in figure 4.11(b) shows the effect of Large $\mathcal{M}a$ on spreading. The trough too is deeper as a result of the higher surface stress. The shock moves faster as $\mathcal{M}a$ increases.

The wave that occurs under large Marangoni numbers evolves for longer times than $\mathcal{M}a \sim \mathcal{O}(1)$. For small $\mathcal{P}e_s$ the wave breaks by falling over of the peak. For large

$\mathcal{P}e_s$ the waves survives much longer since the induced velocity field at the front spreads more surfactant than that delivered to the front by the bulk flow advection. The effect of influx can be seen but the time it takes to build up before destabilising the wave is comparatively long.

In the simulation for $\mathcal{M}a = 100$, the initially localised effect of shear is felt by the boundaries fairly quickly. Therefore the domain has to be increased. Due to the time and machine limitations it hasn't been simulated beyond t = 50. However it follows the same behaviour as for any $Ma > 1$.

When the large Marangoni numbers are simulated with large $\mathcal{P}e_s$, the strong nonlinearity dominates over the dissipation in the system, giving rise to non-physical numerical oscillations. One way to eliminate this numerical error is the use of the total variance diminishing (TVD) method [107, 108] in place of centred differences. However we used a more simple and accurate upwind difference scheme with artificial viscosity. The new scheme was tested against the results generated by centre difference method for small $\mathcal{P}e_s$ numbers. The L_2 norm of errors between the two schemes fall less than 1.0% for most of the cases. The artificial viscosity used was 0.1% except for $\mathcal{M}a = 100$. For $\mathcal{M}a = 100$, the artificial viscosity used was 1.0%.

Small Marangoni numbers($\mathcal{M}a \ll 1$) show a different behaviour. The initial stress is large enough to cause a surface disturbance but so small that the influence on bulk flow is minute. The disturbance amplitude is very small compared to the cases with ($\mathcal{M}a > 1$). We observe a wave separation at late times for large $\mathcal{P}e_s$. The ridge moves away from the trough while both moving in the direction of bulk flow. From (4.7) it is evident that in the limit ($\mathcal{M}a \rightarrow 0$) the evolution of surface height becomes decoupled from concentration reducing it to a nonlinear wave equation. The concentration evolution equation is reduced to contain only advection by the bulk flow and the diffusion (that plays a minor role when $\mathcal{P}e_s \gg 1$). Therefore one can expect the surface evolution to be less affected by the concentration profile and the wave to behave differently when $\mathcal{M}a \ll 1$. The evolution of the peak resembles

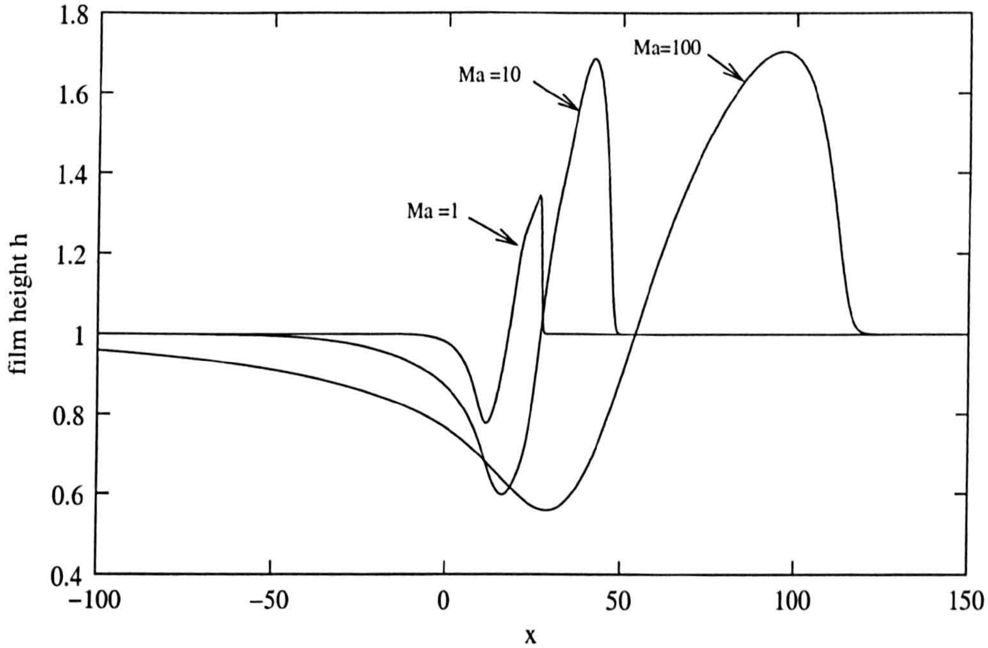

(a)

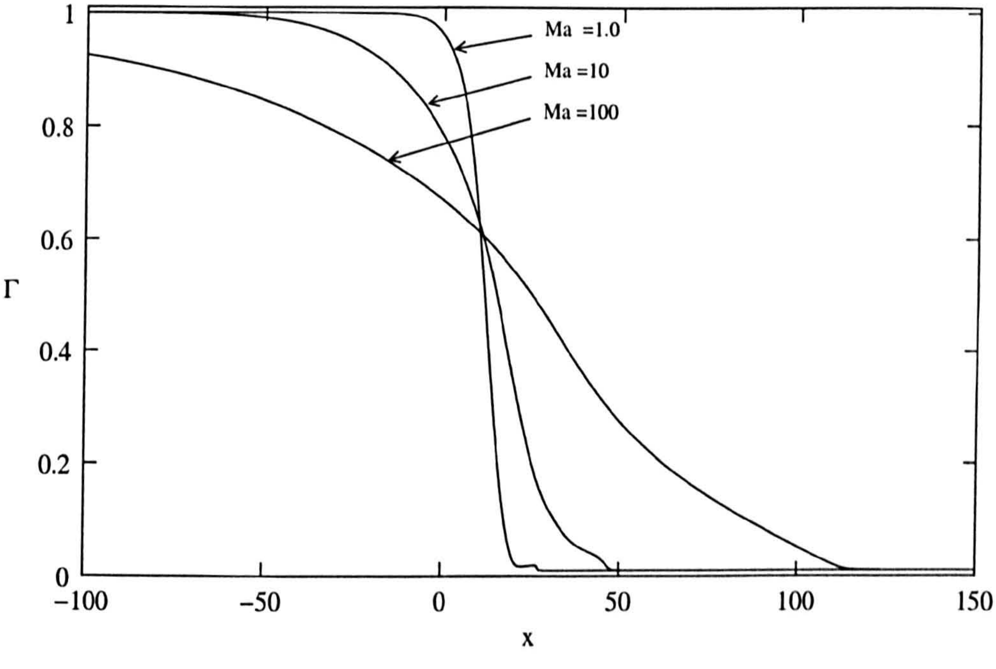

(b)

Figure 4.11: Evolution under large $\mathcal{M}a$. Plots indicate the profiles at $t = 50$ for $\mathcal{M}a = 1, 10$ and 100. (a) The surface profiles.(b) shows the corresponding concentration curves. $\mathcal{P}e_s = 100$, $P_x Re = 0.25$ and the contamination down stream $\Gamma_{+\infty} = 0.01$.

the soliton solution of the Korteweg–de Vries equation. The small nonlinear effect caused by the Marangoni terms ($0 < \mathcal{M}a \ll 1$) eventually destroys the wave by breaking it after a considerably long time.

Figure 4.12(a) shows the transition of the wave from the familiar combined trough-peak configuration to a separate peak and a trough. Figure 4.12(b) shows the corresponding concentration profiles. 4.13 (a) and (b) illustrate the late time evolution of surface height and concentration respectively. The concentration profiles, unlike for $\mathcal{M}a \geq 1$, shows no influence of surface corrugation. Diffusion is active behind the peak resulting in the reduction of trough depth. The trough remains with the surfactant front where the shear stress due to surfactant gradient exists. The peak on the other hand does not carry any surfactant on it (or the amount it carries is insignificantly small). Instead it acts like a capillary gravity wave. In most of the studies so far the $\partial\sigma/\partial\Gamma$ in the equation of state is either set to 1 [68, 56] or absorbed into the scaling [99]; an assumption that keeps the generality but denies the actual behaviour. Here, we did not make any simplifying assumptions but include the $\partial\sigma/\partial\Gamma$ in the solutal Marangoni number which naturally arises from nondimensionalisation and kept it a free parameter. This limiting case resembles a situation that a surfactant is added to a flowing substrate with higher degree of contamination or a very weak surfactant. Distinguishing these two cases is evident in the definition of the Marangoni number.

The front velocity is mapped by plotting the position of the peak and the trough. Figure 4.14 shows the positions of the peak and the trough at $\mathcal{M}a = 0.01$. Once separated, at large times, the peak moves with a constant speed of 0.261. This is twice the surface velocity of the undisturbed substrate. The trough moves at a slower speed of 0.128 which is 3.3% above the undisturbed substrate flow velocity. The surfactant layer is moving mainly due to the advection with little diffusion and Marangoni advection. Figure 4.15 plots the peak height and trough depth against time. The peak, once separated, moves with very little change to the height and

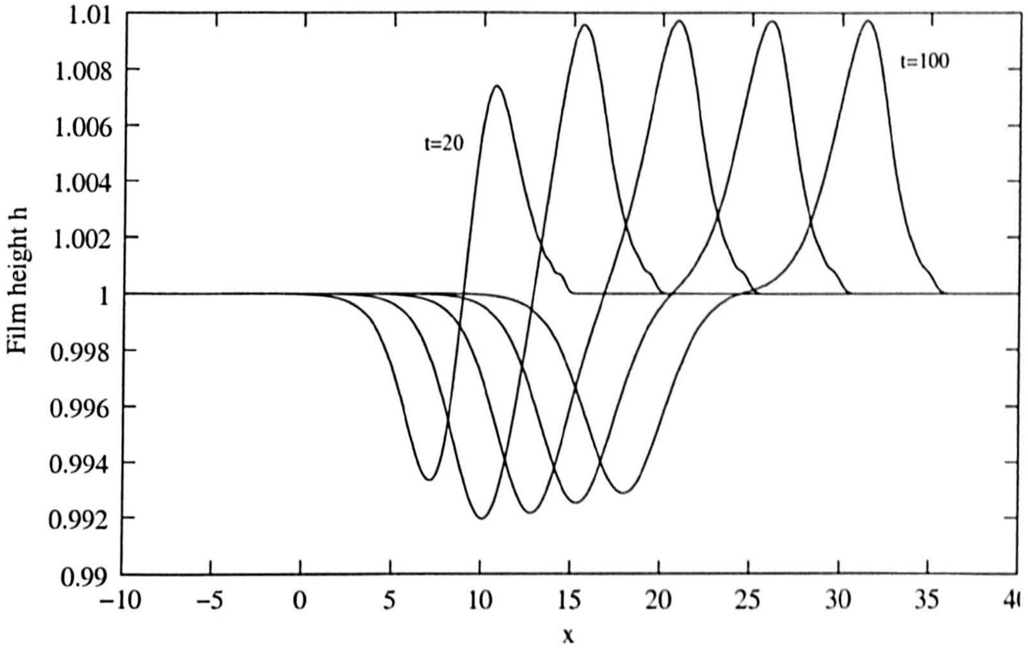

(a)

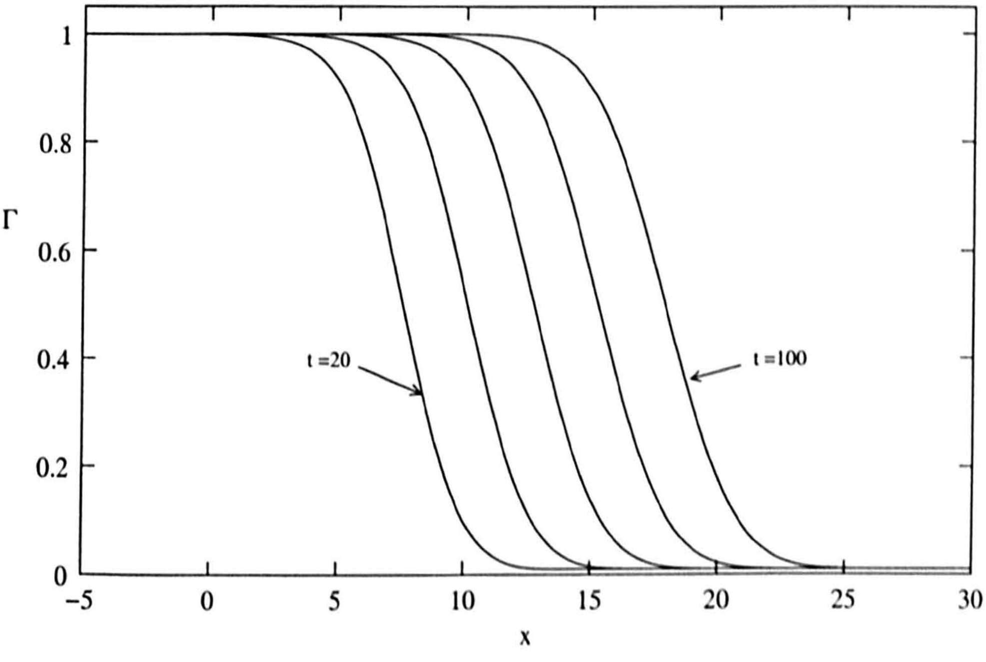

(b)

Figure 4.12: Wave separation at small $\mathcal{M}a$. Plots indicates the evolution of (a) the surface and (b) the surface loading from t = 20–100 in Δt = 20 steps. $\mathcal{M}a$ = 0.01, $\mathcal{P}e_s$ = 100, $P_x Re$ = 0.25 and the contamination down stream $\Gamma_{+\infty}$ = 0.01. The wave, small in amplitude, evolves as for general case for some considerable time. The separation sets in around t = 100. See also 4.13.

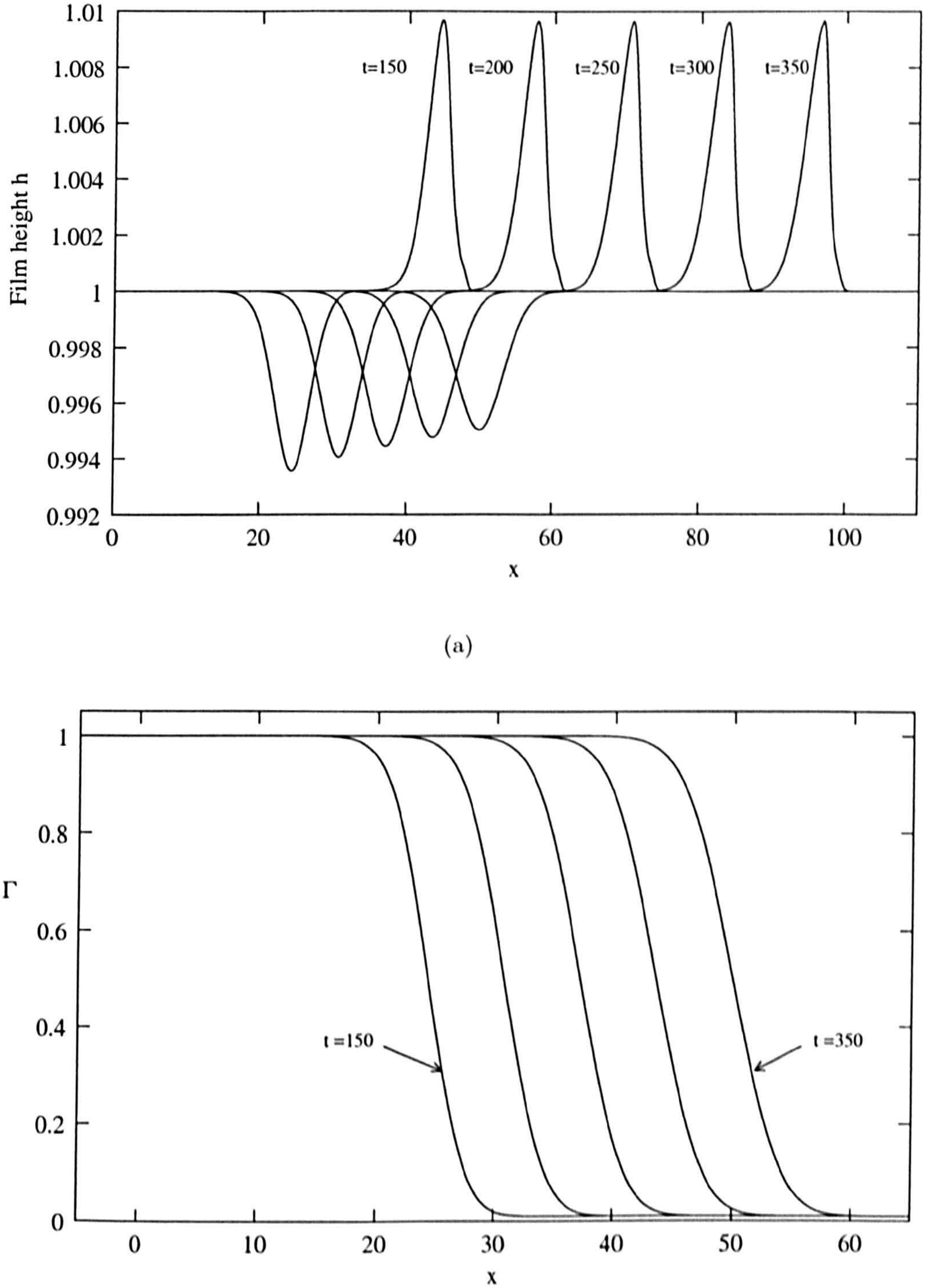

(a)

(b)

Figure 4.13: Long time evolution of the separated wave for small Marangoni numbers. (a) Surface and (b) surface loading evolution in time $t = 150$–350 in $\Delta t = 50$ steps. The depression closely follows the maximum gradient point of the concentration profile and reduces in depth. The peak grows very slowly and travels faster than the depression. Parameter values are as same as for Figure 4.12.

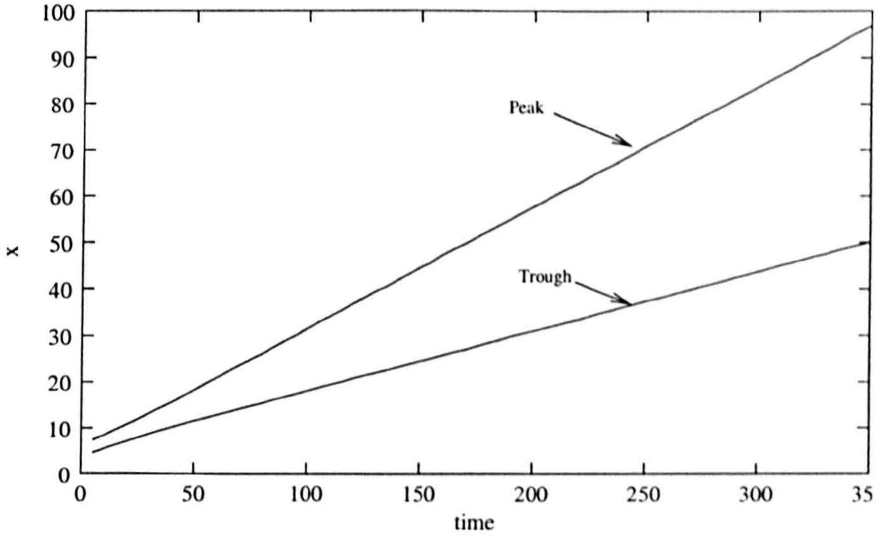

Figure 4.14: The peak and trough position against time. once the wave separates (i.e. $t > 100$) the positions for either case increase linearly with time indicating they travel with approximately constant speeds (See text). The parameter values are as same as for 4.12.

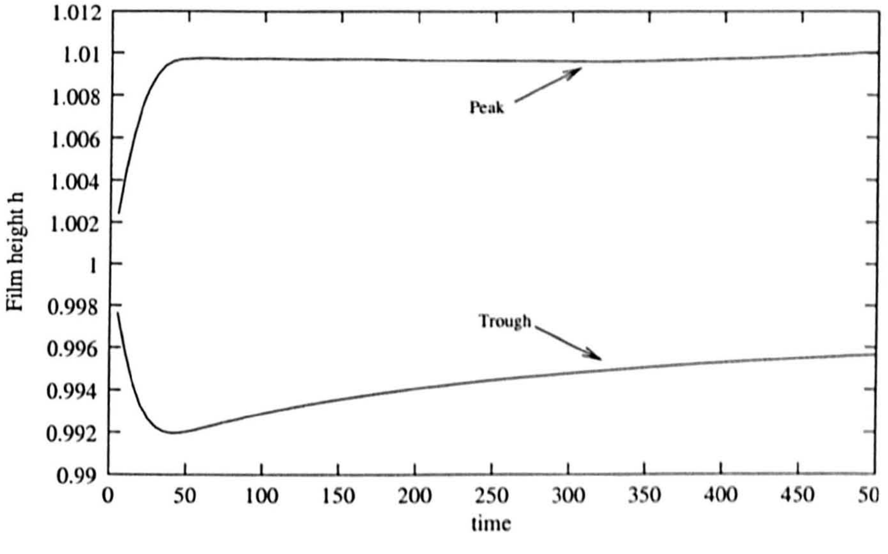

Figure 4.15: The peak height and trough depth development in time corresponding to the evolution presented in Figure 4.12. The peak grows to its maximum height well before the separation. The trough attains maximum depth around the same time as the peak reach its maximum height. Trough, once attain the maximum depth, continuously decrease the depth whereas the peak fluctuates very little.

shape. The nonlinear terms that make the wave grow are associated with Marangoni numbers with very small magnitudes. Hence the KdV type behaviour.

Evidence for the existence of a solitary wave for all Re on flowing thin films subjected to differential surface tension is pointed out by Kalliadasis [57] in a different analysis to ours. Instead of the usual lubrication theory, an integral–boundary–layer (IBL) theory is used to analyse a simillar situation. IBL also uses a long wave approach but does not impose overly restrictive stipulations on the order of amplitude. It slaves the volumetric flow of the disturbance to surface height (hence the velocity field) while the self-simillarity of the background flow is used to approximate the velocity field. In this respect the small Marangoni number limit in our case resembles a subset of the more global IBL analysis.

4.5.4 Effect of P_xRe on evolution of the surface

The term $P_x Reh^2h_x$ in (4.7) provides the interaction of bulk flow with an otherwise purely Marangoni driven evolution equation for the surface. Similarly the $\frac{ReP_x}{2}(\Gamma h^2)_x$ determines the advective spreading due to the bulk flow. We examine the combine effect of P_x (imposed pressure gradient or body force in the case of an inclined plane that drives the bulk flow) and Reynolds number, Re, rather than study the effect separately. This is because the global bulk flow rate is characterised by the combined term. By setting the $Re\,P_x$ to constant we set the overall volumetric flow rate of the bulk. We numerically solve the evolution equations (4.7) and (4.8) subject to the initial and boundary conditions (4.10)–(4.13) for different values of P_xRe. Figure 4.16(a) shows the surface evolution at $t = 100$ for different values of P_xRe ranging from 0.05 to 0.5. The larger the P_xRe gets, the quicker the wave breaks. For instance, for $P_xRe = 0.1$, the breaking time $T_b = 825$, while for $P_xRe = 0.5$, the life span of the wave $T_b = 82$. As flow rate increases, for $\mathcal{P}e_s = 100$ and $\mathcal{M}a = 1$, the breaking time decreases rapidly asymptotically approaching $T_b = 6$. For $PxRe$ up to 20 the breaking time T_b remains around the value 6. The higher the $PxRe$ gets, the more the system behaves like that for very small $\mathcal{M}a$, with negligible Marangoni effects. However, since the life span is small, we cannot draw valid conclusions. The limiting T_b value is highly dependent on Marangoni number and has higher values for higher $\mathcal{M}a$. The breaking times for different P_xRe are given in Figure 4.18. The breaking mechanism is not affected by P_xRe, leaving $\mathcal{P}e_s$ as the determining parameter for the dynamics of breaking.

The amplitude of the wave decreases with increase in background flow. Though the induced Marangoni stress increases with increasing P_xRe (see Figure 4.17), the wave amplitude become small (as in Figure 4.16) since the back ground flow harnesses the development of the wave. The wave get stretched with increasing flow rate. The limit $P_x Re \rightarrow 0$ produces the stationary substrate (studied by Grotberg *et al.* [33, 52]), re-generating the same results as in [33]. The larger surface stress corresponding to larger values of P_xRe is due to the fact that the surfactant layer is carried along the free surface by advective transport at a faster rate than the diffusion at the contact line.

The higher the $P_x Re$ gets, the higher will be the inflow of substrate and surfactant. This causes the wave to break at shorter times. Figure 4.17 shows the corresponding surface stresses to the cases given in Figure 4.16. If we take an individual case, for instance, say $P_xRe = 0.5$, the maximum value of surface stress behaves similarly to the behaviour shown in Figure 4.5. It decays for a considerable time and then increases slightly before the breaking of the wave. But when we compare the stresses induced by the Marangoni effect for different bulk flows, higher stresses occur at high flow rates. This is due to the fact that the bulk flow transports more material towards the contact line. With large $\mathcal{P}e_s \gg 1$, higher Marangoni numbers increases the breaking times though the general trend remains the same. This is due to the fast spreading at the surfactant front due to the strong Marangoni advection at early times. The effect of $\mathcal{P}e_s$ is as same as described in §4.5.2 except for greatly reduced breaking times with higher P_xRe values.

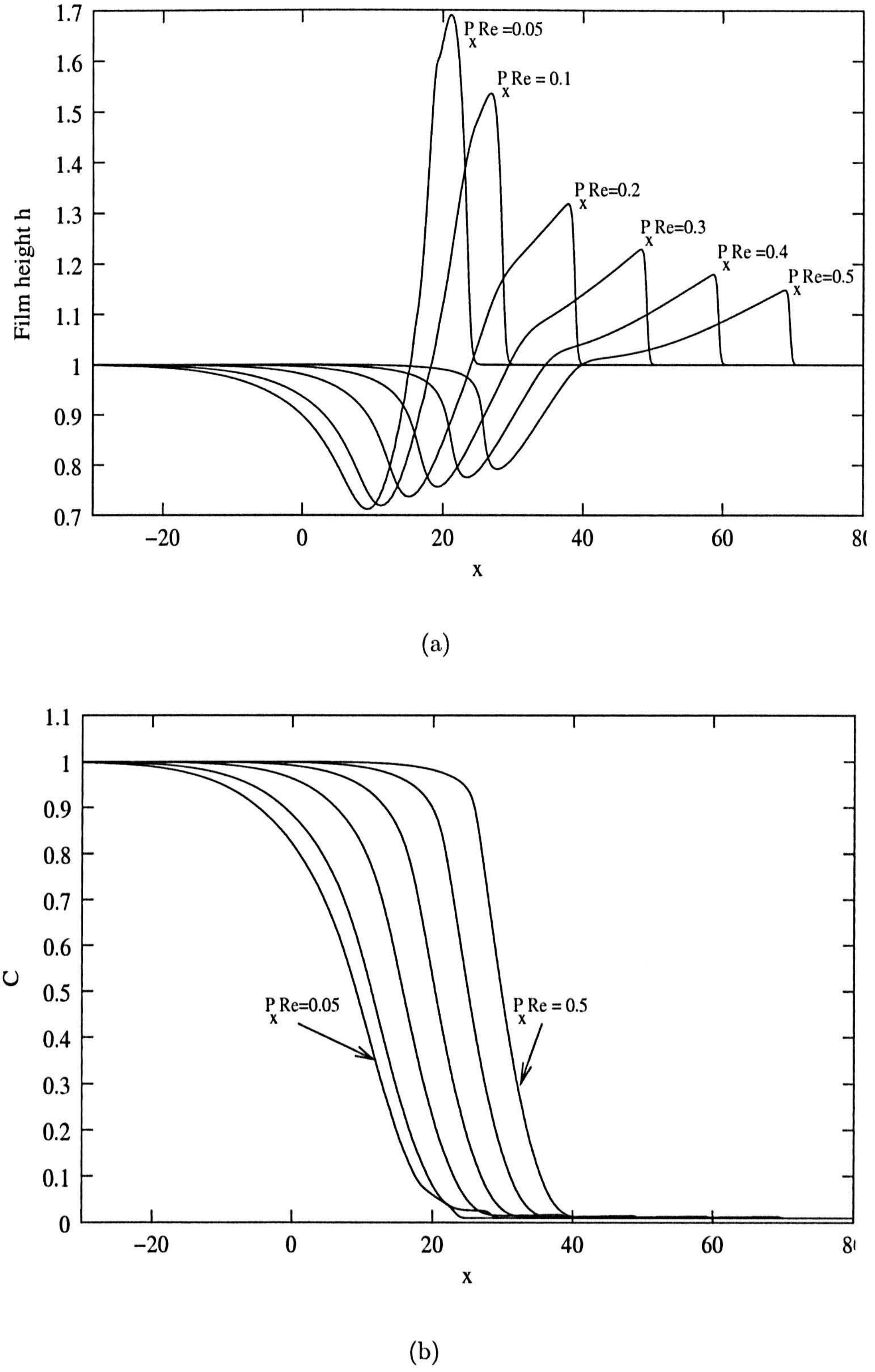

Figure 4.16: Influence of background flow on wave evolution. The flow defining union of parameters $P_x Re$ is varied through 0.05 to 0.5 keeping $\mathcal{M}a = 1$ and $\mathcal{P}e_s = 100$. The plots represent the surface evolution (a), and concentration (b) at $t = 100$.

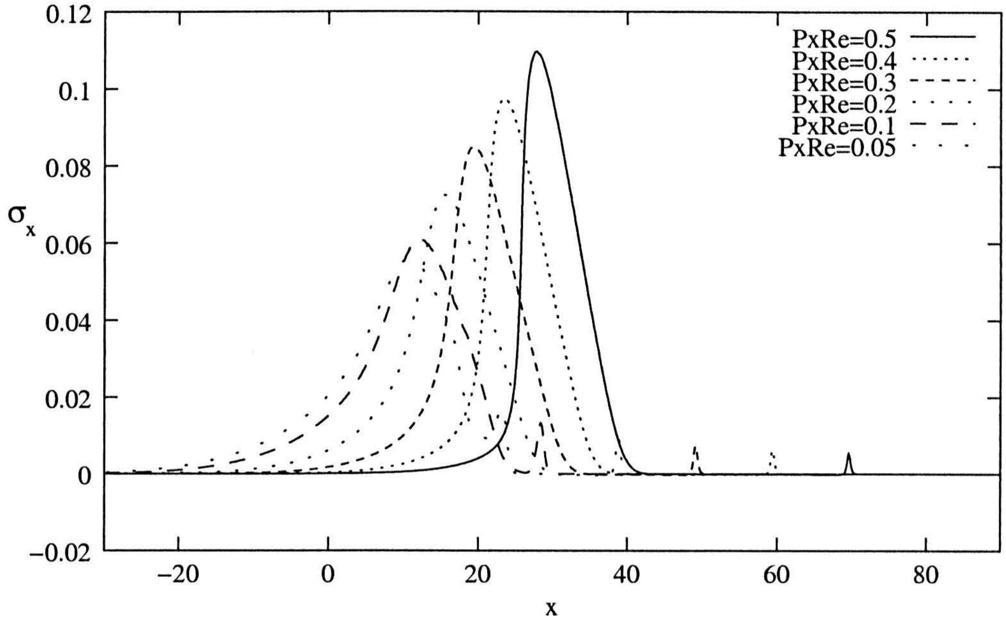

Figure 4.17: Surface stress plots for $P_xRe = 0.05, 0.1, 0.2, 0.3, 0.4, 0.5$ at t=50 for $\mathcal{P}e_s = 100$ and $\mathcal{M}a = 1.0$. Surface stress decay lowly with increasing flow rate. This is due to the faster advection of surfactant than the diffusion at the contact line.

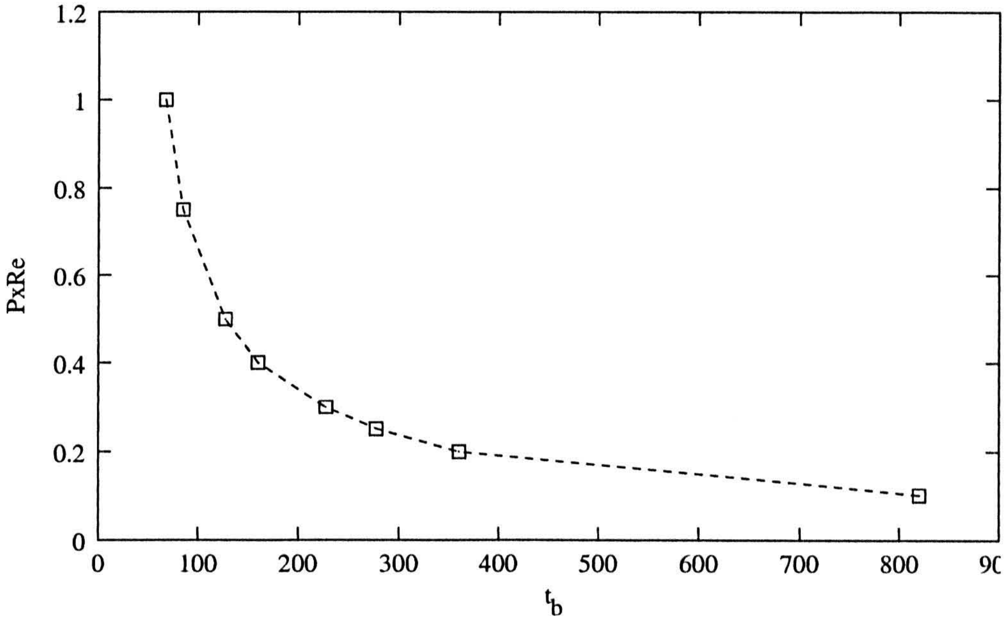

Figure 4.18: Breaking time T_b for various $PxRe$ values. The other parameters are the same as for 4.17. As $P_xRe \to 0$, the breaking time $T_b \to \infty$, resembling the stationary substrate. With increasing P_xRe, the breaking time achieves different threshold values depending on $\mathcal{M}a$.

4.6 Adverse surfactant gradient

As we mentioned in §4.2, the case of a pre–existing surfactant layer with an influx of pure liquid, i.e. a gradient opposing the flow, is considered here. Figure 4.1(b) shows the configuration schematically. The surface tension drops downstream giving a surface stress field opposing the bulk flow. The combine effect of Marangoni stresses and the bulk flow is examined. Once again the equations (4.7) and (4.8) were solved numerically using initial and boundary conditions that match the flow configuration.

Initial conditions become

$$\begin{aligned} \Gamma(x,0) &= \frac{\Gamma_I}{2}\Big(1.0 + Tanh\Big[\frac{(x-x_0)}{\Delta l}\Big]\Big) && (4.15)\\ h(x,0) &= 1.0. && (4.16)\end{aligned}$$

The boundary conditions that describe the physical situation of the problem are:

$$\begin{aligned} \Gamma &= \Gamma_{-\infty} = 0.0 && \text{at} \quad x = -\infty && (4.17)\\ \Gamma &= \Gamma_{+\infty} = 1.0 && \text{at} \quad x = +\infty && (4.18)\\ h &= 1 && \text{at} \quad x = \pm\infty && (4.19)\end{aligned}$$

We choose $\Gamma_I = 1.0$ and $\Delta l = 2.0$ as in the previous case. The upstream substrate contamination $\Gamma_{-\infty} = 0$. The initial conditions for surface loading and film height are shown in Figure 4.19. The surfactant layer is flowing out of the domain at the right far field ($+\infty$). The expression (4.6) still holds but becomes negative indicating that the mass leaves the domain. Again the domain is so selected that the perturbations at the contact line are not felt at the boundaries during the observation period.

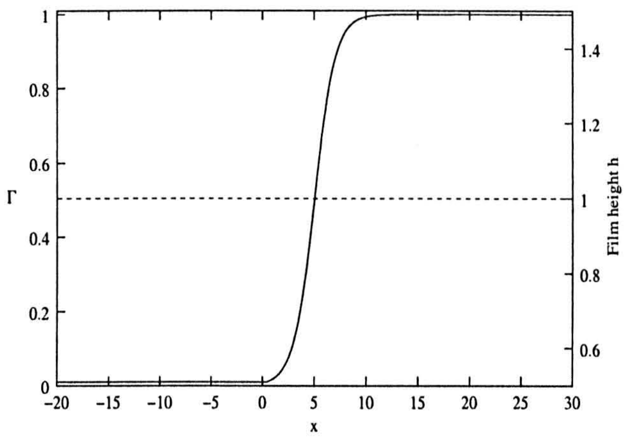

Figure 4.19: Surfactant forming a gradient opposing the flow. Thick line gives the surface loading configuration while dotted line represent the initial film height.

4.6.1 Spatio-temporal evolution under adverse surfactant gradients

Increasing surfactant concentration (along the flow direction) imposes an adverse surface tension gradient. The resulting velocity field opposes the bulk flow. The strength of this adverse velocity gradient is proportional to the Marangoni number since $\sigma_x = \epsilon^{-1}\mathcal{M}a\Gamma_x$. The localised stress field gives rise to a surface corrugation. The evolution of this corrugation has to be described according to the magnitude of $\mathcal{M}a$. The wave (or the disturbance) exists for short times compared to the previous case studied in §4.2.

For $\mathcal{M}a \leq 1$, we can observe two distinct evolution patterns based on the effectiveness of the dominant force. There is a period where Marangoni induced flow is dominant. During this time the capillary ridge grows in height and either moves upstream or stays stationary. Once the opposing Marangoni stress falls below the force exerted by the flowing bulk (due to the decrease of Γ_x), the ridge begins to move downstream. Figure 4.20(a) shows the evolution for $\mathcal{M}a = 1$ at early time while Marangoni stress dominates. Arrows A and B show the direction of evolution with increasing time. Initially the ridge grows in height to an almost stationary position. A depression forms just down stream. The growth rate slows down with time. Figure 4.20(b) shows the concentration profiles corresponding to the surface evolutions shown in figure 4.20(a). The concentration behind the contact line (shown by arrow A) drops rapidly as the surfactant layer moves down stream with the bulk flow. The detailed inset shows the concentration evolution at the contact line. The Marangoni spreading is hindered by the counteracting bulk advection making the concentration gradient sharp. Diffusion is active and smooths out the concentration at the contact line though greatly affected by the bulk advection. The arrow C in inset shows the relative retraction of the concentration front.

Once the induced shear force has fallen below the bulk inertial force, the ridge is pushed down stream. The late time evolution is presented in Figure 4.21. The thickness of the ridge continues to grow but the height hardly changes. The ridge wall facing downstream steepens, eventually destabilising the structure. It breaks down at $t = 32$ for the case of $\mathcal{M}a = 1$. The concentration plots at late times (Figure 4.21(b)) shows that the whole surfactant layer moves down stream with little diffusion at the tail end contact line. The tendency to oppose the bulk flow still exists as the shear stress remains about 60% of the initial magnitude (initial $\sigma_x|_{max} = 0.25$). The concentration becomes almost linear across the ridge. The concentration behind the ridge drops as surfactant monolayer moves further downstream. The surface stress due to concentration gradients $|\sigma_x|$ is plotted in Figure 4.22. The maximum stress occurs across the ridge peaking at the highest point of the ridge. This is parallel to the spreading of a surfactant drop on a stationary substrate.

When $\mathcal{M}a > 1$, the shear stress due to concentration gradient exceeds the inertial force exerted by the bulk flow for a considerable time. In fact, the wave breaking occurs before the Marangoni stress falls below the inertial forces. Large Marangoni numbers form shock fronts that would travel upstream decaying in speed against the flow direction. Figure 4.23 (a),(b) and (c) shows the film height, concentration and surface stress due to concentration gradient respectively for $\mathcal{M}a = 10$. The

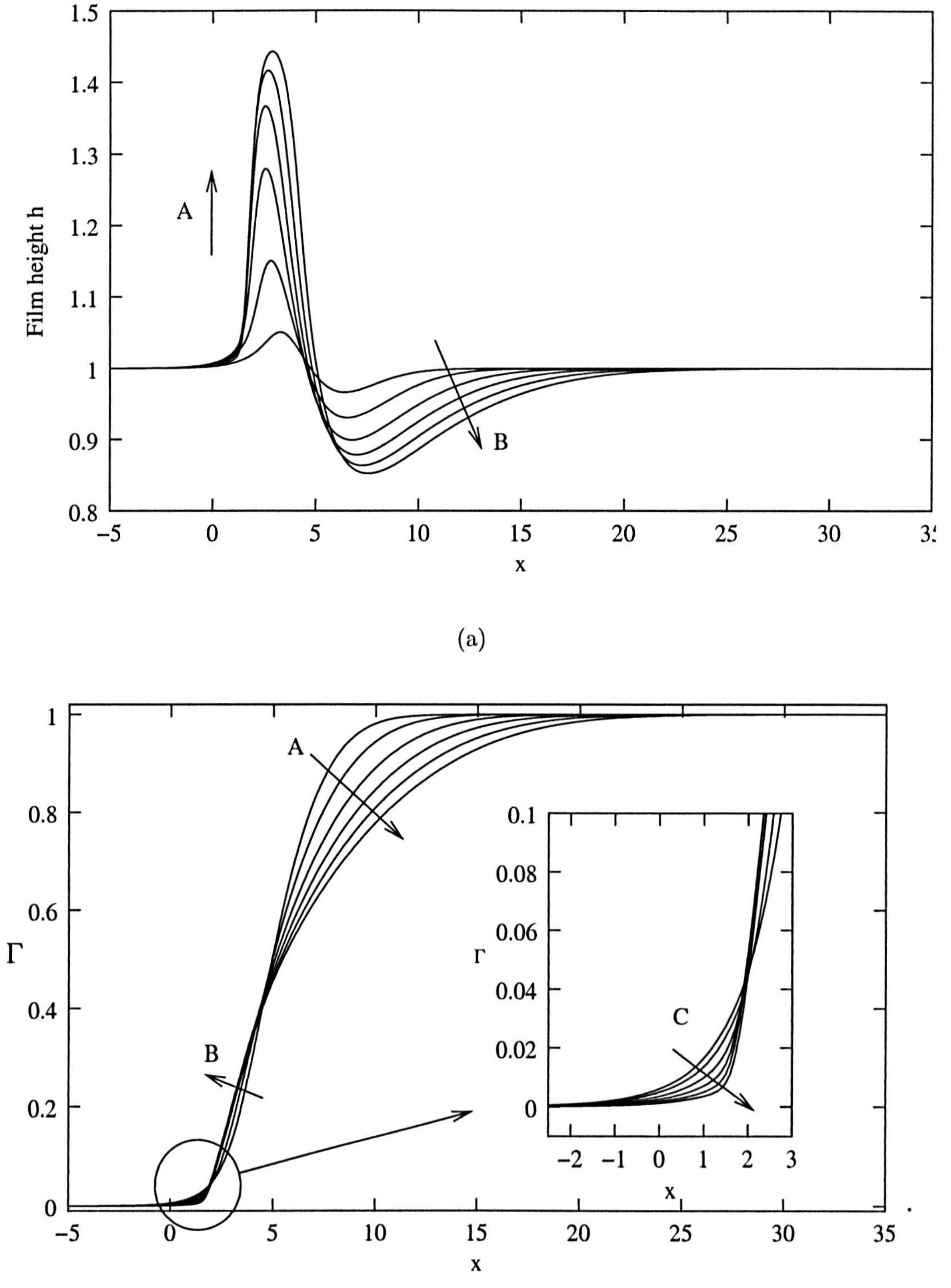

(a)

(b)

Figure 4.20: Early time evolution of the surface and concentration for parameter values $\mathcal{M}a = 1.0$, $\mathcal{P}e_s = 100$ and $P_x Re = 0.25$. (a) Surface height evolution and (b) is the corresponding surface loading profiles. Curves are plotted for $t = 1.0 - 15.0$ in $\Delta t = 3$ steps. Arrows mark the direction of evolution with increasing time. The Inset in (b) shows the details of the circled area.

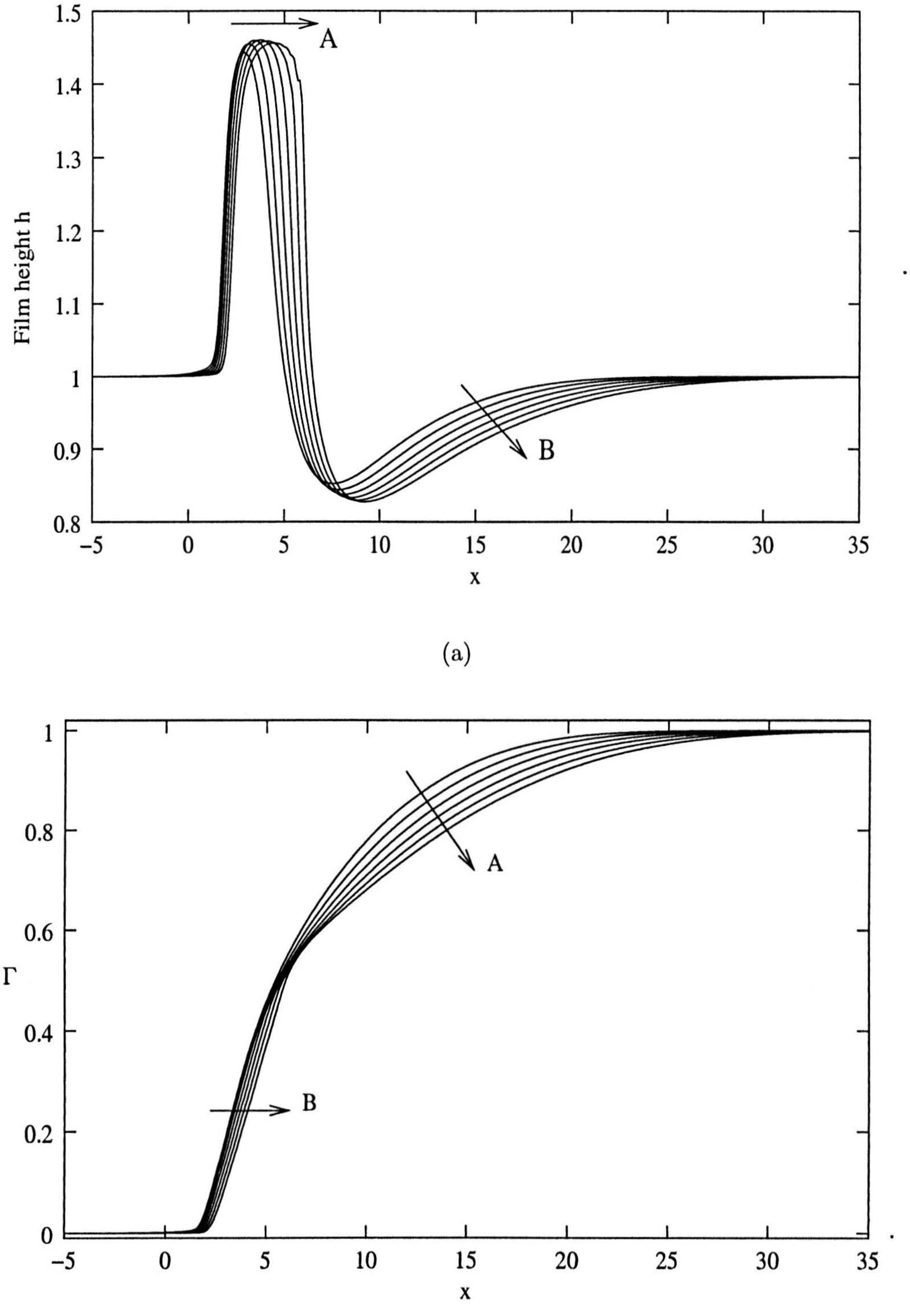

(a)

(b)

Figure 4.21: Late time evolution of (a) surface and (b) surface loading for $t = 15.0 - 30.0$ in $\Delta t = 3.0$ steps. Parameters are same as for figure 4.20. The arrows mark the direction of evolution with increasing time.

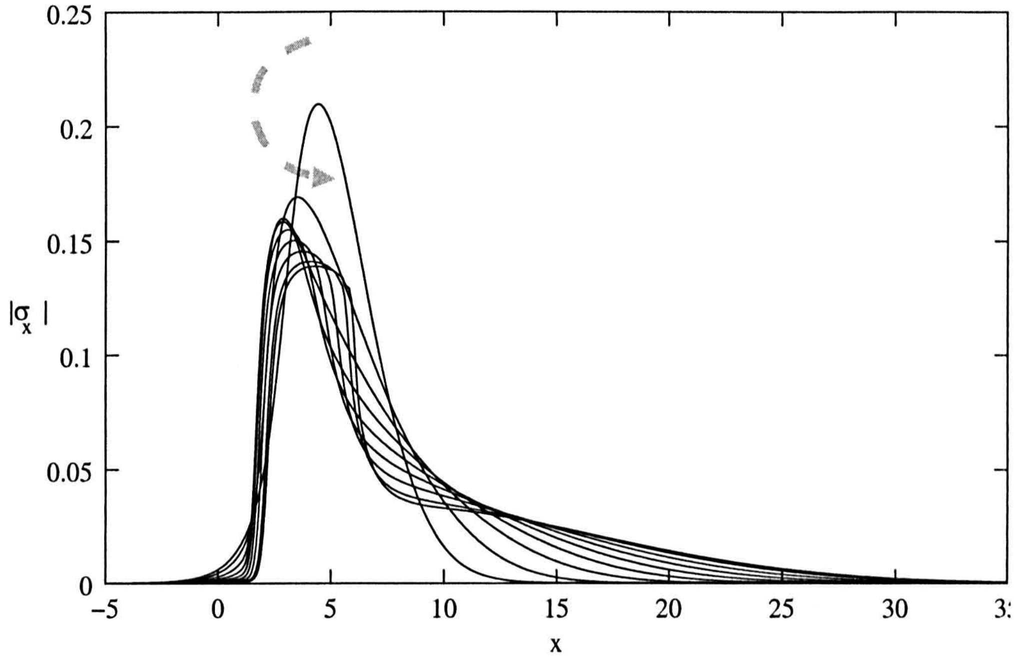

Figure 4.22: Change of Surface stress $\mathcal{M}a\,\Gamma_x$ with time. $t = 1.0 - 32.0$ in $\Delta t = 4.0$ steps. Parameters are as same as for figure 4.20. The arrow marks trend of the movement of the Maximum stress point

surface height increases forming a shock front initially and then as the shock travels upstream the height falls slowly. The initial stress (Figure 4.23(c)) that appears at the contact line is approximately six times stronger than that for $\mathcal{M}a = 1$. This causes strong Marangoni advection of the surfactant (where as $\mathcal{P}e_s \gg 1$ limits the diffusion) opposing the flow of the bulk. The concentration curves in Figure 4.23(b) shows roughly a linear profile near the contact line because of this strong localised advection. The effect of diffusion can be observed for a short time until the sharp shock forms in surface stress.The effect of adverse stress on the flow is discussed in §4.7. The magnitude of the shock in stress falls with time. The speed of shock front in film height slows down in accordance with decreasing stress. The thickness of the capillary ridge increases again, destabilising it in the same manner as for $\mathcal{M}a = 1$.

The existence of the shock front is supported by the fact that diffusion is limited (i.e. $\mathcal{P}e_s \ll 1$). Large $\mathcal{P}e_s$ hinders the development of a fore-running surfactant layer due to lack of diffusion producing a sharp change in surface tension [33]. This

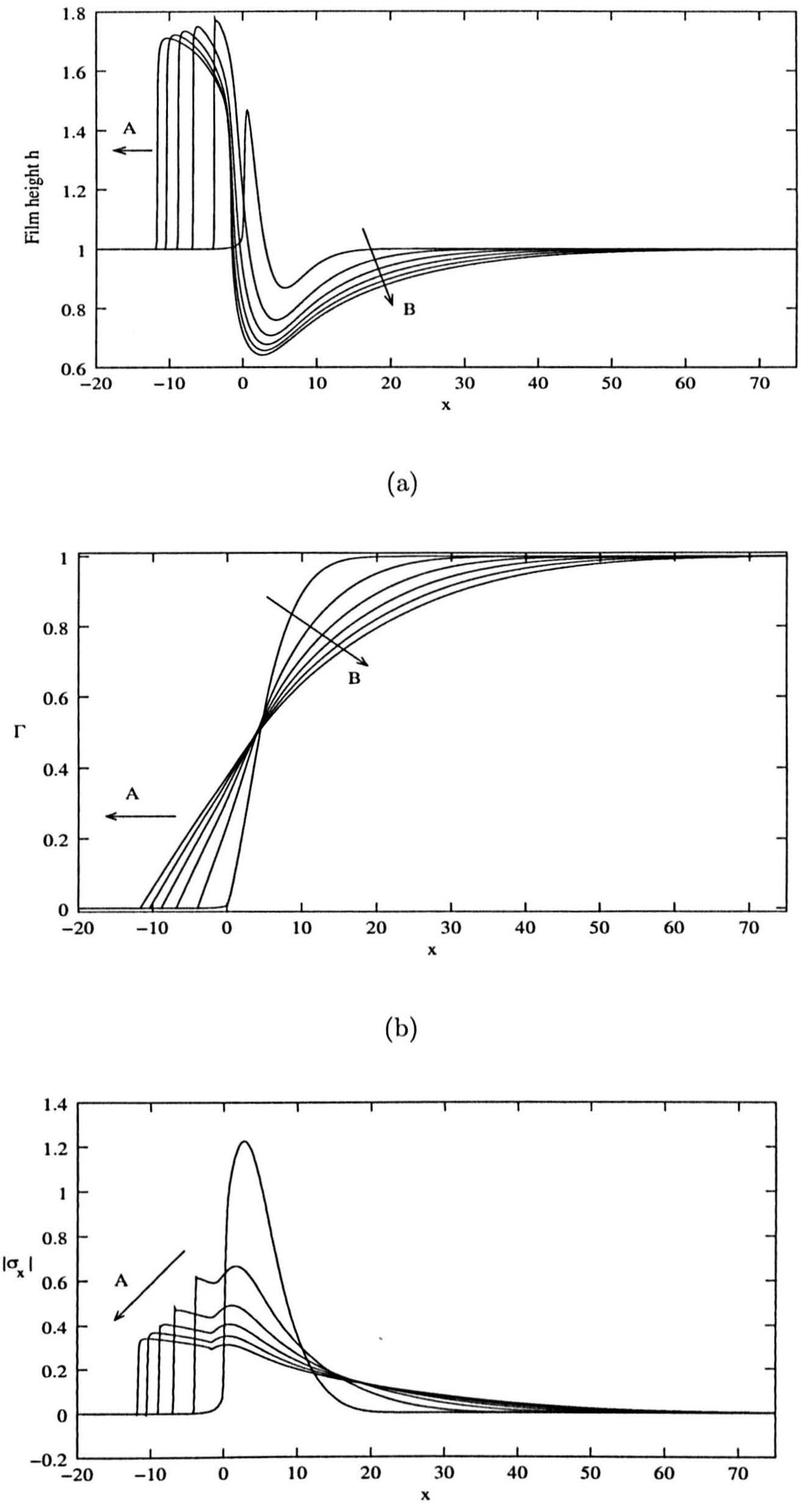

Figure 4.23: The film height (a), surface concentration (b) and surface shear stress (c) for $\mathcal{M}a = 10.0$ from $t = 1$ to 25 in $\Delta t = 5$ steps. Arrows mark the direction of evolution with increasing time.

change in surface tension produces the shock front. The larger the $\mathcal{P}e_s$ the sharper the shock. Unlike the case of surfactant gradient in the direction of flow, here we observe only one method of destabilisation. That is the destruction of the fluid face behind the shock front by excessive steepening.

Figure 4.24 shows the comparison of film height, surfactant spreading and stress for different values of $\mathcal{P}e_s$ with constant $\mathcal{M}a = 1.0$. The smaller the $\mathcal{P}e_s$, the smaller the surface deformation. This is due to the spreading of surfactant by diffusion. The diffusion process produces a precursor contamination of the substrate ahead of the hump. The rapid diffusion of surfactant reduces the jump in stress drastically, making the surface corrugation smaller. This, on the other hand, increases the life time of the wave. For smaller $\mathcal{P}e_s$, the surface wave exists for longer periods. The wave more or less becomes sinusoidal in shape rather than a sharp shock smoothing back into upstream. For $\mathcal{P}e_s \leq 1$ the diffusion is faster than the localised Marangoni advection. Therefore the concentration curve lacks the near-linear profile across the capillary hump as in $\mathcal{P}e_s \gg 1$. The surface stress behind the capillary ridge remains almost the same for all $\mathcal{P}e_s$ since the changes to concentration are taking place due to bulk flow advection (downstream), which is least affected by the perturbations at the contact line.

The life time of the wave is very short compared to that of the shock generated by a surface tension gradient along the flow direction. The larger the shock wave amplitude the shorter will be the life time. Large $\mathcal{P}e_s$ result in shock fronts with large amplitudes. Marangoni number has the same effect on the shock evolution. Hence both $\mathcal{P}e_s$ and $\mathcal{M}a$ contribute to wave destruction.

The surface evolution and surface stress, however, does not describe the whole gamut of processes that happen at the contact lines for both cases. To throw more light on to the effects of surfactant gradients we examine the streamfunctions to understand the flow patterns that follow the initial conditions.

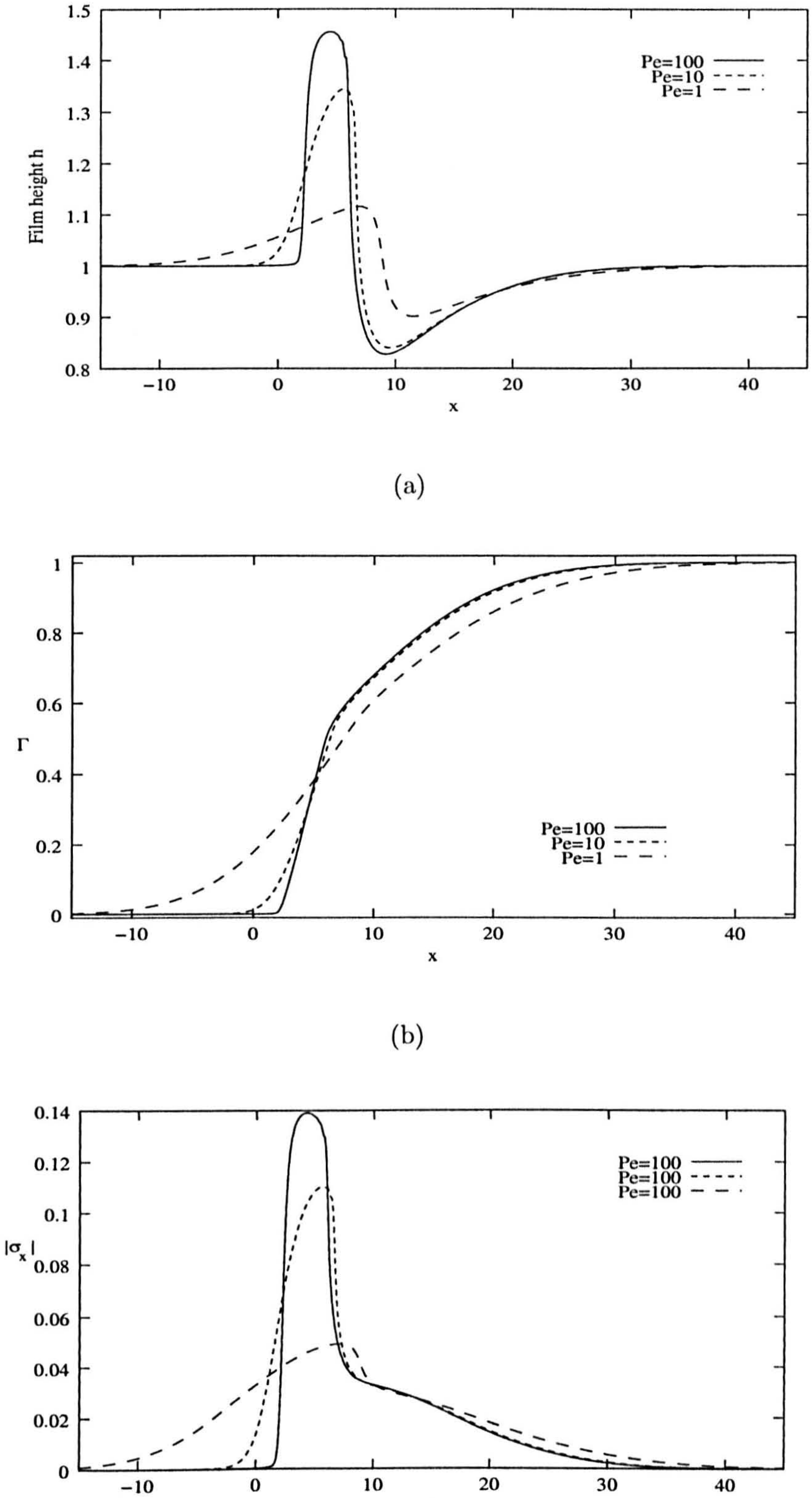

(a)

(b)

(c)

Figure 4.24: Comparison of the effect of $\mathcal{P}e_s$. The film height (a), the concentration (b) and the surface stress (c) was plotted against position for $\mathcal{P}e_s = 1, 10$ and 100. $\mathcal{M}a = 1$, $P_x Re = 0.25$. The curves represents a snapshot at $t = 30$.

4.7 Effect of Marangoni stress on bulk flow

The spreading of a surfactant induces a surface stress in the neighbourhood of the contact line forcing the substrate underneath to move locally. If the substrate is stationary, then the flow is totally a result of the unbalanced force exerted by the surface tension gradient (as a result of Marangoni stresses) and exists only around the contact line, thus the flow field expands as the monolayer spreads. The flow field penetrates only a very small distance beyond the expanding contact line. The flow underneath a surfactant drop was described by Gaver and Grotberg [33].

However, when there is a flow in the bulk to begin with, the existence of a surfactant layer modifies the flow patterns. The wave breaking phenomenon we described in previous sections is not a result of surface movements alone but of the interactions between bulk flow and local surface force field. To describe the event fully, we need to examine the flow in the bulk. To this end we define a stream function $\psi(x,z,t)$. For the case of a planar front the changes to the flow field in the direction of y co–ordinate axis is uniform and therefore we can reduce the system to 2–dimension x (along the rigid flat plane) and z (normal to rigid plane). Making use of continuity equation $\frac{\partial u}{\partial x}+\frac{\partial w}{\partial z}=0$, we define the stream function as:

$$u=\frac{\partial \psi}{\partial z} \qquad w=-\frac{\partial \psi}{\partial x} \tag{4.20}$$

In chapter 3, §3.4.2, we derived expressions for u and w.

$$\begin{aligned} u &= \frac{Re\,P_x}{2}(2hz-z^2)-\mathcal{M}a\Gamma_x z && (3.43)\\ w &= \frac{Re\,P_x}{2}\,h_x z^2+\frac{\mathcal{M}a}{2}\Gamma_{xx}z^2 && (3.45) \end{aligned}$$

By substitution of (3.43) or (3.45) in the appropriate expression in (4.20), we can obtain an expression for stream function.

$$\psi(x,z,t)=\frac{1}{6}P_x Re\,(3\,h\,z^2-z^3)-\frac{Ma}{2}\Gamma_x\,z^2 \tag{4.21}$$

The stream function (4.21) consists of two parts. First term on the RHS is the flow due to external force. The second term describes the flow due to Marangoni stresses. This term has finite values only around the neighbourhood of the contact line where a concentration gradient exists. For gradients along the flow, two terms add up to give the flow rates. When the adverse surfactant gradients occur, there is a possibility of balancing the flows that occur in opposite directions. This is envisaged as the adverse velocity might penetrate into the bulk due to viscous effects. Zimmerman [118] has shown that the Marangoni induced velocity fields (thermal Marangoni effects on stationary fluid films) with no-slip boundary conditions penetrate deep into the bulk.

A concentration gradient along the flow direction excites a wave. Figure 4.25 shows three occasions of the evolution of such a wave for parameter values $\mathcal{M}a = 1, \mathcal{P}e_s = 100$ and $P_x Re = 0.25$. At very early times as shown in Figure 4.25(a), the liquid substrate beneath the surfactant layer closer to the contact line is dragged into the wave. Toward the front end of the shock, the upward bent of the closely packed stream lines shows that the w-velocity has a larger magnitude. The liquid velocity just in front of the ridge is substantially smaller than to the Marangoni induced local velocity at the contact line. This discontinuity forces the stream lines to take the upward turn contributing to the rapid growth in height at initial instances. As a result of this displacement of substrate a trough forms behind the capillary ridge. As explained by Zimmerman [118], the induced velocity discontinuity penetrates into the bulk. As a result, flow beneath the ridge become accelerated locally, making a shock (represented by the bent stream lines below the front end of the ridge). The open stream lines as shown in the figures, originating or terminating on the free surface are customary to free surface flows.

After a considerable time (Figure 4.25(b) at t=100), once the induced stress substantially faded (refer to figure 4.5), the displacement of liquid into the ridge diminishes. Instead, the wave transforms into a slowly evolving (in the inertial time scale) prop-

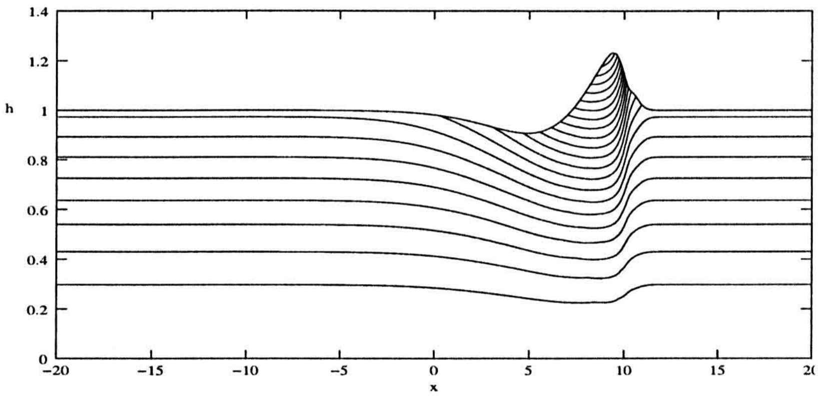

(a) t=5

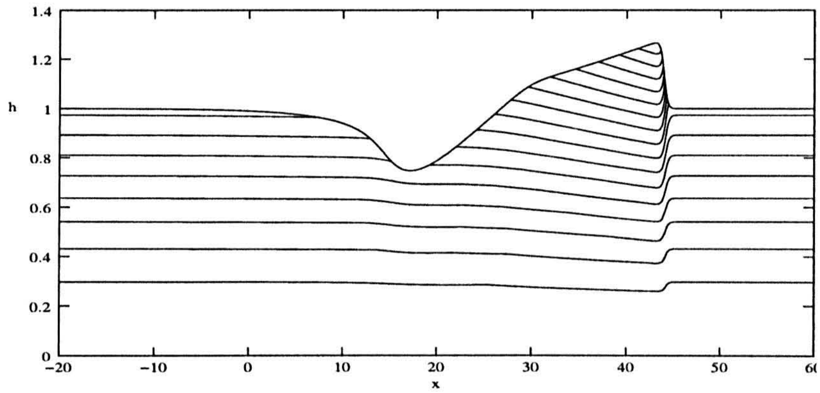

(b) t=100

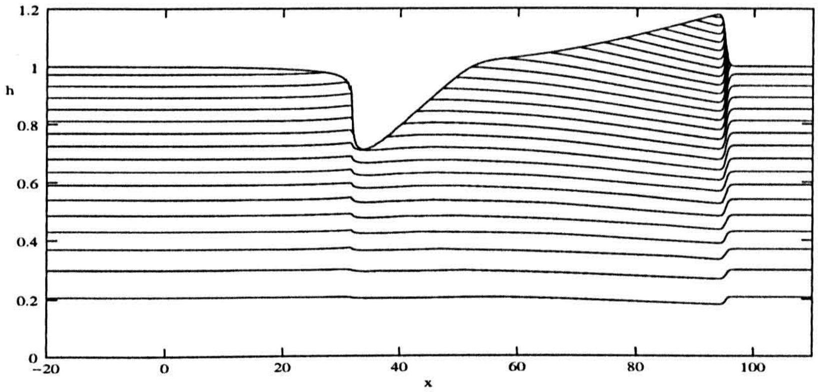

(c) t=265

Figure 4.25: Stream functions for the flow with surfactant gradient along the flow direction. (a) shows the growth of the capillary ridge at very early time t=5. The flow after a long time after initiation (t=100) is given in (b) and (c) shows the flow patterns just before breaking at t=265. $\mathcal{M}a = 1, \mathcal{P}e_s = 100$ and $P_x Re = 0.25$

agating structure. This transition takes place as the induced stress becomes weaker. Thus the influence of local velocity field on the bulk velocity field is minute. The velocity shock at the front end still exists, though in diminished strength, generating an upward flow. The ridge stretches under the inertial force exerted on the fluid mass , causing the peak height to drop. The displaced mass seems to be contained in the hump since the integral $\int_{-\infty}^{+\infty} h dx$ at any time is fixed. However it should be stressed that there is an inflow and an outflow at left and right boundaries maintaining a constant mass flux. As we have seen in §4.5.1, this inflow brings in the surfactant layer towards the edge of the trough forming a cusp (see Figure 4.3(b)). This surfactant flow keeps the maximum surface stress a constant in contrast to the case of spreading of a drop [33, 52]. At the same time, substrate is transported to the trough wall within the bulk exerting an inertial force on the facing surface, making it steeper(see 4.25(c)). The breaking down is a combined effect of inertial forces and surface tension gradient, with the latter playing a minor role. As the trough wall becomes steep, the depth increases which is consistent with conservation of bulk mass.

Unlike for the cases of large $\mathcal{P}e_s$, there is no strong upward flow for small $\mathcal{P}e_s$ since the rapid diffusion suppresses the occurrence of strong Marangoni stresses. The initial wave is smooth and wider compared to the high Péclet number flows. Since there are no surfactant shock formations in the vicinity of the peak (the surfactant contact line move faster than the wave and is located farther downstream of the peak), the flow within the wave resembles a gravity wave [77]. Figure 4.26(a), (b) and (c) shows the transformation of the initially smooth wave to an overturning wave. Stream functions, to a certain extent, support the explanation on the wave breaking mechanism that it is the influence of momentum that causes the overturning. The sharp "pointy" streamfunctions in Figure 4.26(c) arise from the numerical instability that develops due to excessive steepening.

At the presence of an adverse surfactant concentration gradient, the dynamics be-

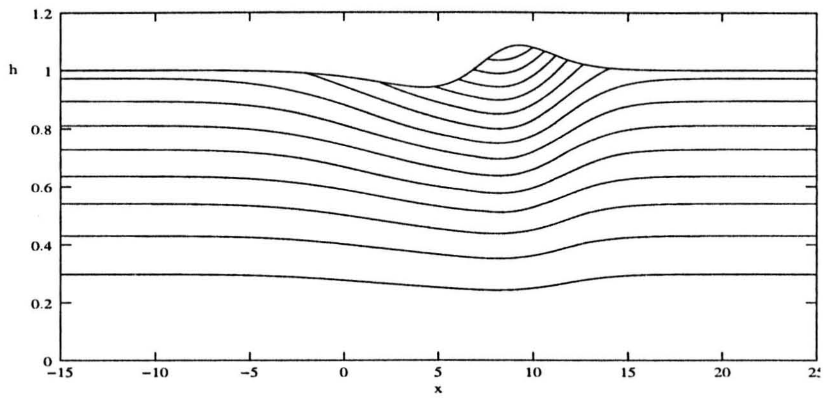

(a) t=5

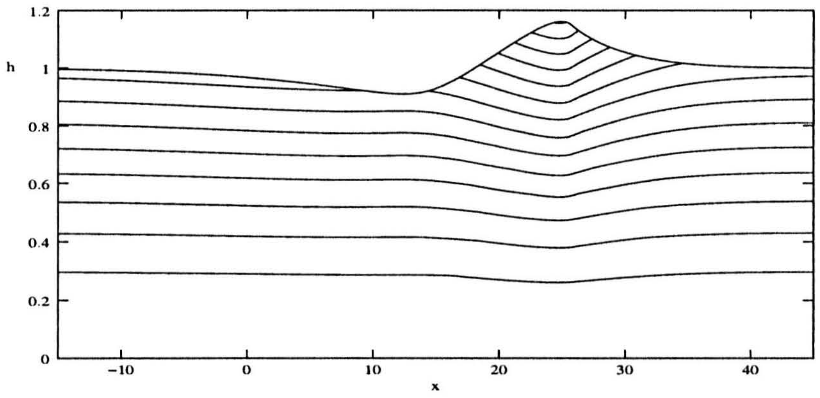

(b) t=50

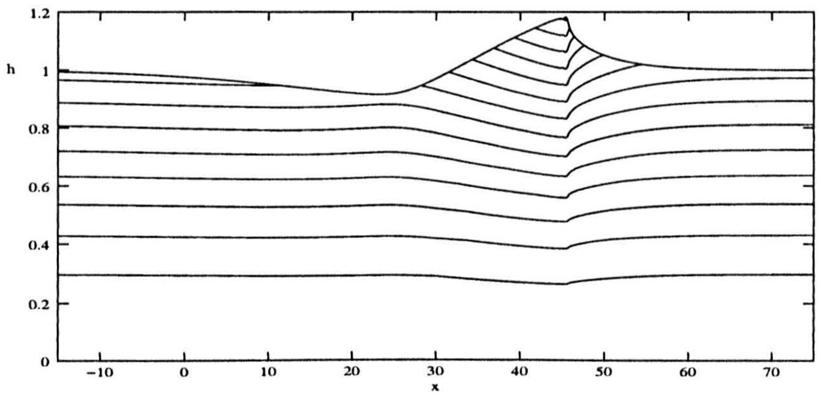

(c) t=110

Figure 4.26: Stream functions for small $\mathcal{P}e_s$. Waves breaks at early times when $\mathcal{P}e_s$ is small. Plots (a), (b) and (c) shows the stream functions for t=5,50 and 110 respectively for $\mathcal{P}e_s = 1$. $\mathcal{M}a = 1$ and $P_x Re = 0.25$.

come more complex. The magnitude of the Marangoni number becomes the definitive feature determining the flow characterisation. In §4.6 we discussed the surface concentration evolution. The resulting wave from an adverse surfactant gradient evolves almost to a steady state, moving upstream or downstream depending on the magnitude of $\mathcal{M}a$.

First we consider the case of $\mathcal{M}a \leq 1$. Figure 4.27 show the streamfunctions at $t = 1, 5$ and 30 for $\mathcal{M}a = 1.0, \mathcal{P}e_s = 100$ with $P_x Re = 0.25$. The flow is toward the positive x direction. The adverse surfactant gradient induces a surface stress field that opposes the flow. At very early times, this stress overcomes the bulk flow momentum. As a result, flow separation takes place behind the contact line, forming a region of reverse flow, i.e. opposing the bulk flow. The dashed line in figure 4.27(a) is the zero stream line that marks the flow separation. Above the zero stream line, the flow increases having a maximum at the fluid surface. Initially, the fluid under the shear force exerted by the Marangoni stress, struggles to flow upstream opposing the bulk flow. This competition adjusts the surface by forming a ridge ahead of maximum stress point. Within the separated region, the substrate flows into the ridge. The flow separation adjusts the flow in the bulk. For early moments ($t < 5$) most of the bulk flow, under the influence of the separated region, takes an upward turn, feeding the capillary ridge. Only a small amount of bulk flow continues to flow all the way downstream in the vicinity of the rigid boundary. Behind the ridge, beyond the zero line, flow continues to flow downstream.

The flow separation exists for a short time only. Figure 4.27(b) shows the stream lines at $t = 5$. As time progresses the separated region diminishes as a result of decreasing Marangoni stress (See figure 4.22). However the Marangoni stress remains finite along the surface of the ridge (where the concentration gradient is increasingly becoming linear). As the separated region diminishes the continuous flow regime grows. A considerable fraction of bulk inflow is fed to the ridge. The ridge grows in height and width due to this feeding process. The feeding stream

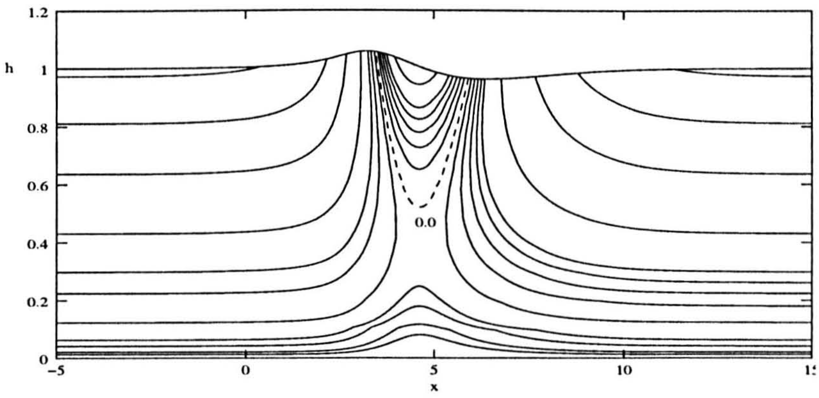

(a) t=1

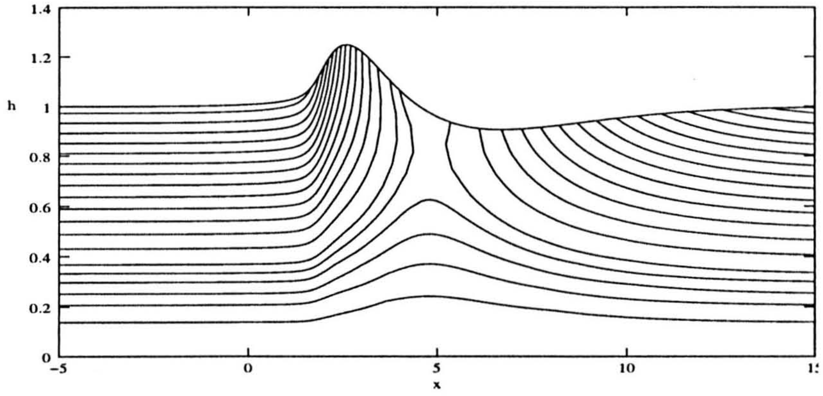

(b) t=5

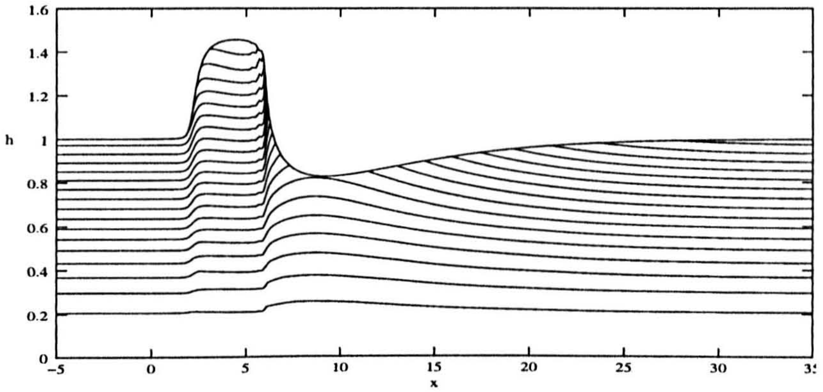

(c) t=30

Figure 4.27: Stream functions for a surfactant gradient opposing the bulk flow with $\mathcal{M}a = 1$. $\mathcal{P}e_s = 100, P_x Re = 0.25$. The changes to the flow are rapid at the beginning (see the text). Therefore the plots (a), (b) and (c) are for t=1,5 and 30 respectively. (c) is just before breakdown of the wave.

decreases with time. As the stress reduces, around $t = 15$, the ridge starts to drift downstream. At the same time the stream lines within and around the ridge start to change from an upward trend to a more horizontal form showing the drift. The streamlines just before breaking are shown in Figure 4.27(c). The substrate that flows into the ridge is readily carried towards the nearly vertical surface downstream and upwards making the surface more vertical. This process ultimately destabilises the ridge.

For large Marangoni number, the induced stress is so large that it overcomes the bulk flow driving force at the locality of the contact line. In such situations we have a region of fluid where the total flow is in the negative x direction. Figure 4.28 shows the flow development for $\mathcal{M}a = 10$ with $\mathcal{P}e_s = 100$ and $P_x Re = 0.25$. Figure 4.28(a) shows the early time development. The dashed lines again mark the zero stream lines. The flow within the region contained by the zero stream lines opposes the upstream flow. The reversal of the flow is induced by the strong shear stress (c.f. Figure 4.23(c)). The interaction between the induced velocity field and the upstream bulk flow around the contact line again forms a fast growing capillary hump. The zero stream line between two interacting velocity fields indicates a discontinuity in material flow at the contact line. The upstream flow turns upwards and flows into the ridge. The upwards material flow at this point is fast. The substrate in the contained region too flows upward initiating a depression behind the ridge. The ridge grows higher and thicker quickly. Substrate beyond the second zero stream line, behind the ridge continues to flow downstream, expanding the depression. The Marangoni stress is so large that the contact line moves upstream. However, the speed of the ridge decays as the concentration gradient decreases. The two movements, upwards and upstream, form a sharp shock front as advection is faster than diffusion of the surfactant.

As the shear stress decreases in time, the induced local velocity field weakens. As a result, the upstream bulk flow forces the region of opposite flow to shrink. This

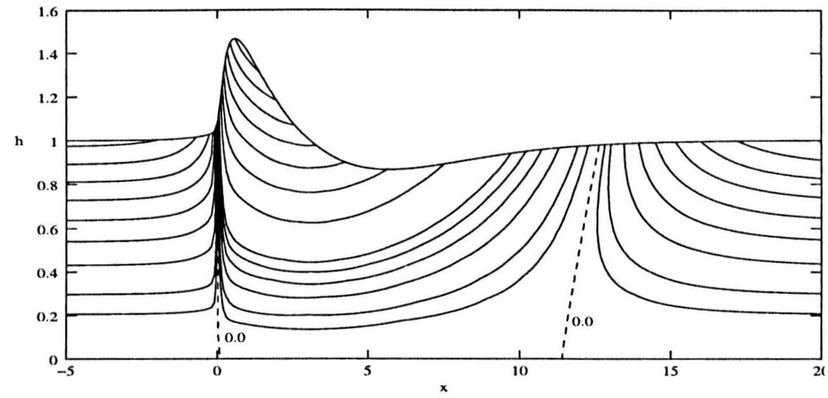

(a) t=1

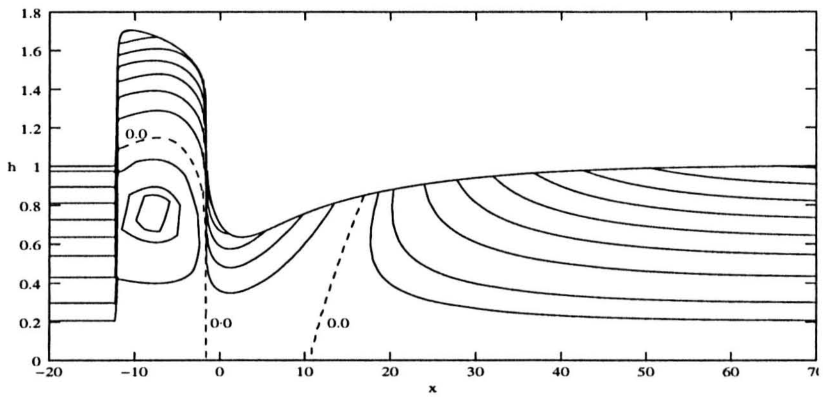

(b) t=27

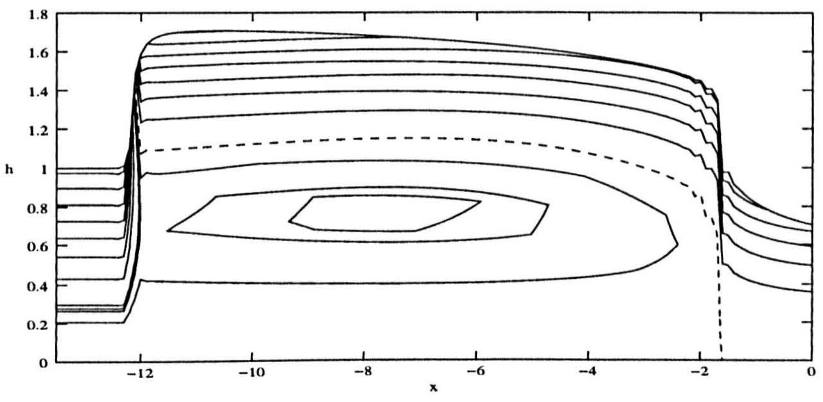

(c)

Figure 4.28: Stream functions for adverse concentration gradient with large $\mathcal{M}a$. Here the $\mathcal{M}a = 10$, $\mathcal{P}e_s = 100$ and $P_x Re = 0.25$. The early time behaviour is shown in (a). (b) presents the stream functions just before breaking. (c) shows the details of the capillary ridge. Flow around the contact line is hindered by the presence of the concentration gradient. The coarseness of the streamlines in flow cell is due to the low resolution of the grid.

interaction forms a recirculation cell beneath the ridge (see figure 4.28(b)). The zero stream line bends to accommodate the recirculation cell. The narrowing negative velocity regime still feeds the ridge flowing in substrate just behind it. This pumping process increase the depth of the depression. One can observe higher velocities along both faces of the ridge. Figure 4.28(b) shows the stream lines just before the ridge become unstable at $t = 27$ (figure 4.28(c) is an enlargement of the flow details around the ridge in (b). The coarseness of the streamlines in the cell arise from the low resolution of the grid). The existence of two zero stream lines indicate that the bulk flow is hindered through out the whole period from formation of the ridge to destruction of it. The destruction occurs similarly as for $\mathcal{M}a = 1$.

4.8 Summary

The predicted behaviour of the thin film spreading system under the influence of bulk flow should be understood by examining the physical relationships included in our model. For instance, surface tension as a restoring force for film flatness is not included; hence the explicit appearance of the capillary number in the evolution equations. The behaviour of evolution of surface and the concentration are nonlinearly coupled through the tangential stress balance at the free surface. This coupling give rise to the surface wave. The nonuniform distribution of the surfactant along the surface gives rise to the transport mechanisms diffusion and Marangoni advection. These two mechanism introduces the surface wave which then interact with the bulk flow and evolve to a breaking point.

The advection of surfactant due to the bulk flow influence the evolution by forming a 'cusp' behind the contact line for large Pe_s. However, the diffusive and advective activities at the contact line do not affect the surfactant inflow. The analytical expression for the total surfactant volume is observed for all simulations. The numerical values differ from the analytical prediction only by 0.01%. This agreement between evaluated and analytic estimates highlight the accuracy of the simulations.

The presence of a background flow causes waves to break. There are two mechanisms of wave breaking for the case of surface tension gradient along the flow; (i) destruction of trough wall and (ii) peak folding over. Péclet number is the sole factor that defines the mode of breaking. It is found that if $Pe_s < 30$ the wave breaks by folding over and for $Pe_s > 35$ destruction of the upstream trough wall occurs. The Marangoni number controls the strength of the disturbance magnitude together with Pe_s. The larger the Marangoni number, the larger will be the physical size of the ridge, but the height remains below $2d$ where d is the undisturbed film height. Smaller $\mathcal{M}a$ with $Pe_s \gg 1$ excites small amplitude waves that separate.

The surface disturbances that occur under the influence of adverse surface tension gradient are short lived. The Marangoni number become the dominant term that control the features of the disturbance. Depending on the magnitude of $\mathcal{M}a$, local flow separation could occur. Formation of a recirculation cell too was observed. The effect of background flow on wave breaking phenomenon was examined.

The evolution equations based on lubrication approximations were used to predict the spreading and flow of the film. These equations represent the actual system loosely. To find out the effects of the terms that are left out during the simplification, we propose a fully nonlinear model. The complexity of the model restricts us to numerical simulations. In next chapter we describe the use of finite element methods to simulate the fully nonlinear simulate the spreading problem. Spreading of a surfactant strip of finite width on a stationary substrate is considered.

Chapter 5

Fully nonlinear simulations for spreading of a surfactant on a liquid substrate

5.1 Introduction

In the previous chapter we examined the onset and evolution of a surface disturbance under Marangoni stresses on a flowing substrate. The evolution equations that were used derived from Navier–Stokes (N–S) equations using *lubrication theory* approximations. The lubrication theory, among its assumptions, demands that the inertial terms of N–S equations be negligible compared to dominant effects of viscous and pressure forces. The geometric requirement $h/L \ll 1$ is used to simplify the flow equations. From the use of different geometric scales for x and z, it follows from the continuity equation that $U/L \sim W/d$ or $\frac{W}{U} \sim \frac{d}{L} \ll 1$. In most applications, the film surface variations in the z direction are also considered to be small, smooth and gradual. However, for spreading of a surfactant, the initial jump in surface stress induces larger vertical velocities as well as sharp changes to the surface, in breach of the lubrication approximations. In most studies, this fact is overlooked [33, 52, 39, 56] while in some cases it is just mentioned [71]. Furthermore, the approximations as carried out in chapter 3 leave out capillary effects related to the curvature of the surface. In some work [69] in the past the capillary effects were included in lubrication theory assuming that the curvature $h_{xx}/(1+h_{xx}^2)^{3/2} \sim \mathcal{O}(\varepsilon^{-2})$. Nevertheless, this point is superfluous as the study focused on spreading rates. Curiously, the predictions made using lubrication theory were close to the measured values [99, 34], irrespective that the dynamics of the substrate layer is not fully explained by it. We can envisage that upon evolving for a long time, the initial surge in surface stress, film height and w velocity decay, limiting the influence of non-lubrication contributions, so that the predictions match with the experimental data.

In our application, inertia of the flow is not required to be negligible so that the effects of inertial terms $\mathbf{v}\cdot\nabla\mathbf{v}$ of the disturbance field cannot be ignored in describing the dynamics. So, also, is the effect of the surface tension (in relation to curvature). The inertial terms at initial moments should play a part in the neighbourhood of the induced velocity field which would affect the wave structure and short time velocity. The surface tension might reduce the ridge height, acting as a restoring force. As a method of examining the appropriateness of lubrication theory approximations in shock evolving systems as well as to study the influences of the inertial terms and capillarity in spreading, we constructed finite element method (FEM) simulations on the fully nonlinear N–S system with a free boundary.

There have been only a few attempts to solve the N–S system with a free boundary for the spreading problem. Tsai and Yue [105] approached the problem by solving the N–S equations and the continuity equation as an initial-boundary-value problem using a combined spectral and finite difference scheme, considering a fixed boundary at the top. The tangential stress balance at the free surface was then used to evaluate the derivatives of $\mathbf{v}$ at the surface. The z deformation is then evaluated using the kinematic condition on the surface. Jensen and Halpern made a similar attempt in analysing stress singularities in surfactant driven thin film flows [54] using a boundary element method (BEM) for, again, a flat surface limit. However, unlike of above attempts we present a method to solve for the evolving boundary as an integral part of the total flow solution. A complete description of the method was given in chapter 3 §§3.5.2.

In this chapter we investigate the possible differences between LT solutions and fully nonlinear simulations. The introduction of inertial terms with more degrees of freedom in parameter space presents a wide range of cases to examine. However, considering the existing work, we decided to simulate the spreading of a surfactant strip with a finite width on a stationary substrate so that we would be able to compare results. We begin with detailed description of our method of implementation in §5.2. There we discuss the new scaling involved and the simulation stratagem with regards to FEM system. The differences in scaling between lubrication theory and nonlinear model is examined to find the parametric compatibility in §5.3. A qualitative and quantitative comparison between the two models is carried out in §5.4. There we present the simulation results of fully nonlinear simulations for the surfactant strip. We use results of an equivalent MOL simulations to compare the two systems though we do not discuss the LT model results separately (see [33, 52] for an in depth description of lubrication theory model).

5.2 Implementation of the spreading problem in FEM

5.2.1 The flow model

The Navier–Stokes equations (3.1) together with the continuity equation (3.2) are again considered. The notable differences of the scheme is the scaling of variables using the same scale for both directions x and z. Therefore we take

$$u \sim w \sim U_s, \qquad x \sim z \sim d, \qquad p \sim \frac{\mu U_s}{d}, \qquad t \sim \frac{U_s}{d} \tag{5.1}$$

where U_s and d are reference velocity and film thickness respectively. The tangential stress balance suggests the scaling for surface tension as $\sigma \sim \mu U_s$. Figure 5.1 shows the schematic representation of the physical domain. We use the aspect ratio $L/d = 20$. The computational domain Ω is confined by the boundary $\partial\Omega$ composed of A,B,S and C as marked in Figure 5.1. Use of the scales (5.1) result in the set of nondimensional equations

$$\begin{aligned} Re_n\left(\frac{\partial v_i}{\partial t} + v_j v_{i,j}\right) &= \sigma_{ij,j} + St_n\, \delta_{3,k} && (5.2)\\ v_{i,i} &= 0 && (5.3) \end{aligned}$$

for flow in the computational domain Ω. The tensor $\sigma_{ij,j} = -p\delta_{ij} + \epsilon_{ij}$ is the stress tensor with the deformation tensor $\epsilon_{ij} = (v_{i,j} + v_{j,i})$, and δ_{ij} is the Kronecker delta. We use no–slip conditions at the bottom boundary so that

$$v_i = 0 \qquad \text{at } z = 0 \qquad (5.4)$$

The upper boundary is free and deformable. The boundary conditions used were

$$\begin{aligned} t_k\sigma_{ij}n_j &= -\mathcal{M}a_n\Gamma_{,i}t_k && \text{at } y = h(x,t) && (5.5)\\ n_i\sigma_{ij}n_j &= \frac{\mathcal{K}}{Ca_n}\sigma(\Gamma)n_i && \text{at } y = h(x,t) && (5.6)\\ h_t &= Nv_i n_i && \text{at } y = h(x,t) && (5.7) \end{aligned}$$

Conditions (5.5) and (5.6) are the tangential and normal stress balances at the free surface (i.e. on S). The condition (5.7) represents the kinematic boundary, i.e. S is a material surface. The symbols appearing in (5.4)–(5.7) are as same as defined in Chapter 3 §3.2.

Apart from the flow equations, there is another equation that describes the species transport in the domain.

$$\frac{\partial \Gamma}{\partial t} + v_i\,\Gamma_{,j} = \frac{1}{\mathcal{P}e_n}\nabla^2\Gamma \qquad (5.8)$$

The boundary conditions we used are discussed in the next section with reference to the simulation setting and implementation. The dimensional analysis produces

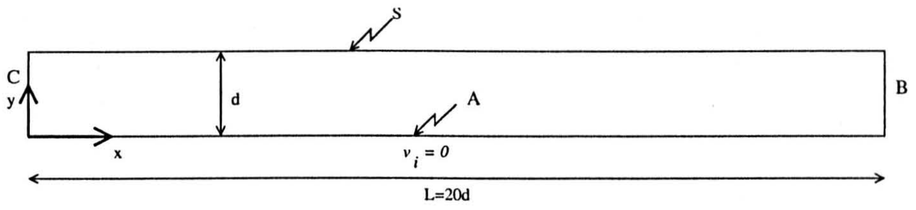

Figure 5.1: The domain on which FEM simulation is based on. The length of the domain $L = 20d$. A, B, S and C compose the rectangular boundary, $\partial\Omega$, that confine the computational domain Ω. The boundary S is the free deformable boundary. Flow can pass through the left and right boundaries C and B.

nondimensional groups as we have seen in chapter 3. The additional nondimensional group that arises is the Stokes number $St_n = \frac{\rho g d^2}{\mu U_s}$. The Stokes number gives the proportional strength of gravity to viscous forces. In the absence of a background flow, this term can be used to characterise the gravity effects in relation to surface tension since $\mu U_s \sim \sigma$ introduces a Bond number as per Gaver and Grotberg [33] in lubrication theory approximations to axisymmetric spreading. With this basic understanding of the equations that govern the flow and species transport, we move on to discuss the implementation of the spreading of a surfactant 'strip'. We use this particular problem to compare the two solution methods, namely the lubrication approximations and fully nonlinear FEM.

5.2.2 Strategy of implementation

To implement a monomolecular layer of a secondary species along the free boundary requires the creation of a 1–D form of (5.8). Creation of extra degrees of freedom only at the boundary nodes to incorporate species transport is cumbersome given that we intended to adapt an existing code [35]. Instead, we used an alternate modelling approach upgrading the existing code to include variations of surface species. Considering the fact that the FEM code solves 2–D species transport equation on the domain we divided the domain into two regions; one very thin region mimicking the monomolecular layer and the other with the thickness of the film. Both

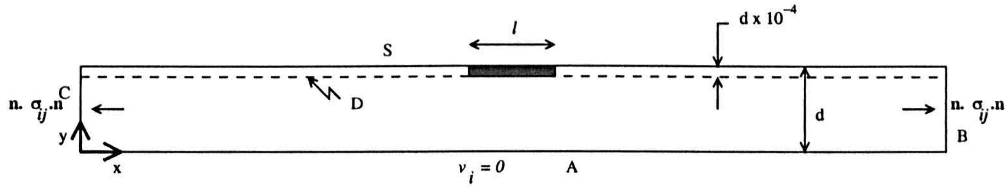

Figure 5.2: Sketch of domain arrangement for a surfactant strip of width l . Dashed line marks the hypothetical boundary D (see text). Out flow boundary condition allows the substrate to leave the domain.

regions contain bulk phase (i.e. the substrate) except for the area occupied by the surfactant. Figure 5.2 shows the setting with division of the domains marked by the dashed line D. The thickness of the thin region is so selected that it has a finite thickness enabling finite elements to resolve the domain without numerical instabilities but small enough to represent the monomolecular layer in physical sense. We choose this thickness to be four orders of magnitude smaller than the film thickness. The selection is arbitrary and required some trial and error attempts to come up with a suitable thickness. We used only a single layer of elements (biquadratic 9 point rectangular elements. See Figure 5.3 for details.) to discretize the thin region. The species transport equation is solved only within the thin domain using a no flux restriction at boundary D and S. This will guarantee that there will be no concentration gradient across the thin region, since an element using biquadratic interpolation has three nodes across as shown in Figure 5.3. In effect we are solving a 1–D species transport equation along three lines of nodes, one at the free surface and two submerged barely below the free surface. This use of selective discretisation to solve species equation (5.8) with a no flux boundary approximates the actual physical system exceedingly well given that the thickness of the secondary region is sufficiently small.

The weak formulation (Galerkin method) employed in FEM allows us to use sharp gradients since the finite integral would hold across the discontinuity. Therefore we can implement the surfactant strip of width l locally at the mid-point of the upper

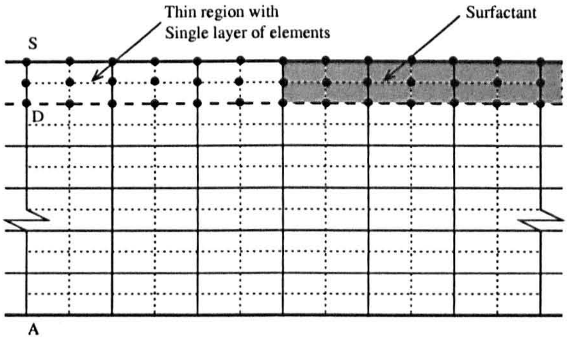

Figure 5.3: Detailed part of the grid that shows the arrangement of elements and nodes within the thin domain that represent the surfactant layer. Lines A, S and D represents the bottom free surface and the division between to phases respectively. Black circles marks the nodes. There are three nodes on the boundary S per element. Dotted lines pass through the nodes.

thin region as

$$\Gamma = \begin{cases} 1 & : \quad \|x - \frac{L}{2}\| \leq \frac{l}{2} \\ 0 & : \quad \|x - \frac{L}{2}\| > \frac{l}{2} \end{cases} \tag{5.9}$$

where L is the domain length. The surfactant mass remains fixed according to

$$M_n = \int_{-\infty}^{+\infty} \Gamma dx \quad . \tag{5.10}$$

The concentration at the far field is set to be zero; i.e. $\Gamma = 0$ as $|x| \rightarrow \infty$. The local value of surface tension is evaluated using the nondimensional equation of state:

$$\sigma = \frac{1}{Ca} + \mathcal{M}a_n \left[\Gamma - \Gamma_{ref}\right] \tag{5.11}$$

Local surface tension values are used in the normal and tangential stress balances to compute surface velocities. The method of establishing the free boundary shape using kinematic boundary condition as a grid boundary is explained in chapter 3 §3.5.2.

The flow boundary conditions are straightforward for the spreading of surfactant strip of fixed mass on a stationary substrate. The stress balances at the free surface are an integral part of the solution. No slip conditions were utilised at the bottom

Figure 5.4: The computational mesh. The elements are packed at the deformable free boundary where the secondary domain of 1×10^{-4} exists. The total height $d = 1$ and the length $L = 20$.

boundary (A). In view of the finite length of the domain bounded by boundary walls B and C (refer to the Figure 5.2) we use outflow conditions which demands that the normal stress nearly orthogonal to the outflow planes.

$$n_i\sigma_{ij}n_j = 0 \qquad\qquad |x| \rightarrow \infty \tag{5.12}$$

the above condition implicitly requires parallel flow at outflow planes which would conflict with the normal stress balance boundary condition for the free surface at corner points. To resolve this, the normal stress condition, (5.6), is given the precedence over outflow boundary condition (5.12) which is now a customary practise first described by Ruschak [89].

The Galerkin finite element method is implemented on the domain discretized using nine node quadrilateral elements to seek approximate numerical solutions. Biquadratic trial functions were used to approximate the velocity components assuming them to be continuous between the elements. The pressure is approximated using linear trial functions over an element and considered to be discontinuous at element boundaries. This combination of velocity and pressure trial functions assures divergence free velocity fields without causing spurious pressure oscillations associated with other combinations. The flow domain is discretized with a stretched grid having higher element density at the free surface (keeping the top most layer within the secondary region as described before). Figure 5.4 shows the discretized computational domain. The rectangular computational domain has dimensions 1×20. We pack more elements in the vicinity of the initial drop to resolve the initially sharp gradients. The mesh contains 40×500 elements giving 62281 nodes although a grid with 60 × 600 is used as a convergence test. The solution method and the grid diffusion method is described in detail in chapter 3 where we described the numerical methods.

Because of the use of a single reference length to scale all distances and a slightly different pressure scale, nondimensional numbers in this model differ from those of the lubrication theory model. In the next section, we seek functional relationships between the parameters in order to compare two systems.

5.3 Parametric compatibility between Lubrication theory and the nonlinear model

The scales used to nondimensionalize the N–S equations in FEM generate nondimensional numbers that contain film depth as the geometric factor involved, whereas in lubrication theory we use both depth d and length L of the film. To compare the two systems we need to match the nondimensional groups. To this end, we formulate the relationships between two methods. Table 5.1 gives the definitions in either system with the relationship to each other. The parameters related to FEM are subscripted with "n". As the main difference comes from the geometric length scales we can envisaged that the aspect ratio ε becomes the combining factor. The Marangoni and Péclet numbers are the two parameters that differ.

Apart from nondimensional parameters, two flow variables require the same conversion due to the difference in nondimensionalization scales. Time and pressure were scaled differently in LT approximations. In comparing the two simulation results, a compatible time scale has to be used. The pressure becomes important when there is a background flow.

Table 5.2 lists these two variables, definitions and the functional relationship to each other (i.e. the scaling between LT and FEM). The relationship between P and P_n shows that in the case of background flow, the inflow velocity of FEM can be defined

Parameter	LT Definition	FEM Definition	Relationship
Reynolds number	$Re = \frac{\rho U_s d}{\mu}$	$Re_n = \frac{\rho U_s d}{\mu}$	$Re_n = Re$
Capillary number	$Ca = \frac{\mu U_s}{\sigma}$	$Ca_n = \frac{\mu U_s}{\sigma}$	$Ca_n = Ca$
Marangoni number	$\mathcal{M}a = \frac{h\sigma_\Gamma \Delta\Gamma}{L\mu U_s}$	$\mathcal{M}a_n = \frac{h\sigma_\Gamma \Delta\Gamma}{h\mu U_s}$	$Ma_n = \varepsilon^{-1}\mathcal{M}a$
Péclet number	$\mathcal{P}e_s = \frac{U_s L}{D_s}$	$\mathcal{P}e_n = \frac{U_s d}{D_s}$	$\mathcal{P}e_n = \varepsilon\mathcal{P}e_s$

Table 5.1: The relationship between nondimensional parameters arising in lubrication theory and FEM formulation due to use of different length scalings. Lubrication theory (LT) requires two length scales L and d to normalise longitudinal and transverse distances respectively.

to match the LT system easily without setting a pressure drop.

The fundamental idea is to run simulations in both systems with matching parameters using the above determined relationships and compare the results at corresponding times to investigate the similarities and differences. We look for the differences between the LT approximated system and FEM that are introduced by the inclusion of inertial terms in the flow as well as the capillarity at the surface. In next section we examine the results from FEM simulations of the fully nonlinear system.

Parameter	LT Definition	FEM Definition	Relationship
Pressure number	$P = \frac{p}{\rho U_s^2}$	$P_n = \frac{p d}{U_s \mu}$	$P_n = P\,Re$
time	$t = \frac{tU_s}{L}$	$t_n = \frac{tU_s}{d}$	$t_n = \varepsilon^{-1}t$

Table 5.2: Two of the nondimensional variables that have different scalings. The functional relationship is listed in the fourth column.

5.4 Comparison of results with the lubrication theory model

The evolution of the surface and advective/diffusive concentration front is simulated for a passive surfactant strip of unit width using FEM for fully nonlinear model and MOL for LT theory equations. Individual features such as concentration profiles and front positions were compared to find out the differences and similarities between the two approaches. The deformable boundary FEM solutions were discussed first in detail since the simulations are unique and novel to the spreading problem.

5.4.1 FEM simulations on spreading of a surfactant strip

The formulation and the method of solving the flow equations together with species conservation equation is described in §5.2. We use the parameter values given in Table 5.3. We have rather a large Péclet number and a small Marangoni number. The Stokes number (St_n) or equivalent Bond number set to zero eliminates the effect of the gravity. The nondimensional film height is normalised using the unperturbed film depth d is set to 1 which in return sets the nondimensional domain length to 20 (details of the computational domain are given in Figure 5.4). This geometry poses

Nonlinear model	Lubrication theory model	value
Re_n	Re	1.0
Ca_n	Ca	1.0
$\mathcal{M}a_n$	$\varepsilon^{-1}\mathcal{M}a$	−1.0
$\mathcal{P}e_n$	$\varepsilon\mathcal{P}e_s$	100.0
St_n	n/a	0.0

Table 5.3: Parameter values for nonlinear simulation. The values represent a weak Marangoni forces with strong Péclet numbers. (n/a: not applicable).

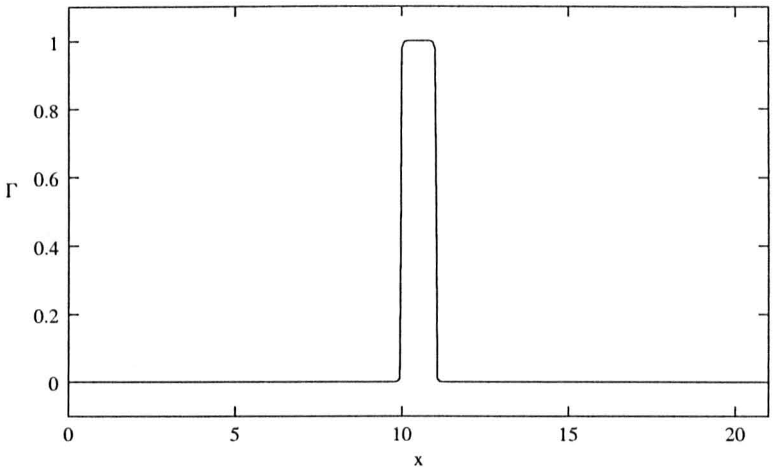

Figure 5.5: The concentration profile used in nonlinear simulations. The initial step change with sharp edges has been smoothed out by letting the species to diffuse in the absence of the substrate flow for a small time period (see the text for more details).

an upper limit on evolution time. Once the wave front move to the end points the simulations would become erroneous since the upper two corners stay fixed. This can be easily overcome with selecting a larger domain in the expense of higher CPU time. The current grid takes 7.75 hours to converge on 0.1 time step on Linux platform with a Pentium 4, 1.7GHz processor.

The sudden injection of the surfactant into a region of unit length at the centre of the upper boundary (as shown in Figure 5.3) generates slightly aphysical concentration values (negative values of $\mathcal{O}(10^{-2})$ and smaller) for the first few moments due to sharp gradients at the edges. Although the weak formulation of FEM accommodates such discontinuities and recover as integration proceeds, we initially allowed the species to diffuse for a short while without flow. This resembles the diffusion of heat through a iron block. Once the anomalies dissipate, the solution is read in as the initial condition to the spreading problem with flow. This is to eliminate any flow anomalies that may occur due to negative concentrations. As a loose check on the integrity of the method, we extract the surface concentration values ($\Gamma(x)$) and evaluate the integral $\int_{\partial\Omega} \Gamma dx$ over the deformable upper boundary for every converged time step. The integral should not change substantially from the initial value if the mass is conserved.

Since we have a patch of surfactant in contrast to the linear model where exact 1-D representation is followed, the integral is expected to fluctuate. However we observed that the integral (mass conservation) holds, fluctuating around the initial value by about 2%. Furthermore we observe the divergence of the velocity field, $\nabla \cdot \mathbf{v}$, in the domain, which remains 10^{-8} or less for all cases.

The parameter values selected as in table 5.3 induces a weak velocity field in both nonlinear and LT model simulations. Diffusion is a weak process as Péclet number is large. Therefore the spreading is mainly due to advection. The weaker Marangoni effects induce a weak velocity field. Even with this weak field, the effect of inertial terms are quite appreciable. The initial surface tension gradient generates a sudden stress change, inducing surface motion. This motion generates two recirculating cells as shown in Figure 5.6(a) and (c). The recirculation cells occur beneath a shallow layer where lateral fluid displacement occurs. This is a direct effect of interactions between nonlinear advective terms. The perturbation at the surface level penetrates the depth almost instantly (also see Figure 5.10). The lateral distance that is excited (centre point outward) is about $1.5d$. The locally initiated flow then develops, engulfing more and more of the film. Figures 5.6–5.9 shows stages of spatio–temporal evolution. The detailed stream functions were shown in Figure 5.6. The dashed line is the zero stream function. The two counteracting cells were separated by the centreline where the velocity is zero. The crossing point of the zero stream lines is marked by a diamond. The maxima and minima of streamfunctions were marked by • and ∘ respectively. The figure caption defines the sign convention. The surface deformation with respect to the depth is small at the beginning. Figures 5.6(b) and (c) shows the contours of u and v velocities. Though $u > v$, at this initial stages $v \sim \mathcal{O}(u)$. A comparison of velocities were present in §5.4.2. The recirculation eddy enhances the vertical motion of fluid. The u velocity component is strong near to the surface at the contact line.

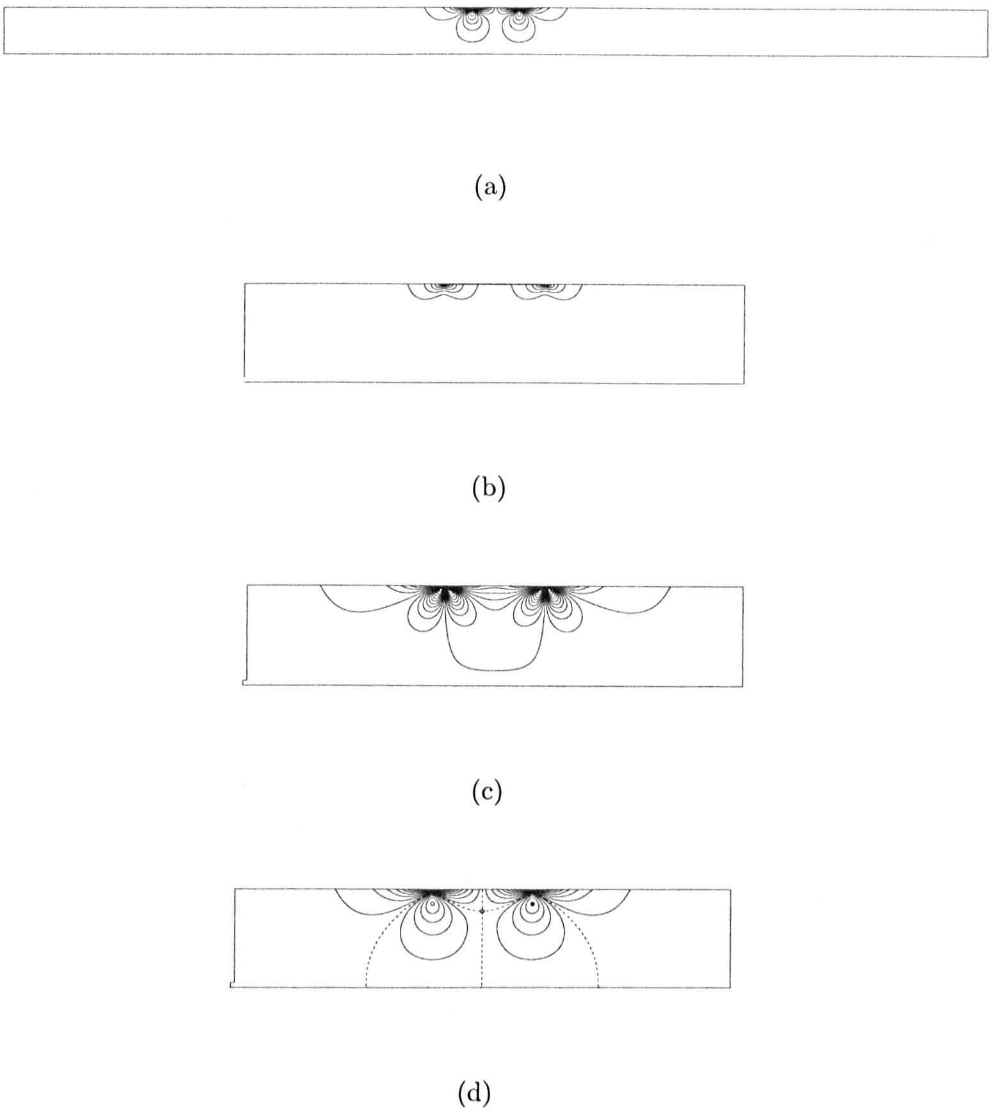
(a)

(b)

(c)

(d)

Figure 5.6: Fully nonlinear flow simulation of spreading of a surfactant strip on an stationary substrate at $t = 0.01$. The flow induced by the surfactant gradient is examined using (a) stream functions, (b) u velocity contours and (c) v velocity contours. (d) is the zoomed view of stream functions. In this and subsequent figures maximum is denoted by $\bullet$ and minimum is denoted by $\circ$ while the saddle point denote by $\diamond$ The maximum and minimum values have same magnitude but different signs depending on the rotation direction. The convention here is to take the clockwise rotation as negative. The critical values of stream functions are $\pm 1.101 \times 10^{-02}$. Flow parameters are as per in Table 5.3.

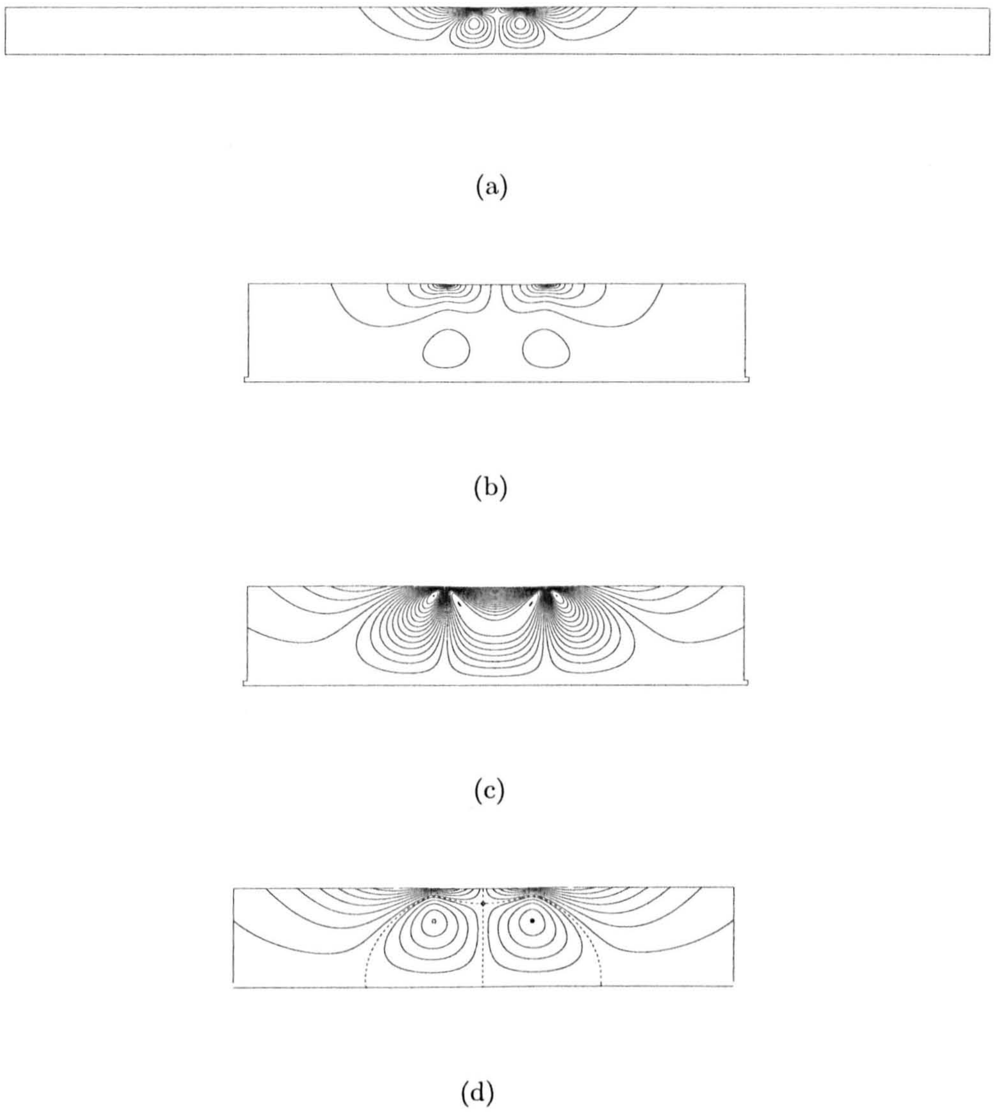

Figure 5.7: Flow characteristics at $t = 0.1$. The vortex intensity become maximum around this time. Plot descriptions are as same as for Figure5.6. Streamfunctions shows two counter-rotating rolls. The v velocity contours shows a wider spreading in the neighbourhood of the strip. The critical values of stream functions are $\pm 3.3228 \times 10^{-02}$.

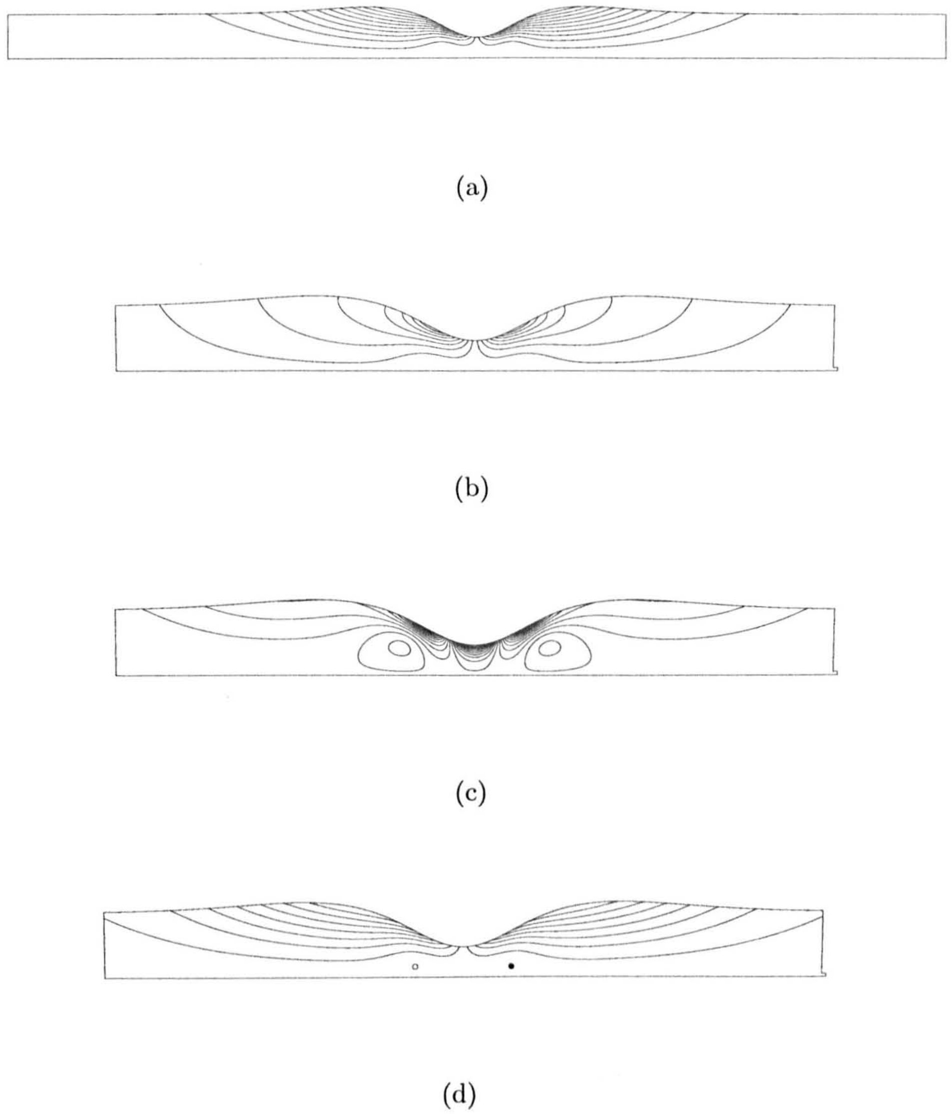

(a)

(b)

(c)

(d)

Figure 5.8: Flow characteristics at $t = 3.5$ just before the vortexes vanish. The streamline contours do not capture the vortices since they are very weak. The critical values of stream functions are $\pm 9.2077 \times 10^{-04}$. Plot descriptions are as same as for Figure 5.6.

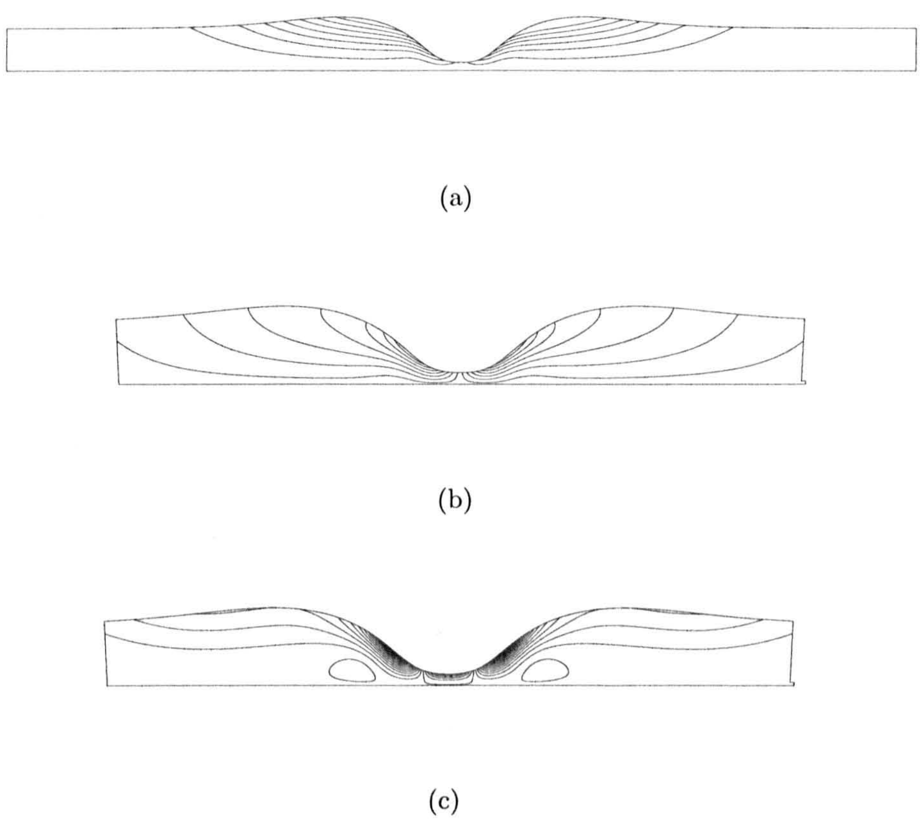

(a)

(b)

(c)

Figure 5.9: Flow characteristics at $t = 6.0$. The vortices were disappeared. Plot descriptions are as same as for Figure 5.6.

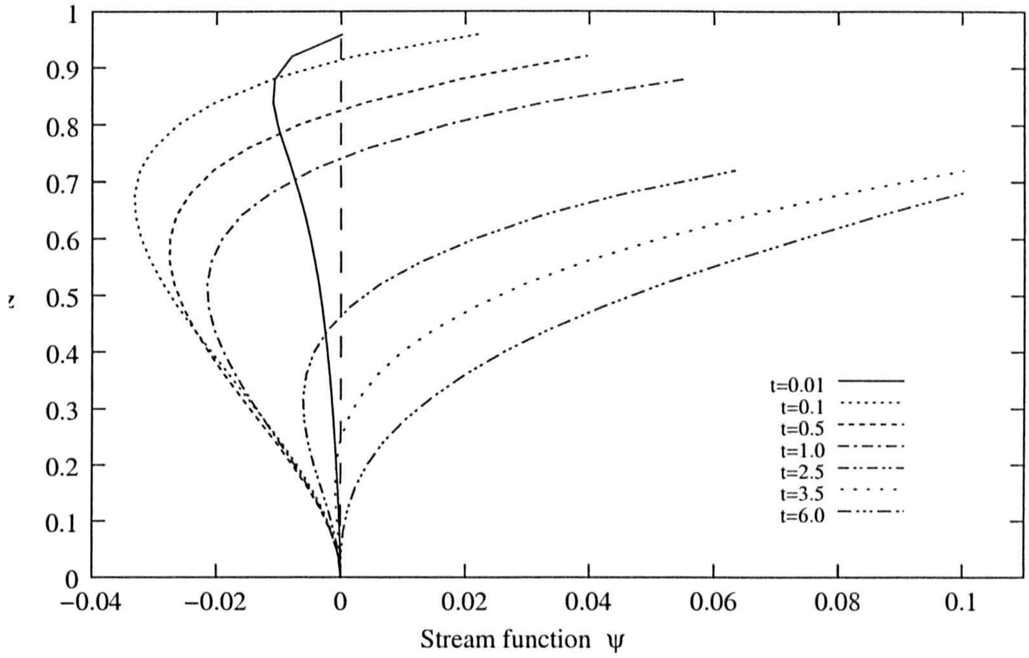

Figure 5.10: Streamfunction values along a line that passes vertically through the maximum point within the circulation eddy (i.e. the point marked by •). The height at which Ψ cross the zero line is the upper limit of the circulation cell. Beyond the crossing point the values indicate the lateral movement of fluid at the surface. The end point height is the location of the surface. The plots suggest that the circulation eddy grows to a maximum intensity within a fairly short time and then decays slowly.

Figure 5.6–5.9 represents four stages identified by the intensity of the vortex. The vortex, once initiated, reaches its maximum intensity in a very short time and then decays. Figure 5.6 shows the formation of the vortices. The vortex centres are very close to the free surface and occur just beneath the contact line where the u and w velocities are maximum. Flow patterns around maximum vortex intensity are given in Figure 5.7. The vortices expand, limiting the thickness of lateral moving layer to a fraction to the undisturbed depth. After reaching the maximum intensity, the vortices begin to decay monotonically and disappear. Figure 5.8 shows the details of the flow just before the disappearance of the vortex. The vortex centre has moved closer to the bottom boundary as the layer thickness of the lateral flow increases. Figure 5.9 shows the flow description a long time after the vortices have vanished. It resembles the streamlines derived from the lubrication model.

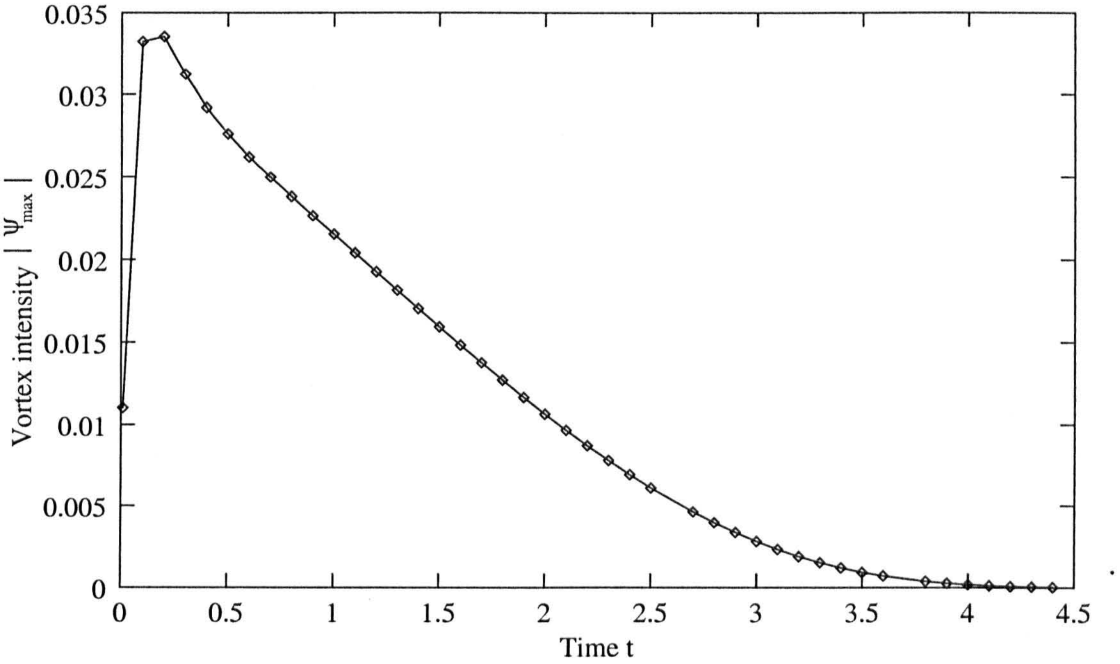

Figure 5.11: The vortex intensity variation with time. The vortex intensity defined by $\psi_{max} - \psi_0$ where ψ denotes the streamfunction. ψ_{max} occur at the centre of the vortex and ψ_0 is the zero streamfunction that encloses the vortex. The difference actually is the total volumetric flow within the vortex. Vortex intensity diminishes with time and ceases effectively beyond $t = 3.5$.

We examine this vortex behaviour by plotting the streamfunction values along a line normal to the bottom boundary that passes through the critical (maxima of the cell) point. Figure 5.10 shows the stream function profiles. The dashed vertical line marks the zero flow. The fact that the flow establishes across the depth practically instantaneously is evident from the streamfunction profile at $t = 0.01$. From Figure 5.10 we can clearly see that the cell centre moves downward, decaying in size as intensity decays. To quantify, we define the intensity of the vortex by the total flow within it. It can be determined by taking the value difference between the zero stream line and the critical point. Figure 5.11 shows the tracking of the intensity with time. After initial growth, it decays in size and intensity and cease to exist after t=3.5. By the time the intensity become zero the film depth is reduced to 53% of its initial value.

Gaver and Grotberg [33] carry out a numerical investigation on evolution equations derived using lubrication approximations and report the formation of a vortex ultimately resulting in flow separation under different conditions. They showed that a vortex begins to spin up closer to a rigid bottom boundary beneath the capillary ridge after a considerable period only if strong body forces are applied.

The vortex in their case eventually engulfs the film behind the moving front. The increasing capillary ridge height increases the hydrostatic head below it and this generates an adverse pressure effect that initiates the vortex and separation. Flow at the surface continues since the concentration gradient exists. We have shown in chapter 4 that the inclusion of different physics into the evolution equations results in formation of vortices. However, in this investigation it is evident that the formation of a vortex due to the high shear stress occurs even without gravity as a surface restoring force. The occurrence of the counter-rotating vortices can be observed independent of the parameter space provided that Reynolds number $Re > 0$.

The shear stress jump causes surface deformations. Figure 5.12 shows the evolution of the substrate surface from the nonlinear model. the corresponding evolution of surfactant concentration is given in Figure 5.13. The arrows show the general direction of evolution. The inset in Figure 5.12 shows the surface profile a few instances after initiation ($t = 0.01$). It resembles the lubrication model. However the two sharp depressions, characteristically present behind the peaks in lubrication theory model, only appear at very early times and are short lived. Instead, a monotonic depression continues to grow. The disappearance of the two edge depressions occurs as the vortex spins up initially. Perhaps, the strong recirculation causes this disappearance. In a linear model, the shear stress is only attributed to the surfactant gradient by means of the linearised tangential stress balance $u_z = \sigma_\Gamma \Gamma_x$. This causes sharp indentations where the maximum surface tension gradients occur. However, in the nonlinear model the surface shear is evaluated by considering the stress tensor at the surface, accounting for the total velocity field and for surface derivatives (See the

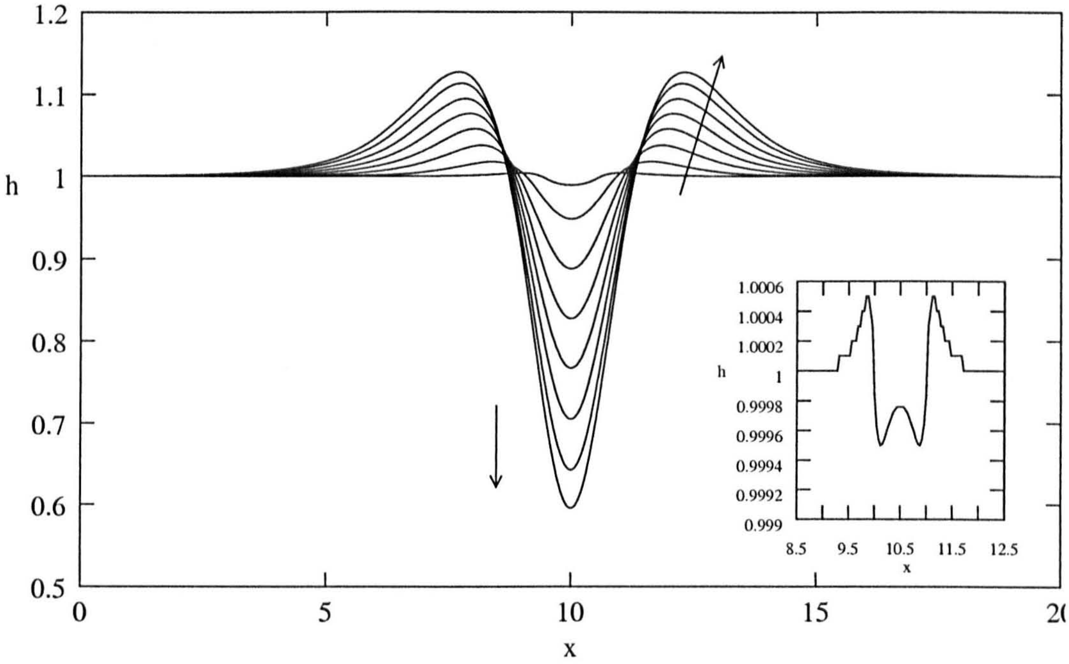

Figure 5.12: Surface profiles at $t = 0.1 - 2.8$ in $\Delta t = 0.4$ intervals. The inset shows the surface profile at $t = 0.01$. The initial surface elevation is very small compared to the film height. Parameter values were given in Table 5.3.

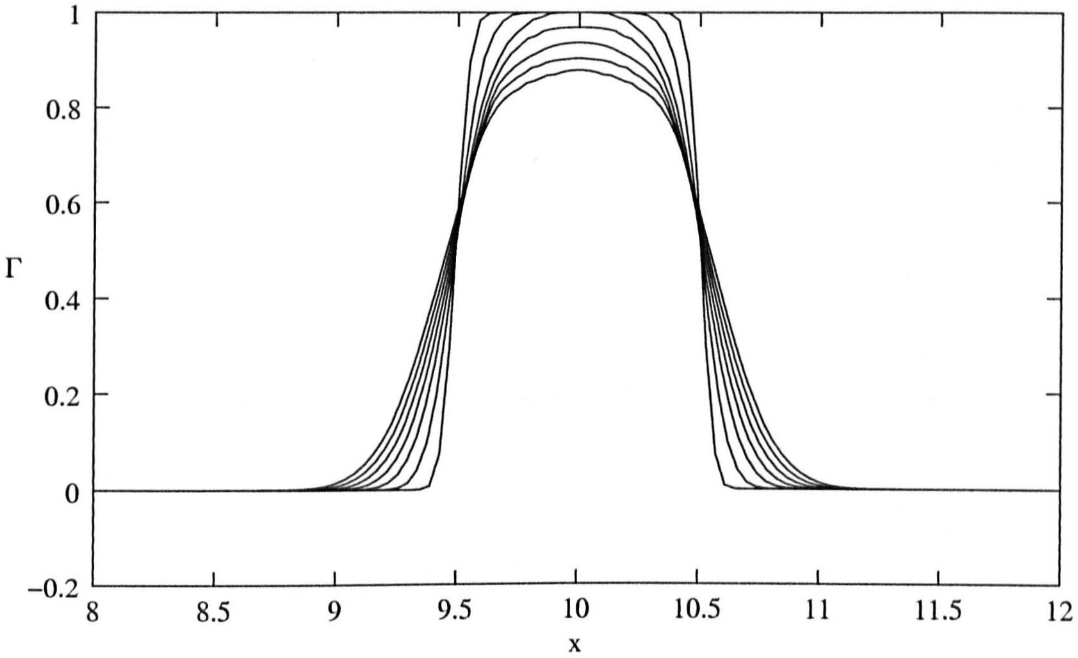

Figure 5.13: Concentration profiles along the free surface corresponding to the curves plotted in Figure 5.12.

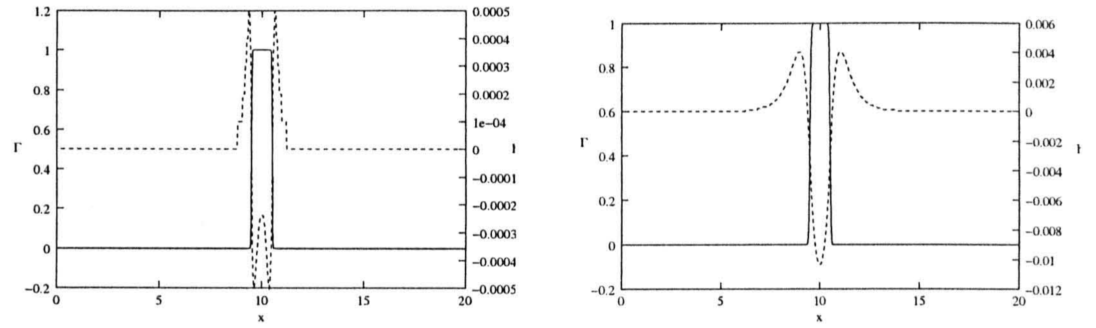

(a) t=0.01

(b) t=0.1

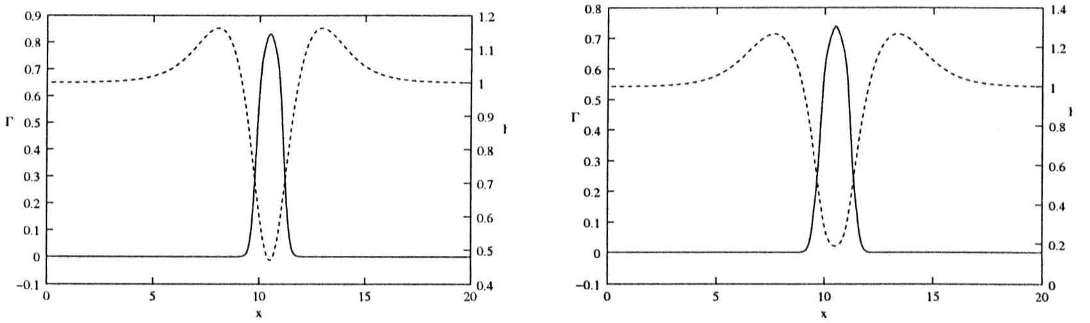

(c) t=3.5

(d) t=6.0

Figure 5.14: Change of surface profile as the evolution continues. The dotted line is the surface of the substrate while the solid line marks the concentration profile. Observe the disappearance and reappearance of the corner depressions.

comparison given in Figures 5.18–5.23). Figure 5.14 shows the sequence of events that takes place with respect to surface evolution and concentration profile. The capillary shock is more spread out. Furthermore, the film thickness reduces beneath the surfactant strip, forming an ultra thin layer. The thinning process becomes faster once the vortices disappear (recirculation reduces the lateral fluid displacement, retarding the thinning). Spreading rates and front positions are discussed in comparison to lubrication model in §§5.4.3.

The nonlinear model as shown above evolves with unique features added by the nonlinearities in flow field. However, in a broad sense the film evolution roughly follows the previously studied [33, 52] lubrication theory model (at least there is a geometric similarity). However, apart from the qualitative changes we discussed thus far, a quantitative evaluation of the similarities/differences are made in next two sections. We begin with extracting the length scale ratio ϵ as a check on the suitability of lubrication theory on free surface film flows with large surface height changes.

5.4.2 Evaluation of scales through nonlinear simulations

The fully nonlinear simulations, without *a priori* assumptions on flow field variables other than Boussinesq assumptions that the density and viscosity of the bulk remain constant despite the presence of a secondary species, should approximate the physical system to a greater degree of accuracy than lubrication theory approximates the system. However, nonlinear simulations of the evolving flow should mimic the actual physical system so that one should be able to adjudge the applicability of the lubrication theory to such systems.

Remarkably, we have already seen that the inclusion of inertial terms, though adjusting the flow field, leaves qualitative behaviour unchanged from the LT solutions. The lubrication theory, as we mentioned before, is based on the geometrical scales that decide the dominance of field variables. In essence,

$$\frac{w}{u} \sim \frac{d}{L} = \varepsilon \ll 1 \tag{5.13}$$

where ε is the aspect ratio. We use (5.13) as a guide to extract the scales involved in the flow regime. The idea is to query whether the ratios of the velocity components from nonlinear simulations hold (5.13) for all times. The velocity distribution is non-uniform and time dependent. The comparison of velocity components based on a fixed point would be erroneous since the selection of such point in a evolving system cannot reasonably justified. Though the maximum values would qualify it would

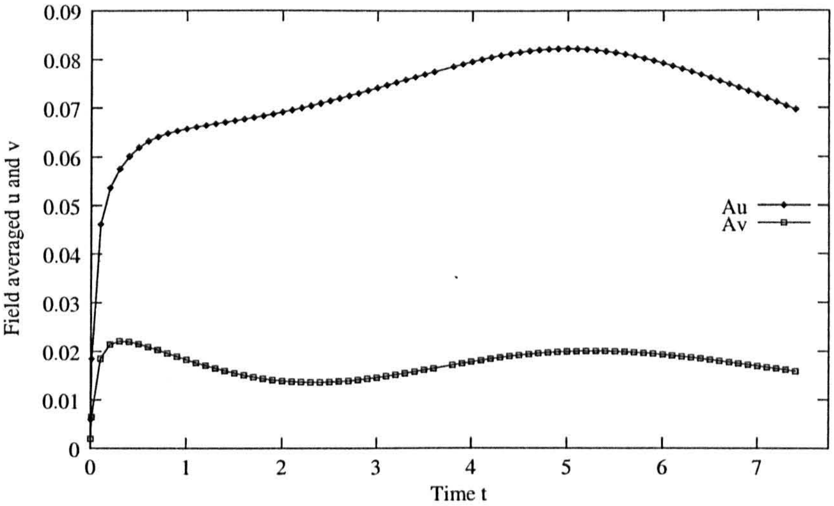

Figure 5.15: Field average of u and v velocity components from nonlinear (FEM) simulations. As the flow develops $\bar{A}_u$ increases in accordance with the growing flow field but then decays as the shear stress drops. $\bar{A}_w$ decreases as the vortexes decay. For initial moments u and v have same order of magnitude.

not be a global measure. Therefore to compare the velocity ratios we employ field averages of the variables. This was decided partially because the lubrication theory employs the height average velocity to reduce the dimensionality of the problem. Therefore the ratios of field averages are more close to the LT approximations.

For any quantity $f(x,z)$ defined over a domain Ω, we define a field average (or RMS) $\bar{A}_f$ such that [87]

$$\bar{A}_f = \sqrt{\frac{\int_\Omega f(x,z)^2 dA}{\int_\Omega dA}} \tag{5.14}$$

f can either be a vector or scalar quantity. We evaluate a quantity ε_{est} using the definition (5.14) as

$$\varepsilon_{est}^{-1} = \frac{\bar{A}_u}{\bar{A}_w} = \frac{\sqrt{\int_\Omega u(x,z)^2 dA}}{\sqrt{\int_\Omega w(x,z)^2 dA}} , \tag{5.15}$$

so that $\varepsilon_{est} \ll 1$.

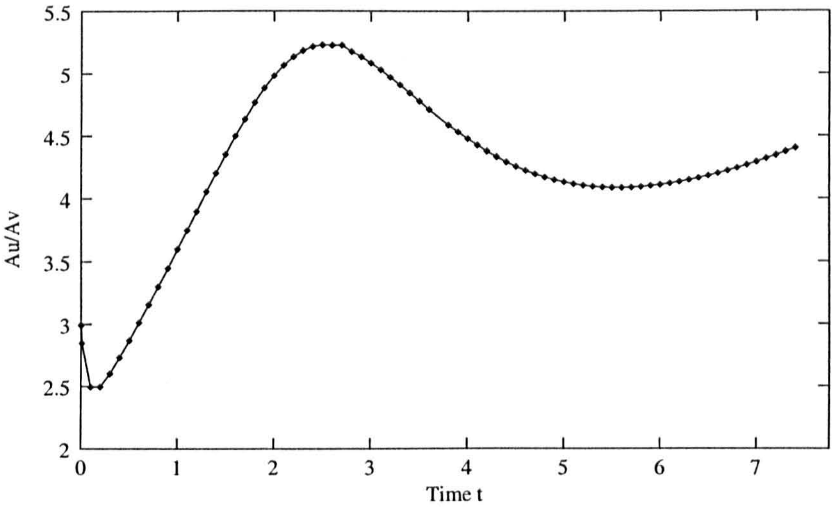

Figure 5.16: The time variation of $\varepsilon_{est} = \frac{\bar{A}_u}{\bar{A}_v}$. For initial instances the estimated $\varepsilon_{est} \sim \mathcal{O}(1)$, fails to hold (5.13). The ratio $\varepsilon_{est} >> \varepsilon$ casts doubts on applicability of lubrication theory in free surface flows with considerable surface deformations.

Figure 5.15 shows the plots of $\bar{A}_u$ and $\bar{A}_w$ against time. It can be seen that $\bar{A}_u > \bar{A}_w$ throughout the simulation period. The initially rapid increase in both field averages slows down within a few time steps. $\bar{A}_u$ keeps increasing at a slower rate while $\bar{A}_w$ decreases after reaching a maximum. Both u and w gain in magnitude once the vortices vanish. Then both velocity components start to decay as the Marangoni stress falls due to spreading. The ratio $\bar{A}_u/\bar{A}_w$ is plotted against time in Figure 5.16. The ratio $\bar{A}_u/\bar{A}_w = \varepsilon_{est}^{-1} \sim \mathcal{O}(1)$ for $t < 7.5$ (simulations were run only up to t=7.5). A local maximum occurs as the vortices achieve maximum intensity. The gain of w after the vortex disappearance causes A_u/A_w to fall. The basic requirement in lubrication theory is $h/L = \varepsilon \ll 1$, a requirement that is not achieved ($\varepsilon_{est} \sim 0.25 - 0.4$) early during the development when the fully nonlinear flow equations are considered. Therefore the applicability of lubrication theory to evaluate spreading rates in real time simulations is questionable. However the use of evolution equations to estimate limiting case $t \rightarrow \infty$ is acceptable since the general trend of $\bar{A}_u/\bar{A}_w$ seems to approach large values at long but finite time (not shown in Figure 5.16).

$\varepsilon \sim \varepsilon_{est} = 0.2$	
Parameter	Value
Re	1.0
Ca	1.0
$\mathcal{M}a$	−0.20
$\mathcal{P}e_s$	500.0
St_n	n/a

Table 5.4: Parameter values for lubrication theory model simulations. The values represent a weak Marangoni forces with strong Péclet numbers. (n/a: not applicable).

In next section, a qualitative and quantitative comparison between the nonlinear and lubrication theory models has been carried out. The estimates made in this section have been used to find the compatible parameter space. The two evolution equation we derived in chapter 3 solved numerically using MOL and matched with nonlinear model results.

5.4.3 Comparison of fully nonlinear system with lubrication theory approximated solutions

In the previous section, using fully nonlinear simulations, we showed that the nonlinearity coefficient ε is not small, as is assumed in lubrication theory. This implies that the geometrical requirement $d/L \ll 1$ does not hold for the bulk flow, a major discrepancy in using lubrication theory. However to match the two models, we use estimated ε_{est} in place of ε of lubrication theory in order to extract compatible parameter values. The estimated nonlinearity coefficient $\varepsilon_{est} = 0.2$. As we can clearly see from table 5.1, Marangoni number and the Péclet number are the only two we are concerned with. Table 5.4 shows the compatible parameter values evaluated from the nonlinear model parameter values given in table 5.3.

The evolution equations (4.7) and (4.8) were used with $P_x \rightarrow 0$, a limit at which the background flow effects diminish. At this limit, the equations takes the general form for surfactant spreading [52]. The reduced equations become:

$$h_t - \frac{\mathcal{M}a}{2}(\Gamma_x h^2)_x = 0 \tag{5.16}$$

$$\Gamma_t - \mathcal{M}a[\Gamma(\Gamma_x h)]_x - \frac{1}{\mathcal{P}e_s}(\Gamma_{xx}) = 0 \tag{5.17}$$

The initial condition for concentration is selected to match the initial condition of the nonlinear model simulations (the step change as in Figure 5.5). The initial conditions are:

$$\Gamma(x,0) = \frac{\Gamma_I}{2}\Big(Tanh\Big[\frac{(x+x_0)}{\Delta l}\Big] - Tanh\Big[\frac{(x-x_0)}{\Delta l}\Big]\Big) \tag{5.18}$$

$$h(x,0) = 1.0 \tag{5.19}$$

By selecting Δl we can achieve a matching initial concentration profile. The boundary conditions used were:

$$\Gamma(-\infty,t) = \Gamma(+\infty,t) = 0 \tag{5.20}$$

$$h(-\infty,t) = h(+\infty,t) = 1 \tag{5.21}$$

The system of equations (5.16)–(5.20) were solved numerically using the method of lines. We do not discuss the results in detail since the case was studied by many and interested readers are referred to [33, 52]. The results presented in Figure 5.17 closely match previous studies [33, 52]. In Figure 5.17(a), spatio–temporal evolution of the surface is mapped. The stress imbalance results in formation of the advection wave front. The concentration evolution is presented in Figure 5.17(b). Since $\mathcal{P}e_s$ is large, advection dominates over diffusion. Therefore, the contact line moves with the wave front. The arrows show the direction of evolution with increasing time. The time mentioned in the figure caption is the equivalent of the nonlinear model evaluated using $t_{LT} = \varepsilon t_{NL}$ where the subscripts LT and NL represents lubrication model and nonlinear model respectively. Within this study we use the nonlinear model time scale.

We compare the evolution of both systems by plotting surface loading, surface profile and shear stress at the deformable surface. To make the comparison easier we plot features of the two system on the same plot. Figures 5.18 through 5.21 shows the evolution of each of those characteristics at different times starting from $t = 0.01$. Of Figures 5.18–5.21, (a) shows the surface loading; (b) maps the film height and (c) presents the surface shear stress. The solid line represent the lubrication theory model solution and the dotted line marks the nonlinear model solution. It is important to mention that throughout the period ε_{est} changes its value.

It can be seen that there is a significant difference between surface height evolution between the two models. The surface profiles are similar in geometry only at initial moments as shown in Figure 5.18(b). However the nonlinear model registers much smaller surface elevation than the lubrication model (In Figure 5.18(b) the nonlinear model surface heights are marked on rhs axis). The capillary ridge that forms is smooth and spreads over a larger area in the case of a nonlinear model. In contrast, the lubrication theory model produces a sharp shock front. The difference is attributed to the flow within the bulk. We previously discussed the vortex that forms beneath the free surface due to shock in surface stresses that grows during the initial moments recirculating the substrate within the bulk rather than pumping into the shock front. The capillary ridge, in the case of nonlinear model grows continuously within the period shown in Figures 5.18 – 5.21.

Despite the differences in surface height evolution, the concentration spreading rates are closely matched. The contact lines in both cases moves outward with almost same speed (a detailed evaluation is given in Figure 5.24). The slight difference between the two concentration profiles (represented by solid and dotted lines) were the relics of the differences at the initial conditions. The nonlinear model initial

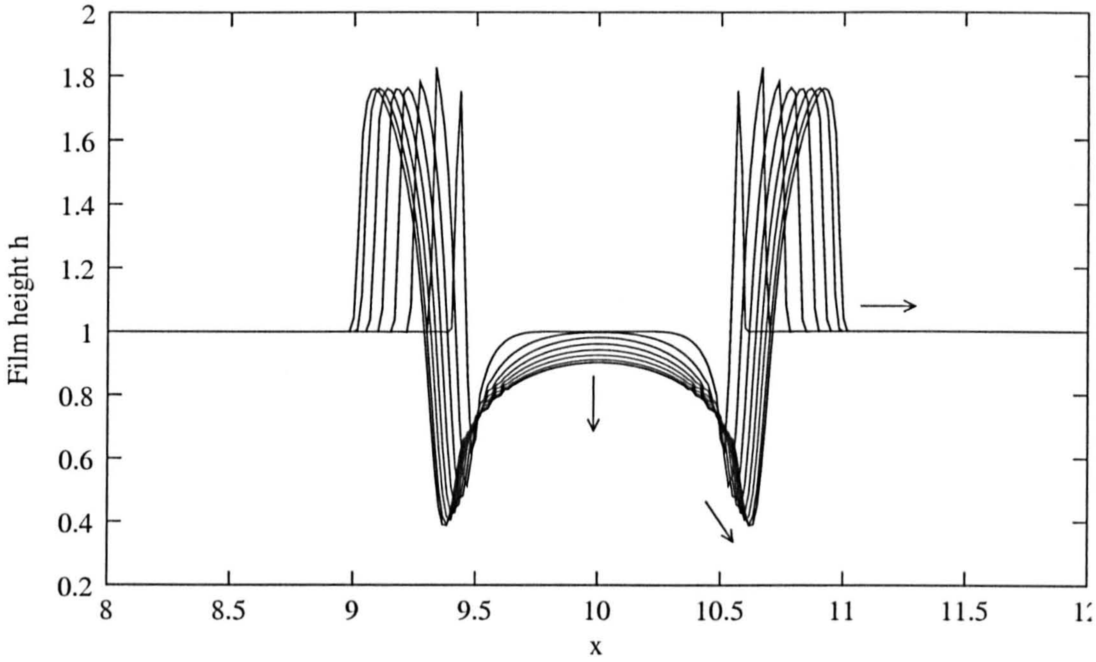

(a)

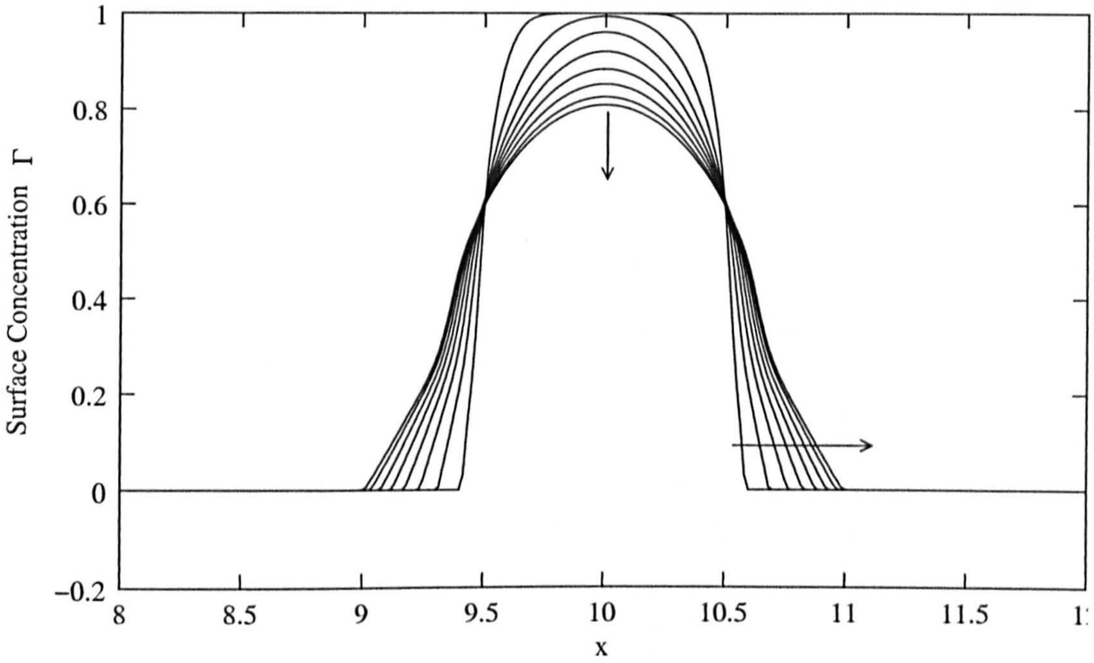

(b)

Figure 5.17: Spreading of a surfactant strip. Simulations on lubrication theory model using parameters compatible to fully nonlinear model. (a) Film height evolution; (b) surface concentration evolution at $t = 0.1 - 2.5$ in $\Delta t = 0.4$ steps. The arrows mark the direction of evolution in increasing time. Parameter values were given in Table 5.4.

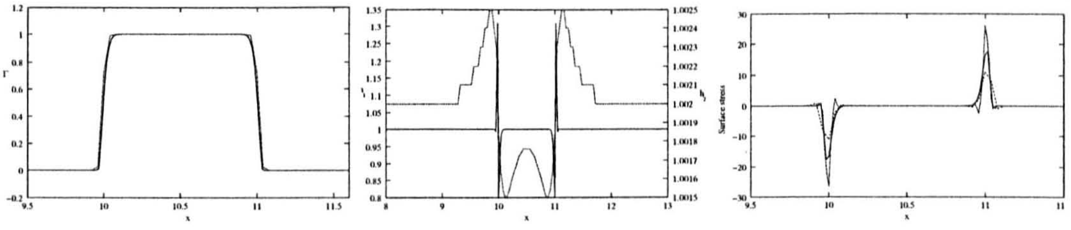

(a) (b) (c)

Figure 5.18: t=0.01

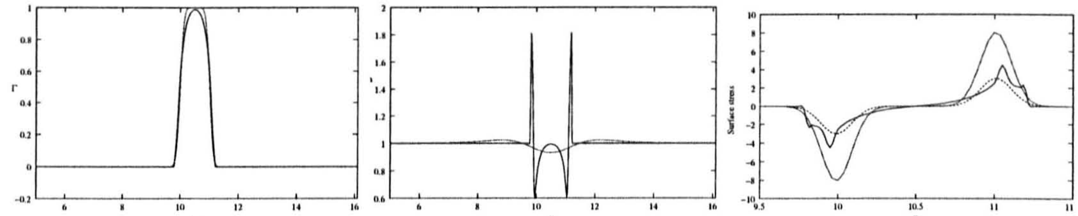

(a) (b) (c)

Figure 5.19: t=0.5

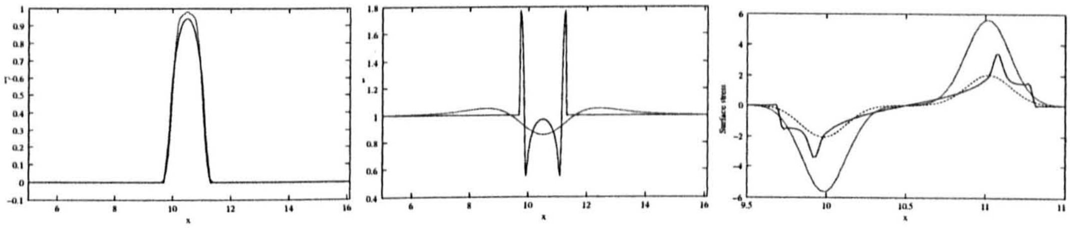

(a) (b) (c)

Figure 5.20: t=1.0

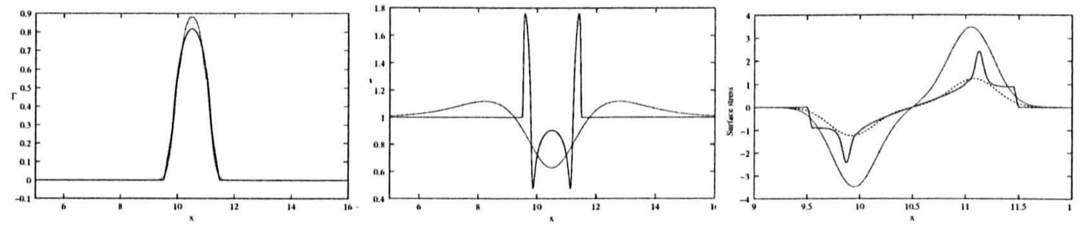

(a) (b) (c)

Figure 5.21: t=2.5

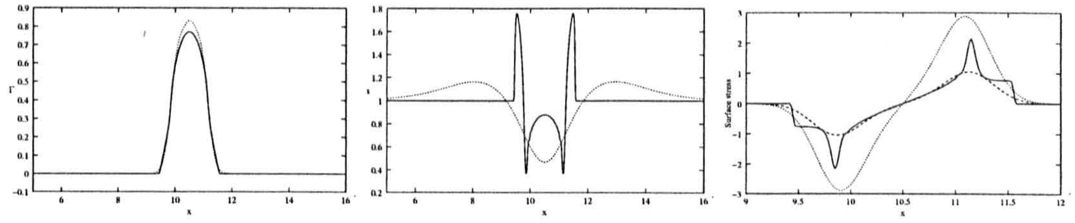

(a) (b) (c)

Figure 5.22: t=3.5

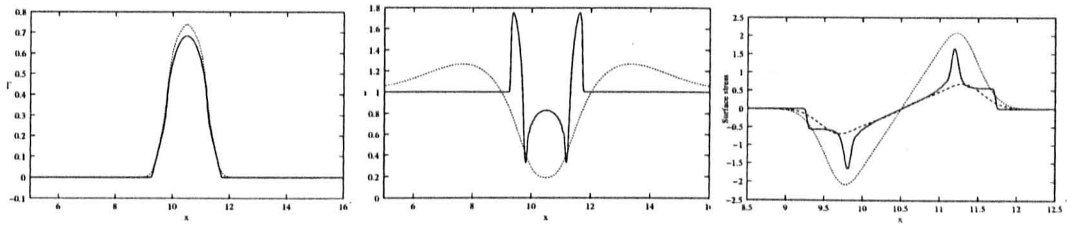

(a) (b) (c)

Figure 5.23: t=6.0 Comparison of spatio temporal evolution of Fully nonlinear model with lubrication theory model. (a) the concentration distribution profile, (b) film heights and (c) surface shear stress. The solid line represents the lubrication model and the dotted line represents the nonlinear model. In (c) the dashed line marks the shear stress (Γ_x) computed using the concentration distribution of nonlinear model.

condition has 3.2% more mass than the lubrication model. Surface stress of both models follows the same form though the peak values were off by a considerable margin. The nonlinear model evaluates the peak stress (dotted line) about 40% higher than the lubrication model (solid line). Surface shear stress in lubrication model was evaluated using $\mathcal{M}a\Gamma_x$ while the stress tensor was evaluated using the velocity components at the surface in the nonlinear model. The existence of nonzero u and v at the surface in the second case might be a cause for larger values. We re-estimated the surface shear stress for nonlinear model by evaluating Γ_x. It is shown in Figures 5.18–5.23 (c) by a dashed line. The evaluated stress for nonlinear model, in general, has the same order of magnitude except at points where sharp changes occur in lubrication model. The depression in the nonlinear model, as we already mentioned, lacks the spike like features at maxmimum stress points. In the LT model, the penetration of the sharp edge depressions marks the thinnest points of the substrate. At initial stages the depression of surface in LT model is fast. As the surfactant gradient falls, the penetration speed drops. However, the nonlinear model forms a thinner area below the surfactant strip. The surface deformation does not resembles a sharp front as in LT model. Instead, it spreads out smoothly in a wider area. The ridge height is smaller than the LT model but grows during the period of observation.

To investigate further the similarities and differences, we use the wave and concentration front movements. Gaver and Grotberg [34] and Starov [99] used front tracking methods to study the spreading rates experimentally using talcum powder. In this numerical study we use a similar strategy to compare the two methods. In each case two fronts are to be traced: (1) the wave front or the convection front and (2) the strip width. The first one is simply tracing the peak position in x direction. Using the symmetry, we measured the peak to peak distance and halved it to get the distance travelled. The strip width taken to be the length between the points where concentration fall below 2% of initial value. To find the exact points we used

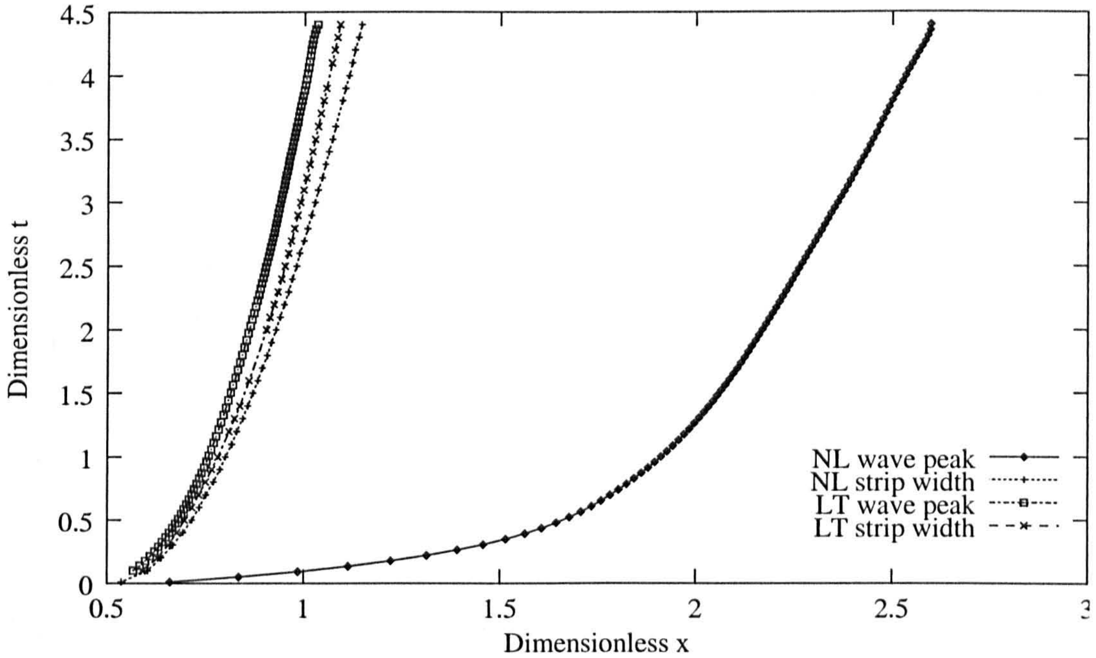

Figure 5.24: Convective and surfactant front positions against time for spreading of a surfactant stripe modelled using fully nonlinear simulations and lubrication theory. The concentration fronts were closely matched. The peak position predictions were considerably different. The dimensionless time is the scale used in fully nonlinear model.

Levenberg–Marquardt nonlinear data fitting technique [82] with a hyperbolic tangent function of the form $a\text{Tanh}(bx - c)$ to interpolate between data points [1]. Half width at any given moment is considered as the distant of spreading. Figure 5.24 shows the comparison of convective and surfactant front positions for both cases. Gaver and Grotberg [34] measured the peak position and the surfactant spreading for a droplet. Although the results are remotely comparable, one can expect the general behaviour to be the same. In their experiments, the convective front extended well beyond the surfactant drop, an observation our nonlinear simulations closely matched. The motion of both the surfactant and convection fronts slows down with increasing time. The lubrication model shows that the peak position and the surfactant front moves close to each other. The peak does not extend far into the

---

[1] The GNUPLOT package offers Levenberg–Marquardt fit as an option. It uses the data produced by the simulations to evaluate the coefficients of the fitting function specified

substrate as in the case of nonlinear model (refer to Figure 5.24). The surfactant front moving with the convection front at same rate is customary for lubrication theory models when the Péclet number is large and gravity effects are neglected [52]. However in both cases, the surfactant front moves almost the same distances at equivalent periods. Two distinctive surface geometries but approximately same spreading rates poses an interesting case. A possible explanation can be given in the light of the findings of Jensen and Halpern [54]. They showed that at flat film limit (i.e. $h \to 1$) with large $\mathcal{P}e_s$, the surfactant distribution is governed by a single nonlinear diffusion equation

$$\Gamma_t = \mathcal{A}(\Gamma\Gamma_x)_x \tag{5.22}$$

where $\mathcal{A}$ is a constant. Equation (5.22) is independent of local film height h. The constant assumes values depending on the flow regime that prevails within the bulk. For instance a return flow, with zero volume flux (the case studied in [54]) produces $\mathcal{A} = 1/4$. In essence, with $h = \mathcal{O}(1)$, one can conclude that the surface deformation only has a modest effect on rate of spreading of a monolayer. Since we used compatible scaling factors in both simulations, though the surface deformations differ, the spreading rate roughly follows (5.22) giving approximately the same results. This is supported by the fact that the both models generate u velocities of same order (cf. Figure 5.25). However, the retention of nonlinear terms effectively adjusts the flow in the bulk, giving rise to the geometric differences of the coherent structures that generates by the surface stresses.

Figure 5.25 shows the time variation of the field averaged u velocities for the two models. The initial values are far apart but within few instances the two values reach the same order of magnitude. The lubrication model shows a rapid decay while the nonlinear model tend to increase slowly. At longer periods both models shows that the velocity components asymptotically reach zero. However, disappointingly the field average of w velocity of lubrication model at initial time steps is too large. The vertical velocity component for LT model w was calculated employing an expression

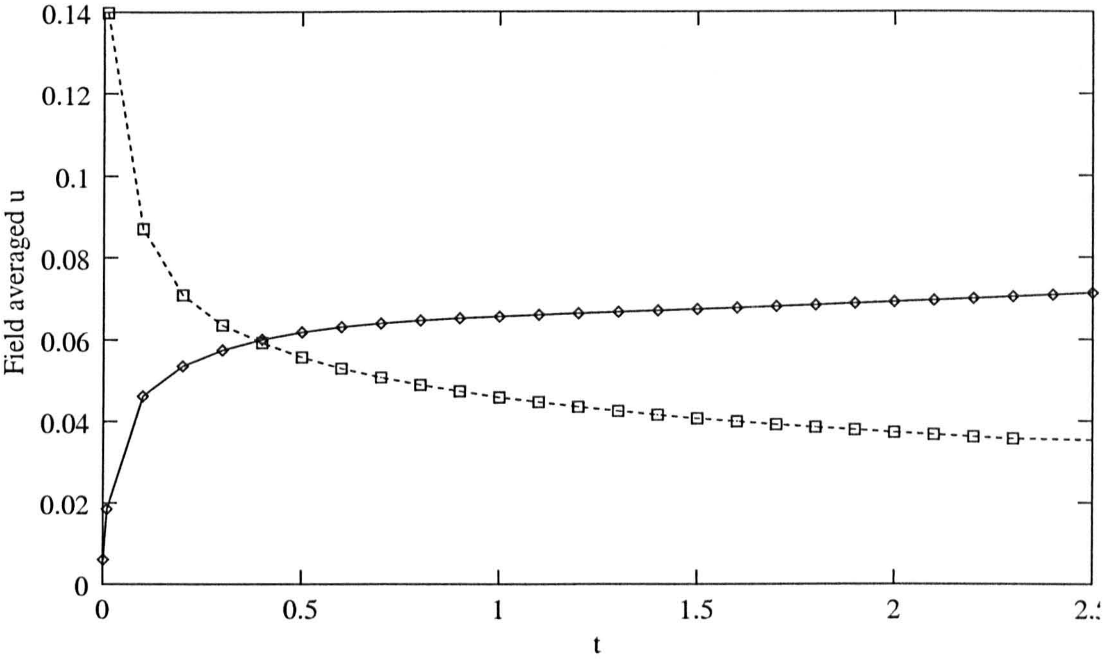

Figure 5.25: Comparison of field averaged u velocities arise in the two models. The dashed line represents the lubrication theory model and the solid line marks the nonlinear model.

derived using the expression for u velocity and the continuity equation. This gives us $w(x, z) = \frac{\mathcal{M}a}{2}\Gamma_{xx}z^2$. Hence w becomes large as Γ_{xx} assumes large values at the neighbourhood of the moving contact line. We evaluated the field average w values for simulations carried out by Jensen and Grotberg [53] and also for Gaver and Grotberg [33] by simulating their model using MOL code to find out that w always results in large values, higher than u by $\mathcal{O}(< 10)$, for a considerable period before falling below u.

The initial linearization of flow equations via lubrication theory remove the inertial terms retaining only viscous diffusion terms that balance the shear force induced by the surfactant gradient. As a result, the stream functions for the lubrication theory model shown in Figure 5.26 do not show the vortices as in nonlinear model (see Figures 5.6–5.8).

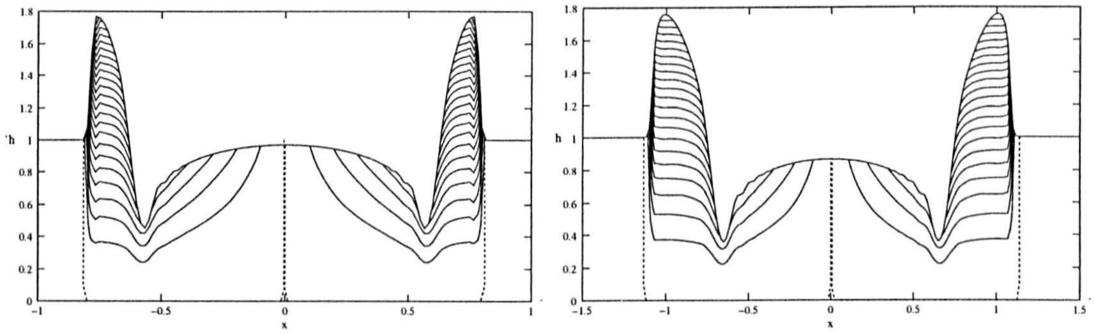

(a) (b)

Figure 5.26: Stream functions for the spreading of a surfactant strip modelled using lubrication theory. No vortex formation occur since the inertial terms were eliminated. Parameters are as given in Table 5.4. The dashed line marks the zero stream line.

5.5 Discussion and Conclusions

The comparison between fully nonlinear model and the classical lubrication theory model shows that the inclusion of the inertial term actually adjusts the flow field. At the same time it shows that the nonlinearity parameter is not small as it is expected to be. However the spreading rates remain close for both cases since the u velocity induced under the tangential shear remain same order of magnitude except for the initial instance. The moving concentration front, as discussed before, is traced by following the point x_c that satisfies $(\Gamma_I - \Gamma(x_c)) <= 0.98\Gamma_I$. The log values of position x_c against time is plotted in Figure 5.27. The position increasingly become linear with gradient 1/3 (the dotted line in Figure 5.27). Jensen and Grotberg [52] quoted that Espinosa [26] had shown the spreading rate $x_c \sim t^{1/3}$ for a planar strip. We can claim the same from the simulations on the fully nonlinear system. However, if one is interested in spreading rates, then the lubrication theory approximates the actual situation with a good agreement. The hydrodynamics of the system is not well explained by the lubrication theory model. The nonlinear model fits in to fill this void. But the simulation process is computationally costly.

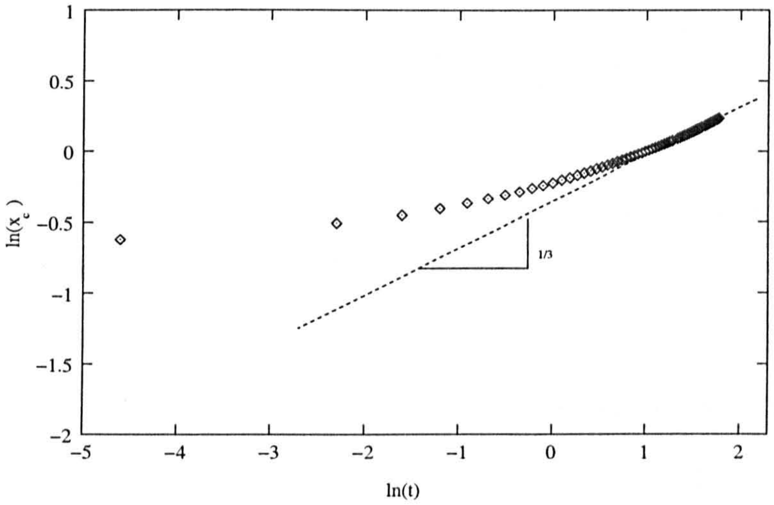

Figure 5.27: Surfactant stripe width spreading rate. An insoluble surfactant stripe with constant mass spreads like $x \sim t^{1/3}$. The position of the edge x_c that engulfs 98% of the initial concentration is traced with time. The spreading rate soon follows the trend line with 1/3 gradient.

Comparison between lubrication theory and nonlinear model using compatible parameters derived by using $\varepsilon = \varepsilon_{est}|_{max}$ seemed to hold. Any independent value for $\varepsilon \ll 1$, for example 0.01, surfactant spreads much shorter distances. However the evaluated ε_{est} vary over the time.

The nonlinear model identifies that there is a vortex formation beneath the surfactant layer with diminishing strength. The vortex disappears as the substrate thickness decreases. The vortex intensity and its period of existence depends on the parameter values. Because of computational time limitations we were unable to examine the full parameter space.

5.6 Summary

The aims of this chapter is to compare the results of two models that simulate the spreading of a surfactant strip with a finite width on a stationary substrate. Two models are distinctively different. One model uses the lubrication approximations to derive two equations that describe the surface height and surfactant concentration evolution. This is the classical approach to thin film flows and uses drastic simplifications on flow equations. In the second model, the fully nonlinear equations that describe flow as well as the surface concentration solved numerically using a finite element scheme which provide a technique to trace the deforming boundary.

The fully nonlinear simulations were used to extract the nonlinearity constant ε. We found that the value of ε, generally considered very small, is quite large. Remarkably the spreading rates of the both models stay close. But the substrate flow is vastly different.

The effects of flow parameters on the evolution of surface instability is examined in the next chapter using the fully nonlinear model.

Chapter 6

Parameter sensitivity of the nonlinear model

6.1 Introduction

In the previous chapter, we compared the fully nonlinear model with the classical lubrication theory model. We observed that the flow and shock evolution of the two systems differ though the surfactant spreading rates match closely. A detailed comparison and conclusions which are drawn on both models is left for chapter 7. The nonlinear model solves the flow equations (5.2), (5.3) in the bulk and species evolution equation (5.8) on the free surface. It includes the fully nonlinear terms in boundary conditions which in most studies are approximated. Furthermore, it includes gravity effects on the flow. Gravity always acts as a surface flattening force, retarding the surface waves. Here we examine the influence of nondimensional parameters on the spreading, emphasising the differences it generates compared to the lubrication theory model. In this chapter we discuss the behaviour of the nonlinear model with respect to spreading of a surfactant strip on a stationary substrate and a surfactant front on a flowing film as in chapter 4.

6.2 Parameter sensitivity on spreading of a strip

The basic parameters that arise in the nonlinear model are $Re_n, \mathcal{M}a, Ca_n, St_n$ and $\mathcal{P}e_n$. The width of the strip is a geometrical parameter that adds an extra degree of freedom in parameter pace. We concentrate on the width of the strip, Reynolds number and Stokes number since they show some alteration to the already known flow patterns. Of these parameters, the Stokes number is the one that does not arise in the lubrication theory model. Stokes number is defined as $St = \frac{\varrho g d^2}{\mu U_s}$. Since the surface tension gradient is the only mechanism that generates the flow, one can scale the reference velocity as $\mu U_s \sim \sigma_0$. By using this similarity with the Stokes number definition, one can deduce a Bond number $Bo = \frac{\varrho g d^2}{\sigma}$ [33]. This can be used as a handle to examine the effect of gravity on the surface evolution. In experimental investigations, gravity plays a role as film thicknesses are around 1mm [34, 99]. However it is a common practise to neglect, gravity effects assuming films are very thin.

The grid structure and the procedures described in chapter 5 §5.2 are followed in all simulations presented in this section except for the grid stretching. The finite elements were closely packed in the neighbourhood of the contact lines between bulk and the surfactant. The grid diffusivities D_ξ and D_η (refer to chapter 3 §3.5.2) were selected so that the concentration of nodes remains constant as the grid deforms. Furthermore we kept the Péclet number constant throughout at 100.

6.2.1 The volume of the strip

The width of the surfactant strip is an important parameter. It simply implies the volume of the droplet. On the other hand the length scale $\mathcal{L}$ used in the LT model is attributed to this geometric factor. The effect of the volume (or the layer width) on the spreading process and subsequent flow within the bulk is examined

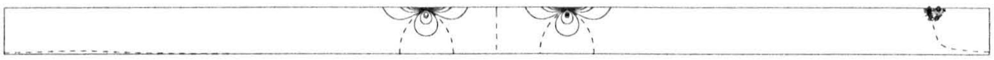

(a) t=0.01

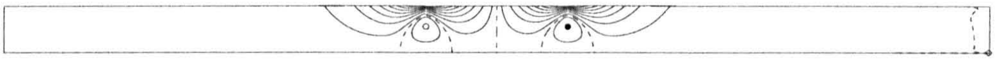

(b) t=0.1

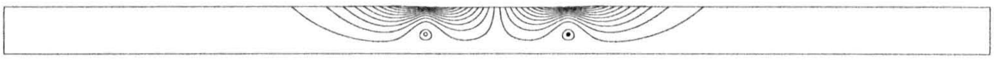

(c) t=0.2

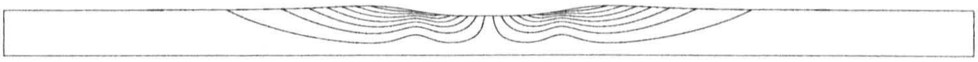

(d) t=1.0

Figure 6.1: Spatio–temporal evolution of a surfactant drop with larger volume. The Vortex that generate due to shear stress decays rapidly and disappear within a short time.

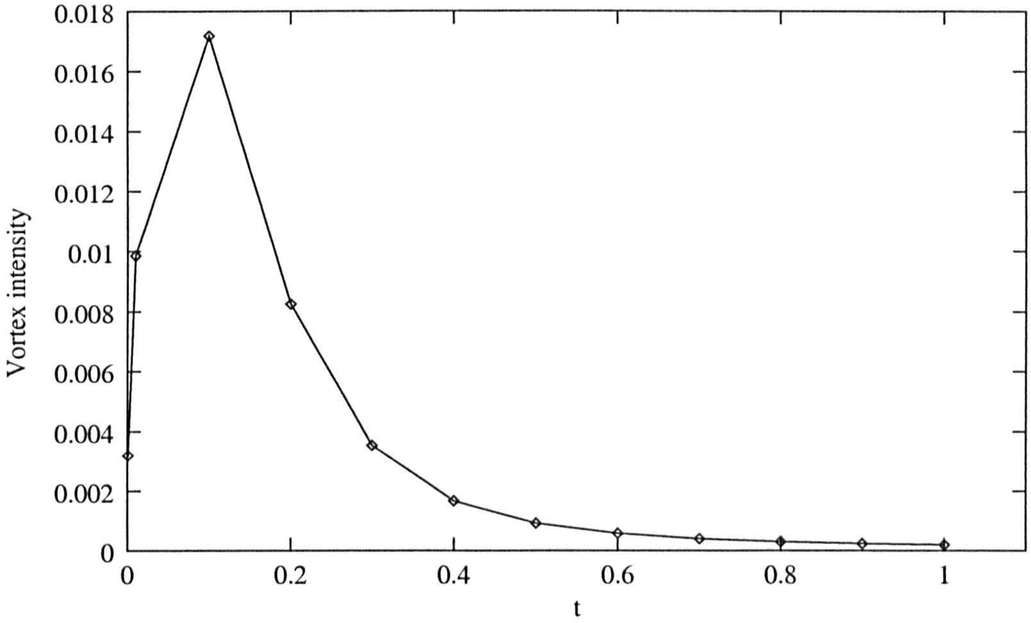

Figure 6.2: The time evolution of the vortex intensity for a surfactant strip of initial with three times the undisturbed substrate depth. The intensity decays faster. The flow parameters are as per table 5.3.

using a surfactant strip three times wider than the depth of the substrate. All other parameter values are kept constant as in table 5.3.

The Figure 6.1 shows the evolution of the flow induced by the surface tension gradient. It shows that the vortices that occur are smaller in size. Interestingly, the vortex has an intensity half that of the case studied in chapter 5. The Figure 6.2 that maps the time evolution of the vortex intensity shows that it lives for a shorter period too. The quantity of the substrate in motion is greater when the width of the strip is larger. The flow initiated by the surfactant gradient sets up the vortices. Both the vortices and the surface tension gradients induce the liquid mass underneath the strip to flow outwards. As a result of the larger volume in motion, the lateral flow regime above the vortex penetrates into the bulk rapidly, limiting the flow within the vortex. Hence the vortex is small in size and short lived.

The volume of substrate so displaced forms bigger capillary ridges. Figure 6.3 shows the surface evolution with time. The excessive surface depressions near contact lines

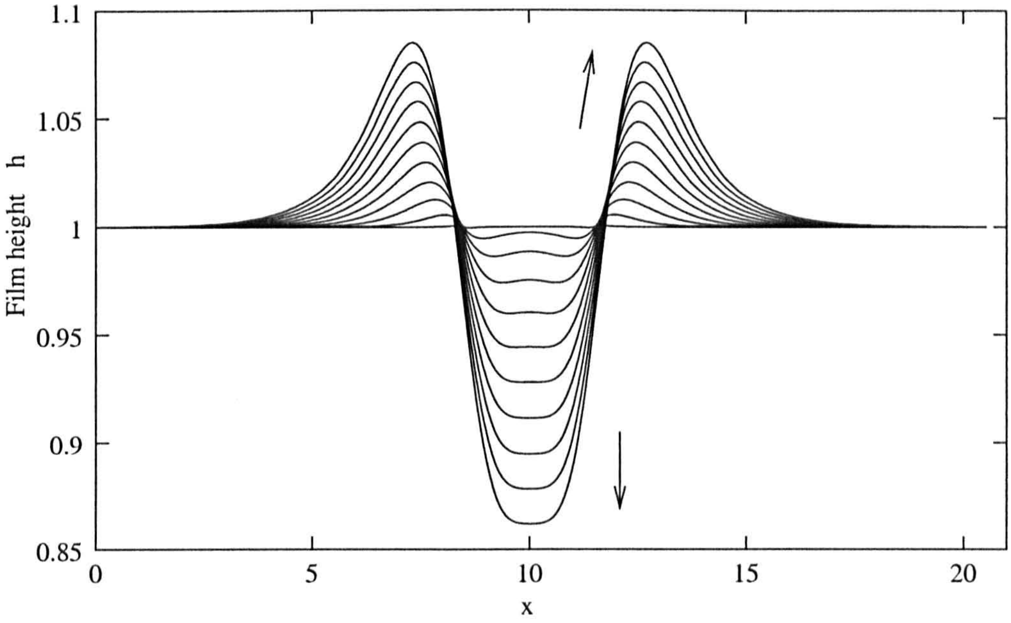

Figure 6.3: Surface evolution for a strip $3d$ wide from t=0 to 1 at $\Delta t = 0.1$ steps. Parameters are as per table 5.3. The arrows shows the direction of evolution.

disappear as time increases. The Marangoni advection at surface level is the main transport mechanism of spreading.

6.2.2 The effect of *Re*

In this section, we observe the effect of Reynolds number over the spreading of a strip. Reynolds number is a relative measure of inertial forces to viscous forces. If the geometry is kept unchanged we can assume either that the physical properties of the fluid have changed or the induced velocity has changed. We set $Re = 5$ and employed the configuration used in chapter 5 with parameters in table 5.3. Again the simulation requires very small step sizes of $\mathcal{O}(10^{-3})$.

The evolution follows the pattern described in chapter 5 but at a faster rate. The events occur approximately four times faster than for the case with $Re = 1$. Figure 6.4 shows the spatio temporal evolution at $Re = 5$. The initial vortex formation develops to fullest intensity and then decays. The lateral flow becomes dominant

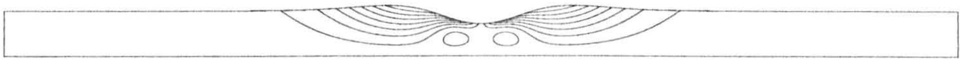

(a) t=0.5

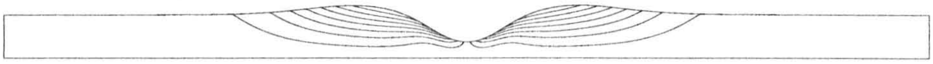

(b) t=1.0

(c) t=1.5

(d) t=2.5

(e) t=3.5

Figure 6.4: Spatio–temporal evolution of a surfactant strip with $Re = 5$. Film thickness beneath the strip thins very rapidly.

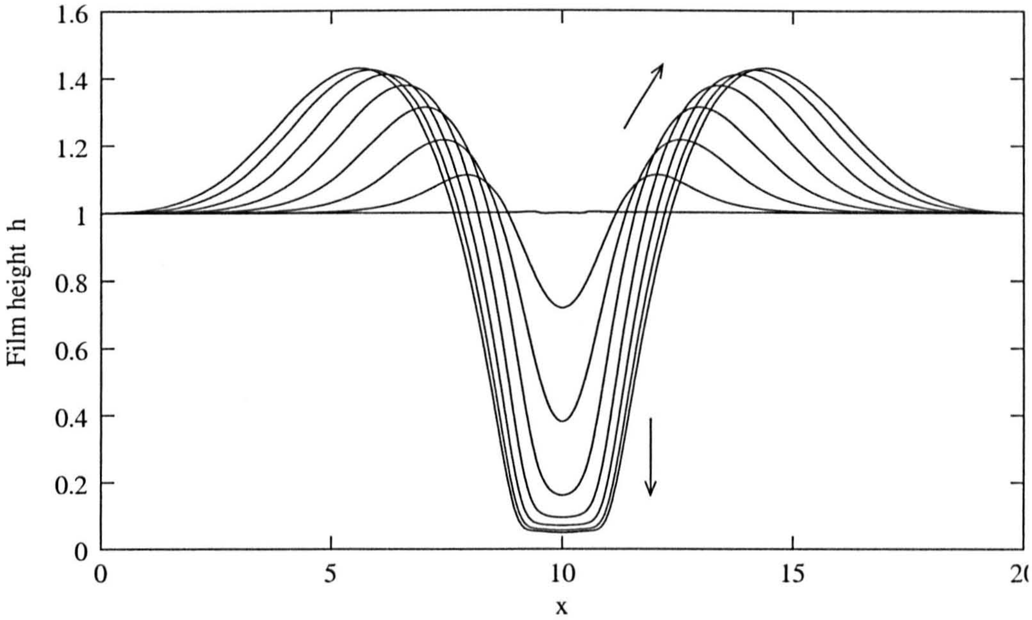

Figure 6.5: Surface evolution profiles for Re=5 from t=0 to 3.5 in $\Delta t = 0.5$ steps. Arrows mark the direction of evolution with increasing time. As time increases the thinning rate slows down and starts to expand sideways. The flow parameters are as per 5.3.

and engulfs the total flow field around t=1. In the nonlinear model, the depression beneath the surfactant drop deepens at a faster rate than the lubrication theory model. However the higher the *Re* in the nonlinear model, the faster will be the surface depression process. Figure 6.4 (c), (d) and (e) show the thinning of the film. At $t = 3.5$, the thickness of the depression $\Delta h = 0.0497$; *i.e.* it has fallen to 5% of the initial thickness. As the film become very thin, it starts to expand sideways, generating more thinned area. To observe this behaviour, we plotted the surface profiles against time. Figure 6.5 shows these profiles. It is evident that the initial tendency is to deepen the depression. As time increases, the rate of film thinning slows down. Instead, it starts to expand the thinned area by moving the walls outwards.

The depression thickness Δh for both $Re = 5$ and $Re = 1$ is plotted against time in Figure 6.6. A remarkable change in the thinning rates can be observed for both cases. First Δh decreases rapidly. Once the thickness falls below approximately 10%

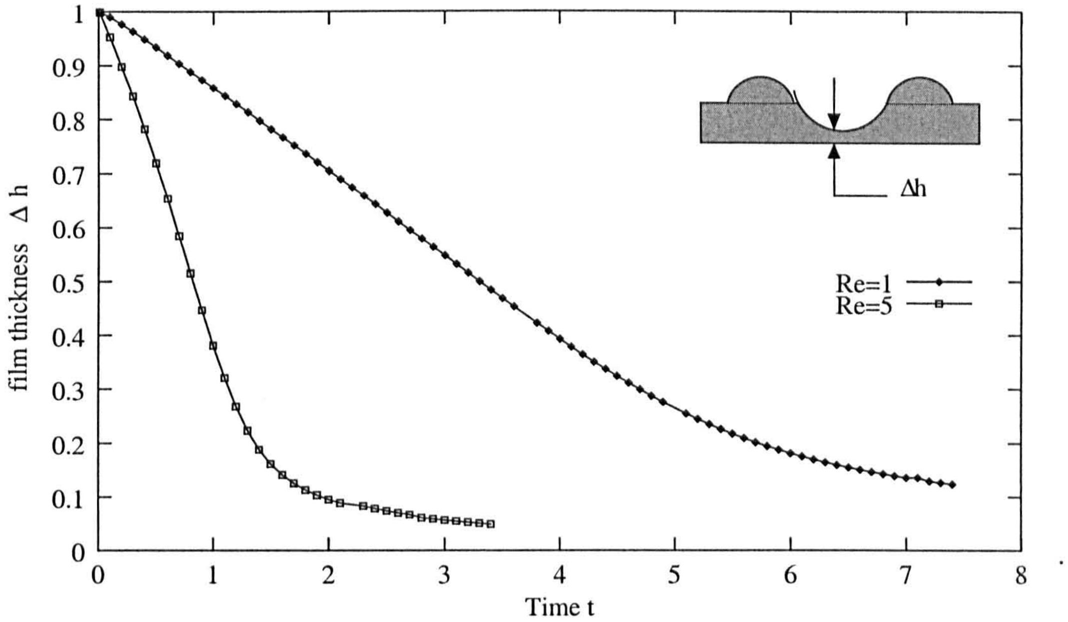

Figure 6.6: The change of film thickness beneath the surfactant layer Δh with time for $Re = 1$ and $Re = 5$. The film thickness decreases rapidly and then slows down dramatically. Regions of two different gradients show that the spreading process has two distinct phases: 1) rapid film thinning and 2) expansion of the thinned region. The other flow parameters are as per table 5.3

of the initial film thickness the rate of change decreases dramatically. Δh continues to decrease. One can envisage that $\Delta h \rightarrow 0$ in finite time. But the FEM fails to treat the situation where $\Delta h \rightarrow 0$ as it does not support topological changes. However the change in thinning rate is not a relic of numerical limitations since $Re = 1$ repeats the same behaviour with a break in the gradients at much larger depression thickness.

The nonlinear model shows that thinning is a very fast process compared to the lubrication theory model. the nonlinear model achieves very small depression thicknesses compared to LT model. In an attempt to resolve the instability leading to film rupture, Halpern and Grotberg [39] included van der Waals forces in to the model which result in thinning the film at edge depressions in the case of the LT model. Warner *et al.* [111] used this extra term to achieve film thicknesses equivalent to what we achieved here in at the absence of such weak forces. The van der

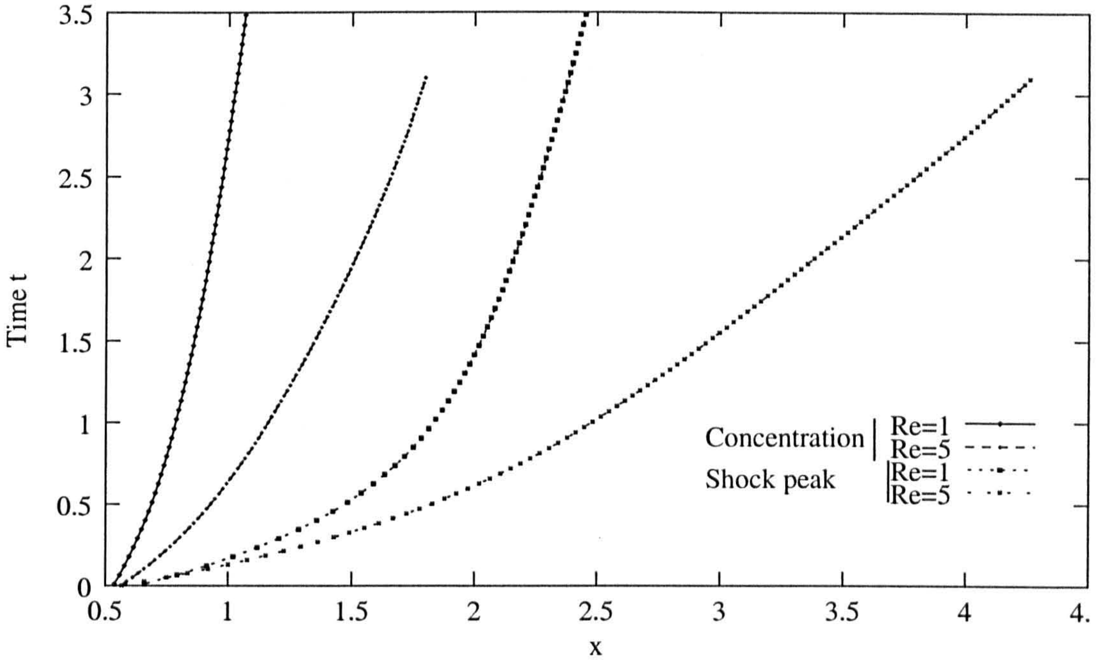

Figure 6.7: Front positions for $Re = 5$ and $Re = 1$ against time. The larger the Re, the faster the spreading rate. The shock peak propagates faster too. Other flow parameters are as per table 5.3.

Waals forces (or the use of disjoining pressure) becomes effective only if the film thickness becomes very small. We think the contribution of the nonlinear terms plays an essential role in film thinning and hence cannot be excluded in attempts to describe the instability.

The sharp change in gradients in the thinning rate suggests that the process takes place in two stages (not only limited to Reynolds number variations but applicable to all cases we have examined here). The first is rapid thinning. Most of the substrate beneath the surfactant layer is displaced during this period. As a result, the capillary ridge (or the shock) grows in amplitude. The second stage is the growth of the thinned area. The amount of substrate displaced from thinned area is very small. Side walls generated by the displacement move outwards. The growth of shock amplitude retards and eventually starts decreasing. In these simulations we considered that stage two is the mature flow displacement situation (time asymptotic) since the changes occur at a very slow rate. This slow evolution persists for

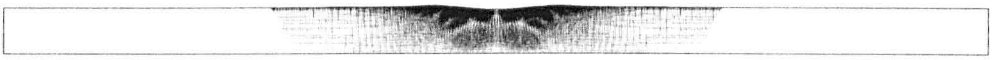

Figure 6.8: The velocity penetration into the bulk at $t = 0.1$ for $Re = 5$. The induced velocity field develops penetrating into bulk, making more substrate to flow outward. In this case, the stream-wise penetration is about $5d$ in either directions from the centreline normal to the rigid horizontal plane.

longer periods than shown the figures.

Reynolds number directly affects the spreading rates. The Figure 6.7 compares the spreading rates for $Re = 5$ and $Re = 1$. Concentration fronts (spatial coordinate points that envelope 98% of the initial surfactant volume) show that the larger Re has higher spreading rate. During the second stage of evolution, the relationship $x \sim t^{1/3}$ holds for both cases, consistent with self similar solutions sought by Jensen and Grotberg [52]. The capillary shock fronts also propagate faster when the Reynolds number is high. However, the shock front movement increasingly becomes linear with time as the speed slows down towards the transition to stage two.

The shear stress induced by the surfactant gradient initially excites substrate near the surfactant strip to flow. In the case of lubrication theory, induced velocity components, $u = \mathcal{M}a\Gamma_x z$ or $w = \mathcal{M}a\Gamma_{xx}z^2$, are directly tied to the concentration gradient. Hence there is no flow beyond the contact line. This result is true only if advection is absent. However, we observe that advection sets in motion liquid substrate well ahead of the contact line. The shaded area in Figure 6.8 shows the velocity field penetration into the bulk at $t = 0.1$ for $Re = 1$. The velocity field occupies $\sim 5d$ stream-wise in each direction at $t = 0.1$. The field grows as time elapses and engulfs the whole computational domain. The velocity field penetrates into the layer depth almost instantly. This contrasts with the findings of the LT theory which heavily depend on the shock front generated due to a sudden discontinuity of the velocity field. Advection smooths out this shock structure.

6.2.3 The effect of gravity: $St \neq 0$

As we discussed in 6.2, the influence of body forces are represented by the Stokes number. Gaver and Grotberg [33], using a strong gravitational force in their LT model, showed the existence of a vortex that eventually engulfs the area that is thinned due to Marangoni flow. The cause is described as the increase in the adverse pressure gradient. Here we use a weak Stokes number, $St = 0.05$. The FEM case settings are as per previous cases with $Re = 1$ and 5. All other flow parameters were as shown in table 5.3.

Figure 6.9 shows the streamlines of spatio–temporal evolution of the Marangoni induced flow. From the very beginning the flow become asymmetric. The body forces oppose the deformation of the surface trying to flatten it. This forces substrate to flow out of the flow regime instead of forming the two capillary ridges. This surface flattening effect enhances the flow development in lateral directions. In previous cases where $St = 0$, the flow develops gradually and slowly in the horizontal direction. But once Stokes number assumes small but finite values the flow regime immediately extends to a wider area, well ahead of the disturbance. The streamlines in Figure 6.9 shows this development.

Upon further investigation we observed that the intensities of the vortices are different. The lhs vortex is stronger than the rhs vortex. Furthermore, the vortex centres become increasingly offset from one another. The weak vortex (marked by a •) moves downward as time elapses. The stronger vortex (marked by ∘) also moves downward, but at a slower pace. The Figure 6.10 shows the vortex intensity (defined as the total volumetric flow within the vortex) of both vortices. The maximum intensity of the left vortex is higher than the vortex intensity of zero Stokes number flow (the vortex intensities are same for $St = 0$). The weaker vortex ceases to alter the flow effectively well before the stronger one disappears.

This symmetry breaking is repeatable and always occurs only if $St \neq 0$. One expla-

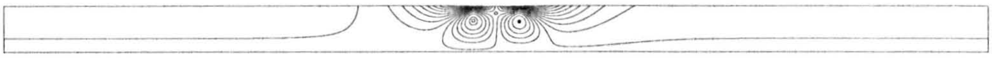

(a) t=0.1

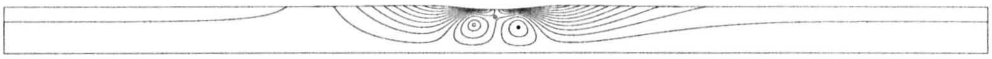

(b) t=0.5

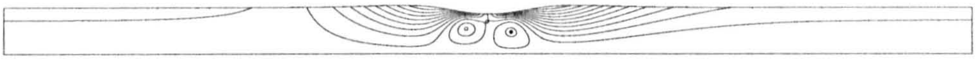

(c) t=1.0

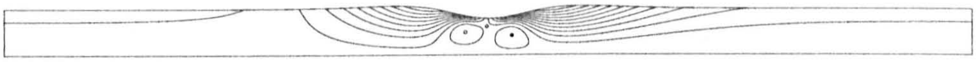

(d) t=1.5

Figure 6.9: Spatio–temporal evolution of a surfactant strip with $St = 0.05$. The vortices forms an asymmetric flow pattern. Left vortex marked by $\circ$ is stronger than the right vortex marked by a $\bullet$. The saddle point is denoted by $\Diamond$. Other flow parameters are as per table 5.3.

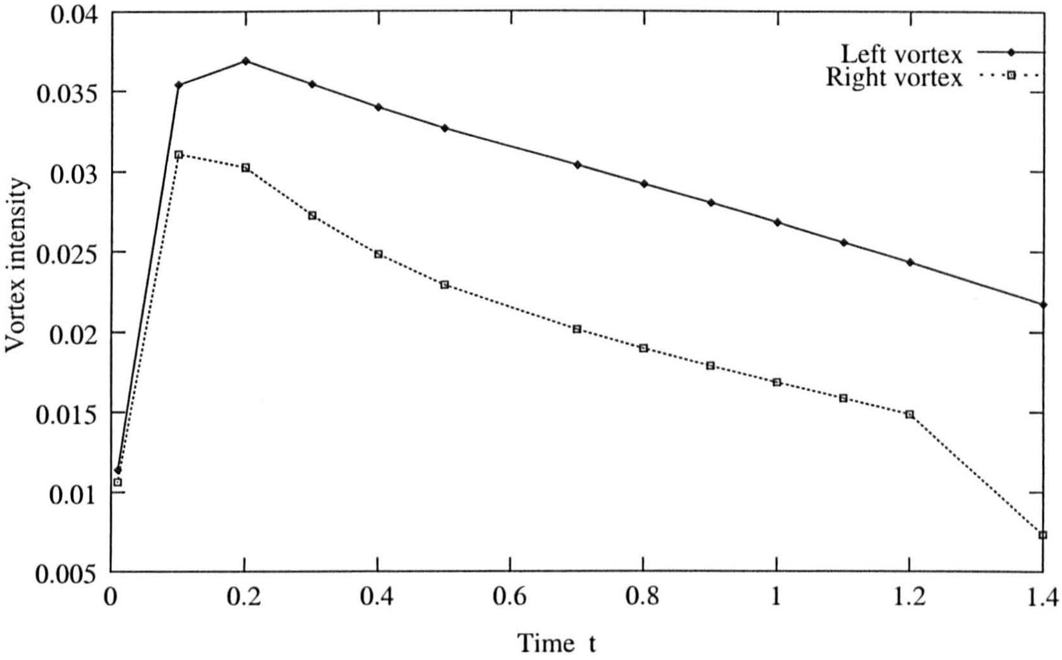

Figure 6.10: Evolution of left and right vortex intensities for the case shown in Figure 6.9. Right vortex is weaker and decay faster.

nation for it is that a minute numerical error is enhanced, supported by the gravity term. To check this we took great care to achieve symmetry of the initial surfactant concentration. Refined grids were used. For the same initial concentration, for $St = 0$, we obtain the symmetric flow patterns presented in previous section. However, the asymmetric flow is inevitable once Stokes number is given a nonzero value. The symmetry breaking is likely to be created as a numerical artifact of the free surface boundary conditions as the coupling to the pressure term is one–sided (first order elements are used for pressure and second order for velocity).

6.2.4 On nonlinearity parameter

As we discussed in §6.2.2, the evolution occurs in two stages; 1) rapid film thinning and 2) slow expansion of thinned region. There may be a third stage where film rupture leads to a very slow fingering instability. The current nonlinear model only captures the first two stages of the flow. Of these two stages, the first shows

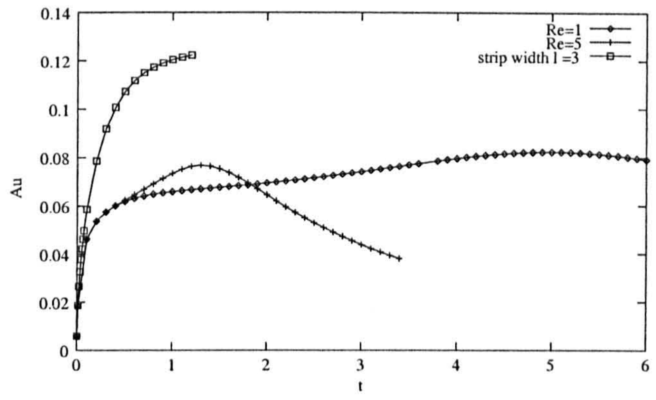

(a) Field averaged u

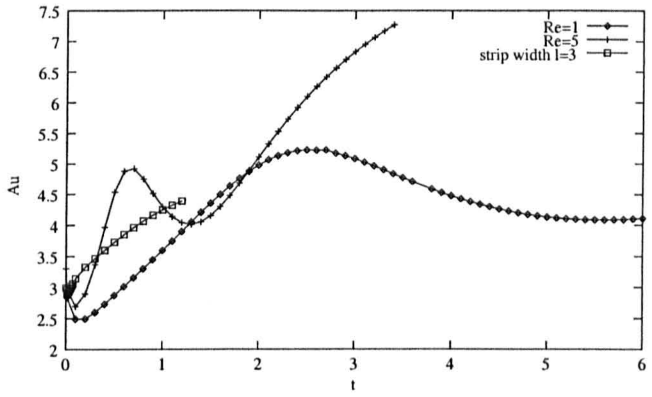

(b) Field averaged v

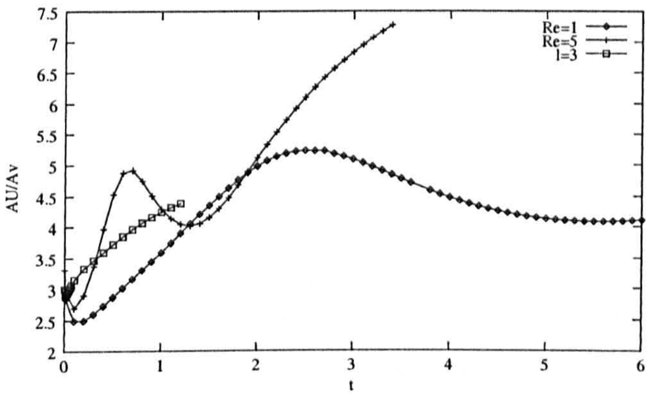

(c) Nonlinearity parameter ε_{est}^{-1}

Figure 6.11: Evolution of A_u, A_v and nonlinearity coefficient ε_{est} in time for various flow parameter values. It remains considerably small for longer period of time even after it reach slow evolution stage for all the cases examined. Most intriguing flow occurs during the first stage of evolution where A_u and A_v are of same order of magnitude.

interesting flow dynamics while second stage is monotonic flow. Earlier in chapter 5 we introduced the estimated nonlinearity coefficient ε_{est} on which the scaling of lubrication theory is based. In that section, we showed that, within the first stage, the nonlinearity coefficient is not *very small* as is generally assumed in lubrication theory. We examine the nonlinearity parameter for different flow parameter values to establish the difference it makes.

The Figure 6.11 shows (a) the field averaged u velocity (b) field averaged v velocity and (c) the ratio of field averages ($A_u/A_v = \varepsilon_{est}^{-1}$) for different cases. Both A_u and A_v, after initial increase, begins to decay when the second stage of the flow evolution is reached. Figure 6.4 (e) and (f) shows that the stream lines increasingly become horizontal. Hence A_v decays faster than A_u. However it takes a longer time for ε_{est} to become very small ($\varepsilon = \varepsilon_{est}$). The rate at which the ε_{est} increases slows down since both field average velocities drops with time. In this sense we face a philosophical question how small the nonlinearity ε would need be in order to neglect the associated physics in lubrication theory. The nonlinear model shows that the nonlinearity coefficient would evolve into a smaller value but would take a substantially long period to do so.

6.3 Fully nonlinear model for a surfactant front on a flowing film

We discussed the effects of a surfactant front on a flowing film in chapter 4. There we used the lubrication theory evolution equations. The evolution equations up to $\mathcal{O}(1)$ include a single term that connects the bulk effects with the surface evolution. Here we implement the fully nonlinear simulations and investigate the differences/similarities between the two models.

The grid is similar to the one used in the previous section. The background flow is

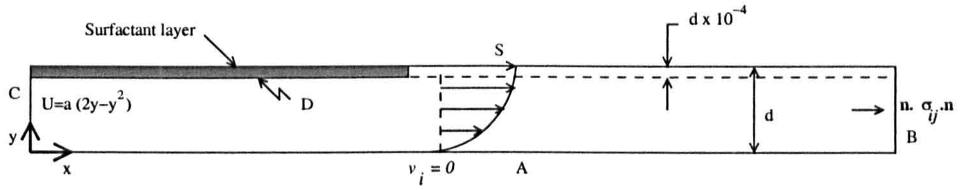

Figure 6.12: Sketch of domain arrangement for a surfactant front flowing in with the substrate. Out flow boundary condition allows the substrate to leave the domain. Dirichlet boundary condition at the inlet sets the inflow velocity.

imposed by setting the inlet flow velocity. In chapter 3 we showed that the mass flow of the film is given by $\mathcal{Q} = \int u(y)$ (equation (3.22)). The nondimensional flow rate is given by $\mathcal{Q} = \frac{1}{3}P_xRe$. We used the same flow rate to evaluate the inlet parabolic flow profile $\bar{U}(y)$ (dimensional analysis in chapter 5 shows that P_xRe sets the pressure gradient across the flow field). The background flow at steady state does not exert any stresses on the free surface. Hence the requirement $\frac{d\bar{U}(y)}{dy} = 0$ at $y = 1$. It also requires $\mathbf{v} = 0$ on the rigid plane at $y = 0$. Therefore $\bar{U}(y) = a(2y - y^2)$. the value of a is determined by the volumetric flow rate, matching it with LT model. All nondimensional parameters are evaluated using $\bar{U}(1)$ at steady state. The surfactant layer is superimposed on the steady flow at time $t = 0$ and transient solutions are obtained in $\Delta t = 0.1$ periods by an adaptive time stepping algorithm. Again the methodology described in chapter 5 §5.2 is used in implementing the surfactant layer. To keep the divergence of the velocity field very small (near zero) time steps have to be very small. The outlet flow is evaluated as an integral part of the solution by applying out flow boundary conditions (i.e. flow is normal to the boundary). The Figure 6.12 shows the conditions as at $t = 0$.

The background flow demands non-zero gravity terms at leading order since a horizontal pressure gradient alone deforms the surface in order to balance the forces. Hence we evaluated the $St = 2.0$ for flat surface flow at steady state without surface tension gradients. Figure 6.13 shows this steady state solution. It is used as the base state upon which the surfactant front is imposed at $t = 0$. For this test case we used $\mathcal{M}a = 1$ (i.e. 0.2 in the lubrication model). Our intent is to show that the fully nonlinear model closely tracts with the LT model. A dense element packing is needed in the neighbourhoods of the contact lines in order to get the necessary convergence. This dramatically increased the CPU time. It required about 13.5 CPU hours to take a 0.1 time step. This factor alone limited this trial to evolve up to $t = 2.5$.

The case we implemented has a surfactant front moving along with the flow (schematically shown in Figure 4.1(a) in chapter 4). The surface deformation however, does not exactly match the LT model, since the strong gravity tends to flatten the free surface. Figure 6.14(a) and (b) shows the surface and concentration evolution with time respectively. The surface deforms, giving a ridge and a trough, as in LT theory. However there is no near vertical shock front present except for a very small period at the beginning. Marangoni advection enhances the spreading at the contact line. However it is important to mention that the capillary ridge is not fully coated with the surfactant as in LT simulations. This is true for the stationary case as well. We discuss this point further in chapter 7.

Diffusion has limited effect as we employ large $\mathcal{P}e_n$. The initial spreading shown in Figure 6.14 is mainly due to Marangoni advection at the contact line. As time grows, one can see the spreading process slowing down. This marks the retardation of the initial surface stress. However, to observe wave breaking, the simulation has to run for longer periods using lengthy domains. Extension of the domain increases the CPU time dramatically. Hence the current simulations were run only up to $t = 2.5$ until the general form of evolution can be identified.

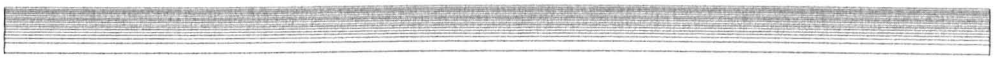

Figure 6.13: Fully developed steady state flow of a thin film. This solution is used as the base state on which the surface tension gradient is imposed.

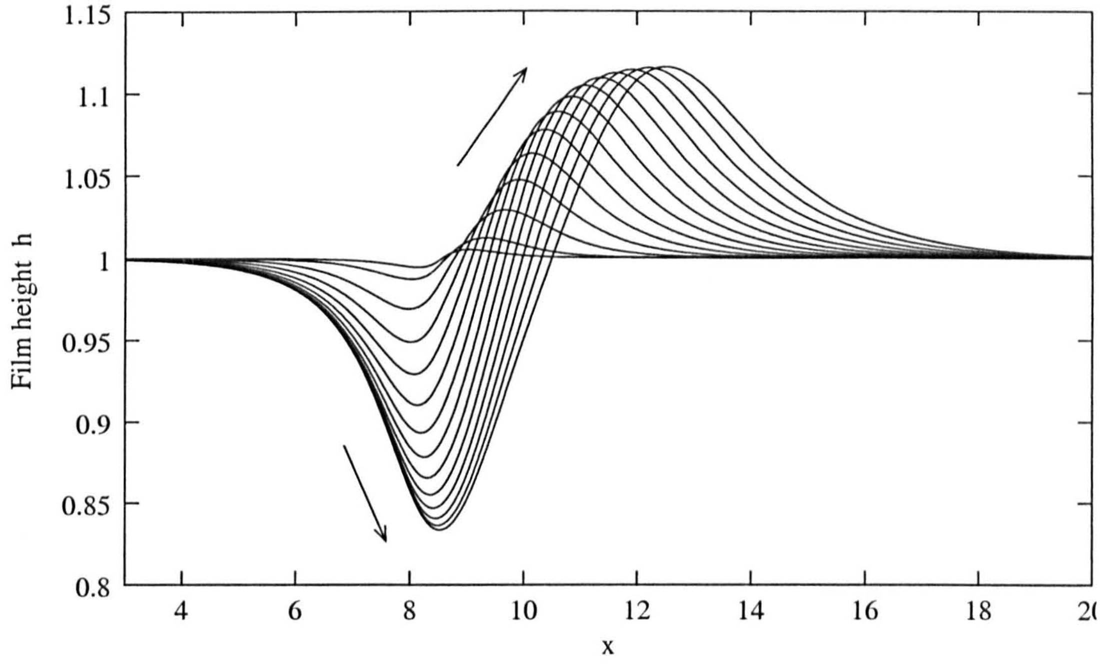

(a) a

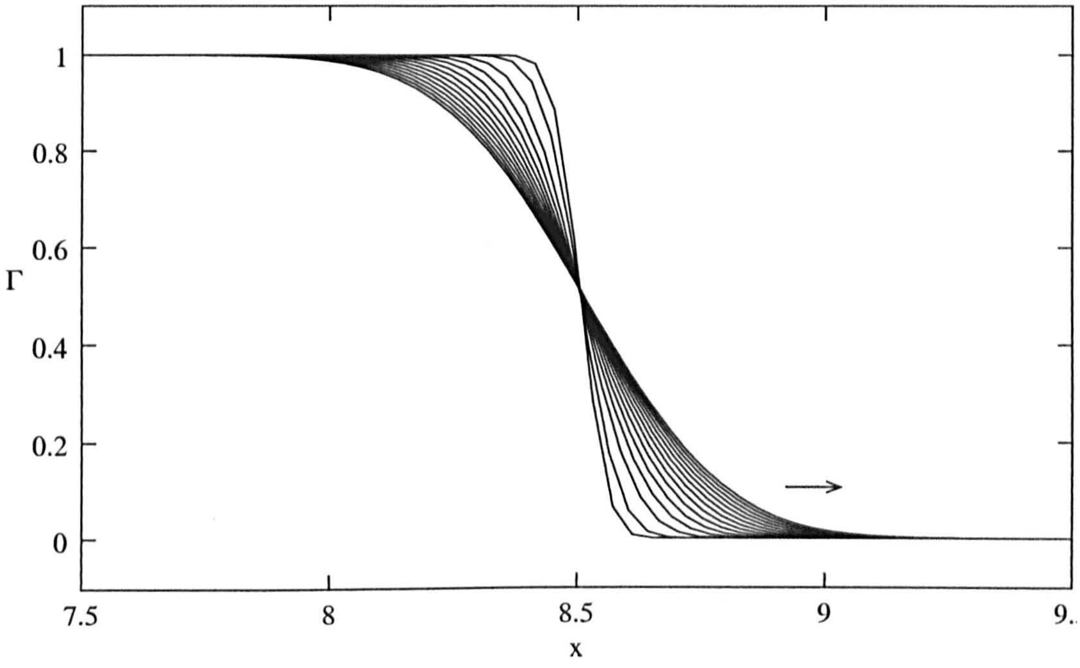

(b) a

Figure 6.14: Surface and concentration profiles from $t = 0.1$ to 2.5 in $\Delta t = 0.1$ steps. The arrows mark the direction of evolution.

Streamlines show that the same mechanisms as in LT model are in play in forming the capillary hump. Figure 6.15 shows the spatio–temporal evolution of the liquid substrate under the influence of a surface tension gradient in the direction of flow. The surface stress generated by the surfactant gradient causes fluid to move relatively fast, forming a hump. Since the Marangoni number is small, the resulting shock front has a small amplitude. The presence of a background flow removes the possibility of vortex formation. A more rapid and large amplitude wave formation can be expected for larger Marangoni numbers. The Marangoni number used in this simulation is ε times smaller than the one used in the LT model. However to obtain convergence in the case of large Marangoni number, a very fine grid resolution is required. This arises partially due to the fact that we solve two diffusion equations for the grid to disperse the nodes according to the deforming boundary. The Jacobian consists of derivatives for those equations, and higher skewness in the elements makes the Jacobian negative preventing convergence by Newton methods employed in our FEM model.

The Figure 6.16 shows the u velocity component along the surface at different nondimensional time steps. The surface velocity has its maximum at the trough bottom where the shear stress is maximum. The wave peak too has a higher velocity than the background flow velocity. As the concentration front spreads, the maximum velocity drops. At this very early stage, the movement of the surfactant front is not clearly captured. However, the Figure 6.14(a) shows that by $t = 2.5$ the peak height attains its maximum value.

6.4 Summary

Important evolution patterns with respect to a few of the parameters were examined in this chapter. The spreading of a surfactant strip on a stationary substrate as well as a surfactant front on moving substrate were presented. The Reynolds number

(a) t=0.5

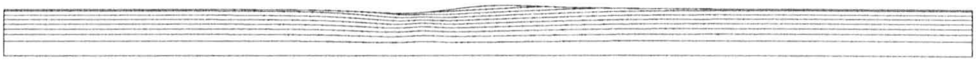

(b) t=1.0

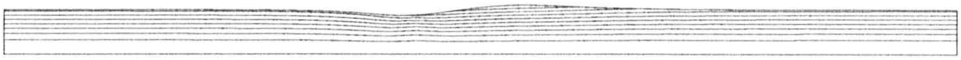

(c) t=1.5

(d) t=2.0

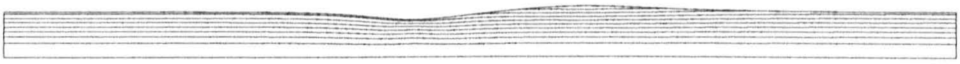

(e) t=2.5

Figure 6.15: Fully nionlinear evolution of a surfactant front on a flowing film. Flow is from left to right. The initial development matches the LT results.

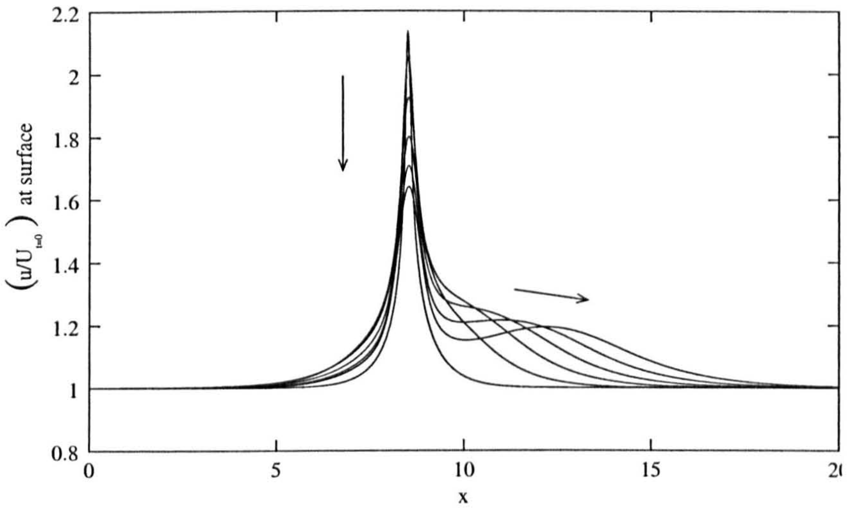

Figure 6.16: Normalized u velocity component along the free surface at $t = 0.1, 0.5, 1.0, 1.5, 2.0$ and 2.5. The trough bottom has the maximum velocity since the Marangoni stress is maximum at the point. The wave peak too has a higher velocity than the background flow velocity. The arrows mark the direction of evolution.

controls the speed of the fluid deformation as well as spreading rates. The deformation of a stationary film under the influence of Marangoni stresses has two stages (with a possibility of a third one which we do not capture here). First is the rapid formation of a depression extensively thinning the film beneath the surfactant layer. The second stage is a slower evolution of the film expanding the thinned area. The possible influence of the surfactant strip width on the flow and on the nonlinearity factor is examined. The ε_{est} remain closer to $\mathcal{O}(1)$ for a substantial period even after the monotonic slow evolution is reached.

The application of body forces by applying nonzero Stokes number introduces asymmetry to the otherwise symmetric flow cells in the case of a surfactant strip on a stationary substrate. The application of body forces influences the flow as it tries to counter the growth of the capillary ridges. This together with the interaction of the vortices violates the symmetry. Very likely the bifurcation can occur in either direction, so numerical artifacts give preference to the stronger vortex.

Finally, the spreading of a surfactant front on a moving film is simulated using the fully nonlinear model. The evolution of the surface is studied for a short period of time. It behaves similarly to the lubrication theory model except for the fact that the shock is spread out into the flow direction.

The possible conclusions from the investigation up to now are presented in the next chapter. The future developments too are discussed.

Chapter 7

Conclusions and recommendations for future work

This thesis examined the effect of background flow on the capillary wave induced by Marangoni stress and proposes a new numerical tool to analyse the spreading problem. Unlike the existing lubrication theory model, the fully nonlinear model we treated in this thesis not only predicts the spreading rates but also provide a clear picture of flow within the liquid substrate. The integrable stress singularity at the tip of the surfactant layer at the beginning, which the lubrication theory fails to capture, is treated in this thesis using the weak formulation of FEM. As a result we observe vortex formation beneath the surfactant tip. However as we used smaller Péclet numbers this singularity does not persist for long. We use the fully *non linear simulations* to extract the ratio of length scales used in determining the region of applicability of *lubrication theory* for predicting spreading rates and surface profiles.

The spreading of surfactant fronts, drops and strips on a stationary substrate are well studied with respect to drug delivery in to lungs [37, 34, 53, 17]. However there are many other applications, especially from the chemical engineering point of view, where surface tension gradients on flowing films occur. We described a few applications where localised surface tension gradients on flowing films alter normal behaviour in chapter 1 §1.2. This thesis deals with the initiation, propagation and destruction of surface instabilities caused by surface tension gradients on flowing films.

The conclusions of the findings in this thesis are presented under three sections: the effects of surface tension gradients on flowing films, lubrication theory model vs nonlinear model and finally the sensitivity of the parameters. Here we discuss the future development of this line of research.

7.1 Onset and evolution of surface instabilities under Marangoni stresses on a flowing film

Surface tension gradients that arise on flowing thin films are a common place problem in chemical engineering as well as in medical sciences. In this thesis we concentrate on the evolution of surface instabilities as well as spreading rates. Furthermore the interaction of the bulk flow with the localised instability is examined. The nonlinear coupling terms are introduced into the evolution equations to this end, and their effects are throughly examined for a wide range of parameter space. The directional background flow (of the film) violates the symmetry of the spreading problem and two distinct cases arise as a result: (1) co-current surfactant gradient and (2) counter-current (or adverse) surfactant gradient. In either case the background flow forces the shock waves to break in a finite time.

Solutions for the evolution equations derived using lubrication theory are sought for both cases using numerical PDE solvers. To this end we developed a solution engine utilising C programming language by way of *method of lines* coupled with an RKF45 integrator.

Surfactant gradient along the flow

The surfactant concentration drops downstream to a proscribed concentration much lower than the CMC generating a surfactant gradient in the direction of flow. The localised shear stress that arises as a result of the surface tension gradient forms a shock front. The extra nonlinearity introduced by the bulk flow controls the evolution of the surface wave as the Marangoni effect diminishes due to weakening concentration gradient. In the case of a stationary substrate, the shock speed slows down as the magnitude of the gradient diminishes. In the presence of a background flow, the coupling term $P_x Re h^2 h_x$, independent of the concentration, dominates the evolution of the surface. At high Péclet numbers, the shock with a sharp front moves faster than the surface velocity of the bulk stretching the surfactant layer. As a result, a very weakly concentrated surfactant layer spreads with the shock front, stabilising the shock.

Unlike for the stationary substrate where the shock fronts live for a longtime, we identified two mechanisms of wave destruction in finite time under the influence of the background flow. The shock wave destruction is solely controlled by the Péclet number. The breaking mechanisms switch as $\mathcal{P}e_s$ decreases. For large $\mathcal{P}e_s$, the trough wall become unstable under the influence of bulk flow as well as the advection of surfactant. For small Péclet numbers the shock wave peak folds over, destroying the wave. The threshold values of $\mathcal{P}e_s$ between two mechanisms fall within the range $30 < \mathcal{P}e_s < 35$. The larger the Péclet number, the lager will be the shock amplitude and steeper will be the shock front.

Marangoni number affects the magnitude of the initial disturbance and short time evolution of the surfactant and the surface. The larger the $\mathcal{M}a$, the larger will be the disturbance and faster will be the initial wave speed. The initial wave consists of a trough and a peak that separates into components when Marangoni number is small. It is strong enough to make a surface disturbance, but the surface evolution is controlled by a nonlinear term that connects the bulk flow to surface wave equation. The peak moves downstream with almost constant speed with little change to the geometry for longer periods. Nonlinearity eventually causes the destruction by destabilising the peak. This situation physically arises when the surface is highly contaminated or the surfactant is very weak.

Surfactant gradient opposing the flow

The adverse surface tension gradient on a flowing liquid film generates a short lived shock front. The behaviour is greatly affected by Marangoni number. Large $\mathcal{M}a$ results in the forming of a shock front that moves upstream, opposing the flow, forming a stagnated liquid regime before destruction of the shock wave. There is only one mechanism of wave breaking: the inner wall of the shock structure overturns under the influence of bulk flow.

Again we observe that the Péclet number has an effect on the lifetime of the shock front. Larger $\mathcal{P}e_s$ generate high amplitude shock fronts which has lower lifetime than the shocks generated by smaller $\mathcal{P}e_s$. The same observation was made with respect to Marangoni number. The larger the amplitude of the shock, the sooner the wave breaks. Both, the Marangoni number and Péclet number collectively contribute to the destruction of the instability. The lifetime of the shock wave is short compared to the previous case we discussed.

In most of the occurrences of differential surface tension gradients, dry spots were formed. This is the cause for the rivulet formation in packed bed distillation towers. As we see here, when an adverse surface tension gradient occurs there is a strong possibility of the formation of a dry spot with a solid liquid contact line, forcing the fluid film to flow around it. This gives rise to rivulet flows. Both numerical procedures we employed here fail to capture the topological changes necessary to describe the formation of the dry spots. In recommended future developments (section 7.3) we propose methods to mitigate this shortfall.

7.2 Lubrication theory model Vs nonlinear model

The use of lubrication theory has become the core to modelling of the spreading problem. The assumptions are too drastic for free surface problems where surface deformation is large. We concentrated on this particular point and proposed a numerical method which would hold for an initial surge of the variables as well as for long time evolutions alike. Fully nonlinear transport equations were solved using finite element methods with special grid dispersing scheme which we described in chapter 3.

The key element in lubrication theory (LT) is the use of the long wave assumption which specifies a dominant geometrical length scale. This is used to define a nonlinearity coefficient used to order the magnitude of the associated terms. Upon application, it removes inertial terms from the Navier–Stokes equations. The fully nonlinear model (NLM) on the other hand retains all nonlinear terms and as a result exotic flow patterns arise at initial stages. Since we do not make any simplifications to flow equations *a priori*, we should be able to extract the order of magnitudes of the flow variables which would decide the value of nonlinearity coefficient. The lubrication theory suggests that $v \sim \varepsilon u$. We extract ε by evaluating the v/u based on the nonlinear model. It shows that ε remains appreciable but less than unity for a considerable time. However, with regard to global measures at large times, the lubrication theory seems to hold. But the local flow may not necessarily follow the lubrication theory. Interesting dynamics appear at the beginning of the evolution process.

The NLM shows that the stress discontinuity at the beginning gives rise to counterotating vortices. Since we used a moderate Péclet number, this singularity vanished as time elapsed. The vortices disappear as lateral flow begins to dominate. NLM simulations shows that the evolution of the surface occurs in two stages (actually there should be three stages). A very fast formation of a depression beneath the surfactant layer due to rapid out flow of the substrate and secondly, once a threshold depression thickness is reached, an expansion of the thinned area. The possible third stage is the film rupture leading to a dry spot and fingering instability. The NLM, due to obvious numerical implementation limitations, cannot capture this topological change.

The NLM simulations shows that the film thickness decreases by 95% within a very short period followed by a quasi steady stage. The surface structure differs from the LT model simulation results but the spreading rates were closely matched. The NL model too observe the similarity $x \sim t^{1/3}$ during the quasi-steady evolution.

A remarkable difference that comes to light is the spreading of the surfactant on the deformed surface. In most of the previous work, the existence of the surfactant layer up to the full length of the deformation is envisaged (i.e. the surfactant covers the deformation up to the tip of the shock front). In both cases analysed using nonlinear FEM model, the stationary and moving substrates, the surfactant front falls short of the full extent of the deformation. It extends beyond the depression but stays behind the peaks of the deformed surface. Starov [99] observed tracer particles moving ahead of the depression. He concludes that the surfactant occupies more surface area than the depressed zone but does not elaborate to which extent (whether it is far away from the depression or not). However, we observe (in our FEM simulations) that the velocity field expands horizontally beyond the total deformed area up to $5d$ within few a short duration (this arises as a result of inertial terms we included in the model. See Figure 6.8). Hence particle movement beyond the depressed area can be due to liquid movement as well as for surface movement of the surfactant.

7.3 Recommendations for future work

Spreading of a surfactant on a liquid substrate poses a heretofore unresolved instability. The thinning of the substrate leads to film rupture forming a dry spot. The contact line formed between the liquid and the solid substrate behind the capillary ridge then penetrates into the bulk liquid, forming fingering patterns [69, 71, 70]. Attempts to resolve this instability by performing non-normal growth analysis on the linearised disturbance operator resulting from LT model has not been successful so far. It shows the existence of pseudo-spectral modes with parasitic growth within early-time spreading but decays with growing time.

The current FEM analysis can incorporate eigenanalysis by means of Arnoldi's method[1]. This allows us to evaluate the most dangerous modes (largest positive eigenvalue forms the most dangerous mode) of the Jacobian of the discretisation matrix. Once the critical eigenvalues of fully nonlinear operator are identified, we can observe the evolution of the system along that branch to see whether it leads to film rupture. The resulting eigenvalue analysis can be extended to pseudo-spectral analysis of a disturbance as well. However the limitation of FEM that it cannot incorporate topological changes (e.g. the initial domain dividing in to independent sub domains as a result of pinching off) would pose a difficulty.

The failure of linear operator analysis to characterze the experimentally observed instability so far clearly shows the need for more sophisticated tools. Use of FEM with weak formulation to simulate the spreading of a surfactant using fully nonlinear flow equations provides a step forward. But the nature of the instability, i.e. film rupture preceding the dendritic growth, might need more flexible methods than grid based systems. To this end we can propose the use of Smoothed Particle Hydrodynamics (SPH) [75]. SPH, though having roots in the early 60s, is relatively new technique for hydrodynamic calculations. It is widely used in astrophysics to

---

[1] ARPACK libraries provides the codes that carry out eigenvalue solvers

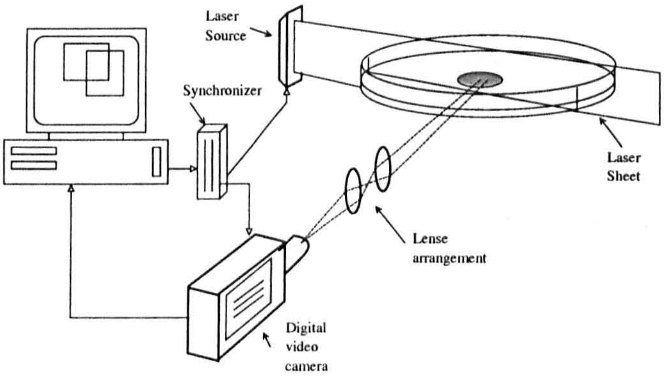

Figure 7.1: Schematic diagram of μPIV experimental arrangement (not to scale).

model gas clouds and star formations [75]. SPH is a gridless Lagrangian method using a pseudo particle interpolation to compute hydrodynamic variables. These variables are interpolated for each particle with respect to the neighbouring particles which may be disorderly positioned. These particles, which contains a small mass, Lagrangian position, velocity and other properties, resemble nodes in finite difference method if the positions are fixed. The interpolation is based on the theory of integral interpolants using interpolation kernels which approximate a delta function. The interpolants are analytic functions which could be differentiated without the use of a grid. This technicality in formulation provides the handle needed to treat film rupture in the spreading problem. The applicability of SPH for free surface flow has been studied by Monaghan [75]. SPH requires the fluid to be compressible which questions the applicability to hydrodynamics. However, in reality almost all liquids are compressible with very small compressibility factor (For a detailed explanation of modelling free surface flows reader is referred to [75]). Since there are no drastic simplifications of flow equations, the use of the method with finite but large number of particles to model the spreading problem would provide a strong tool in the investigation of film rupture.

Though there are numerous theoretical works carried out on spreading of a surfactant covering many aspects, not many experiments have been carried out. Even in the experiments (these work has been discussed in detail in chapter 2 §2.4.2), attention predominantly is on the spreading rates. Gaver and Grotberg [33] carried out some flow visualisation using powder suspensions and ink drops. But the tracking of surface elevation or the change of shape of the surface has not been done. This lack of knowledge on thinning deprives the understanding of the instability. As we have shown, the depression could form ultra thin films beneath the surfactant drop within a fairly short time. There should be a critical thickness below which disjoining pressure becomes active. Since there are new technologies with laser beam tracking systems, new experiments should be carried out. For instance, micro-Particle Image Velocimetry (μPIV) provides the facility of flow imaging across a selected plane. μPIV is capable of measuring flow velocities in microchannels would produce better results by far to those available to-date. PIV in essence is a method of using consecutive images to determine flow field. The liquid is doped with micro-sized particles (in some cases luminous). A flow plane is marked by a laser sheet. The laser beam flicker in synchronous with the high speed video camera which grab images of the illuminated plane. Relative particle movements were processed using images and correlations defined to generate velocity field and other required data. However μPIV would not be able to measure the concentration on the surface directly. As alternatives selective dye particles or a secondary non invasive spectrophotometric measuring techniques could be used. Figure 7.1 shows the schematic diagram of a possible μPIV experiment. The surface evolution of spreading on a flowing film also needs to be experimentally validated.

7.4 Concluding remarks

Within the scope of this thesis we described the evolution of a surface instability due to Marangoni stresses on flowing films in an attempt to describe some observations made in some chemical engineering applications. Analysing a problem using as many tools as possible would result in improving the knowledge and understanding. Analysis of the spreading of a surfactant layer on a liquid substrate was limited to lubrication theory thus far. Here, a new model/method is proposed to resolve the limitations posed by lubrication theory. We believe that the new tool would widen the understanding of the spreading problem.

Appendix A

The Runge–Kutta–Fehlberg Method (RKF45)

A.1 RKF coefficients

In RKF45 method the fifth order solution is compared with the fourth order solution to estimate the error. If the error is larger than a specified accuracy, then the step size h is reduced. If the answer agree to more significant digits than required, then the step size is increased. The maximum reduction of step size is 1% of the previous step size while the maximum increase is limited to 10% of it.

There are six coefficients to be calculated for each step taken.

$$K_i = hf\Big(t_k + \alpha_i\, h,\ \ y_k + \sum_{j=1}^{i} \beta_j\, k_j\Big), \qquad i = 1, 2, \ldots, 6 \tag{A.1}$$

The table A.1 gives the coefficients β_j and α_i for each expansion of k_i.

The numerical solution to the initial value problem is made using Runge–Kutta method of order 4:

$$y_{k+1} = y_k + \frac{25}{216}K_1 + \frac{1,408}{2,565}K_3 + \frac{2,197}{4,104}K_4 - \frac{1}{5}K_5 \tag{A.2}$$

	β_1	β_2	β_3	β_4	β_5	α
K_1	0					0
K_2	$\frac{1}{4}$					$\frac{1}{4}$
K_3	$\frac{3}{32}$	$\frac{9}{32}$				$\frac{3}{8}$
K_4	$\frac{1{,}932}{2{,}197}$	$-\frac{7{,}200}{2{,}197}$	$\frac{7{,}296}{2{,}197}$			$\frac{12}{13}$
K_5	$\frac{439}{216}$	-8	$\frac{3{,}680}{513}$	$-\frac{845}{4{,}104}$		1
K_6	$-\frac{8}{27}$	2	$-\frac{3{,}544}{2565}$	$\frac{1{,}859}{4{,}104}$	$-\frac{11}{40}$	$\frac{1}{2}$

Table A.1: Coefficients that incorporate the evaluation of k_i in (A.1)

The error is evaluated using$\left(\|(y_{k+1})_{4^{th}order} - (y_{k+1})_{5^{th}order}\|\right)$.

$$\text{Error} = \left|\frac{1}{360}K_1 - \frac{128}{4275}K_3 - \frac{2197}{75240}K_4 + \frac{1}{50}K_5 + \frac{2}{55}K_6\right| \tag{A.3}$$

A.2 Algorithm

$y' = f(t,y)$ on $[A,B]$ with $y(A) = y_0$

```
Tol:= $1 \times 10^{-5}$                      Error control tolerence
INPUT A,B and Y(0)                            End points and initial value
INPUT N                                       Tentative number of steps
H:= [A - B]/N                                 Initial step size
$H_{min}$:= H/64 and $H_{max}$:=Hx64          Minimum and maximum step sizes
T(0):= A, J:= 0, T := A                       Initialize
WHILE T <B DO                                 Beginning the loop
.   IF T+H >B THEN H := B-T                   The last step
.   T := T(J), Y := Y(Y)
.   $K_1 = \ldots$                            As in(A.1)
.   $K_2 = \ldots$
.   $K_3 = \ldots$
.   $K_4 = \ldots$
.   $K_5 = \ldots$
.   $K_6 = \ldots$
.   ERROR := $\|\ldots\|$                     As in (A.3)
.   IF ERROR < Tol THEN                       Accept solution
.      Y(J+1):= ...                           As in (A.2)
.      $H = 0.9(ERROR/Tol)^{0.2}H$            Next step size
.      T(J+1):= T + H
.      J=J+1
.   IF ERROR > Tol THEN                       If the test fails then
.      $h = 0.1 * H$                          reduce the step size
END
```

Bibliography

[1] A.W. Adamson. *"Physical chemistry of surfaces"*. Interscience, New York, 1960.

[2] J. Adler and L. Sowerby. "Shallow three–dimensional flows with variable surface tension". *J. Fluid Mech.*, 42:549–559, 1970.

[3] J. Ahmed and S.H. Hansen. "A simple quantitative treatment of the spreading of monolayers on thin liquid films". *J. Collid Int. Sci.*, 38 (3):601–604, 1972.

[4] jr. J.D. Anderson. *"Computational Fluid Dynamics: the basics with applications"*. McGraw Hill Inc., New York, 1995.

[5] R. Aris. *"Vectors, Tensors and the Equations of Fluid Mechanics"*. Dover Publications Inc, New York, 1989.

[6] G.K. Batchelor. *"An introduction to fluid dynamics"*. Cambridge University Press, Cambridge, 1987.

[7] T.B. Benjamin. "Wave formation in laminar flow down an inclined plane". *J. Fluid Mech.*, 2:554–574, 1957.

[8] A.L. Bertozzi, A. Münch, X. Fanton, and A.M. Cazabat. "Contact line stability and undercompressive shocks in driven thin film flow". *Phys. Rev. Lett.*, 81(23):5169–5172, 1998.

[9] A.L Bertozzi, A. Münch, and M. Shearer. "Undercompressive shocks in film flows". *Physica D*, 11(10):431–464, 1999.

[10] M.S. Borgas and J.B. Grotberg. "Monolayer flow on a thin film". *J.Fluid Mech.*, 193:151–170, 1988.

[11] D.W. Camp and J.C. Berg. "The spreading of oil on a water in the surface–tension regime". *J. Fluid Mech.*, 184:445–462, 1987.

[12] C.M. Casiola and M Landrini. "Nonlinear long waves generated by a moving pressure disturbances". *J.fluid Mech.*, 325:399–418, 1996.

[13] H.C. Chang. "Wave evolution on a falling film". *Ann. Rev. Fluid Mech.*, 26:103–136, 1994.

[14] K.A. Cliffe, S.J. Tavener, and A.A. Wheeler. "An orthogonal mapping technique for the computation of a viscous free–surface flow". *Int. J. Num. Methods Fluids*, 15:1243–1258, 1992.

[15] J.H. Clint. *"Surfactant Aggregation"*. Blackie, London, 1992.

[16] P. Colinet, J.C. Legros, and M.G. Velarde. *"Nonlinear Dynamics of Surface–Tension–Driven Instabilities"*. Willey–VCH, New York, 2001.

[17] R.V. Craster and O.K. Martar. "Surfactant transport on mucus film". *J.Fluid Mech.*, 425:235–258, 2000.

[18] K.N. Cristodoulou and L.E. Scriven. "Discretization of free surface flows and other moving boundary problems". *J. Comput. Phys.*, 99:39–55, 1992.

[19] S.H. Davis. "Thermocapillary instabilities". *Ann. Rev. Fluid Mech.*, 19:403–435, 1987.

[20] R. Defay, I. Prigogine, A. Bellemans, and D.H. Everett. *"Surface Tension and Adsorption"*. Longmans, London, 1966.

[21] N. Dipietro, C. Huh, and R.G. Cox. "The hydrodynamics of the spreading of one liquid on the surface of another". *J. Fluid Mech.*, 84:529–549, 1978.

[22] P.G. Drazin. *"Solitons"*. Cambridge University Press, London, 1983.

[23] P.G. Drazin and W.H. Reid. *"Hydrodynamic Stability."*. Cambridge University Press., Cambridge, 1981.

[24] I.S Duff and A.M. Erisman. *"Low dimensional models of thin film fluid dynamics."*. Oxford University Press., New York, 1989.

[25] D.A. Edwards, H. Brenner, and D.T. Wassan. *"Interfacial Transport Process and Rheology"*. Butterworth-Heinemann, New York, 1991.

[26] F.F. Espinosa. *Spreading of surfactant in a small pulmonary airway.* PhD thesis, Massachusetts Institute of Technology, 1991.

[27] M. Foda and R.G. Cox. "The spreading of thin liquid films on a water–air interface". *J. Fluid Mech.*, 101:33–51, 1980.

[28] M. Foda and R.G. Cox. "The spreading of thin liquid films on a water–air interface". *J. Fluid Mech.*, 101:33–51, 1980.

[29] M. Foda and R.G. Cox. "The spreading of thin liquid films on a water-air interface". *J. Fluid Mech.*, 101((1)):33–51, 1980.

[30] B. Frank and S. Garoff. "Origins of the complex motion of advancing surfactant solutions". *Langmuir*, 11:87–93, 1995.

[31] G.L. Gaines. *"Insoluble Monolayers at Liquid–Gas Interface "*. Interscience, New York, 1966.

[32] P.L. Garcia-Ybarra and M.G. Velarde. "Oscillatory Marangoni–Bénard interfacial instability and capillary–gravity waves in single and two component liquid layers with or without Soret thermal diffusion. ". *Phys. Fluids*, 30 (6):1649–1655, 1987.

[33] D.P. Gaver and J.B. Grotberg. "The dynamics of a localised surfactant on a thin film". *J.Fluid Mech.*, 213:127–148, 1990.

[34] D.P. Gaver and J.B. Grotberg. "Droplet spreading on a thin viscous film". *J. Fluid Mech.*, 235:399–414, 1992.

[35] R.T. Goodwin and W.R. Schowalter. "Arbitarily oriented capillary–viscous planar jets in the presence of gravity". *Phys. Fluids*, 7 (5):954–963, 1995.

[36] J.B Grotberg. "Pulmonary flow and transport phenomena". *Ann. Rew. Fluid Mech.*, 26:529–571, 1994.

[37] J.B. Grotberg and O.E. Jensen. "Respiratory fluid mechanics and transport process.". *Ann. Rev. Biomed. Eng.*, 3:421–457, 2001.

[38] O.E. Grotberg, J.B Jensen and D. Halpern. "Theoretical study of surfactant and liquid delivery into the lung". *J. App. Physio.*, 85(1):333–352, 1998.

[39] D. Halpern and J.B. Grotberg. "Dynamics and transport of a soluble surfactant on a thin film". *J.Fluid Mech.*, 237:1–11, 1992.

[40] J.F. Harper. "The leading edge of an oil slick, soap film, or bubble stagnant cap in Stokes flow". *J. Fluid Mech.*, 237:23–32, 1992.

[41] J.F. Harper and J.F. Dixon. "The leading edge of a surface film on contaminated water". *Proc. Fifth Australian Conf. Hydraulics Fluid Mech., Christchurch NZ*, Vol. 2:499–505, 1974.

[42] S. He and J.B. Ketterson. "Surfactant–driven spreading of a liquid on a vertical surface". *Phys. Fluids*, 7 (11):2640–2647, 1995.

[43] B.N. Hewakandamby. Enhancement of the phase separation of oil water dispersions at a stationary hydraulic jump. Master's thesis, University of Manchester Institute of science and technology, 1999.

[44] B.N. Hewakandamby and W.B. Zimmerman. "Characterisation of hydraulic jumps/falls with surface tension variations in thin film flows". *Dynamics of Atmospheres and Oceans*, 34:349–364, 2001.

[45] G.M. Homsy and E. Meiburg. "The effect of surface contamination on thermocapillary flow in a two–dimensional slot". *J. Fluid Mech.*, 139:443–459, 1984.

[46] L.W. Horn and S.H. Davis. "Apparent surface tension hysteresis of a dynamical system". *J. Colloid Interface Sci.*, 51(3):459–476, 1975.

[47] K.H. Huebner. *"Finite Element Method for Engineers"*. John Wiley, New York, 1975.

[48] Z. Hussain, M. Faitma, and J. Ahmed. "The rate of spreading of monolayers on liquids". *J. Collid Int. Sci.*, 50 (1):44–48, 1974.

[49] J.N. Israelivich. *"Intermolecular and surface forces"*. Academic Press, London, 1998.

[50] O.E. Jensen. "Self Similar, surfactant–driven flows". *Phys. Fluids*, 6(3):1084–1094, 1994.

[51] O.E. Jensen. "The spreading of insoluble surfactant at the free surface of a deep fluid layer". *J.Fluid Mech.*, 293:349–378, 1995.

[52] O.E. Jensen and J.B. Grotberg. "Insoluble surfactant spreading on a thin viscous film: shock evolution and film rupture". *J.Fluid Mech.*, 240:259–288, 1992.

[53] O.E. Jensen and J.B. Grotberg. "The spreading of heat or soluble surfactant along a thin liquid film". *Phys. Fluids*, 5 (1):58–68, 1992.

[54] O.E. Jensen and D. Halpern. "The stress singularity in surfactant-driven thin-film flows. Part 1. Viscous effects". *J.Fluid Mech.*, 372:273–300, 1998.

[55] O.E. Jensen and D. Halpern. "The stress singularity in surfactant-driven thin-film flows. Part 2. Inertial effects". *J.Fluid Mech.*, 372:301–322, 1998.

[56] O.E. Jensen, D. Halpern, and J.B Grotberg. "Transport of a passive solute by surfactant–driven flows". *chem. Eng. Sci*, 49:1107–1117, 1994.

[57] S. Kalliadasis. Private communications. Department of Chemical Engineering, University of Leeds.

[58] S.F. Kistler and L.E. Scriven. Coating flows. In J.R.A. Pearson and S.M. Richardson, editors, *Computational Analysis of Polymer Processing*, pages 243–299, 1983.

[59] N.M. Kovalchuk, V.I. Kovalchuk, and D. Vollhardt. "Numerical study of the Marangoni instability resulting in surface tension auto-oscillations: General regularities of the system evolution". *Phys. Rev. E*, 63, 2001.

[60] V.I. Kovalchuk, H. Kamusewitz, D. Vollhardt, and N.M. Kovalchuk. "Auto-oscillation of surface tension". *Phys. Rev. E*, 60:2029–2036, 1999.

[61] P.K. Kundu. *"Fluid Mechanics"*. Academic Press Inc, San Diego, 1990.

[62] P. Lam, K.J. Wynne, and G.E. Wnek. "Surface-tension-confined Microfluidics". *Langmuir*, 18(3):948–951, 2002.

[63] L.D. Landau and E.M. Liftshitz. *"Surface Tension and Adsorption"*. Pergamon, Oxford, 1989.

[64] V.G. Levich. *"Physicochemical hydrodynamics"*. Prentice Hall, New York, 1962.

[65] J. Lucassen. "Lingitudinal capillary waves. Part 1. Theory". *Trans. Farade Soc.*, 64:2221–2229, 1968.

[66] V. Ludviksson and E. N. Lightfoot. "The dynamics of thin liquid films in the presence of surface-tension gradients". *AIChE J.*, 17(5):1166–1173, 1971.

[67] A. Marmur and M.D. Lela. "Dissolution of a drop on a liquid surface leading to surface waves and interfacial turbulence". *Chem. Eng. Commun.*, 13:133–137, 1981.

[68] O.K. Matar and S.M. Troian. "Linear stability analysis of an insoluble surfactant monolayer spreading on a thin liquid film". *Phys. Fluids*, 9:3645–3657, 1997.

[69] O.K. Matar and S.M. Troian. "Growth of non-modal transient structures during the spreading of surfactant coated films". *Phys. Fluids*, 10:1234–1236, 1998.

[70] O.K. Matar and S.M. Troian. "Spreading of a surfactant monolayer on a thin liquid film: Onset and evolution of a digitated structures". *Chaos*, 9:141–153, 1999.

[71] O.K. Matar and S.M. Troian. "The development of transient fingering patterns during the spreading of surfactant coated films". *Phys. Fluids*, 11:3232–3246, 1999.

[72] J.H. Mathews. *"Numerical Methods for Computer Science, Engineering and Mathematics".* Prentice–Hall, New York, 1987.

[73] J.C. McDonald, D.C. Duffy, D.T Anderson, J.R. Chiu, H.K. Wu, and G.M. Schueller, O.J.A. Whiteside. "Fabrication of microfluidic systems in poly(dimetylsiloxane)". *Elecrophoresis*, 21(1):27–40, 2000.

[74] G.P. Moeckle. "Thermodynamics of an Interface". *Arch. Ration. Mech. Anal*, 57:255–280, 1975.

[75] J.J. Monaghan. "Simulating free surface flows with SPH". *J. Comp. Phys.*, 110:399–406, 1994.

[76] A. Münch and A.L. Bertozzi. "Rarefaction–undercompressive fronts in driven films". *Phys. Fluids*, 11(10):2812–2814, 1999.

[77] C. Nakaya. "Long waves on a thin fluid layer flowing down an inclined plane ". *Phys. Fluids*, 18:1407–1412, 1975.

[78] A.A. Nepomnyashchy, M.G. Velarde, and P. Colinet. *"Interfacial Phenomena and Convection"*. Chapman and Hall, Boca Raton, 2002.

[79] A. Oron, S.H. Davis, and S.G. Bankoff. "Long–scale evolution of thin liquid films". *Rev. Mod. Phys.*, 69(3):931–980, 1997.

[80] R. Parrot. *Nonlinear Instability of Driven Contact Lines.* PhD thesis, University of Leeds, 2001.

[81] S.M. Pimputkar and S. Ostrach. "Transient thermocapillary flowing thin liquid layers". *Phys. Fluids.*, 23(7):1281–1285, 1980.

[82] W.h. Press, B.P. Flannery, S.A. Teukolsky, and S.A. Vetterling. *"Numerical recipes in C: The art of scientific computing"*. Cambridge University Press, Camebridge, 1988.

[83] R.F. Probestein. *"Physicochemical Hydrodynamics"*. John Wiley and Sons, New York, 1994.

[84] S.J. Proctor, M.W. Biddulp, and K.R. Krishnamurthy. "Effects of Marangoni surface tension forces on modern distillation packings". *AIChE Journal*, 44(4):831–835, 1998.

[85] B. Ramaswamy, S. Chippada, and S.W. Joo. "A full-scale numerical study of interfacial instabilities in thin-film flows". *J. Fluid Mech.*, 325:163–194, 1996.

[86] F.J. Ramsay. *Dispersion of Passive Scalars in Stratified Systems.* PhD thesis, University of Manchester Institute of science and technology, 1998.

[87] K.F. Riley, M.P. Hobson, and S.J. Bence. *"Mathematical Method for Physics and Engineer".* Cambridge University Press, Cambridge, 1997.

[88] A.J. Roberts. "Low dimensional models of thin film fluid dynamics.". *Physics Letters A*, 212:63–71, 1996.

[89] K.J. Ruschak. "A method for incorporating free boundaries with surface tension in finite element fluid–flow simulators". *Int. J. num. methods in eng.*, 15:639–648, 1980.

[90] M.N.O. Sadiku and C.N. Obiozor. "A simple introduction to the method of lines". *Int. J. Elect. Eng. Edu.*, 37(3):282–296, 2000.

[91] M. Santiago-Rosanne, A. Vignes-Adler, and M.G. Velarde. "Dissolution of a drop on a liquid surface leading to surface waves and interfacial turbulence". *J. Collid Int. Sci.*, 191:65–80, 1997.

[92] M.F. Schatz and G.P. Neizel. "Experiments on Thermocapillary Instabilities". *Ann. Rev. Fluid Mech.*, 33:93–129, 2001.

[93] W.E. Schiesser. *"The Numerical Method of Lines: Integration of partial differential equations".* Academic Press, San diego, 1991.

[94] J.C. Scott. "Flow beneath a stagnant film on water: The Reynolds ridge". *J. Fluid Mech.*, 116:283–296, 1982.

[95] L.E. Scriven. "Dynamics of a fluid interface: Equation of motion for Newtonian surface fluids". *"Chem. Eng. Sci"*, 12:98–108, 1960.

[96] L.E Scriven and C.V. Sternling. "The Marangoni Effects". *Nature*, 187:186–188, 1960.

[97] L.F. Shampine and H.A. Watts. "Global error estimation for ordinary differential equations". *ACM Trans. on Mathematical software*, 2:172–186, 1976.

[98] M.K. Smith. "The mechanisms for the long wave instability in thin liquid films". *J. Fluid Mech.*, 217:469–485, 1990.

[99] V.M. Starov, A. de Ryck, and M.G. Velarde. "On Spreading of an Insoluble Surfactant over a Thin Viscous Liquid Layer ". *J. Colloid Interface Sci.*, 190:104–113, 1997.

[100] M. Takashima. "Surface tension driven instability in a horizontal liquid layer with a deformable free surface. II. Overstability". *J. Phys. Soc. Japan*, 50(8):2751–2756, 1974.

[101] J.F. Thompson, Z.U.A. Warsi, and C.W. Mastin. *"Numerical Grid Generation Foundations and Applications"*. North–Holland, New York, 1985.

[102] B.S. Tilley, S.H. Davis, and S.G. Bankoff. "Nonlinear long-wave stability of superposed fluids in an inclined channel". *J. Fluid Mech.*, 277:55–83, 1994.

[103] S.M. Troian, E. Herbolzheimer, and S.A. Safran. "Model for the fingering instability of spreading surfactant drops". *Phys. Rev. Lett.*, 65 (3):333–336, 1990.

[104] S.M. Troian, L.X. Wu, and S.A. Safran. "Fingering instability in thin wetting films". *Phys. Rev. Lett.*, 62:1496–??, 1989.

[105] W.T. Tsai and D.K.P. Yue. "Effect of soluble and insoluble surfactant on laminar interactions of vortical flows with free surface". *J. Fluid. Mech*, 289:315–349, 1995.

[106] H.W. Van der Klooster and A.A.H. Drinkenburg. "The influence of gradients in surface tension on the mass transfer in a packed bed". *IChemE Symp. Ser.*, 56(2):2.5/21–2.5/31, 1979.

[107] B. Van Leer. "Towards the ultimate conservative difference scheme I. The quest of monotonicity.". *Lecture notes in physics*, 18:163–168, 1973.

[108] B. Van Leer. "Towards the ultimate conservative difference scheme II. Monotonicity and conservation combined in a second order scheme.". *Lecture notes in physics*, 18:361–370, 1974.

[109] S.J. Vanhook, M.F. Schatz, J.B. Swift, W.D. McCormick, and H.L. Swinney. "Long–wavelength surface–tension–driven Bénard convection: experiment and theory". *J. Fluid Mech.*, 345:45–78, 1997.

[110] M. Verschueren, F.N. van de Vosse, and H.E.H Meijer. "Diffuse–interface modelling pf thermocapillary flow instabilities in a Hele–Shaw cell". *J. Fluid Mech.*, 434:153–166, 2001.

[111] M.R.E. Warner, Craster R.V., and O.K. Matar. "Unstable van der Waals driven line rupture in Marangoni driven thin viscous films". *Phys. Fluids*, 14(5):1642–1654, 2002.

[112] G.M. Whiteside and A.D. Stroock. "Flexible Methods for Microfluidics". *Physics Today (Online edition)*, 54:42, 2001.

[113] A.V. Wouwer, Ph. Saucez, and W.E. Schiesser. *"Adaptive Method of Lines"*. Chapman & Hall, Boca Raton, 2001.

[114] A. Yeckel. Department of Chemical Engineering, University of Minnesota, USA, yeckel@min.edu. He is maintaining/developing the CHARISMA code currently.

[115] C.S. Yih. Stability of parallel laminar flow with a free surface. In *Proc. 2nd U.S. Congr. App. Mech. ASME*, pages 623–628, 1954.

[116] C.S. Yih. " Fluid motion induced by surface-tension variation". *Phys. Fluids*, 11 (3):477–480, 1968.

[117] C.S. Yih. "Three-dimensional motion of a liquid film induced by surface-tension variation or gravity". *Phys. Fluids*, 12 (10):1982–1987, 1969.

[118] W.B. Zimmerman. "Excitation of surface waves due to thermocapillary effects on a stably stratified layer". *Submitted to J.Fluid Mech.*

[119] W.B. Zimmerman. Formation of a stationary hydraulic fall at an abrupt change of surface tension on a shallow fluid layer. In Weaire D. and Banhart J., editors, *Foams and films: proceedings of International workshop on foams and films*, pages 33–40, 1999.

[120] F.J. Zuiderweg and T. Yanagi. "Marangoni effect, liquid phase resistance or maldistribution". *IChemE Symp. Ser.*, 128:A181, 1992.